Structural and biochemical investigations of the cornea and the trabecular meshwork

Thesis submitted to Cardiff University for the degree of Doctor of Philosophy

December 2013

Elena Koudouna

Structural Biophysics Research Group
School of Optometry & Vision Sciences
Cardiff Centre for Vision Sciences
College of Biomedical and Life Sciences
Cardiff University

Abstract

The experiments which comprise this thesis focused on structure-function relationships in two distinct collagen-rich connective tissues of the eye, the cornea and the trabecular meshwork. The cornea is the transparent tissue that covers the front of the eye and has the ability to transmit and refract light. Corneal transparency is the result of the unique organisation of collagen fibrils in the corneal stroma matrix, of which sulphated proteoglycans are key regulators, owing to the presumed importance of the sulfation pattern of corneal proteoglycans. The trabecular meshwork is the sponge-like tissue located around the cornea through which the bulk of the aqueous humor flows towards the juxtacanalicular tissue and the inner wall of Schlemm's canal to exit the eye and control intraocular pressure. First part of the current research examined the chemical composition and sulphur speciation during corneal embryogenesis in order to elucidate important changes in the biochemical signature of the corneal matrix associated with the acquisition of transparency. It also investigated the content and distribution of distinct sulphur species through the depth of the mature corneal stroma and assessed biochemical-functional relationships that ultimate render tissue transparency. The research also studied the three-dimensional ultrastructure of the human trabecular meshwork, particularly the ultrastructure of the juxtacanalicular tissue that lies adjacent to the inner wall of Schlemm's canal and the three-dimensional assembly of collagen type VI in the trabecular meshwork itself.

X-ray fluorescence microscopy revealed key differences in the chemical composition of the cornea of the developing chick. In particular, the chemical signature of phosphorus, chlorine, sulphur, potassium and calcium were observably different during the developmental period from day 12 to day 16. S k-edge x-ray near edge structure spectroscopy showed that the main sulphur species present in the embryonic cornea were thiols, organic monosulfides, ester sulphate and inorganic sulphate. The chemical signature of these sulphur species was also noticeably different during embryonic corneal development. The changes in the chemical signature of phosphorus with development are believed to underline changes in the presumptive keratocyte population within the embryonic corneal stroma. Chlorine, potassium and calcium are important elements involved in the regulation and balance of the net negative or positive charge of the embryonic cornea and may influence the interactions

of corneal matrix molecules. The changes in the sulphur speciation character amongst different developmental corneas are associated with changes in the sulphation status of corneal proteoglycans which play a fundamental role in governing tissue structure and function, and thus transparency. With regards to the sulphur speciation across the depth of the mature corneal stroma, it was found that there is an inconsistency in the sulphur content and distribution throughout the depth of the tissue, from the stromal region closest to the epithelium against the deeper stromal regions near the endothelium. The heterogeneity of the sulphur species in the most anterior part of the mature corneal stroma, at the interface with the Bowman's layer supports the view that the differentiation and the transition between these two corneal layers is not very abrupt. The rest of the mature corneal stroma depth does not show any differences regarding its content in the sulphur-containing compounds indicating that the distribution and sulfation status of the corneal glycosaminoglycans have very little impact on the overall sulphur speciation. The three-dimensional ultrastructure of the human trabecular meshwork in large volumes and at high resolution identified giant vacuoles in the endothelial cell layer of the inner wall of Schlemm's canal and these were grouped into four categories based on whether they formed pores, basal and apical, or not. Interestingly, the distribution of these vacuoles was found to be non-uniform. It was discovered that the juxtacanalicular tissue was not homogenous with respect to the proportion of the electron lucent, matrix free spaces throughout the tissue's depth away from the inner wall of Schlemm's canal. Three-dimensional reconstructions of collagen type VI in the trabecular meshwork showed that there is no structural regularity in the organisation of type VI collagen assemblies, or their association with sulphated proteoglycans, suggesting a role in aqueous humor outflow. This data allow us to propose a model of aqueous humor outflow and how this is funneled through the juxtacanalicular tissue towards the lumen of Sclemm's canal.

Acknowledgments

First and foremost, I would like to express my sincere gratitude to my supervisors Professor Andrew Quantock, Dr Carlo Knupp, Dr Craig Boote and Professor Bruce Caterson for the continuous support of my PhD research, for their patience, motivation and enthusiasm. I could not imagine having better supervisors for my PhD. I cannot thank my primary supervisors Professor Andrew Quantock and Dr Carlo Knupp enough for their support and encouragement and for helping me become a confident researcher. They have always been there for me, given me advice and supported me in several aspects. I would like to thank them for being the people they are as they have always made me feel comfortable to ask silly questions.

Besides my supervisors, I would like to express my deep gratitude and respect to Dr Rob Young whose advice and insights have been invaluable to my PhD study. Dr Young has taught me numerous techniques and I would like to thank him for his patience while training me and for all the useful discussions we have had. Thank you to Rob for always encouraging me and being positive when my experiments did not work straight away.

During my PhD studies, I had the privilege to collaborate with Prof. Frank Martin, Dr Giulia Veronesi, Dr Imran Patel and Dr Marine Cotte. I would like to thank them for all their help and motivation and for teaching me everything I know with respect to synchrotron x-ray techniques. Thank you to Dr Morio Ueno for his expert knowledge of trabecular meshwork/glaucoma and for performing the dissection of the trabecular meshwork tissue used for this thesis. I would also like to thank Prof. Vic Duance and Dr Jim Ralphs for allowing me to use their lab and for spending time to teach me Immunohistochemistry, even if this work is not included in this thesis.

My greatest appreciation and friendship goes to my close friends Frances Jones and Siân Morgan (two of the “Three Degrees”) for all the good times we have spent together in the last four years, the endless late nights we worked together and for all their support and continuous encouragement throughout my PhD. I know for sure that my PhD experience would not have been the same without them.

My sincere thanks also go to all the members of the Structural Biophysics Research group and every student that has been part of this group for all their support, advice and the good times we have shared.

Thank you to my advisors, Dr Malgorzata Rozanowska and Dr Jonathan T. Erichsen for all the interesting meetings we have had and for all the suggestions they have given on how to keep improving my work throughout my PhD.

I would also like to thank all the support staff in the School of Optometry & Vision Sciences, including secretaries and technicians, past and present, for all their kindness and help. With special thanks to Steve Morgan for all his encouragement and help.

Thank you to Cardiff University President’s Research Scholarship for funding this PhD.

Thank you to all my friends for always cheering me up when I was feeling down and giving me strength to complete my project.

Last but not least, I would like to thank my parents, my sister and my brother for their endless love, encouragement and support. I cannot express how much I appreciate the fact that they have always been there for me, in the good times and the bad and always believed I would succeed.

Table of contents

List of Figures

Chapter 1: Introduction

Chapter 2: Principles and concepts of experimental procedures

Chapter 3: Molecular signatures and matrix morphogenesis elucidated by XRF microscopy and XANES spectroscopy

Chapter 4: XANES spectroscopy for the interrogation of the S speciation of the mature corneal tissue

Chapter 6: Three-dimensional aspects of the ultrastructure and outflow resistance in the human juxtacanalicular tissue

List of Tables

Chapter 1: Introduction

Chapter 3: Molecular signatures and matrix morphogenesis elucidated by XRF microscopy and XANES spectroscopy

Chapter 4: XANES spectroscopy for the interrogation of the S speciation of the mature corneal tissue

List of Abbreviations

ECM	Extracellular Matrix
KS	Keratan Sulphate
DS	Dermatan Sulphate
CS	Chondroitin Sulphate
FACIT	Fibril-associated collagens with interrupted triple helix
CS/DS	Chondroitin/Dermatan sulphate
KS	Keratan sulphate
HS	Heparan sulphate
SLRPs	Small leucine-rich proteoglycans
LRR	Leucine-Rich repeat
GlcNAc	N-acetyglucosamine
Gal	Galactose
KSG6ST	KS galactose 6-O sulfotransferase
Gn6ST	N-acetylglucosamine 6-O sulfotransferase
Lum $^{-}$/$^{-}$	Lumican null
XRF	x-ray fluorescence
S	Sulphur
ESRF	European Synchroton Radiation Facility
TEM	Transmission electron microscopy
XANES	X-ray absorption near edge-structure
PCA	Principal component analysis
LDA	Linear discriminant analysis
PCs	Principal Components
LD	Linear Discriminant
JCT	Juxtacanalicular Connective Tissue
RER	Rough Endoplasmic Reticulum
Ca	Calcium
P	Phosphorus
K	Potassium
Cl	Chlorine

Chapter 1: Introduction

The eyeball is an organ that detects light to obtain an image from the environment and convert an image to electro-chemical impulses in neurons in the brain, giving an organism the gift of vision and the ability to see the world. Ocular connective tissue ultrastructure is highly important for tissue specific function. The tissues examined here are the cornea and the trabecular meshwork which have diverse functions. This chapter will first introduce the major matrix components; collagen and small leucine-rich proteoglycans and glycosaminoglycans, particularly in their sulphated form, and then describe the structure and function of the cornea and the trabecular meshwork.

1.1. Collagen

Collagen is a fundamental component of the extracellular matrix (ECM) (Lisenmayer, 1991). Connective tissues are abundant in distinct collagen types and their primary role has been regarded as structural one. Twenty-nine different types of collagens have been identified thus far and these can be further divided into classes such as fibril-forming collagens, fibril-associated collagens with an interrupted triple helix (FACIT), network-forming collagens, anchoring fibril collagens, transmembrane collagens and multiplexins (van der Rest and Garrone, 1991; Prockop and Kivirikko, 1995; Gelse et al, 2003; Knupp and Squire, 2005). Table 1.1 summarizes the major collagen families, the collagen types and their characteristics.

Table 1.1: Distinct families and types of collagens

Collagen families	*Examples of collagen types*	*Characteristic features*
Fibril forming collagens	I, II, III, V, XI	Uninterrupted triple-helix domain, with about 340 G-X-Y repeats per α-chain
FACIT collagens	IX, XII, XIV, XVI	Associate with the surface of collagen fibrils, modifying their interactive properties.
Non- fibrillar collagens Basement membrane Anchoring fibrils Microfibrillar	 IV VII VI	Localized on the surface of the cell.
Other collagens	XIII, XV, XVIII, XX	

FACIT= Fibril-associated collagens with interrupted triple-helix domains.

Despite the different types and families of collagens, there are some structural features held in common among collagens, such as the fact that they all have one or more triple helical domain (Figure 1.1). This triple-helix domain is composed of three polypeptide chains, widely known as α-chains which in turn consist of G-X-Y repeats, where G is glycine, X is any amino acid and Y is usually proline or hydroxyproline. In the triple-helix domain, every α-chain is staggered axially by one residue relative to the other chains and the three α-chains wind in a right-handed fashion around a common axis (Lisenmayer et al, 1991).

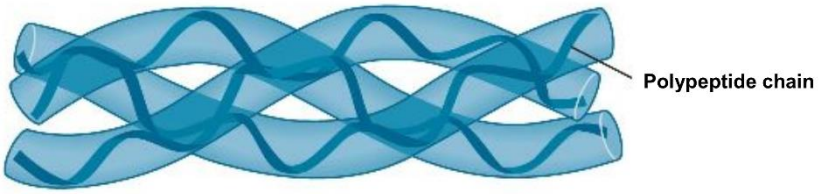

Figure 1.1: Collagen triple helix domain structure. Three polypeptide chains (α-chains) fold together forming a coil triple helical structure of collagen. Adapted and modified from http://bio3400.nicerweb.com/bio1151/Locked/media/ch05/collagen.html

1.1.1. Collagen biosynthesis

Collagen protein synthesis follows the common biosynthetic pathway as illustrated in Figure 1.2. Collagen gene transcription and mRNA take place in the nucleus of the cell (Robert et al, 2001; Kielty and Grant, 2003; Michelacci, 2003). Mature mRNA is transported to the cytoplasm and collagen translation products are transported in the rough endoplasmic reticulum (RER) where precursor pro-α chains are synthesized. Precursor pro-α chains consist of a signal sequence of 20 amino acids, the N-terminal propeptide, a short non-triple-helix domain that bears the proteolytic cleavage sites of N-terminal peptides, the major triple-helix domain and at last the final 220 residues that form a globular structure possessing disulphide bridges.

A number of post-translational modifications of the procollagen peptide occur as the peptide is elongated such as cleavage of the signal peptide, hydroxylation of proline to form 3- and/or 4- hydroxyproline, and hydroxylation of lysine, followed by the formation of the triple helix. Collagen triple-helical molecules are then transported to the Golgi apparatus where N-linked oligosaccharides may be processed. Procollagen molecules are then packaged into secretory vacuoles and upon exocytosis are secreted into the extracellular space.

Once the procollagen molecules are into the extracellular space, the procollagen N-proteinase and the procollagen C-proteinase cleave the N- and C- propeptides, respectively, a critical requirement for normal fibril morphology. After cleavage of the N- and C- propeptides, collagen molecules assemble into fibrils.

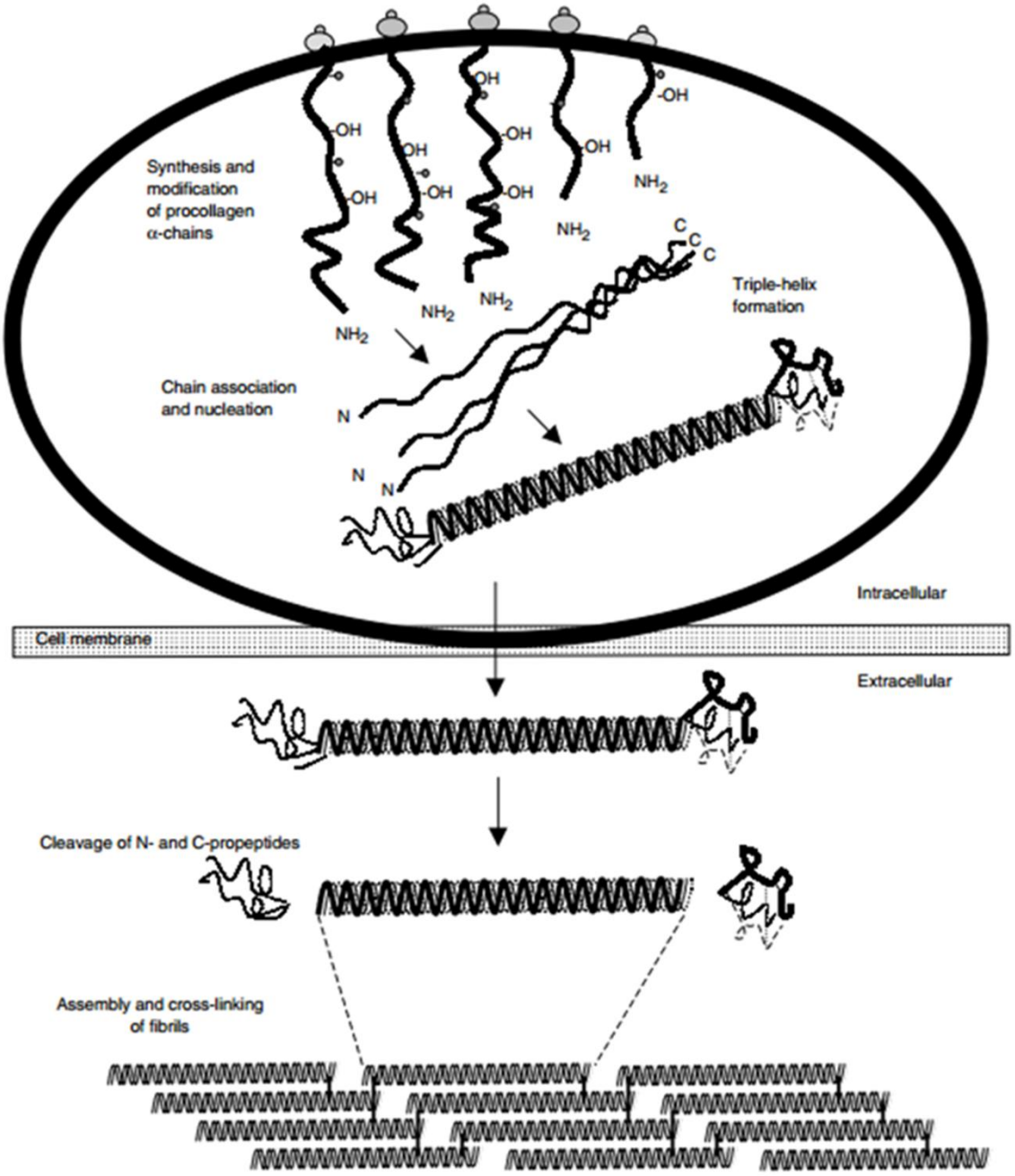

Figure 1.2: Collagen biosynthesis. Post-translational modifications of the procollagen molecule take place in the rough endoplasmic reticulum (RER). Once the triple-helix is formed and N-Oligosaccharides are transported in the RER, further processing occurs in the Golgi apparatus and then packaged in secretory vesicles. Upon exocytosis, the N- and C- propeptides are removed and the collagen molecules aggregate into collagen fibrils. Adapted from Kielty and Grant, 2003.

As stated above, following collagen biosynthesis, collagen molecules assemble together, with axially staggered ends at one-quarter of their length, to generate long cross-striated fibrils with a characteristic axial D-periodic structure (Chapman et al., 1990; Kadler et al., 1996). D is the axial periodicity of hydrated rat tail tendon collagen and has a value of 67 nm; however, the axial periodicity of the collagen in cornea is 65 nm (Meek et al., 1981; Meek and Holmes, 1983). Staining with heavy metals like uranyl acetate and examination with the transmission electron microscope reveals a characteristic banding pattern of collagen arising within the fibril's repeat (Figure 1.3).

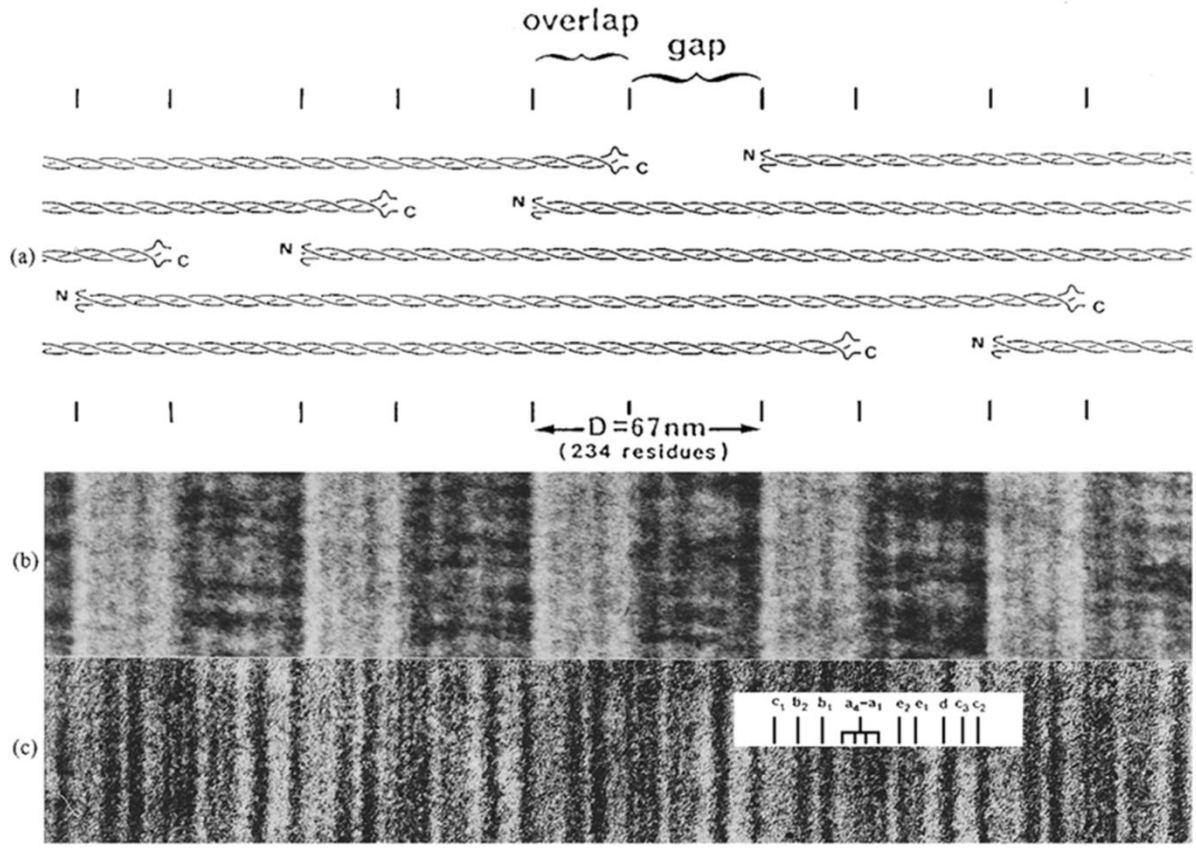

Figure 1.3: Axial periodicity of collagen. (a) Schematic diagram of the collagen molecules assembly forming long striated fibrils. The D-axial periodicity encompass gap and overlap regions. **(b)** Collagen fibril stained with sodium phosphotungstic acid showing preferential staining into the gap regions. **(c)** Collagen fibril staining with uranyl acetate following staining with sodium phosphotungstic acid revealing the transverse bands within the D-period, as a result of the heavy metal ions uptake. Adapted from Kadler et al., 1996.

1.2. Proteoglycans/Glycosaminoglycans

1.2.1 Glycosaminoglycans

Proteoglycans are composed of one or more glycosaminoglycan side chains covalently bound to a protein core and often N- and O-linked oligosaccharides are also bound to the core protein. Glycosaminoglycans are large linear chains of repeating disaccharides (Figure 1.4) with highly charged sulphate ester and carboxylate groups which are covalently attached to a core protein (Gandhi and Mancera, 2008).

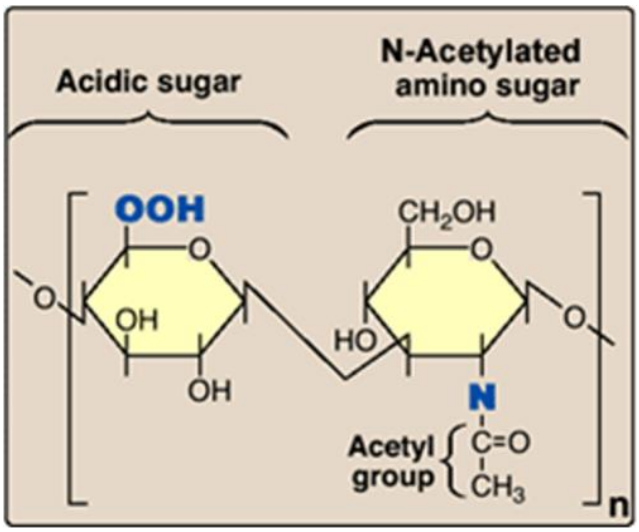

Figure 1.4: Main dissacharide unit. Dissacharides are composed of an acidic and an amino sugar with an acetyl group. The acidic sugar is negatively charged and along with the sulphate groups that can bind to the amino sugar give a strong negative charge to glycosaminoglycans. Adapted from http://www.studyblue.com/notes/note/n/lecture-6-intro-to-carbs/deck/6708629

Not only the repeating disaccharide chain length can vary between different glycosaminoglycans, but the physical state too, as some glycosaminoglycans can be soluble, surface bound or exist as soluble ectodomains. These characteristics create a potential

glycosaminoglycan diversity that may facilitate control and specificity for different ligands and their biological impact.

Under physiological conditions, the sulphate and carboxylate groups become charged, consequently providing glycosaminoglycans with a high negative charge which influences their interaction and association with other molecules.

Numerous proteins such as cytokines, growth factors, proteases, growth factors, lipid- and membrane-binding proteins which are involved in a broad range of biological processes (cell signalling, cell adhesion mechanisms, receptor engagement and protein function) interact with glycosaminoglycans emphasizing their role in these physiological processes (Jackson et al, 1991).

1.2.1.1. Classification of glycosaminoglycans

There are three classes of glycosaminoglycan side chains and these are chondroitin/dermatan sulfate (CS/DS), keratan sulfate (KS), heparin and heparan sulfate (HS) (Kjellén and Lindahl, 1991; Gandhi and Mancera, 2008). KS side chains are covalently attached to asparagines, found within one residue of either a serine or a threonine. On the contrary CS/DS and HS chains are covalently linked to serine residues on the core protein.

Unlike to the other classes of glycosaminoglycans, hyaluronan (hyaluronic acid) is a nonsulfated glycosaminoglycan that is not covalently attached to the protein core of proteoglycans (Itano, 2008). It is uniquely synthesized in the cytoplasm at the plasma membrane, in contrast to other glycosaminoglycans which are processed in the Golgi. Hyaluronan exhibits high viscosity with viscoelastic properties, and is distributed widely in vitreous humor and joint tissues. Moreover, hyaluronic acid has been found to have a functional role in signalling during embryonic morphogenesis (Toole, 1997).

1.2.2 Small leucine-rich proteoglycans

Small leucine-rich proteoglycans (SLRPs) are members of the Leucine-Rich Repeat (LRR) superfamily of glycoproteins (Hocking et al, 1998; Iozzo, 1999). Thirteen members of the SLRP gene family have been discovered to date and grouped into four different classes (Table 1.2) based upon their evolutionary protein conservation, the presence of a cysteine-rich cluster in the N-terminal region and the amount of the LRR. The LRR domain is common for the members of the SLRP family, utilized in protein/protein interactions and molecular recognition mechanisms like cell adhesion, signal transduction pathways and DNA repair. The LRP domain consists of about 20 to 29 amino acids, in which asparagine and leucine are residue in conserved positions (Hocking et al, 1998; Iozzo, 1999).

Table 1.2: Classification of small Leucine-Rich Proteoglycans (SLRPs)

Class	Proteoglycan	Glycosaminoglycan chain (s)	Number of LRRs	N-terminal Cys consensus sequence
I	Decorin Biglycan	CS or DS CS or DS	10	CX_3CXCX_6C
II	Fibromodulin (i) Lumican (i) Keratocan (ii) PRELP (ii) Osteoadherin (iii)	KS and polylactosamine (unsulfated keratan sulfate)	10	CX_3CXCX_9C Clusters of Tyr-sulfate residues (polyanionic nature)
III	Epiphycan Mimecan	CS or DS KS	6	CX_2CXCX_6C
Others	Chondroadherin Nyctalopin		11	CX_3CXCX_8C or CX_3CXCX_6C

The number of LRR region as well as the consensus sequences for the N-terminal cysteine rich region are indicated. X represents any amino acid while C represents a cysteine amino acid. CS: Chondroitin sulfate, DS: Dermatan sulfate, KS: Keratan sulfate. Modified from Iozzo, 1999 and Hocking et al, 1998.

Horseshoe-shaped SLRPs interact with collagen molecules including types I, II, V, VI, XII and XIV (collagens type I, V and VI are key components of the cornea and the trabecular meshwork) and control collagen fibrillogenesis in vitro (Bidanset et al, 1992; Font et al, 1993). Interaction occurs through the concave surface of horseshoe- shaped SLRPs (Figure 1.5), that allows the formation of several binding points favouring the interaction with biological ligands such as the triple helix of collagen molecules (Weber et al, 1996). For instance, decorin controls collagen fibrillogenesis in vitro by its interaction with collagen, mediated by the protein core via the central LRR domain. The glycosaminoglycan chains regulate the interfibrillar space by extending outside the protein core.

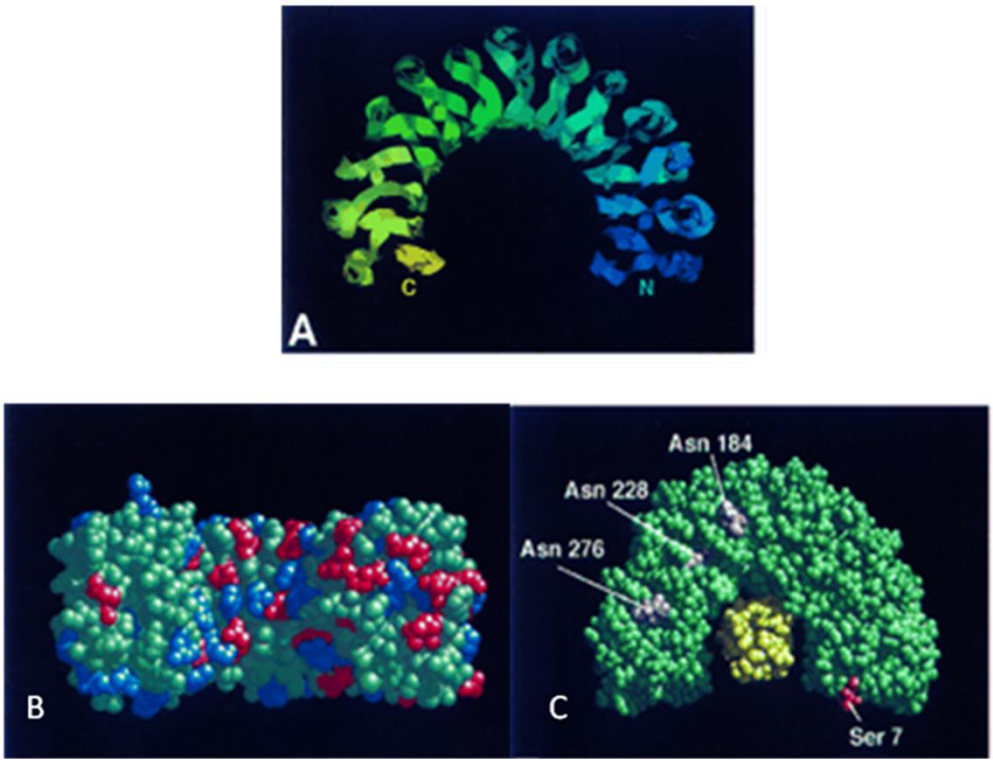

Figure 1.5: Model structure of decorin with a triple helix of collagen type I molecule. (A) The LRRs form a central cavity with the β-sheet on the inside of the concave surface and the α-helices on the outer surface. **(B)** A space-filling representation of decorin indicating the presence of charged residues with basic (positively) charged residues (blue) and acidic (negatively) charged residues (red) as well as other residues (green). **(C)** A model of decorin interacting with a triple helix of collagen (yellow). The glycosaminoglycan binding site on Ser^{7} is shown in red while the N-linked oligosaccharide binding sites are shown in purple. Modified from Weber et al, 1996.

1.2.3 Keratan sulphate

One can assume that KS is the most important glycosaminoglycan in the cornea since it interacts with proteoglycans to define collagen fibrillar corneal stromal architecture and when it is altered it leads to corneal injury or disease (Hassell et al, 1980; Hassell et al, 1983). KS is substituted to asparagine residues in the proteoglycan core proteins of lumican, keratocan and mimecan (Blochberger et al, 1992a; Corpuz et al, 1996; Funderburgh et al, 1997).

It was first identified by Suzuki in 1939 and since then many scientists have investigated its structure, biosynthesis and biochemistry (Suzuki, 1939). Corneal KS consists of short repeats of N-acetyglucosamine (GlcNAc) and galactose (Gal) units (Figure 1.6). Oeben et al. (1987) studied sulfation of KS I utilizing porcine corneal KS supporting that sulfation occurs in a judicious pattern; disaccharides close to the reducing end are not nonsulfated followed by sulfated disaccharides solely on the 6-O position of GlcNac moiety.

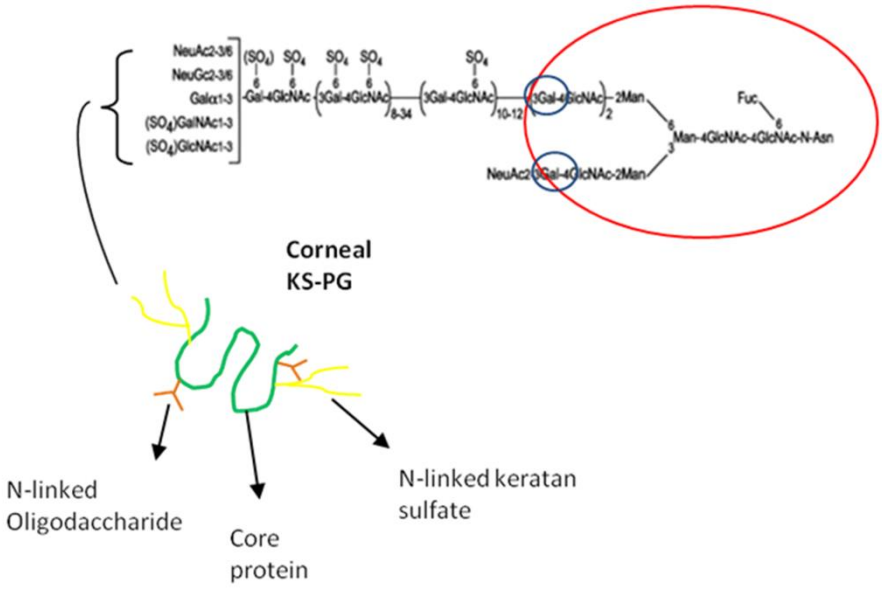

Figure 1.6: A schematic depicting the structural features of the keratan sulfate proteoglycan found in cornea. The red circle shows the keratan sulphate linkage region while the blue ones indicate the galactose residues in which the chains are attached. Modified from Greiling and Scott, 1989.

1.2.4. Lumican and keratocan

Lumican is one of the members of the SLRP family (Blochberger et al, 1992a), and one of the major KS proteoglycans in corneal stroma (Blochberger et al, 1992b). Lumican is also expressed in assorted tissues such as skin (Chakravarti et al, 1988), bone (Raouf et al, 2002) and cartilage (Grover et al, 1995). Even though four potential binding sites of N-linked KS within the LRR region have been identified, only three of them are substituted in the chick cornea (Dunlevy et al, 1998). The structure of lumican is shown in Figure 1.7.

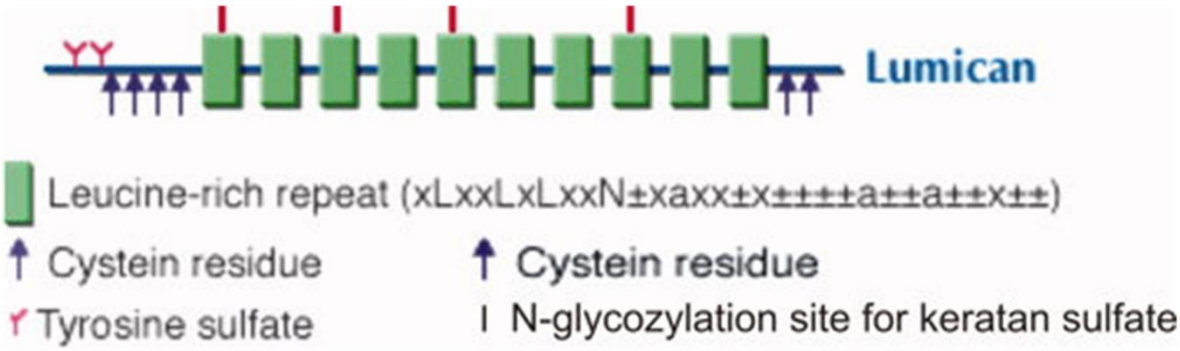

Figure 1.7: Structural model of lumican. The structural domains of lumican include the N-terminal, about 6-10 leucine-rich repeat domains which contain four N-glycosylation sites for keratan sulfate and the C-terminal domain that contains two conserved cysteine residues. Adapted from Nikitovic et al, 2008.

Lum $^{-}/^{-}$ mice were characterized by bilateral corneal opacification and irregular collagen fibril diameter accompanied by abnormal interfibrillar spacing (Figure 1.8), establishing a role of lumican in the regulation of ECM assembly and most importantly in collagen fibrillogenesis (Chakravarti et al, 1998; Chakravarti et al, 2000; Quantock et al., 2001). Nevertheless, the way lumican inflects collagen fibrillogenesis *in vivo* still remains to be delineated.

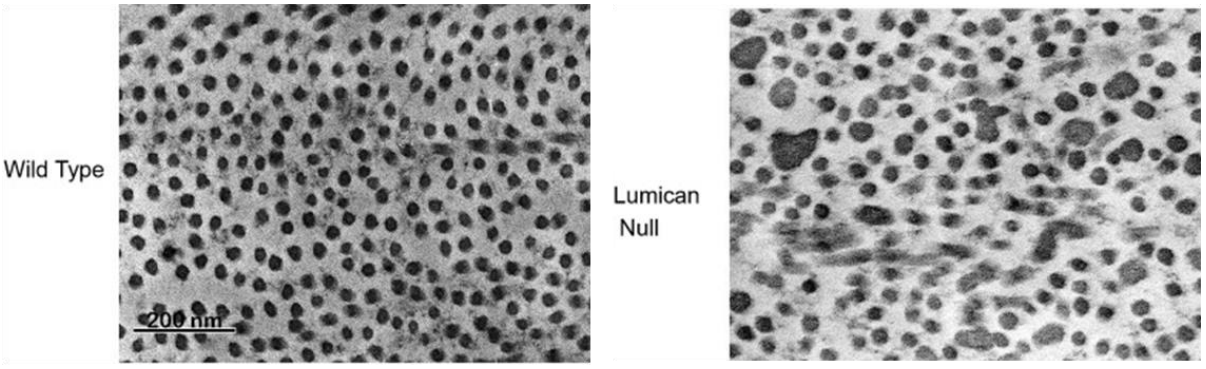

Figure 1.8: Wild type and lumican null mouse corneal stromal fibril structure. The wild type stroma is composed of small collagen fibrils regularly organized (left), whereas, lumican null mice are characterized by irregular collagen fibril diameter and abnormal interfibrillar spacing (right). Modified frrom Hassell and Birk, 2010.

Keratocan shares many similarities in amino acid sequence, post-translational modification, localization and function with lumican. Both lumican and keratocan have long been thought to regulate ECM assembly through their bi-functional property; that is to bind to collagen fibrils, regulating therefore fibril diameter, and with their glycosaminoglycan chains extend out regulating interfibrillar space.

1.3 The Cornea

The cornea is a transparent connective tissue that forms the outermost layer of the eyeball and possesses several fundamental functions. The most important among these is the ability to transmit and refract the light. In addition to this, the cornea has a protective role since it forms a defensive barrier, protecting the eye from both chemical and physical external factors, as for instance, dust, harmful bacteria and other pathogens that can penetrate the eye. Moreover, it prevents the eye from damage caused by mechanical forces as it provides the eye with tensile strength.

1.3.1 The structure of the cornea

The cornea is composed of five distinct layers (Figure 1.9) and from the exterior to the interior these are known as the epithelium, Bowman's layer, stroma, Descemet's membrane and endothelium. However, recent studies propose the existence of a sixth layer in the pre-Descemet's cornea called Dua's layer (Dua et al., 2013). The cornea is an avascular tissue and the unique organisation of corneal collagen fibrils, probably the most important ECM component of the corneal stroma, are highly important for tissue clarity and transparency. The aqueous humor constantly provides nutrients and oxygen to the cornea.

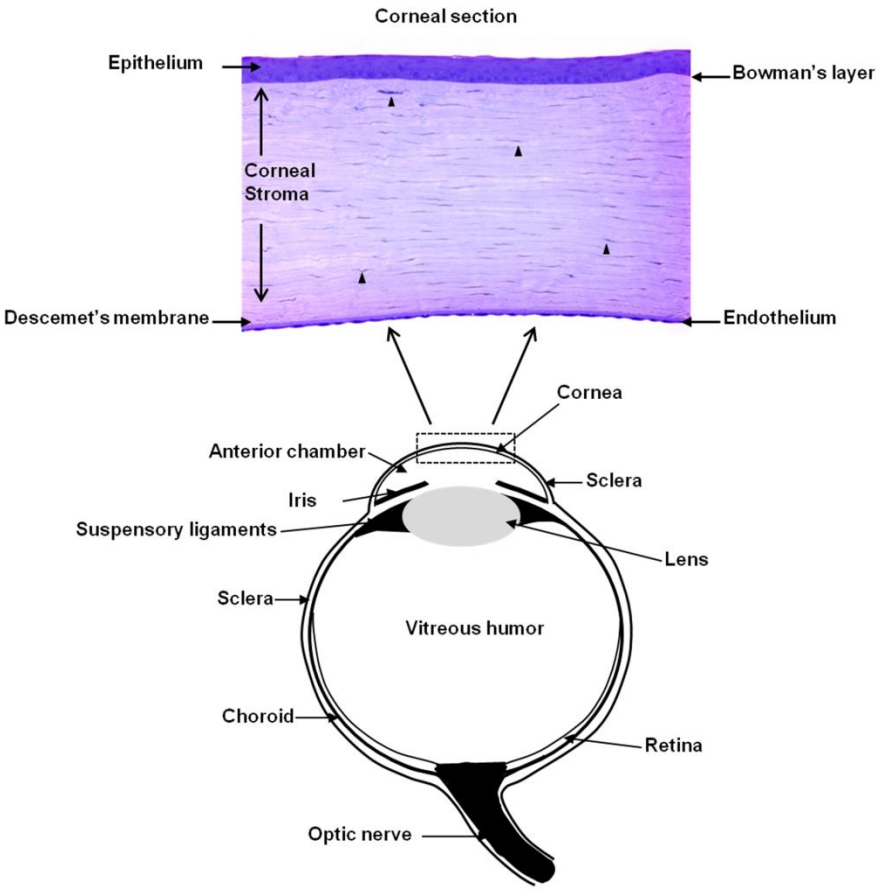

Figure 1.9: Schematic diagram of the anatomy of the human eye and the structure of the cornea. At the bottom, a schematic diagram of the eye and its major compartments. At the top, a corneal tissue section showing the five layers of the cornea, from the outside to the inside, the epithelium, Bowman's layer, the stroma, Descemet's membrane and the endothelium. The corneal section at the top has been stained with Toluidine-blue and it was kindly provided by Dr Rob Young. The arrowheads indicate stromal cells, known as keratocytes. Adapted from Veronesi et al., 2013.

1.3.1.1 Epithelial layer

The outer corneal layer is the squamous, non-keratinizing epithelium, a multilayer of non-secretory epithelial cells that serves as a first line of defence against fluid loss and deleterious microorganisms. Three different types of cells constitute the corneal epithelium and these are from the front to the back; the superficial cells, the wing cells and the basal cells (Hogan et al, 1971). Cell mitosis occurs in the innermost basal cells, which lie on a basement membrane. These cells are the source of new cells above them. As the proliferation and differentiation of the corneal epithelial daughter cells take place in the corneal limbus, the cells migrate towards the centre of the cornea to become transient amplifying cells and corneal basal epithelial cells (Tseng, 1989; Wolosin et al, 2000). Under normal conditions; corneal epithelium replenishment occurs every seven days (Hanna et al, 1961). Replenishment of the corneal epithelium at a constant level is crucial for proper function.

1.3.1.2 Bowman's layer

Beneath the epithelium layer of the cornea lies Bowman's layer, an acellular layer with nerve axons traversing it in the direction of the corneal epithelium (Wilson and Hong, 2000). Striated collagen fibrils in Bowman's layer are disorderly adjusted giving a characteristic felt-like appearance (Jacobsen et al, 1984). A number of studies have shown that the collagen fibrils present in Bowman's layer are mainly types I, III and V (Marshal et al, 1991a; Marshal et al, 1991b; Gordon et al, 1994). Collagen VII are present in Bowman's layer and help adhere the epithelial cells via hemidesmosomes (Tisdale et al, 1988). There is a hypothesis that the corneal epithelium is partly responsible for the development of Bowman's layer (Gordon et al, 1994). This hypothesis is based on the fact that smaller collagen fibrils in Bowman's layer have more collagen type V composition than the collagen fibrils in the stroma which is located

below Bowman's layer and this excess in collagen type V composition comes from collagen type V production from the corneal epithelium.

The function of the Bowman's layer still remains to be elucidated but it has been suggested to protect the eye from viral penetration and additionally to maintain corneal structural architecture (Wilson and Hong, 2000).

1.3.1.3 Stroma

The corneal stroma, a fibrous and highly transparent structure, lies below Bowman's layer and accounts for about 90% of the corneal thickness (Bron, 2001; Hogan et al, 1971). The corneal stroma is mainly composed of proteoglycans and collagen fibrils (Figure 1.10). Keratocytes, corneal fibroblasts, are the primary cells found in the stroma accountable for the development and maintenance of the stromal ECM (Hogan et al., 1971).

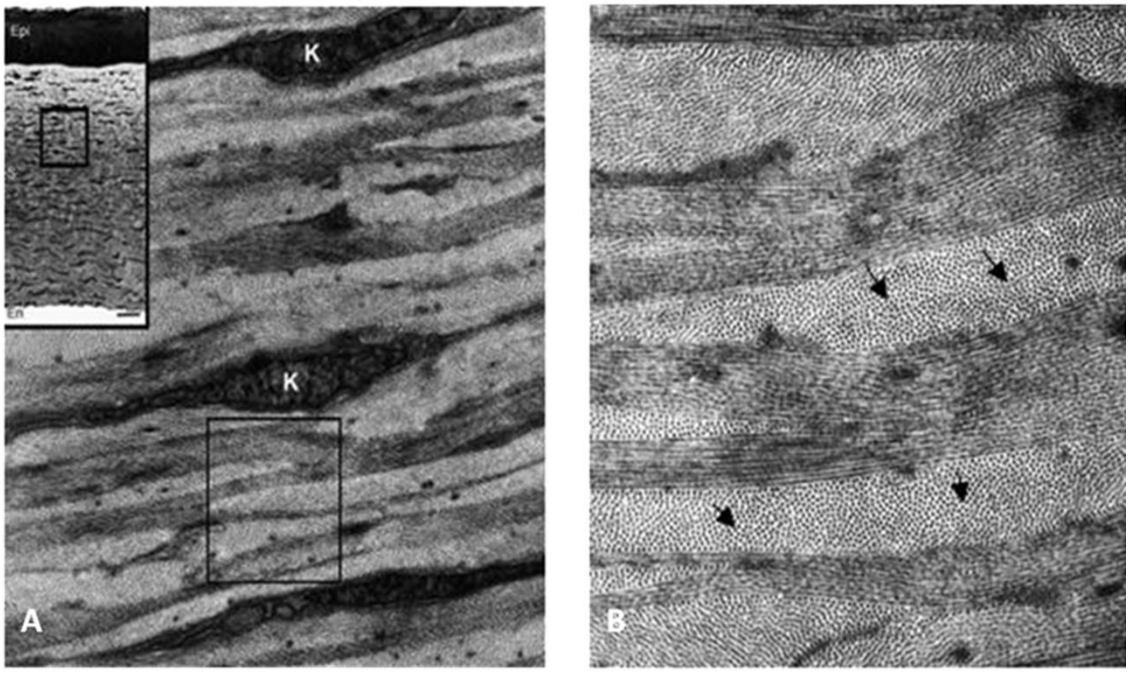

Figure 1.10: Transmission electron micrographs of corneal stroma structure. (A) The stroma contains keratocytes (K) organized parallel to the corneal surface. **(B)** Enlargement of area in rectangle in A. The stroma is composed of regularly organized collagen fibrils (arrows). Adapted from Hassell and Birk, 2010.

The corneal stroma is not structurally homogeneous throughout its depth and there are a number of differences between the anterior and posterior stroma. For instance, the posterior stroma is better arranged (Freund et al, 1995), more hydrated (Turss et al, 1971), and more susceptible to swelling than the anterior stroma. On the contrary the anterior stroma is thinner and has a higher refractive index compared to the posterior stroma (Patel et al, 1995).

As explained in more detail later, the novel arrangement of collagen fibrils in the stroma renders corneal transparency and any disturbance in the fibril organization can lead to a loss of corneal transparency (Maurice, 1957; Hart and Farrell, 1969; Benedek, 1971; Müller et al, 2004).

1.3.1.3.1 Corneal stroma collagens

Collagen proteins are major components of the ECM of connective tissues and the corneal matrix exhibits several types of collagen which are summarised in Table 1.3. Primarily the corneal stroma is composed of collagen protein molecules, in particular collagen type I (Birk et al, 1986). Collagen types III (Cintron et al, 1988; Davison et al, 1979), V (Birk et al, 1986), VI (Zimmerman et al, 1986) and XII (Wessel et al, 1997) are also present but at minor levels compared to type I. Collagen fibrils are assembled into bundles or lamellae and there are about 300 in the centre of the cornea and 500 as you move towards the limbus where the cornea is thicker (Radner et al, 1998).

Type I is present in a heterotrimeric form; consisting of two α1 and one α2 chains. Collagen type II is present in the developing cornea (Gelse et al, 2003) and is a homotrimer molecule. Two new collagen types, recently discovered, types XII and XIV belonging to the FACIT family of collagens were localized in the developing cornea. Type XII is believed to maintain fibril organization and matrix assembly while type XIV may control collagen fibrillogenesis (Young

et al, 2002). Type III collagen is also homotrimer, present in the adult human corneal stroma (Keene et al, 1987; Cintron et al, 1988; Marshall et al, 1991a) at low proportions and seems to increase during corneal wound healing and inflammation (Nakamura, 2003).

Table 1.3: Corneal collagens and their localization in the cornea

Collagen type	Localization
I	Stroma
II	Developing corneal stroma
III	Corneal wound healing, inflammation
V	Stroma
VI	Stroma
XII	Developing corneal stroma
XIV	Developing corneal stroma
XVIII	Epithelium
VIII	Descemet's membrane

In addition to types I, II and III; type V collagen was also found in the cornea. Intriguingly, it was found to co-assemble with type I fibrils and later it was suggested that its function is to modulate fibril growth (Birk et al, 1986). Moreover, it was proposed that the interaction between type I and V collagen fibrils regulates the diameter of the corneal fibrils (Birk et al, 1990). The rationale and mechanism behind this is not clear yet, but it has been suggested that since type V collagen retains its N-terminal domain after cleavage, may restrict the lateral extension of the heterotypic type I/V fibrils and this may play a role in the regulation of the corneal fibrils' diameter (Birk, 1988), along with the impact of corneal proteoglycans (Rada et al, 1993).

Type VI collagen, a non-fibrillar collagen, was discovered in the ECM of the human cornea (Zimmerman et al, 1986). Type VI collagen forms microfibrillar structures by lateral

aggregation with a 100 nm periodicity (Linsenmayer et al, 1986a; Linsenmayer et al.,1986b; Nakamura et al, 1993) that run along and between the collagen fibrils (Hirano et al, 1989) and it is likely to interact with the proteoglycans in the interfibrillar space and stabilizes the architecture of the corneal collagen fibrils (Nakamura et al, 1997).

1.3.1.3.2 Corneal stroma proteoglycans

The most prevalent proteoglycans in the corneal stroma are lumican (Blochberger et al, 1992a), keratocan (Corpuz et al, 1996) and mimecan (Funderburgh et al, 1997a), which bear KS side chains (Table 1.4). The other main proteoglycans in cornea exhibit CS/DS hybrid side chains and these are decorin and biglycan (Li et al, 1992; Zhang et al, 2009).

Table 1.4: Corneal Proteoglycans

Proteoglycan	Glycosaminoglycan (number of chains)
Lumican	Keratan sulfate (3-4)
Keratocan	Keratan sulfate (4-5)
Mimecan	Keratan sulfate (2-3)
Decorin	Dermatan /chondroitin sulfate (1)
Biglycan	Dermatan/ chondroitin sulfate (2)

KS appears to be related to corneal hydration, a pivotal necessity for corneal transparency. The importance of KS to the maintenance of corneal hydration is supported by a number of studies that have shown that KS and DS proteoglycans have a noticeable water-binding character (Hedbys, 1961; Bettelheim and Plessy, 1975).

Mice that lack lumican, one of the corneal KS proteoglycans have shown a decrease in the amount of corneal KS and had an analogous loss in stromal hydration (Chakravarti et al, 1998). Corneal macular dystrophy is characterized by corneal clouding and can be categorized into

type I, type IA and type II (Quantock, 1994; Klintworth, 2008). Individuals with corneal macular dystrophy type I are characterized by inadequate sulfation of the GlcNAc unit of KS, an effect of CGn6ST deficiency or insufficient enzyme amounts in their serum and cornea. Individuals affected with type II have detectable-to-normal levels of sulphated KS-glycosaminoglycan in their serum (Yang et al, 1988) whereas patients with type IA have no detectable levels in their serum (Klintworth et al, 1997).

KS also appears to be associated to the motility of corneal endothelial cells in wounded corneas. Normally, corneal endothelial cells possess a distinct distribution of KS at their surface; however in wounded corneas the amount of KS was found to be declined or absent on migrating cells; until the cells stop migration (Davies et al, 1999).

These findings implicate the importance of generating a highly sulphated KS glycosaminoglycan chain and advocate potential biological functions of KS.

1.3.1.3.3 Corneal stroma keratocytes

The keratocytes are found mainly between corneal lamellae having the appearance of long, thin, flattened cells. The fact that they are lying between the lamellae implies that keratocytes also regulate collagen fibrils arrangement, accrediting corneal transparency (Hogan et al, 1971; Müller et al, 1995). It has been shown that the production of the stromal collagen and subsequently its preservation thereafter is driven by keratocytes (Beales et al, 1999). Three molecules of a pro-α chain are hydroxylated, glycosylated and assembled to form procollagen molecules which are then secreted by keratocytes into the extracellular space and following cleavage they produce mature collagen molecules. Keratocytes become activated and transformed into fibroblasts or myofibroblasts when a wound healing response is triggered after corneal injury (Jester et al, 1994; Jester and Chang, 2003). Active keratocytes transmit

chemical or electric signals through the gap junctions found between cells and are able to induce temporary dislocation of the collagen fibrils and remodelling of the ECM, allowing them to adjust to their environment.

1.3.1.3.4 Corneal stroma transparency

The cornea is transparent due to its unique ability to transmit and refract the light that passes through the tissue. A number of factors are involved in the mechanism underlying corneal transparency and many investigators have proposed several transparency theories over the years.

In 1957, Maurice proposed the first theory for corneal transparency based on the corneal architecture, in terms of the uniform organisation of collagen fibrils which are consistent in size (25-30 nm) and regularly spaced (64 nm) (Maurice, 1957). Maurice's theory, known as the "lattice theory" stated that the corneal collagen fibrils are parallel and arranged into a defined lattice resulting to lateral scattering from individual collagen fibrils that subsequently destructively interferes with any adjacent scattered waves excluding the ones in the incident beam direction. However, later studies supported that a less organised collagen arrangement would also render corneal transparency (Hart and Farrell, 1969; Cox et al., 1970).

Another transparency theory proposed by Smith (1969) states that corneal transparency is based on the consistent refractive index properties of the corneal components leading in light passing through the tissue with negligible scattering (Smith, 1969). However, this transparency theory is invalid as following studies have shown that there are differences on the refractive index throughout the cornea (Leonard and Meek, 1997).

Goldman and Benedek proposed another attempting to explain the transparency of the cornea. Their theory asserted that light scattering does not occurs when the distance between

scattering components, as for instance collagen fibrils, is small or less than half the wavelength of light (Goldman and Benedek, 1967; Goldman et al., 1968; Benedek, 1971).

To date, none of the proposed corneal transparency theories entirely explains the tissue's ability to transmit and refract the light. Nevertheless, it is widely accepted from the scientific community that the density of corneal scattering components (collagen fibrils and proteoglycans), as well as collagen fibril spacing and diameter are important factors for corneal transparency. As previously mentioned, proteoglycans are key factors in maintaining interfibrillar spacing (Hassell et al., 1980). Comparative studies between scleral and corneal scar tissue opposed to normal corneal tissue, showed that the KS proteoglycan levels were less in the non-transparent tissues and the sulphation patters of KS proteoglycans were also structurally different too, emphasizing the importance of the proteoglycans and their sulphation signature (Funderburgh et al., 1988; Funderburgh et al., 1989).

1.3.1.4 Descemet's membrane

The basal lamina of the corneal endothelial cells is known as Descemet's membrane, which is generated by endothelial cells (Bron et al, 2001). At birth, Descemet's membrane is thinner (5 μm thick) than the endothelium, but its thickness increases by adult life (Wulle, 1972; Jun et al, 2006). Even though Descemet's appears to be homogenous and structureless under light microscopy it actually encompasses an unusual structure of repeatedly aligned stratified structures that can be observed by polarization or electron microscopy (Baud and Balvoine, 1953). These structures are collagenous lattices that bind to each other forming either hexagonal or linear structures (Jakus, 1956). Immunohistochemical studies reveal that fibronectin, laminin (Gordon et al., 1989), collagen type IV (Kefalides et al., 1976) and VIII (Tamura et al., 1991) are present in Descement's membrane (Johnson et al, 1982).

1.3.1.5. Endothelial layer

In the posterior surface of the cornea a single layer of approximately 500,000 endothelial cells is found (Hogan et al, 1971; Bron et al, 2001). Endothelial cells are well arranged giving a mosaic appearance of this corneal layer. They are polygonal in shape with 70-80% of them being hexagonal. These cells are metabolically active and have a secretory function, defined by a large oval nucleus usually located at the centre of the cell and many cellular organelles like Golgi apparatus, endoplasmic reticulum, ribosomes, as well as, an incredibly large number of mitochondria. Gap junctions are also found enabling cell-to-cell transport of small molecules (ions) and electrolytes between them. Noteworthy, endothelial cells do not undergo mitosis and hence they do not degenerate. In fact, they decrease in density and become flat in shape. They also increase in shape and become more polymorphic with age (Sherrard et al, 1987).

An important function of the endothelium is the regulation of corneal hydration and more precisely regulation of the amount of water present in the corneal stroma (Hodson and Miller, 1976; Maurice, 1972). This is important because abnormalities in corneal hydration may result into deficiency of the corneal transparency, corneal oedema and subsequently of a clear vision.

1.4. Chick corneal development

The chick has been extensively used as a model organism to study various, critical events of the development of the cornea (Anseth, 1961; Dunlevy et al; 2000) as the eye of the chick develops relatively early and experimental systems can be easily obtained. Also, chick corneal

developmental phenomena especially in the secondary stroma are very much alike to the mammalian one.

At stage 9, that is after 30 hrs of incubation, the optic vehicles appear at the forebrain and by stage 11 (40 hrs) they are attached to their bases being in close contact with the overlying ectoderm (Hay and Revel, 1969). The overlying ectoderm increases in thickness in order to form the lens placode (stage 13- day 2). At stage 14 (50 hrs) the optic vesicle acquires a cup-shaped structure and the lens placode shaped to fit its structure.

Then, at day 3 (stage 18) the lens placode is completely formed and the lens vesicles detach from the overlying ectoderm and mesenchymal cells start migrating from the ectoderm towards the primary stroma. It has been well established that the ectoderm gives rise to the primary corneal stroma and by the end of day 3 the first collagen fibrils, orthogonally arranged, emerge. The primary stroma starts to swell and hyaluronate, a key glycosaminoglycan is synthesized during this period (Toole and Trelstad, 1971). Hyaluronate exerts an osmotic pressure and is often associated with swelling and invasion of the stroma.

Approximately two developmental days later, vascular mesenchymal cells give rise to endothelial cells which in turn migrate at the posterior surface of the primary stroma to form the corneal 'Brille' that includes the epithelium layer, the stroma and the endothelium layer (Hay and Revel, 1969). With the corneal 'Brille' formation secondary mesenchymal cells invade the primary stroma. Secondary mesenchymal cells rapidly migrate and fully differentiate into corneal keratocytes by day 7, which will start to secrete collagen and non-collagenous molecules of the secondary (mature) stroma. The newly secreted collagen fibrils are orthogonally arranged and laid down onto the platform of the lamellae of the primary stroma.

On about day 8 to 9, hyaluronate is removed from the corneal stroma by hyaluronidase enzyme activity and the tissue water content begins to decrease and the stroma becomes more compact (Toole and Trelstad, 1971; Quantock et al, 1998; Siegler and Quantock, 2002). Concurrently, the transparency of the cornea increases from 40% at day 14 to 96% at day 19 (Coulombre and Coulombre, 1961; Hay and Revel, 1969; Quantock et al, 1998).

Bowman's layer is formed by day 14 of incubation as well as Descemet's membrane (Hay and Revel, 1969). Metachromasia starts to appear in the posterior layers of the stroma and then spreads towards the epithelial surface. Cell division stops after day 14 and stromal dehydration, condensation and more orderly array of the collagen fibrils, lead to transparency of the cornea. A general outline of the key phenomena that take place in the developing chick cornea is shown in Figure 1.11. Figure 1.12 shows the major developmental events that lead to the development of the corneal stroma.

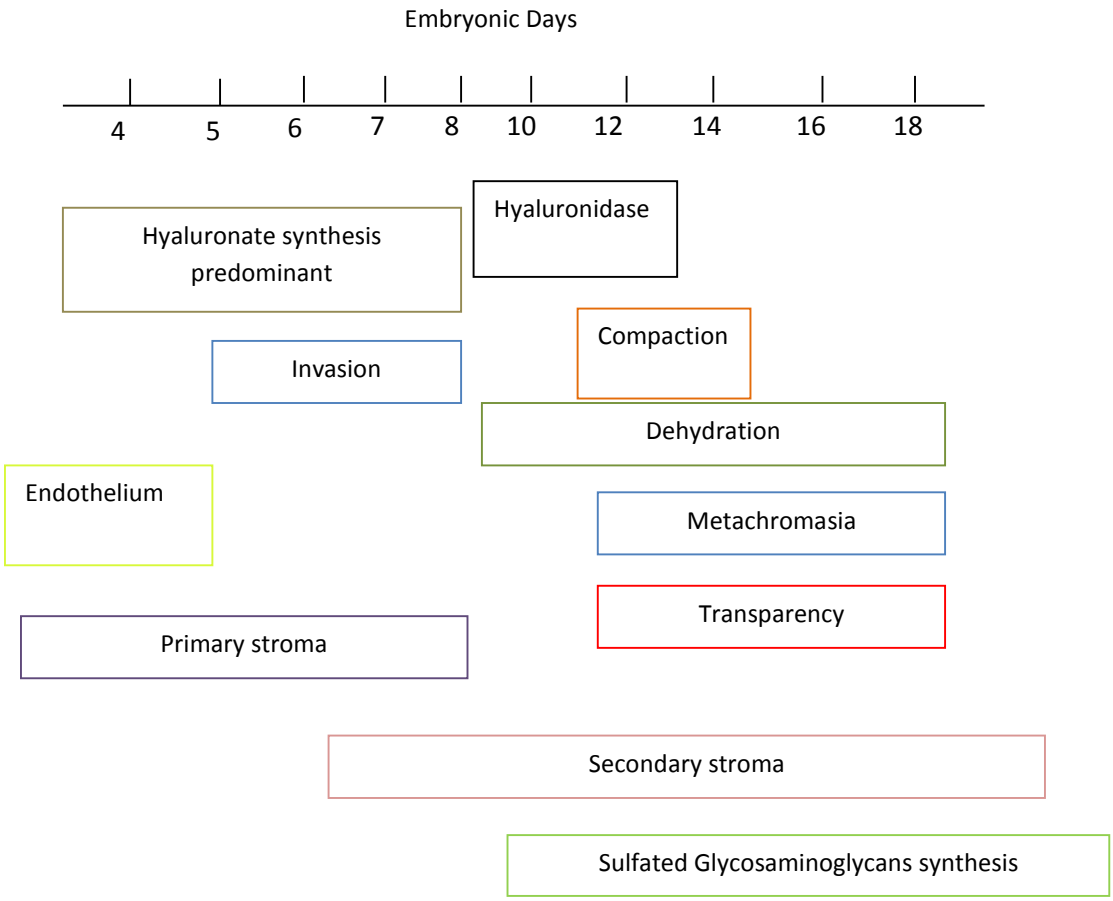

Figure 1.11: An outline of the chick corneal developmental events. Hyaluronate is synthesized between days 4-10, whereas between days 9-12 hyaluronidase is produced and its levels are decreased. The primary stroma is synthesized by day 9 and then endothelial cells migrate at the posterior stroma which then swells. Mesenchymal cell invasion begins until the stroma is fully occupied (day 9). The secondary stroma starts forming at approximately day 6. Compaction (9-14) and dehydration of the stroma takes place and by day 14 metachromasia appears and the cornea becomes transparent. Modified from Toole and Trelstad, 1971.

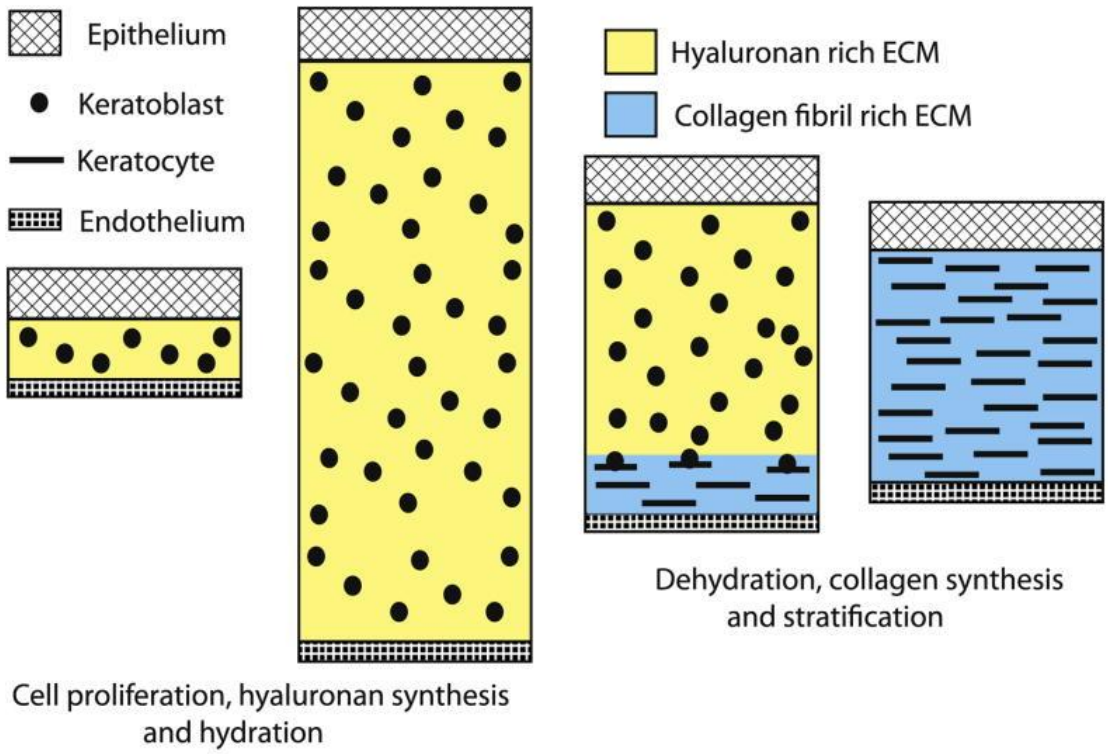

Figure 1.12: Development of the corneal stroma. At first, keratoblasts are present in a hyaluronan rich stroma. Following differentiation of keratoblasts to keratocytes secretion and deposition of collagen fibrils/Proteoglycans will result to a mature transparent corneal stoma. Adapted from Hassel and Birk, 2010.

1.4.1 Proteoglycans-Glycosaminoglycans in the developing corneal stroma

Distinct alterations in the expression and the sulphation pattern of the proteoglycans take place during the transition between an opaque cornea to a mature transparent tissue. In 1961, Anseth proposed that there is a correlation between the biosynthesis of KS at embryonic day 14 (the most predominant glycosaminoglycan of the corneal stroma) and the onset of transparency (Anseth, 1961). However, later studies by Hart (1976) challenged this statement and instead proposed that there is a correlation between the sulphation pattern of the corneal glycosaminoglycans and the onset of corneal transparency (Hart, 1976).

More recent studies, demonstrated that the concentration of KS monosulfated and disulfated disaccharides in chick corneas alters with development (Zhang et al., 2005). More specifically it was shown that the concentration of KS monosulfated and disulfated disaccharides was low at embryonic day 10, increased by day 14 (when the corneal transparency just begins to increase) and then decreased again by day 18 and peaked again by embryonic day 20 (when the cornea reaches maximum transparency) and subsequently remained high in adult chick corneas. On the contrary, CS/DS disaccharides were found to gradually decrease with corneal development and remained at low levels in the adult chick cornea (Zhang et al., 2005).

In addition to this, immunoelectron microscopy using monoclonal antibodies 5D4 and 1B4 which recognise high- and low-sulphated epitopes on KS revealed that the high-sulphated KS proteoglycans are more abundant compared to the low-sulphated ones throughout the chick corneal developmental period from day 8 to day 18 (Figure 1.13) (Young et al., 2007). These findings are in agreement with a more recent study from Liles and colleagues which also demonstrated the presence of high levels of high-sulphated KS during chick corneal embryogenesis (Liles et al., 2010).

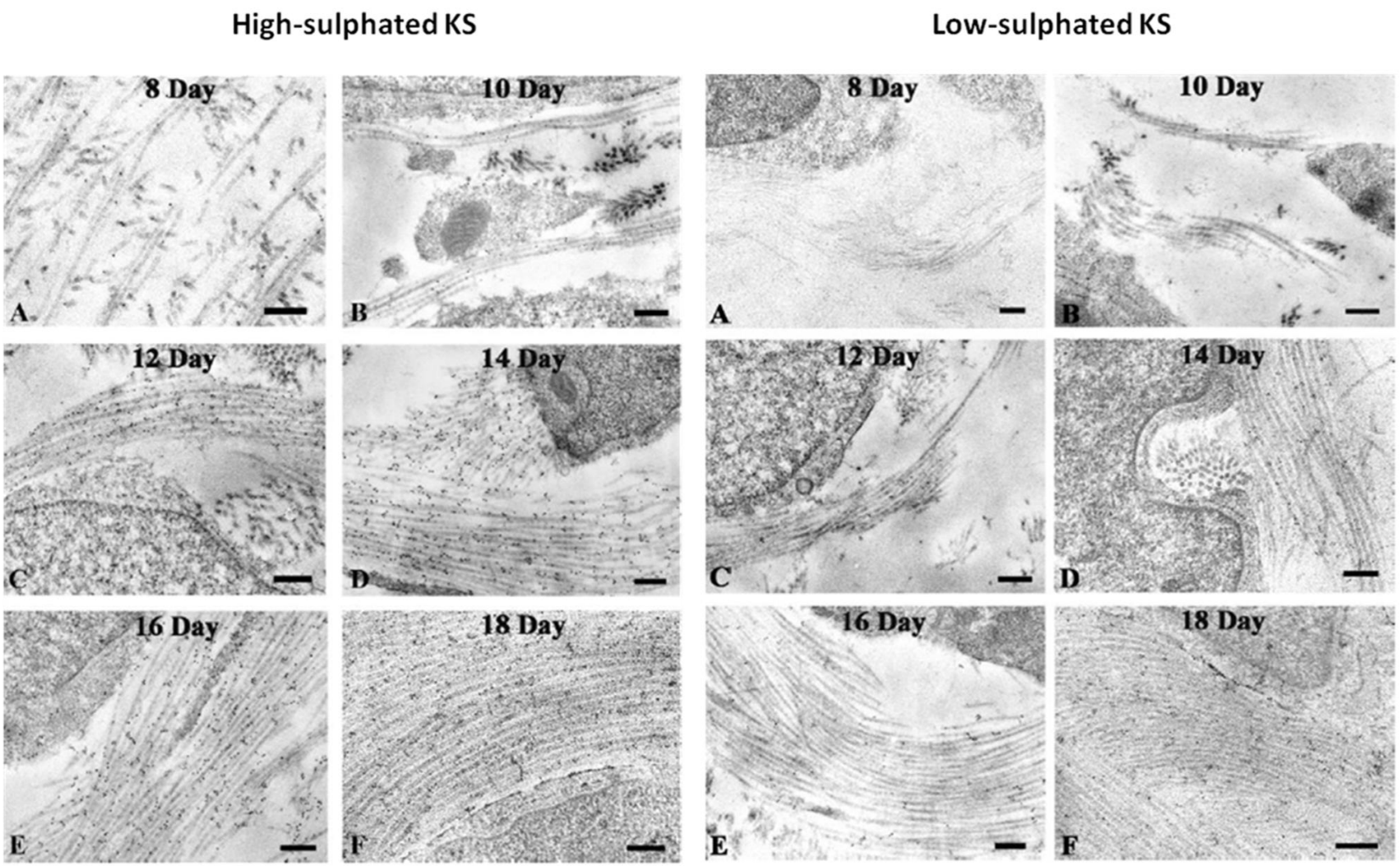

Figure 1.13: High- and low-sulphated KS proteoglycans in the developing chick corneal stroma. Immunoelectron microscopy studies showed that the high-sulphated KS proteoglycans are more abundant through the corneal development (left panel) opposed to low-sulphated KS proteoglycans that are clearly less prevalent (right panel). Figure adapted from Young et al., 2007.

1.5 The trabecular aqueous humor outflow pathway

The trabecular meshwork is critically involved in aqueous humor outflow in health and disease. The aqueous humor is a clear, nutritive fluid that fills the anterior and posterior chambers of the eye. Its main functions are to provide oxygen and nutrients to the avascular tissues of the eye, as for instance, the cornea and also to maintain a physiological intraocular pressure of approximately 15mmHg. Intraocular pressure is critical for maintaining the refracting components of the eye in their proper location, alignment and subsequently preserving their optical properties. Production site of the aqueous humor is the ciliary epithelium of the ciliary processes of the ciliary body**.**

Prior to Leber's proposal in the 19th century (Leber, 1873) for the existence of an aqueous humor circulation through tissues located near the limbal area or at an angle of the eye, it was believed that the aqueous humor is a stagnant fluid. Following Leber's proposal, a number of studies supported the existence of an outflow pathway provided evidence for a pressure-dependent flow (Leber, 1873; Knies, 1975; Smith, 1888). These findings emphasised the importance of the aqueous humor outflow pathway in the regulation of the intraocular pressure and its association with an elevated intraocular pressure. Elevated intraocular pressure is one of the risk factors for the development of glaucoma (Sommer et al., 1991; Haefliger, 1997), the second leading cause of blindness worldwide (Quigley and Broman, 2006), as it can cause damage of the optic nerve and ultimately vision loss. Therefore, any obstructions to the aqueous humor outflow pathway can lead to an increase in intraocular pressure and the development of glaucoma.

Aqueous humor is constantly being secreted by the ciliary epithelium and first enters the posterior chamber of the eye and then passes through the pupil to reach the anterior

chamber of the eye where it nourishes the cornea, the lens, the anterior vitreous and the trabecular meshwork. It then drains out of the anterior chamber of the eye returning into the systemic circulation, as shown in Figure 1.14.

There are two well-known aqueous humor outflow pathways, both commencing at the anterior chamber angle, through which the aqueous humor leaves the anterior chamber angle of the eye; the uveoscleral, also known as unconventional pathway and the trabecular or conventional pathway.

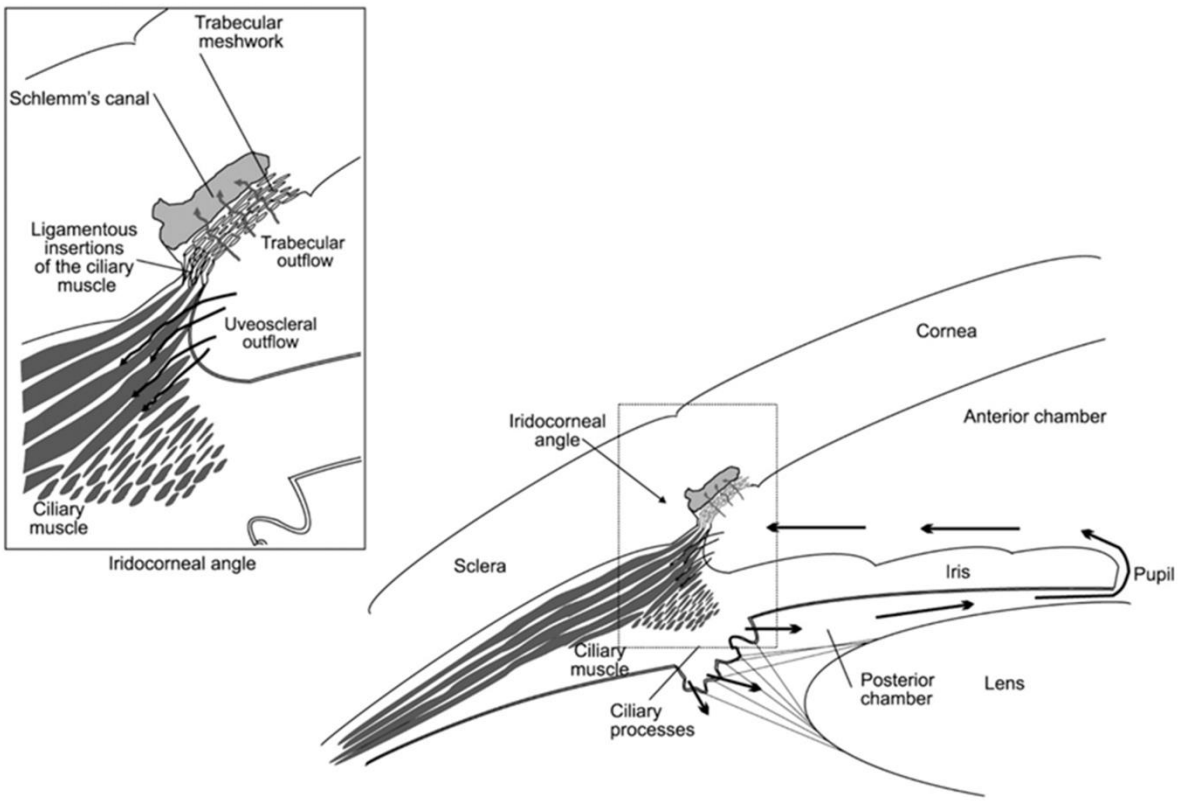

Figure 1.14: Schematic diagram of the aqueous humour outflow pathway and the related eye structures involved in the aqueous humor cycle. The aqueous humor is constantly being secreted by the ciliary processes of the ciliary body and then enters the anterior chamber of the eye to provide nutrients and oxygen to the avascular tissues. The inset displays the two distinct aqueous humor outflow pathways, the uveoscleral outflow pathway and the trabecular outflow pathway. The bulk of the aqueous humour exits the eye via the trabecular outflow pathway which is composed of the trabecular meshwork and Schlemm's canal. Figure adapted from Llobet et al., 2003.

1.5.1. The uveoscleral (unconventional) outflow pathway

The uveoscleral outflow pathway, first described in the mid-1960s by Anders Bill (Bill, 1965; Bill and Hellsing, 1965; Bill 1966a; Bill 1966b), consists of aqueous humor passing through the intercellular spaces among the ciliary muscle bundles, into the suprachoroidal space, from which it is then drained through the sclera (Bill, 1965; Bill and Philips, 1971; Bill, 1975; Inomata and Bill, 1977) or is reabsorbed by the vortex veins (Pederson et al., 1977; Sherman et al., 1978). In humans, about 5-35% of total aqueous humor outflow drains out via the uveoscleral pathway (Bill and Philips, 1971; Bill, 1975; Nilsson, 1977).

1.5.2. The trabecular (conventional) outflow pathway

The trabecular or conventional outflow pathway accounts for the majority of the aqueous humor outflow and it comprises of the aqueous humor passing through the trabecular meshwork, draining into Schlemm's canal and then to collector channels and aqueous veins which eventually drain into scleral veins (Goldmann, 1950; Ascher, 1954). Aqueous humor outflow through the trabecular pathway is driven in a pressure-dependent flow.

The trabecular meshwork is a sponge-like tissue that has a somewhat triangular shape, located at the outer periphery of the iris. The trabecular meshwork is divided in three distinct regions (Figure 1.15), the more superficial uveal meshwork found closest to the anterior chamber, the deeper corneoscleral meshwork and the juxtacanalicular connective tissue (JCT) found adjacent to Schlemm's canal (Virchow, 1910; Hogan et al., 1971).

1.5.2.1. Uveal and corneoscleral trabecular meshwork

The trabecular uveal meshwork is composed of irregular cords of connective tissue covered by trabecular-endothelial cells with spaces of different sizes found in between them (Flocks, 1956). Several studies have proposed that negligible flow resistance is generated by the uveal

meshwork because of the large number and size of the intercellular spaces of the meshwork (McEwen, 1958; Grant, 1963).

The corneoscleral trabecular meshwork extends from the scleral spur and consists of trabecular sheets or beams covered by flat trabecular meshwork cells and intertrabecular spaces of various sizes and shapes, forming an irregular net-network (Flocks, 1956; Hogan et al., 1971). The trabecular beams interconnect with each other and are characterised by collagen and elastic fibers. The intertrabecular spaces of the corneoscleral meshwork decrease progressively in size as the deeper regions of the meshwork and Schlemm's canal are approached (Flocks, 1956; Hogan et al., 1971; Bill, 1975).

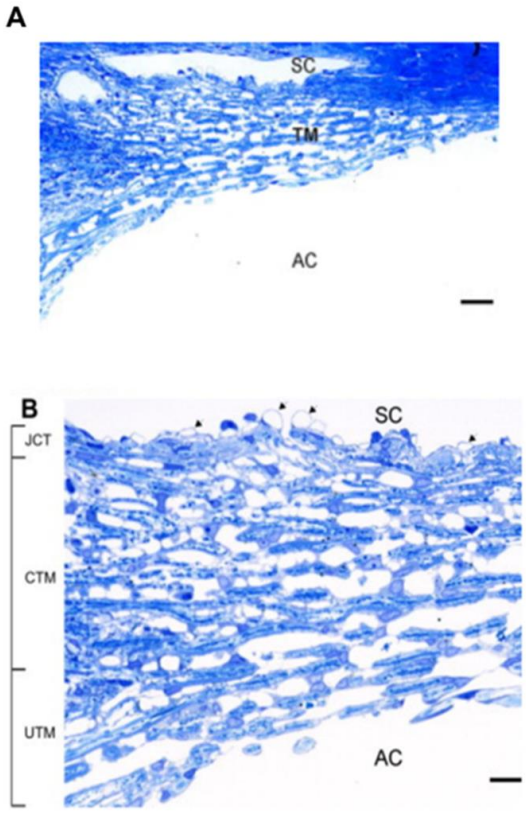

Figure 1.15: Light micrograph of the trabecular meshwork (TM). (A) The trabecular outflow pathway is composed of the TM and the Schlemm's canal (SC). Scale bar = 20 µm **(B)** Higher magnification view of (A). The TM is divided into three different portions, the uveal trabecular meshwork (UTM), the corneoscleral trabecular meshwork (CTM) and the juxtacanalicular tissue (JCT) which is located adjacent to SC. Arrowheads point the giant vacuoles which are formed by the inner wall endothelium of SC. Scale bar = 5 µm. AC: Anterior chamber. Figure adapted and modified from Tamm, 2009.

1.5.2.2. The Juxtacanalicular Tissue

The third and smallest region of the trabecular meshwork, the JCT, was first identified by Holmberg in 1959 (Holmberg, 1959) who described it as a thin layer between the inner wall of Schlemm's canal and the last corneoscleral trabecular beam. The JCT is less organised compared to the uveal and the corneoscleral meshwork and has the appearance of a typical loose connective tissue with relative large optically empty spaces. The thickness of the JCT and its porosity appears to vary (2-20 μm) at different levels of intraocular pressure (Ten Hulzen and Johnson, 1996; Overby et al., 2009; Keller and Acott, 2013).

The composition of the JCT includes loose ECM material and fairly free cells that through their processes appear to attach and communicate with each other, with the trabecular cells of the nearby corneoscleral meshwork and also with the endothelial cells that line the inner wall of Schlemm's canal (Gierson et al., 1978; Inomata et al., 1972; Johnson and Erickson, 2000; Keller and Acott, 2013). It has been reported that JCT cells have fibroblastic-like characteristics and do not possess a basal lamina but instead they are surrounded by an amorphous basement membrane-like material (Rohen et al., 1981; Rohen and Lütjen-Drecoll, 1989). The ECM material of the JCT appears to contain a large number of proteoglycans (Tawara et al., 1989; Gong et al., 1992), hyaluronan, DS, CS, laminin, fibrobectin and collagen types I, III, IV, V and VI (Gong et al., 1992; Ueda et al., 2002). Moreover, a network of elastic fibers, known as the cribriform plexus, has been identified in the JCT, whose elastic fibers are composed of an electron dense core of elastin and an outer sheath of banded material. Elastin, decorin, glycosaminoglycan chains, fibronectin and collagen types III and VI have been found to be associated with the sheath of the cribriform plexus (Rohen et al., 1981; Lütjen-Drecoll et al., 1981; Hann et al., 2001; Kielty et al., 2002; Ueda et al., 2002; Keller and Acott, 2013). This network of elastic fibers fills the space between the JCT cells and provides the JCT tissue with

the ability to stretch and recoil, an ability that plays a critical role in sustaining tissue structure and function in response to fluctuations in intraocular pressure.

1.5.2.3. Schlemm's canal

As aqueous humor flows through the uveal, the corneoscleral trabecular meshworks and the JCT it then traverse the inner wall of Schlemm's canal, passes through the lumen of the canal and ultimately exits the eye via direct drainage into the episcleral venous system.

Schlemm's canal can be divided into two parallel portions that reassemble together after some distance, the outer and the inner wall of the canal (Figure 1.16). The outer wall of the canal is comparatively smoother than the inner wall portion and it is found near the limbal stroma, neighbouring with the sclera. The outer wall of Schlemm's canal is characterised by the presence of approximately 30 collector channels lining along the wall of the canal which directly connect the canal with the venous system of the eye (Dvorak-Theobald, 1934; Rohen and Rentsch, 1968; Hogan et al., 1971).

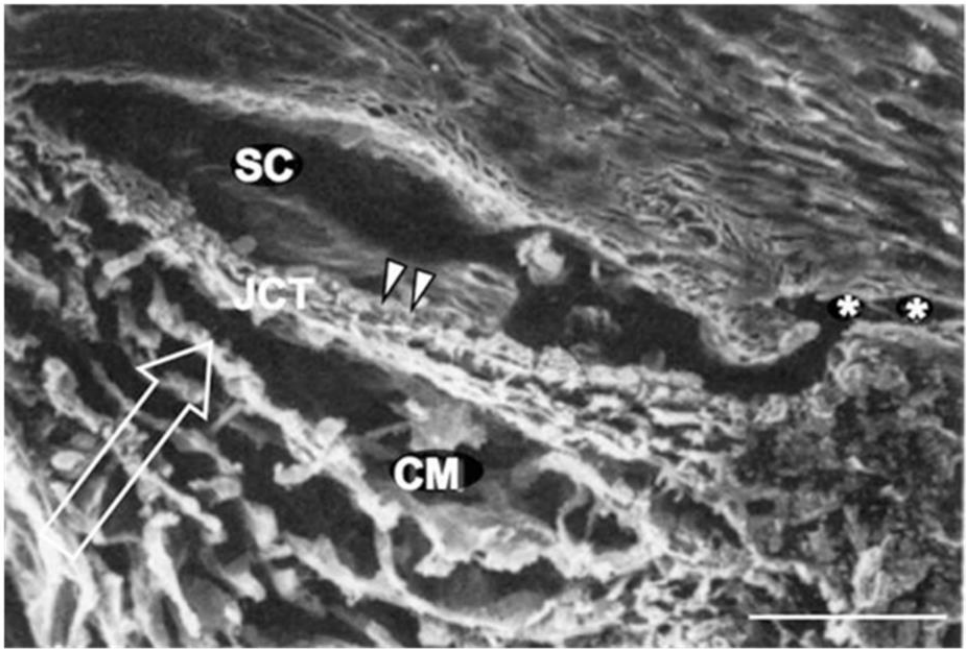

Figure 1.16: Scanning electron micrograph of the trabecular outflow pathway. The inner wall (arrowheads) of Schlemm's canal (SC) are shown. The collector channels (asterisks) lie along the outer wall of the canal. The direction of the aqueous humour outflow is also shown by the arrow. JCT: Juxtacanalicular tissue; CM: Corneoscleral meshwork. Scale bar= 50 µm. Adapted from Overby et al., 2009.

A single layer of flattened, elongated endothelial cells line up along the inner wall of Schlemm's canal mainly orientated parallel to the longitudinal axis of the inner wall. The endothelial cells along the inner wall are have a bigger diameter opposed to the average diameter of most endothelial cells (20-50 µm versus 10 µm) with a length of 40-100 µm (Hogan et al., 1971; Gong et al., 1996; Johnson and Tamm, 2010). Tight junctions joined adjacent endothelial cells to one another. The cytoplasm of these endothelial cells is similar to the cytoplasm of most endothelial cells, shown to consist, for example, of a central nucleus, small mitochondria, lysosomes and Golgi apparatus.

The most striking feature of these cells is the formation of intracellular outpouchings, known as giant vacuoles (Figure 1.17) (Hogan et al., 1971; Gong et al., 1996; Tripathi, 1972). These giant vacuoles are formed in response to the pressure gradient related with aqueous humor flow, in particular, when the aqueous humor pushes the endothelial lining cells of Schlemm's canal (Johnstone and Grant, 1973). The size and shape of the vacuoles are variable, with vacuole diameters ranging from 2 µm to 6 µm, even though bigger vacuoles can occasionally be observed (Tripathi, 1972).

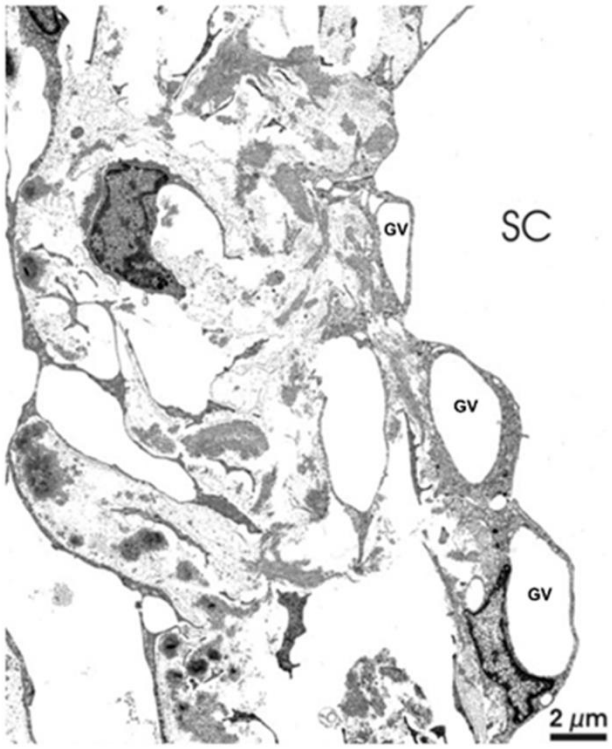

Figure 1.17: Transmission electron micrograph of the inner wall endothelium of Schlemm's canal (SC). The endothelial cells of the inner wall of the canal form giant vacuoles (GV). Scale bar is 2 µm. Adapted and modified from Ethier et al., 2006.

Many studies have been done on this area investigating the structure, function and importance of the giant vacuoles in aqueous humor outflow. Early investigators focusing on the ultrastructure of the giant vacuoles of the endothelium lining of Schlemm's canal have provided data supporting that these vacuoles have openings. The majority of these vacuoles

possess openings (Figure 1.18) into the connective tissue of JCT and the nearest optically empty spaces, and a small proportion of these vacuoles have openings on the Schlemm's canal luminal aspect. However, it has been reported that some vacuoles show openings on both the JCT aspect and the luminal aspect suggesting that some of these vacuoles represent intracellular channels (Holmberg, 1959; Hogan et al., 1971; Tripathi, 1972; Gong et al., 1996). The shape and size of these vacuoles vary widely, with openings, or pores, measuring from 0.3 to 2 µm in diameter. Several groups have estimated the pore density of the inner wall of Schlemm's canal with the use of scanning electron microscopy and found that the pore density varies between 1000 to 2000 pores/mm^2 (Kayes, 1967; Bill, 1970; Bill and Svedbergh, 1972; Segawa, 1973; Lee and Grierson, 1975; Svedbergh, 1976). However, it has been reported that fixation affects pore formation and that some of the pores are more likely to be fixation artifacts with the pore density being less than 1000 pores/mm^2 in normal living eyes (Sit et al., 1997; Ethier et al., 1998).

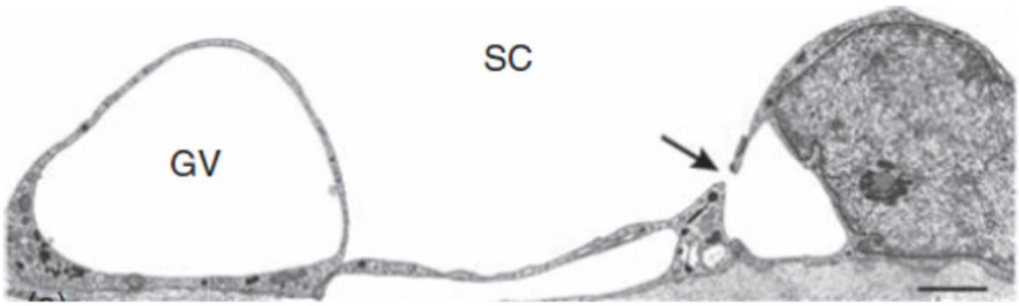

Figure 1.18: Pore formation on the giant vacuoles (GV). Arrow indicates the formation of an apical pore towards the lumen of SC. Scale bar equals to 2 µm. Adapted and modified from Johnson and Tamm, 2010.

The discovery of giant vacuoles formation by the endothelial cell lining of Schlemm's canal has led to extensive investigations being carried out to elucidate whether the vacuoles provide a direct aqueous humor outflow pathway. In 1966, Feeney and Wissig (Feeney and Wissig, 1966) perfused ferritin, a positively charged electron dense tracer which binds to

negatively charged surfaces of cellular membranes or collagen fibers, in the anterior chamber of the eye and found that whereas ferritin was accumulated in some vacuoles, it was not present in some others. Similar results were observed by Tripathi, 1971 when he also noted accumulation of ferritin within the vacuoles and also ferritin flowing from some vacuoles via their luminal openings into Schlemm's canal (Tripathi, 1971). These findings suggest that aqueous humor passes initially through the vacuoles trabecular openings (on the JCT aspect) and then via their luminar openings enters the lumen of the canal. Taking this into consideration, Tripathi, 1972 proposed a dynamic cyclic process of endothelial vacuolation (Figure 1.19) and an aqueous humor outflow mechanism through which aqueous humor is transported from the trabecular meshwork towards the lumen of Schlemm's canal (Tripathi, 1972). The first stage of endothelial vacuolation begins with the formation of a small invagination at the connective tissue of the JCT aspect at the endothelial cell surface (Stage 2). The first stage is pressure-dependent across the endothelial cell layer of the inner wall of Schlemm's canal. Subsequently, this invagination gradually gets bigger leading to the formation of a giant vacuole (Stage 3 and 4) that in the end burst in the lumen of the canal, generating an intracellular channel (stage 5) facilitating aqueous humor outflow. At a certain period of time, movement of the cytoplasm of the cell obstructs the basal opening or pore and the cell goes back its normal stage (Stage 1). However, Tripathi's model is not accepted much anymore and there are arguments against this model, primarily because it does not describe the giant vacuole and pore as a transendothelial channel, but rather as a process of macro-pinocytosis where the fluid is transported in a bolus across the endothelium.

There are two points of view in respect to the way aqueous humor flows through the inner wall and reaches the lumen of Schlemm's canal. One school of thoughts support that the aqueous humor passes through the inner wall of the canal in a paracellular manner, thus passing between the cells. Support from this school comes through studies that have showed that not all the vacuoles serve as intercellular channels and noticeably a portion of pores formed at the border of adjacent endothelial cells (Raviola and Raviola, 1981; Ethier et al., 1998). These paracellular pores, do not merge the extracellular fluid with the cell cytoplasm. On the other hand, others argue that the aqueous humor flows through the giant vaucoles and the intracellular channels formed by the endothelial cells across the inner wall of Schlemm's canal. At present, the majority of scientists support that aqueous humor flow is mainly achieved via the vacuolar intercellular channels.

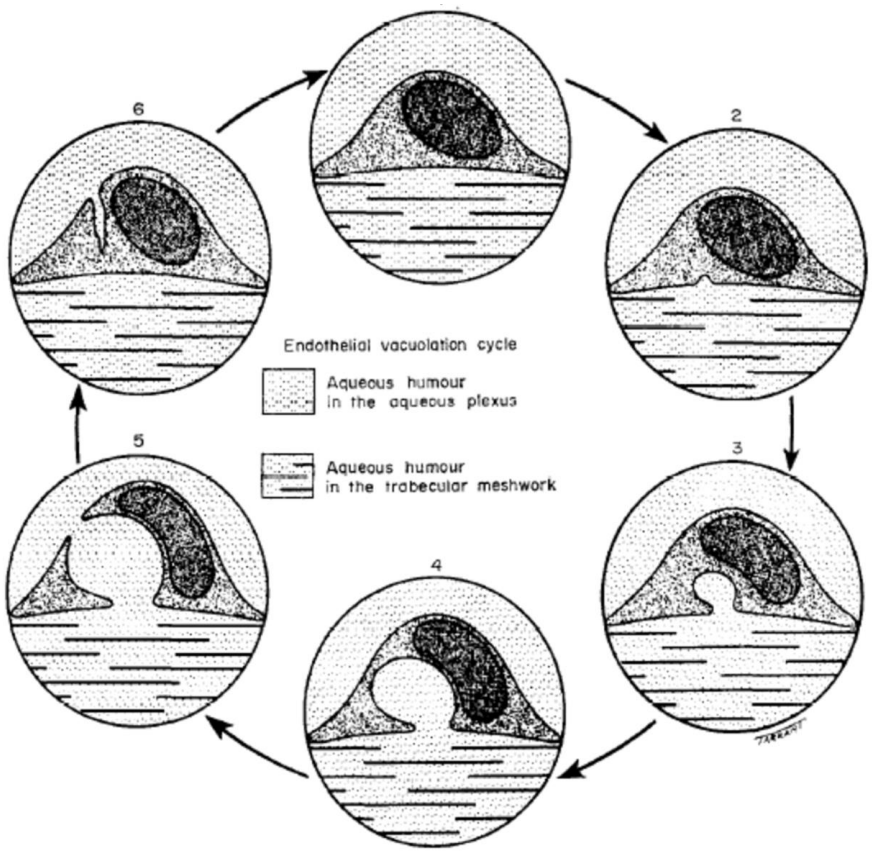

Figure 1.19: Endothelial vacuolation mechanism. Adapted from Tripathi and Tripathi, 1972.

1.5.3 Ultrastructural changes of the trabecular meshwork in glaucomatous eyes

Several groups have investigated the ultrastructural changes that take place in the trabecular meshwork in glaucomatous eyes (Tripathi, 1972). With respect to changes in the uveal and corneoscleral meshwork, it was shown that the intertrabecular spaces and the intratrabecular spaces were in general open and only inconsiderably narrowed in the trabeculectomy specimens.

Remarkably, the most important ultrastructural changes in glaucomatous eyes in comparison to normal eyes appeared to be in the JCT and the inner wall of Schlemm's canal. All the studies supported the fact that the number of pores and giant vacuoles was decreased, especially in advance stages of glaucoma (Tripathi, 1972; Allingham et al, 1992; Johnson et al, 2002). This decrease in the number of vacuoles in glaucomatous eyes suggests that either the membrane of the endothelial cells of Schlemm's canal offers greater resistance or that the cell activity has been diminished or a combination of both cellular phenomena might take place. Other glaucomatous changes include thickening of the basement membrane and an increase in the ECM components of the JCT with a decrease in the cellular component (Tripathi, 1972).

1.5.4 Aqueous humour outflow resistance

Decreased aqueous humor outflow facility results in enhanced intraocular pressure which is highly associated with glaucoma. Moses in 1977, investigated the effect of intraocular pressure on resistance to aqueous outflow and he noted that there is a linear relationship between pressure and flow resistance, thus, increased intraocular pressure is associated with increased flow resistance (Moses, 1977). It is of critical importance to identify which site in the outflow pathway generates the majority of the outflow resistance in a healthy eye and then examine how this resistance is changed in glaucomatous eyes and which ultrastructural

alterations underline this change. Despite the fact that there is on-going international research aiming to understand and characterise the aqueous humor outflow pathway in the human eyes and much progress has been made, the primary site of aqueous humor outflow resistance and its underlying mechanism have yet to be determined. Possible candidates for the principal site of aqueous outflow resistance include the uveal and corneoscleral meshworks, the collector channels and aqueous veins, Schlemm's canal, the inner wall basement membrane of the endothelial lining of Schlemm's canal, the inner wall endothelial cell layer of Schlemm's canal and the JCT (Johnson, 2006; Overby et al., 2009).

1.5.5 Sites of outflow resistance generation

1.5.5.1. Aqueous outflow resistance generated by the uveal and corneoscleral meshworks

It is generally accepted by the scientific community that the uveal and corneoscleral meshworks generate negligible aqueous outflow resistance. As stated above, these meshworks are highly porous with multiple openings constituting them insignificant sites for aqueous outflow resistance. Theoritical and experimental evidence for this statement has also been provided by studies of McEwen, 1958 and Grant, 1963, respectively (McEwen, 1958; Grant, 1963). Additionally, it has been shown that the size of the openings within the uveal and corneoscleral meshworks become wider with an increase in intraocular pressure, intuitively resulting to a decrease in outflow resistance (Johnstone and Grant, 1973), but if we consider that an increase in intraocular pressure is associated with an increase in outflow resistance as well, then we can conclude that the uveal and corneoscleral meshworks are not the sites for aqueous outflow generation (Johnson and Kamm, 1983).

1.5.5.2. Aqueous outflow resistance generated by the collector channels and aqueous veins

Two considerations preclude the collector channels and aqueous veins from being the principal sites of aqueous outflow resistance. Firstly, the big size of the collector channels and aqueous venins (Dvorak-Theobald, 1934; Rohen and Rentsch, 1968, Overby et al., 2009) indicate that these structures cannot cause an appreciable resistance and secondly, theoretical studies did not provide evidence to allow us to conclude that these structures can generate significant resistance (Rosenquist et al., 1989).

Experimental data from Mäepea and Bill studies (Mäepea and Bill, 1989; Mäepea and Bill, 1992) is in agreement with the theoretical evidence as they showed that there is minor difference between the pressure found in Schlemm's canal and the pressure found in the aqueous veins of monkey eyes. On the other hand, other studies investigating flow resistance in enucleated primate and human eyes before and after trabeculotomy, showed that after trabeculotomy 25% of outflow resistance still remains (Grant, 1958; Grant, 1963; Ellingsen and Grant, 1972; Van Burskirk and Grant, 1973; Peterson and Jocson, 1974; Van Buskirk, 1977). In spite of the fact that there is no agreement between the experimental data from various research groups, considering that Laser trabeculoplasty is efficient in reducing outflow resistance in glaucomatous eyes (Wise and Witter, 1979) it is suggested that even if some level of outflow resistance is generated by the collector channels and the aqueous veins it is unlikely to cause the increased outflow resistance, observed in glaucomatous eyes. Nevertheless, further studies are needed to elucidate the outflow resistance generated by these structures.

1.5.5.3 Aqueous outflow resistance generated by Schlemm's canal

Schlemm's canal has also been ruled out as the site for aqueous outflow resistance, since even at low intraocular pressure the size of the canal is too big to generate significant resistance (Moses, 1979). Moreover, although it has been shown that the lumen of the canal collapses when the intraocular pressure is increased (Johnstone and Grant, 1973), it is not eligible to generate a high resistance as the one observed in glaucomatous eyes, pointing out that collapse of the canal is not the cause of glaucoma (Brubaker, 1975; Van Burskirk, 1976; Moses, 1977; Johnson and Kamm, 1983).

1.5.5.4 Aqueous outflow resistance generated by the inner wall basement membrane

A discontinuous basement membrane supports the endothelial cell lining of the inner wall of Schlemm's canal. It has been proposed that the inner wall basement membrane is a potential candidate for the generation of aqueous outflow resistance. This proposition stems from the fact that the hydraulic conductivity for a variety of biological basement membranes are very similar to the hydraulic conductivity of the aqueous humor outflow network, as estimated by Johnson, 2006 (Johnson, 2006). However, unlike most of the biological vascular basement membranes, the basement membrane of the inner wall of Schlemm's canal is characterised by its discontinuity (Grierson et al., 1978; Gong et al., 1996) eliminating therefore the flow resistance generated by the tissue.

1.5.5.5 Aqueous outflow resistance generated within the endothelial lining of the inner wall of Schlemm's canal

The endothelial cell layer that lines across the inner wall of Schlemm's canal is another possible locus for the generation of aqueous outflow resistance. In support of this statement, it has been shown that the inner wall endothelium of Schlemm's canal has the highest

hydraulic conductivity, in comparison with that of the other endothelial to other tissues in the human body (Johnson, 2006; Overby et al., 2009; Johnson and Tamm, 2010).

As stated above, a special feature of the endothelial lining of the inner wall of Schlemm's canal is the formation of large pores that can be mostly found transcellularly, but a portion of them can also be seen paracellularly. Pore formation of the endothelium of Schlemm's canal could explain why this endothelium is characterised by the highest hydraulic conductivity of all endothelia in the human body. In 1972, Bill and Svedbergh, estimated the outflow resistance generated by the inner wall endothelium of Schlemm's canal by evaluating the pore size distribution of the tissue and by calculating the hydraulic conductivity of a single pore (Bill and Svedbergh, 1972). The results obtained from this study demonstrated that the inner wall endothelium of Schlemm's canal could attribute for only about 10% of the normal outflow resistance (Bill and Svedbergh, 1972), a finding that has also been observed by later studies (Svedbergh, 1976; Eriksson and Svedbergh, 1980; Moseley et al., 1983).

On the other hand, studies in which proteolytic enzymes (α-chymotrypsin) or chelating agents (EDTA, EGTA) were perfused in living primates (Bill et al., 1980; Hamanaka and Bill, 1987; Hamanaka and Bill, 1988). The findings from these studies showed that perfusion of these enzymes and agents caused rupture of the inner wall endothelium resulting in a decrease in outflow resistance, more than could be explained by the initial proposed calculations. A greater decrease in outflow resistance has been seen most likely because these enzymes or chelating agents enhanced the hydraulic conductivity of the cell layer or the ruptures observed altered the ECM of the inner wall basement membrane or JCT.

Subsequent studies reported that there is a relationship between the density of the intracellular pores and the amount of fixative used to perfuse the conventional outflow

pathways. In particular, it has been shown that the number of the intracellular pores increased with increasing amount of fixative (Sit et al., 1997; Johnson et al., 2002).

Thus, even though there is enough data to support that the endothelial cell lining of the inner wall of Schlemm's canal can generate aqueous outflow resistance, the precise amount of resistance generated by this region is still debated.

1.5.5.6. Aqueous outflow resistance generated within the JCT

To date, it is universally accepted that the JCT is the source of the greatest aqueous outflow resistance generation in the conventional pathway.

Of particular interest, Maepea and Bill attempted to characterise the primary site of outflow resistance using micropipettes to measure the pressure drop at different regions of the conventional outflow pathway in monkeys (Maepea and Bill, 1989; Maepea and Bill, 1972). They found that the majority of the pressure drop occurs within 14 μm upstream of the inner wall of Schlemm's canal, specifically, within the JCT but recently there is a debate with regards to the spatial resolution of their results.

As discussed previously, the structure of JCT is a combination of optically empty spaces surrounded by ECM material. Scientists have characterised these optically empty spaces as micron-sized tortuous pathways for aqueous humor to enter the inner wall of Schlemm's canal and examined their potential in generating resistance. Interestingly, both morphometric and theoretical studies showed that unless these optically empty spaces are in fact filled with an ECM that cannot be detected by the routine conventional transmission electron microscopic techniques, these spaces are too large to generate significant outflow resistance (Seiler and Wollensak, 1985; Ethier et al., 1986; Ten Hulzen and Johnson, 1996). It has been proposed that these optically empty spaces are most likely to be filled with

glycosaminoglycans which collapse once the tissue is being processed for conventional transmission electron microscopy and thus become invisible when visualised under the microscope (Ethier et al., 1986).

Further support for the hypothesis that glycosaminoglycans are important players in the regulation of the aqueous outflow comes from a number of earlier studies that showed a significant decrease in aqueous outflow resistance after perfusion with hyaluronidase, an enzyme that digests hyaluronan in a variety of species, including bovine and rabbits (Bárány and Scotchbrook, 1954; Van Buskirk and Brett, 1978; Knepper et al., 1984).

One would expect a similar phenomenon to also characterise the human eyes but it is interesting to note that studies which investigated the role of glycosaminoglycans as barriers of the outflow in humans, do not clearly support this statement. More exactly, early studies by Grant, 1963 failed to show a clear effect of hyaluronidase enzyme treatment (Grant, 1963). In addition, recent investigations of Keller and co-workers, 2008 tried to shed a light in the actual role of glycosaminoglycans in the regulation of outflow facility in two distinct ways (Keller et al., 2008). At first, they either inhibited the elongation or the sulfation status of glycosaminoglycans and secondly they depleted the glycosaminoglycans following enzyme digestion. Although, biochemical interference of the glycosaminoglycan status was found to be associated with a decrease in outflow resistance, no relationship between the glycosaminoglycans and the outflow facility was found in the enzyme treated eyes.

In an attempt to uncover the glycosaminoglycans presence in the empty spaces of the JCT, Gong and colleagues 2002, have used quick-freeze/deep-etch microscopy to investigate the structure of the JCT (Gong et al., 2002). Even though their data demonstrated a more detailed ECM network of the JCT as opposed to what it has already been observed with transmission

electron microscopy, it was still unable to expose the presence of glycosaminoglycans within the empty spaces. Their findings do not necessarily exclude the possibility that the empty spaces are filled with glycosaminoglycans as it is uncertain whether this technique is able to preserve and demonstrate glycosaminoglycan presence in their uncollapsed state.

1.6 Aims and Objectives

The aims of this research were to apply state of the art techniques for the structural and biochemical investigation of the cornea and the trabecular meshwork.

The first part of this study aimed to examine the chemical composition and S speciation of the embryonic and adult corneal tissue. Any observable biochemical alterations in the element composition and S speciation in the embryonic cornea will provide new insights into the controlled developmental events that lead to the transition of an opaque cornea to a mature cornea. S is a fundamental element in corneal tissue architecture and examination of the S-containing compounds across the depth of the mature corneal stroma will improve our knowledge on the maintenance of a transparent corneal matrix.

The second part of this project was focused on the trabecular meshwork. The aim of this part was to reveal the three-dimensional ultrastructure of the trabecular meshwork with a particular interest on the ultrastructure of the JCT and the inner wall of Schlemm's canal and elucidate the aqueous humor outflow pathway. Taking into consideration that collagen type VI is a primary component of the ECM of the trabecular meshwork an additional aim for this study was to determine the assembly of collagen type VI in the trabecular meshwork in three-dimensions.

Chapter 2: Principles and concepts of experimental procedures

In this chapter the principles of all the experiments used for the purposes of this project will be introduced. Details of the materials and specific aspects of the methods employed, from tissue/sample preparation to data acquisition and data analysis will be provided later on for each individual chapter.

2.1. Basic principles and concepts for experimental design in Chapters 3 & 4

The results presented in Chapters 3 and 4 have been obtained by applying synchrotron techniques to the study of biological bulk tissue. Scientists have long used synchrotron radiation to probe the ultrastructure of biological tissues, as for example the cornea, including that of the developing chick (Quantock, et al., 1998; Meek and Quantock, 2001) as synchrotron facilities can produce a wide range of x-ray energies that can be used to probe the majority of the elements in the periodic table.

A major necessity for understanding synchrotron techniques is to introduce the Bohr's atomic model (Schwarz, 2013). In 1913, Bohr proposed a model that describes the structure of an atom. As illustrated in Figure 2.1, Bohr proposed that electrons revolve in distinct orbits, or shells, that have different energies around the nucleus of the atom.

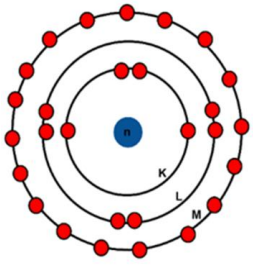

Figure 2.1: The Bohr's atomic model. The atomic model proposed by Bohr states that the atom has a positively charged nucleus (n, blue) which is surrounded by electrons (depicted in red) that are travelling in orbits or shells (K, L, M) with various energy levels.

Bombarding a sample with a focused ion beam or x-rays will automatically cause an interaction of the electromagnetic radiation with the electrons bound in an atom within the specimen, affecting its atomic state (Newville, 2004). Several phenomena can occur upon irradiation of a sample. When x-rays interact with a sample, the electrons bound in an atom will either scatter x-rays or the electrons will absorb or excite energy as radiation.

In this project, synchrotron techniques have been employed to firstly investigate changes in the chemical composition and examine any alterations in the sulphur (S) speciation of the developing chick cornea and secondly to explore changes in the S species of the mature bovine cornea across the depth of the tissue. All experiments were conducted at the endstation ID21 of the European Synchroton Radiation Facility (ESRF, Grenoble, France).

2.1.1. X-ray fluorescence microscopy

2.1.1.1 Principle and instrumentation of x-ray fluorescence microscopy

In recent days, especially with the development of third-generation synchrotron facilities, synchrotron x-ray fluorescence (XRF) microscopy has become a powerful technique for imaging the elemental composition of the tissue of interest with increased sensitivity and submicron resolution. XRF microscopy uses ultra-high X-ray energy to determine and quantify the elemental composition of a sample. The advantages of this technique are that it is fast, minimal sample preparation is required and most importantly the fact that it is a non-destructive technique. XRF microscopy was used to examine the chemical nature of atoms in molecules that characterise the embryonic chick corneal stroma and additionally to uncover any chemical compositional changes that take place with development of embryonic chick cornea.

As stated above, the fundamental aspect of all synchrotron techniques it the use of electromagnetic radiation which is emitted by electrons, accelerated by the synchrotron apparatus, to irradiate the sample. The basic principle of XRF is that once a sample is irradiated by x-rays, a core-shell electron (usually one from the lower energy levels shells, like K and L) is ejected, generating an electron vacancy (Figure 2.2) (Brouwer, 2010). This vacancy is subsequently filled by a higher-shell electron and this process will ultimately cause the emission of a photon, or in other words the emission of fluorescent x-ray radiation, whose energy is equal to the difference in binding energies of the two shells involved in the change. Fluorescence radiation is commonly used to describe the fact that absorption of radiation is followed by re-emission of radiation of a different energy. The energy of the emitted fluorescent x-ray is characteristic of the elements of the target atom; therefore, by measuring the energies of the emitted radiation one is able to define the elemental composition of the sample. Figure 2.3 shows the main elements of an XRF microscope.

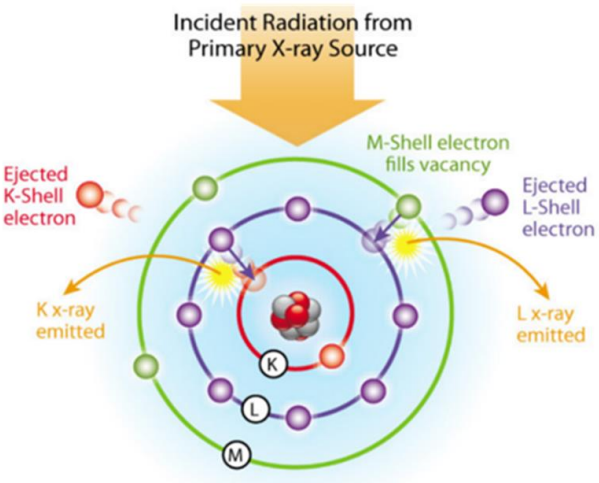

Figure 2.2: The principle behind x-ray fluorescence microscopy. When an atom is being excited a core-shell electron is being ejected generating an electron vacancy which will then be filled by an electron that travels at a higher-energy orbit. The electron vacancy filling process requires that the electron will emit energy that is equal to the difference of the energies of the two orbits that are involved. The emitted energy is characteristic for every element. Adapted from http://www.niton.com/sf-images/general-images/xrf-excitation-diagram.jpg?sfvrsn=2.

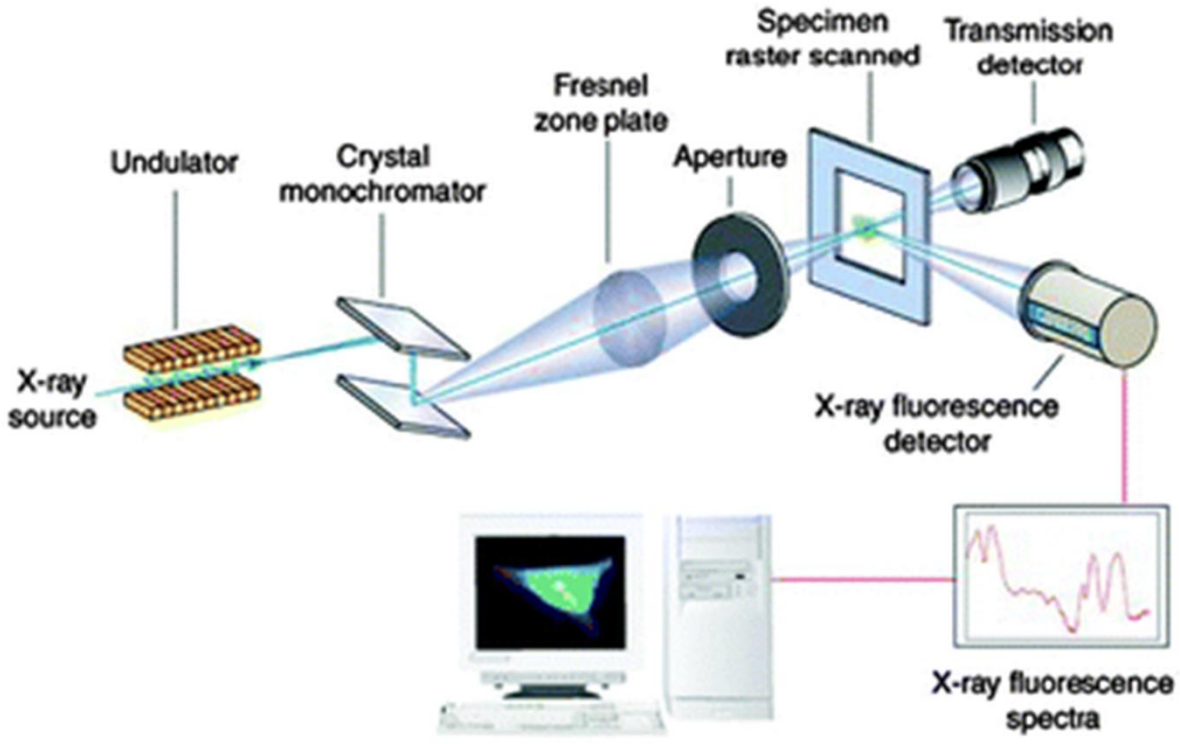

Figure 2.3: The x-ray fluorescence microscope. A schematic representation of the structure and the main elements of an x-ray fluorescence microscope. An x-ray source, as for instance, a synchrotron will provide beams of photons and with the use of a crystal monochromator, the energy of interest will be selected. The energy will then be focused with a Fresnel zone plate on the sample. Orientation of the specimen is achieved through a transmission detector. Once the sample becomes excited, emitted x-rays are collected by an x-ray fluorescence detector which is connected to a computer. Adapted and modified by Fahrni, 2007.

2.1.2. X-ray absorption near edge-structure spectroscopy

2.1.2.1 Principle of X-ray absorption near edge-structure spectroscopy

X-ray absorption near edge-structure (XANES) spectroscopy was the second synchrotron technique used in this study. XANES spectroscopy allows one to acquire information regarding the oxidation state and the coordination environment of various metal atoms. In our study, XANES spectroscopy was applied to elucidate changes in the S speciation, or in other words changes in the S species, as for instance, thiols, organic monosulfides and inorganic sulphate, of the embryonic chick cornea (Chapter 3). In addition to this, S k-edge XANES spectroscopy

was also applied to probe the S speciation of the mature cornea across the whole corneal depth (Chapter 4).

The fundamental concept behind XANES spectroscopy is that this technique characterises a specimen by assessment of unoccupied electronic states and it can be element specific. In cases where the incident x-ray beam energy is equal to that of the binding energy of core shell electron, the absorption enhances and produces an absorption edge, which is basically an absorption discontinuity in the absorption spectrum of an element. The term absorption edge denotes that the incident energy is the least energy that can be used at which a core-shell electron vacancy can be created. The resultant photoelectron will jump into unoccupied states. XANES spectroscopy evaluates the photoelectron intensity for photon energies found near the edge region; within 50 eV from the absorption edge (Figure 2.4).

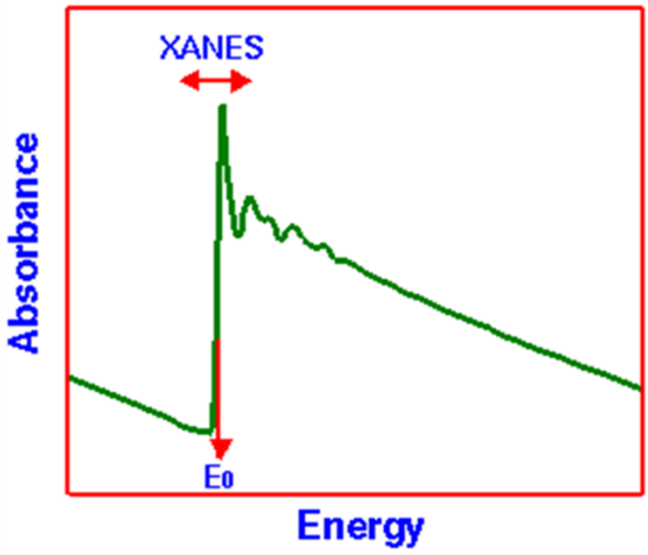

Figure 2.4: XANES spectroscopy. XANES spectroscopy assesses the structures near the absorption edge, up to approximately 50 eV from the absorption edge. Figure adapted and modified from http://leung.uwaterloo.ca/MNS/102/Lectures%202007/SSNT-4-Surface%20Structure%20Determination%20Techniques%20I_files/image027.gif.

2.2. Basic principles and concepts for experimental design in Chapters 5 & 6

2.2.1. Transmission electron microscopy

Transmission electron microscopy (TEM) has found widespread applications in a broad range of biomedical disciplines. TEM can be classified as one of the most valuable tools in biomedical research since it offers the capability of the ultrastructural investigation of tissue anatomy and morphology and its application has profoundly enhanced our understanding of tissue structure and function and especially the anatomy and physiology of the cell. As the name denotes, TEM employs the use of high energy electrons to irradiate the specimen under investigation. Transmission of the electrons through the specimen will produce a two-dimensional projection image of the specimen.

The current study has applied TEM to study the structure and organisation of collagen type VI in the human trabecular meshwork (Chapter 5). In addition to this, TEM has also been used for the ultrastructural investigation of the human trabecular meshwork, a sponge-like tissue located at the anterior chamber of the eye and plays a fundamental role in the aqueous humor outflow pathway (Chapter 6). The TEM used for these experiments was a JEOL 1010 transmission electron microscope with a Gatan ORIUS SC100 CCD camera.

2.2.1.1 General sample preparation

A specific sample preparation procedure must be performed prior tissue observation under the TEM (Figure 2.5). There are three critical steps in the preparation of sample for investigation in the TEM and these are fixation, dehydration and infiltration and tissue embedding.

The fixation is probably one of the most critical steps in TEM sample processing as tissue and cell structure preservation to a state as possible closest to the living state is achieved. The fixative agents will cross-link cellular structures into a matrix to protect them and stabilize them from subsequent sample preparation treatments and also from beam damage when they are examined under the microscope. Despite the fact that glutaraldehyde penetrates a sample at a relatively slow rate, compared to paraformaldehyde, another commonly used fixative agent, it provides a better and stronger fixation. Osmium tetroxide is often used as a secondary fixative agent. Osmium tetroxide permeabilizes cell membranes and reacts with lipids present in the sample and more specifically it oxidizes the unsaturated bonds of fatty acids. The resulting reduced chemical form of osmium tetroxide is electron dense and thus fixation through this agent also gives contrast to biological tissues.

Taking into consideration that TEM operates in vacuum and that biological materials contain water, the dehydration step is also an important step in the preparation of sample for TEM. The aim of the dehydration step in the sample processing is therefore the removal of water from biological materials by immersing the sample through a series of ethanol.

Infiltration and tissue embedding steps underline the tissue position in the embedding medium that is allowed to polymerise. As a result, tissue resin blocks are generated which can be subsequently used for tissue ultramicrotomy and acquisition of thin tissue sections on copper grids that can be then studied in the TEM.

2.2.1.2 Routine sample processing and embedding protocol for TEM

Biopsies of the human trabecular meshwork that were to undergo routine sample processing for TEM were primary fixed in 2.5% glutaraldehyde in 0.1M sodium cacodylate buffer (pH 7.2-7.4) for 3 hours at room temperature, immediately after tissue dissection. Following primary fixation, the samples were washed twice for 10 minutes in 0.1M sodium cacodylate buffer for 3 hours at room temperature. The samples were then kept frozen, in the buffer, at 4^{o}C overnight. In the morning of the following day, post fixation was carried out by placing the samples in 1% osmium tetroxide in 0.1M sodium cacodylate buffer for an hour at room temperature, in a fume hood. Then, the samples were washed three times in distilled water for 10 minutes each. The samples were further contrasted in 0.5% aqueous uranyl acetate for an hour. Dehydration is then followed by immersing the samples in a graded series of ethanol of 70%, 90%, 100% (x2), for 15 minutes each time. After dehydration, the samples were immersed twice in propylene oxide, for 15 minutes each time, and then to 1:1 propylene oxide: Araldite resin for an hour before sample resin infiltration. Resin infiltration step was performed for two days including three changes of resin per day. A slow rotation was used to facilitate resin penetration in the tissue block. The last step of sample processing for TEM is tissue embedding in specific TEM moulds with further resin which were allowed to polymerise at 60^{o}C for 72 hours. At this step, prior resin polymerisation, tissue orientation is determined.

Ultramicrotomy was subsequently performed to obtain ultrathin sections on copper grids that were inserted on the transmission electron microscope. Tissue blocks are trimmed down and tissue sections are collected on glass knives ‘boats’ filled with filtered distilled water. For this study, a LEICA EMKMR2 glass cutter (Leica, Austria) was used to cut glass knives whose top

sides are covered and sealed by tape to produce a 'boat' in which tissue sections can be then collected. Ultramicrotomy was carried out using a Reichart-Jung Ultracut Microtome.

At first, semi-thin tissue sections, about 500 nm thick, were obtained and after being transferred on a microscope slide were stained with 1% Toluidine blue dye to aid tissue histology and identification of the tissue area/position within the tissue block. Once the cutting surface is the desirable one, ribbons of ultrathin sections of about 90-100 nm thick were collected on copper grids. Sectioning may compress the tissue sections and chloroform is used to stretch out the sections.

In order to obtain even better electron dense contrast enhancing areas within our tissue, the grids were stained with uranyl acetate for 13 minutes in the dark, washed four times in filtered distilled water (1 minute each time) and left to dry before visualisation under the transmission microscope.

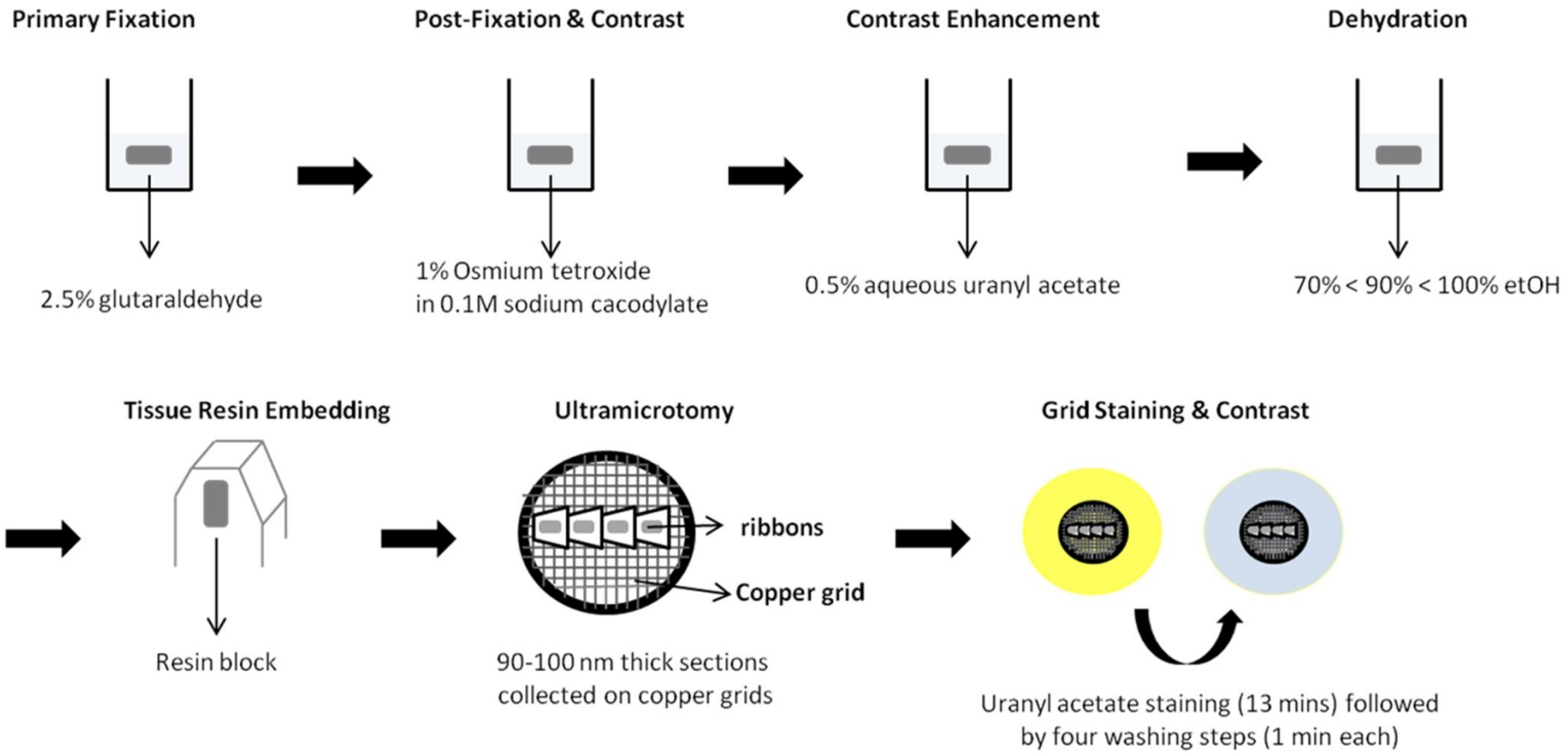

Figure 2.5: Routine sample preparation for TEM. Schematic diagram showing the main steps, namely primary fixation, post-fixation and contrast, contrast enhancement, dehydration, embedding, ultramicrotomy and post staining, for the conventional sample prosessing prior investigation under TME.

2.1.3 Cuprolinic blue staining - Sample processing and embedding protocol for TEM

Some samples of the human trabecular meshwork underwent through a slightly different sample processing and embedding protocol for TEM (Figure 2.6) to aid the investigation of the ultrastructural localization of proteoglycans in tissue with a particular interest on the assessment of proteoglycan-collagen VI structural interactions in the trabecular matrix. In particular, the initial steps of the sample processing protocol involved tissue staining with the cationic Cuprolinic blue dye, an electron microscopical dye. Cuprolinic blue dye is widely used in the scientific community to visualise and localize the proteoglycan molecules with TEM (Scott and Haigh, 1988). The mechanism of action of Cuprolinic blue is based on its interaction with the highly anionic sulphated glycosaminoglycan side chains of the proteoglycan molecules.

Straight after tissue dissection, the samples that were to undergo Cuprolinic blue processing were fixed/stained overnight in 2.5% glutaraldehyde in 25 mM sodium acetate buffer (pH 5.7) containing 0.1 M magnesium chloride and 0.05% Cuprolinic blue. The next day, the samples were rinsed three times, for 10 minutes each time, in sodium acetate buffer (pH 5.7) to remove excess of the fixative agent and unbound dye. Three additional washing steps (10 minutes each) in aqueous 0.5% sodium tungstate were carried out prior tissue dehydration. In contrast to the dehydration procedure followed for the routine sample processing, this sample protocol has an extra step which involves tissue immersion in a solution of 50% ethanol and 0.5% sodium tungstate for 15 minutes. After this, the tissue is immersed in a graded series of ethanol (70%, 90%, 100%) as described above. The following steps are the same as for the routine sample processing protocol.

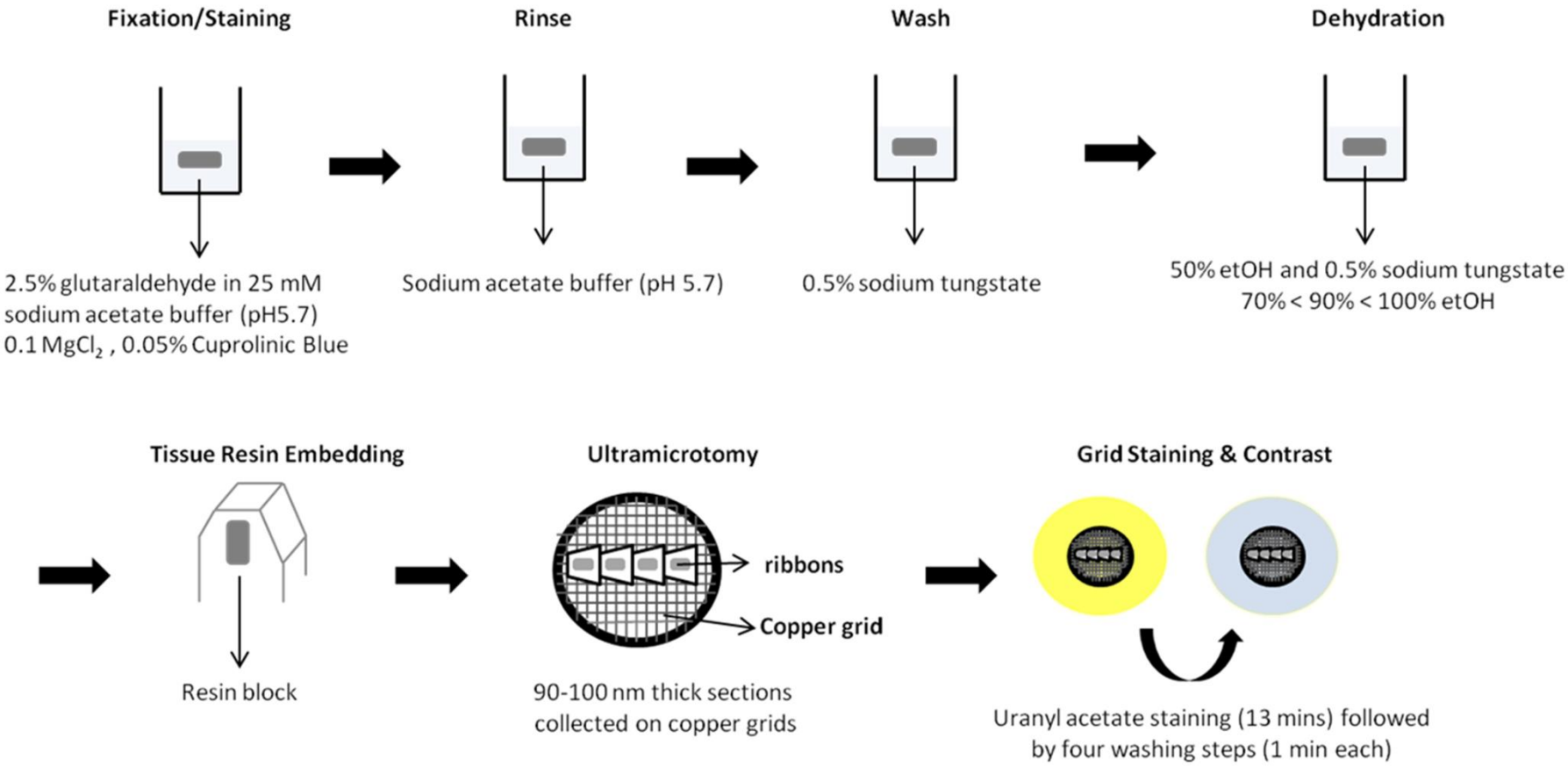

Figure 2.6: Cuprolinic blue sample preparation for TEM. Schematic diagram showing the main steps, namely primary fixation, post-fixation and contrast, contrast enhancement, dehydration, embedding, ultramicrotomy and post staining, for the conventional sample prosessing that involves tissue staining with Cuprolinic blue dye, prior investigation under TME. Cuprolinic blue dye is used for visualisation and examination of the sulphated glycosaminoglycans.

2.2.2 Serial block face scanning electron microscopy

2.2.2.1 Principle and instrumentation of serial block face scanning electron microscopy

Serial block face scanning electron microscopy, also known as volume scanning electron microscopy, is a technique that allows the study of three-dimensional ultrastructure of large volumes at high resolution. As the name indicates, serial block face scanning electron microscopy branches from scanning electron microscopy. Scanning electron microscopy is primarily a surface imaging technique; so the fundamental principle for volume scanning electron microscopy is to sequentially automatically acquire an image on a fresh resin embedded block sample surface. In detail, once the sample surface of a resin embedded tissue block is imaged, an ultramicrotome equipped with a diamond knife, -or alternatively, a focused ion beam- is used to automatically slice and renew the sample surface and consecutively image the new sample surface. Figure 2.7 illustrates the principles and instrumentation of serial block face scanning electron microscopy. A backscatter electron detector is used to capture the image which has the appearance of a classic TEM image.

The current study has applied serial block face scanning electron microscopy in order to visualise and reconstruct large volume three-dimensional ultrastructure of the human trabecular meshwork, for the first time. Serial block face scanning electron microscopy was then carried out using a FEI Quanta FEG 250 scanning electron microscope fitted with a Gatan 3View® system that uses an ultramicrotome to slice and renew the sample surface (Figure2.8).

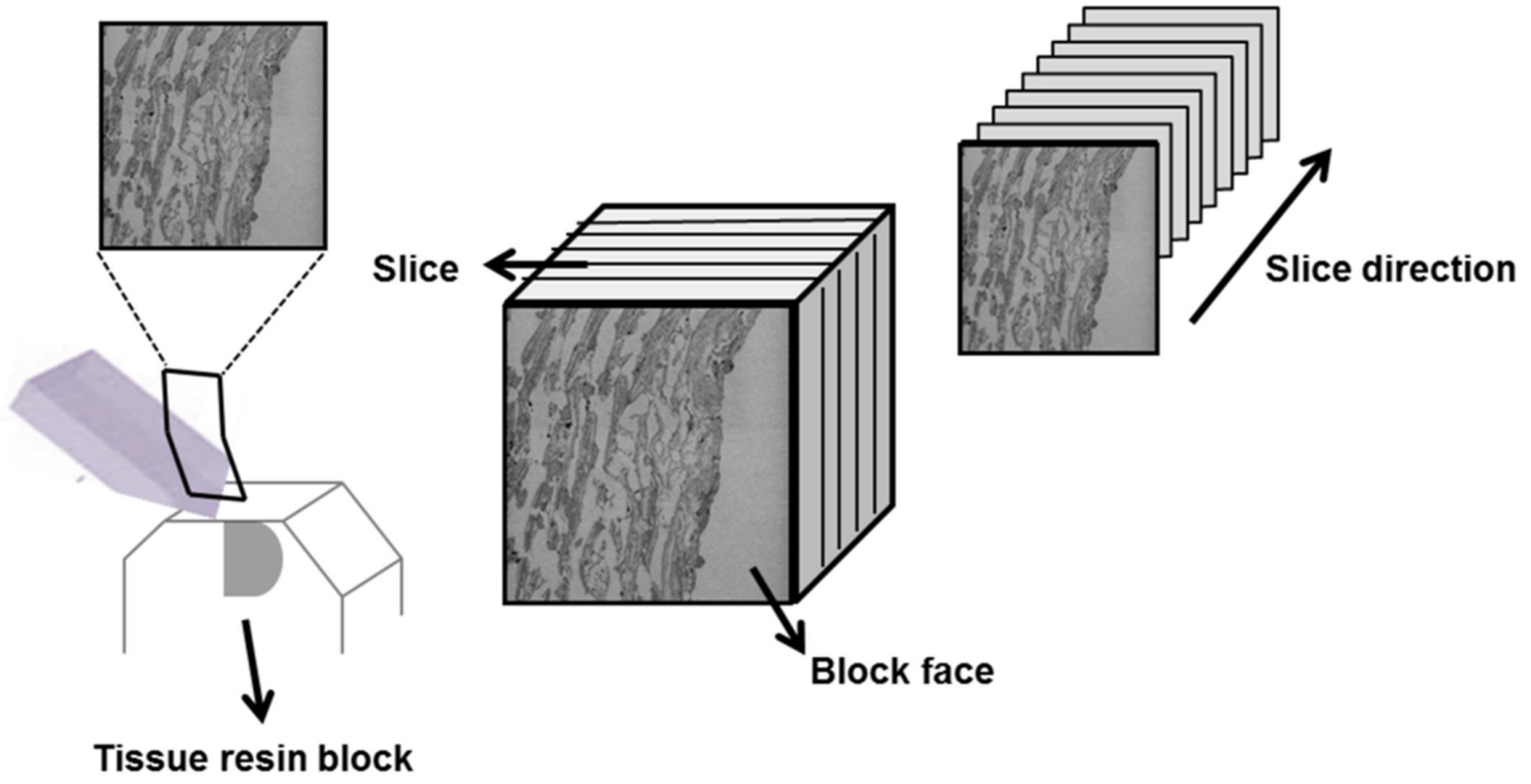

Figure 2.7: The principle of the serial block face scanning electron microscopy. Serial block face scanning electron microscopy is a surface image technique that acquires an image of the block face and then a diamond knife (purple) which is embedded in a microtome, located inside the microscope, is used to renew the block face. The block face shown here is from the actual stack used in this study.

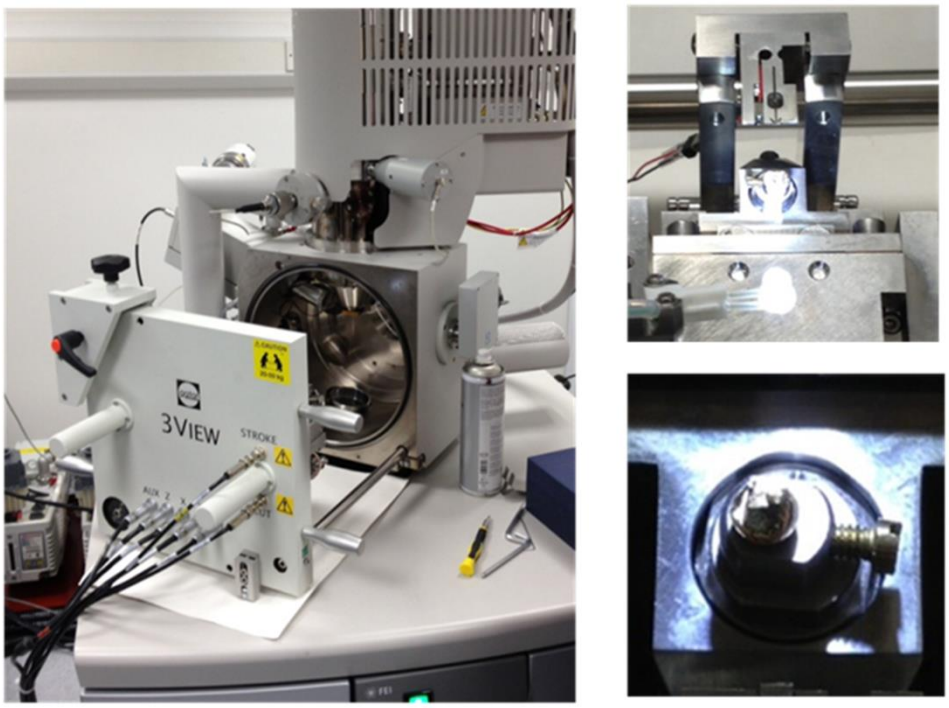

Figure 2.8: FEI Quanta FEG 250 scanning electron microscope fitted with a Gatan 3View® system. On the right hand side the ultramicrotome which is fitted inside the microscope is shown. The sample surface is sliced and renewed with a diamond knife and then image is acquired.

2.2.2.2 Sample preparation for serial block face scanning electron microscopy

Tissue specimens are prepared by much the same method that would be used for TEM, namely chemical fixation, through dehydration and tissue embedding to produce a conventional resin block, as shown above in Figure 2.5. An important addition in the sample processing for serial block face scanning electron microscopy is the inclusion of infiltration with several heavy metal salts, as for example, lead, osmium and uranium. The purpose of this is to bind significant high atomic number elements to imaged tissue structures in order to generate a strong backscatter electron signal which can be subsequently detected in the scanning microscope via the backscatter electron detector. Resin blocks are faced according

to conventional methods for TEM; sections can be taken for preliminary light and TEM to enable tracking of the desired region to be investigated.

2.2.3 Three-dimensional electron tomography

As being noteworthy above, TEM provides important structural details of the specimen through the formation of a two-dimensional image of the specimen, a projection. The term projection images underlie the fact that the images encompass all the information obtained from the areas of the imaged object through which the electron beam has been transmitted. However, one caveat of TEM is that structural details across the depth of the specimen are laid over another to create a two-dimensional projection image whilst keeping out of sight, obscuring, critical aspects of the ultrastructure and molecular organisation of the tissue.

Recent advances in electron microscopic technologies lead to the development of transmission electron tomography, a powerful imaging technique that has the capacity to reveal the three-dimensional structure of the imaged object (McEwen and Marko, 2001; Baumeister, 2002; Subramaniam et al., 2003).

2.2.3.1 Principle of electron tomography

The principle of electron tomography technique involves the use of the transmission electron microscope and the acquisition of two-dimensional images of the specimen, however, unlike TEM the two-dimensional images are collected while tilting the specimen at various angles around a single axis (Figure 2.9). In order to reconstruct the three-dimensional structure of the imaged specimen, the whole tilt series image sequence is aligned and subsequently subjected to back projection by using specific softwares for electron tomographic reconstructions. The concept of the back projection algorithm is based on projecting back the

density of every tilted view acquired towards the beam line in a theoretical box. The height of this theoretical box is identical to the thickness of the specimen.

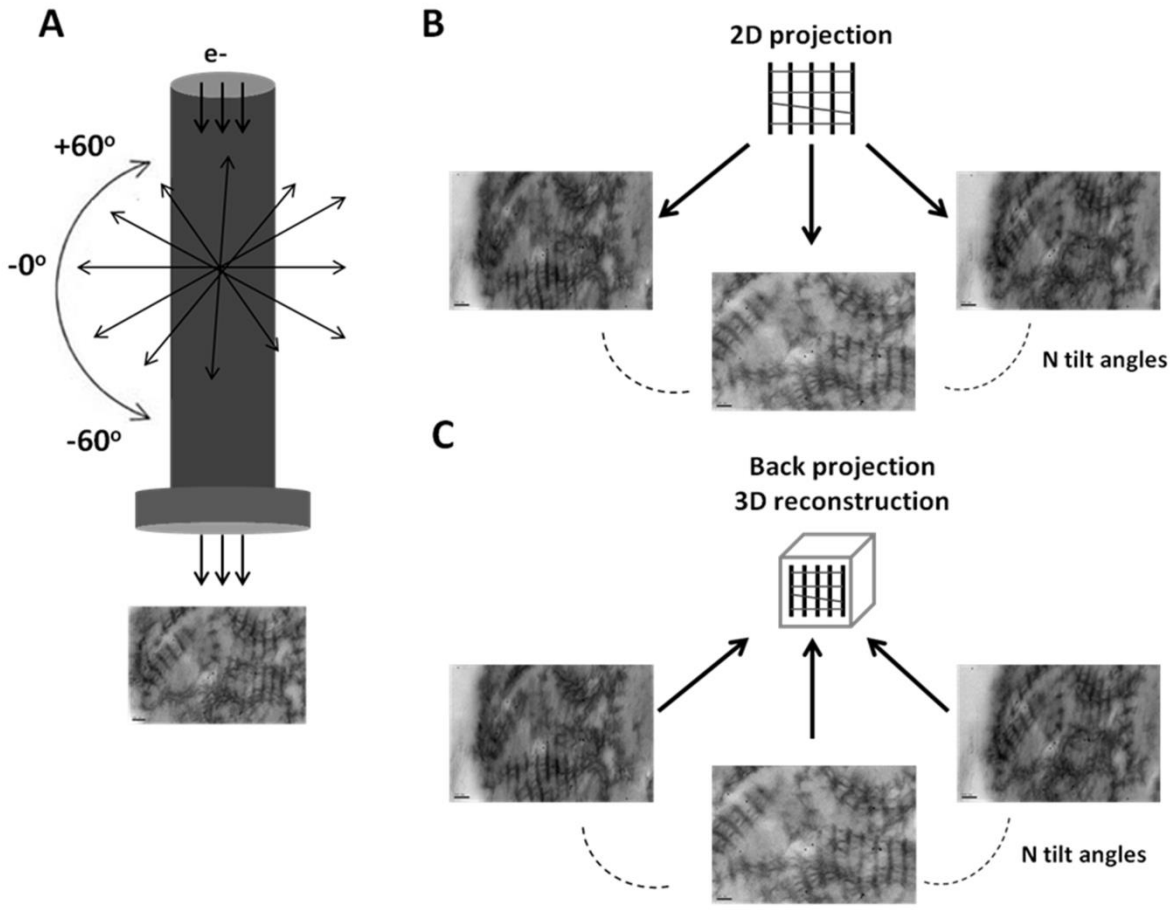

Figure 2.9: The principle of transmission electron tomography. (A) The specimens are investigated using a TEM and two-dimensional images are acquired by tilting the specimen at different angles, for example from +60°C to -60°C. **(B)** Projection two-dimensional tilt series image sequence is obtained which is subsequently digitally processed. **(C)** Digital processing includes the application of back projection algorithm which is necessary for the generation of a three-dimensional reconstruction.

2.2.3.2 Specimen preparation and data acquisition

Sample preparation processing for electron tomography follows the same protocol for either the routine or the Cuprolinic blue sample processing for TEM, from tissue fixation to tissue embedding. There are two distinguishing steps for the sample processing for electron tomography as opposed to the one applied for TEM. The first one is the requirement for the acquisition of slightly thicker tissue sections. More specifically, due to the fact that the specimen is exposed to the electron beam for a longer period of time, tissue sections of about 100-120 nm thick are obtained to avoid tissue damage when examined under the microscope. In addition to this, it is important to mention that when tissue sections are collected on the copper grids it is required to be positioned as near as possible to the center of the grid. The reason for this is that the tissue areas located at the edge of the grid are not suitable for electron tomography since when tilted at high angles the edge of the grid will mask the region under investigation.

The second difference in the specimen preparation process between the two electron microscopy approaches is the application of fiducial markers which serve as reference points and aid image position to the same co-oordinates at each tilt angle and ensure alignment with the previous captured image. In particular, following grid staining the grid is coated on both sides with fiducial colloidal gold (10 nm; Agar Scientific; R14078-2) for approximately 4 minutes at each side of the grid.

In the current study, the human trabecular meshwork tissue samples that already underwent Cuprolinic blue processing for TEM were also utilised for electron tomography with the scope of revealing the three-dimensional structure of collagen VI and the supramolecular organisation of collagen VI-proteoglycan interactions (Chapter 5). Single-axis tilt series of

electron micrographs of collagen type VI in the trabecular meshwork were obtained from +60^{o} to 60^{o} in both one and two degree increments at x20k magnification using a a JEOL 1010 transmission electron microscope with a Gatan ORIUS SC1000 CCD camera.

2.2.2.3 Alignment of the tilt series

Upon acquisition of the tilt series image sequence, data was converted into a .st image stack with the use of Cygwin software prior digital analysis with the IMOD software package (Kremer et al., 1996) that is commonly used in electron tomography. Alignment of the tilt series image sequence was performed in eTOMO software which is a sub-program of IMOD. A series of specific automated and manual processing steps, as for instance, coarse alignment, fiducial model generation, final alignment and tomogram generation, are executed in eTOMO to generate a final aligned tomogram. Along these processing steps, the gold fiducial markers are manually tracked bringing all the images into alignment (Figure 2.10). Moreover, once stack alignment is generated, eTOMO employs the back projection algorithm to create a three-dimensional tomogram.

2.2.2.4 Segmentation of three-dimensional reconstruction

Following the generation of the final tomogram, EM3D software (Ress et al., 2004) is used for visualization, segmentation, rendering of the three-dimensional reconstruction and to create a three-dimensional model, representative of the ultrastructural character of the object under investigation. A three-dimensional model is established by firstly manually positioning contours around the perimeter of the elements of interest on every slice of the volume reconstruction (Figure 2.11). At last, the segmented features of interest are rendered and give rise to a three-dimensional reconstruction.

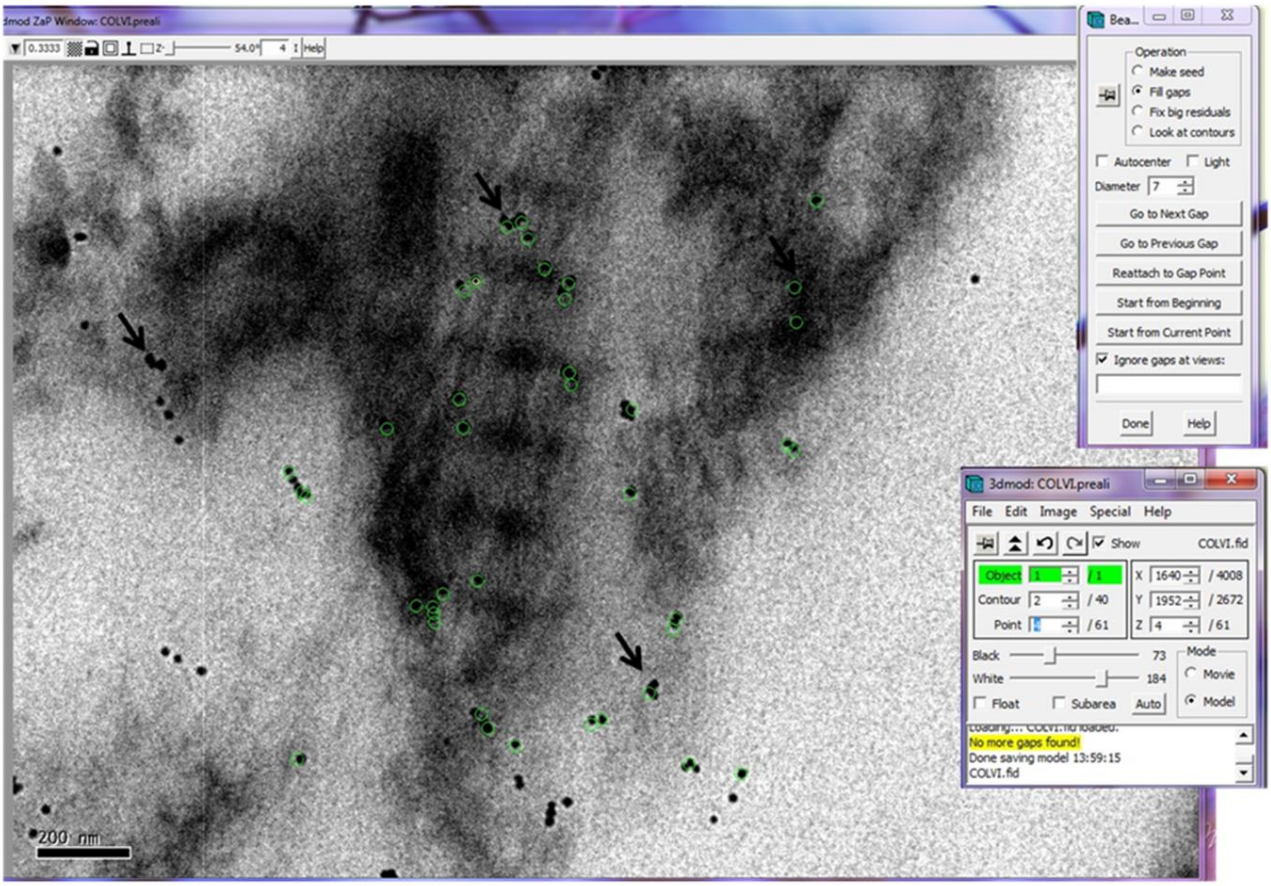

Figure 2.10: Schreenshot of the final alignment stage using eTOMO software package. The specimen was coated with fiducial gold markers (arrows) prior investigation with the TEM. At first, using the 0^{o} tilted micrograph the fiducial markers are manually traced and encircled by contours (green circles).For a good align tilted image sequence approximately 40 contours are required. The final alignment step involves tracing and fixing the contours which may not properly encircle all the fiducial markers in every tilted micrograph.

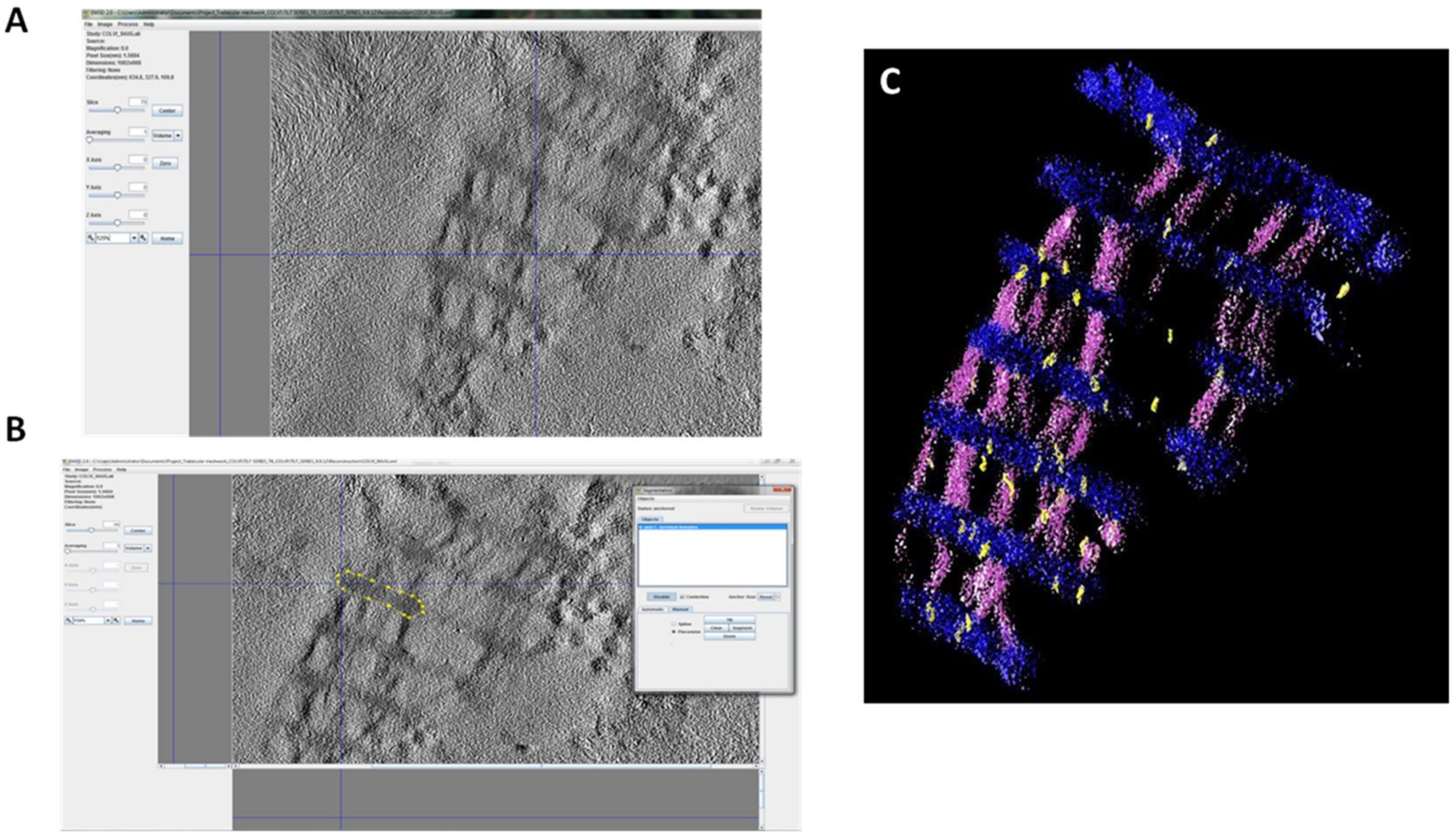

Figure 2.11: Screenshot of the visualization, segmentation and rendering stages in EM3D software. (A) The tilted image sequence is visualised in X, Y and Z directions. **(B)** The features of interest are manually segmented by drawing contours (yellow stars) around the perimeter of the object. **(C)** Rendering of the segmented objects give rise to the three-dimensional reconstruction.

Chapter 3: Molecular signatures and matrix morphogenesis elucidated by XRF microscopy and XANES spectroscopy

3.1. Introduction

XRF microscopy and XANES spectroscopy are synchrotron based techniques, whose principles and concepts have been described in Chapter 2, sections 2.1.1 and 2.1.2. In this chapter these techniques have been used to establish their application for the chemical and S speciation investigation in intact biological tissue, specifically in the embryonic chick cornea, with the aim to elucidate molecular signatures and matrix morphogenesis alterations, associated with the chemical composition and S speciation of the cornea that take place with embryonic development and acquisition of transparency.

3.2. Materials and Methods

3.2.1. Experimental model

Fertilized white Leghorn chicken eggs were collected from a commercial hatchery (Henry Steward & Co, Lincolnshire, UK) and incubated at 37.5^{o}C in a humidified chamber. Based on the Hamilton-Hamburger staging (Hamburger and Hamilton 1951; Hamburger 1992) chicks at embryonic days 12, 14 and 16 of incubation were sacrificed in accordance with the Association for Research in Vision and Ophthalmology statement for the use of animals for Ophthalmic and Vision Research and local ethical regulations. All the chick corneas were carefully dissected with the use of surgical tools and processed for analysis by synchrotron techniques.

3.2.2. Synchrotron XRF microscopy

Synchrotron XRF microscopy was used to examine changes in the chemical composition of the chick cornea during embryonic development at day 12, day 14 and day 16 (Figure 3.1A). Four chick corneas per embryonic day were sandwiched and flattened between parafilm-covered glass slides and left to dry overnight at room temperature (Figure 3.1B). The data were collected using a scanning electron microscope at the endstation ID 21 at the ESRF. The scanning electron microscope at the ID21 is working with energies from 2 – 9 keV and is optimized for x-ray microfluorescence and microspectroscopy experiments (Barrett et al, 2000). On the day of the experiment, the samples were sandwiched between Ultralene foil (SPEX-CERTIPREP), mounted on the sample holder at room temperature (Figure 3.1C) and afterwards were introduced to the scanning x-ray microscope (Figure 3.1D). The system was calibrated before the experiments began by the beam line scientist and then the specimens were measured at high vacuum.

Data acquisition included the assessment of five randomly selected regions, from the central region of the cornea, for every corneal sample per embryonic day of development, as shown in Figure 3.1E. An XRF spectrum was acquired per region with an integration time of 60 s and a beam size of 100 μm that was attained using a pinhole. The energy of the incident x-ray beam was set up at 4.1 keV because the scope of this experiment was to excite and thus examine the core electrons of elements up to Ca, with a flux of 3.6 x 10^9 photons/s. As explained in chapter 2, section 2.1.1., the x-ray scanning electron microscope has an x-ray fluorescence detector that facilitates the measurement of the emitted fluorescence signals. The fluorescence detector at the endstation ID21 was an energy dispersive silicon drift diode

detector (XFlash 5100, Bruker, Germany) and was used to measure the fluorescence signals emitted after irradiation of the embryonic chick corneal samples.

PyMCA software (Solé et al, 2007) was utilized to extract the XRF spectra of the developing corneas. It is important to note that background subtraction was not carried out in the XRF spectra. The detecting geometry and the fact that data were acquired under vacuum resulted to a minimal background contribution to the XRF spectra. Comparability of the data gathered was achieved by keeping the distance between the fluorescence detector and the sample, the size of the beam, as well as, the photon flux constant throughout the experiments. OPUS 5.5 software (Bruker Optics) was used to limit data analysis in the energy range 1-4.3 keV.

3.2.3. Synchrotron x-ray spectroscopy

Synchrotron XANES spectroscopy was also carried out at the endstation ID 21 at the ESRF to investigate changes in the S species composition between embryonic chick corneas at day 12, day 14 and day 16. For XANES spectroscopy studies, three corneas at embryonic day 12 and day 14 and four corneas at embryonic day 16 were dissected (Figure 3.2A), sandwiched and flattened between ultralene foil-covered glass slides (Figure 3.2B). Due to the fact that there was a time interval between sample preparation and conduction of the XANES experiments, once samples were sandwiched between ultralene foil-covered glass slides they were placed onto dry ice and kept frozen at -80^{o}C until the experiments could be performed. On the day of the experiment, it was necessary to defrost the corneal samples and to prevent any oxidation events for taking place and to achieve this, samples were left to defrost in a chamber with slow nitrogen flow for about 1 h (Figure 3.2C). Once the corneas were defrosted, in a similar manner as described above for the XRF microscopy studies, they were mounted in air at room temperature on the sample holder (Figure 3.2D) and subsequently

were introduced in the microscope for data acquisition (Figure 3.2E). The system was calibrated before the experiments began by the beam line scientist. Thirteen randomly selected regions across the diameter of the cornea, as illustrated in Figure 3.2F, were examined per cornea per embryonic day. For every selected area five XANES spectra, with an integration time of 0.5 s per point, were obtained. The incoming photon energy was tuned from 2.46 to 2.53 keV, with a flux of 5.4 x 10^9 photons/s. The S speciation of the embryonic chick corneas was acquired by extracting the data using PyMCA software (Solé et al, 2007). OPUS 5.5 software *(*Bruker Optics) was used to first perform a linear fit of the pre-edge region which in turn gave a linear background that was subtracted from the spectra. Data normalization was performed using MATLAB (The MathWorks, Natick, MA) by setting the jump to 1. The jump refers to the height of the absorption edge, which has to be taken into account when normalising the S XANES data (see Figure 2.4).

A

Chick corneas were dissected

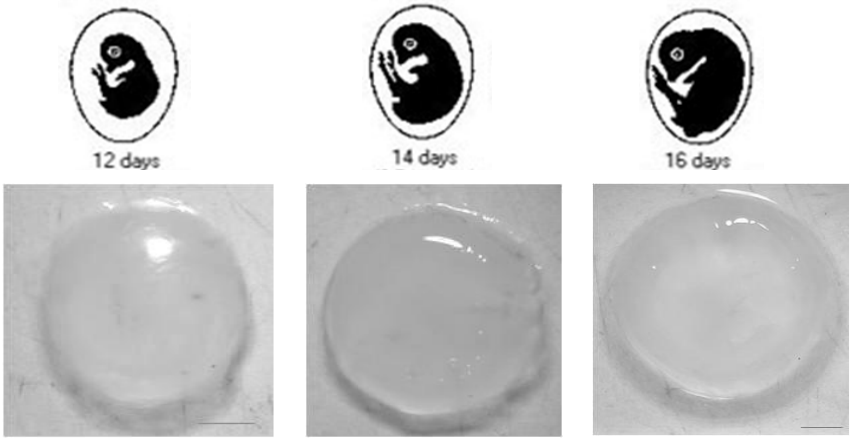

B

Sandwiched & flattened in parafilm-covered glass slides

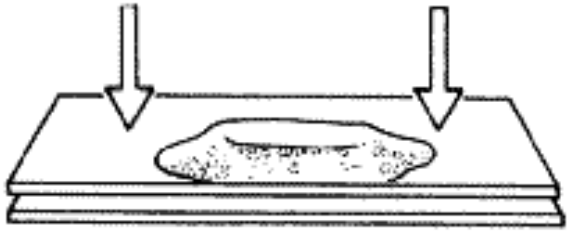

C

Sandwiched between ultralene foil, mounted in air at room temperature on the sample holder

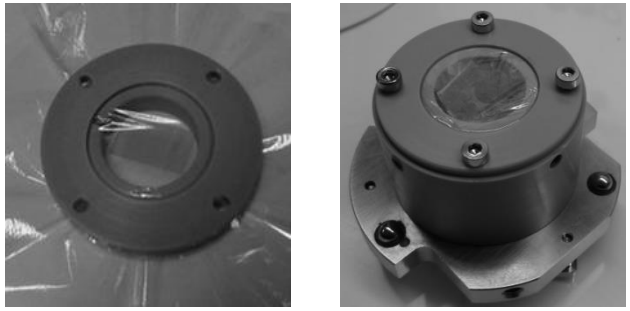

D

Introduced to the x-ray microscope and placed in high vacuum

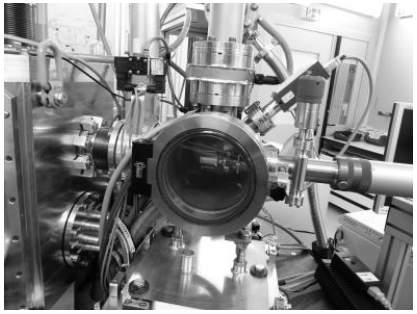

E

Five randomly chosen regions – Acquisition of spectra

Figure 3.1: Schematic diagram illustrating the sample procedure for the XRF microscopy experiments at the endstation ID21 at the ESRF.

A

Chick corneas were dissected

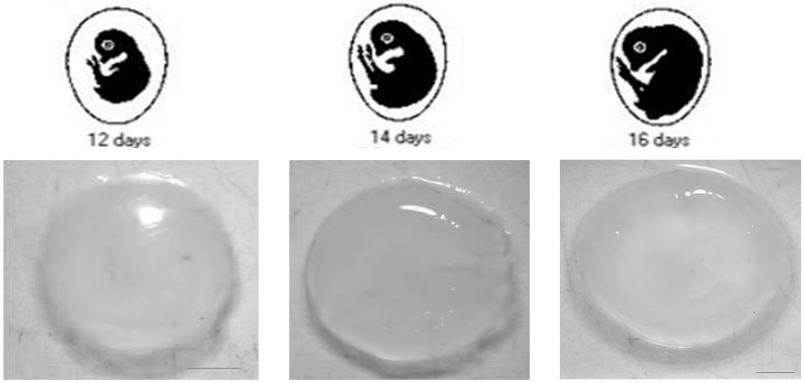

B

Sandwiched & flattened in Ultralene foil-covered glass slides. Kept frozen at -80°C

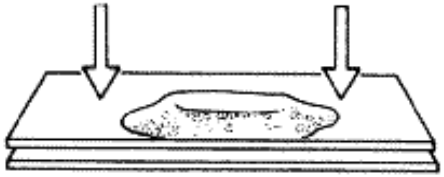

C

Corneas were defrosted in slow nitrogen flow chamber

D

Sandwiched between ultralene foil, mounted in air at room temperature on the sample holder

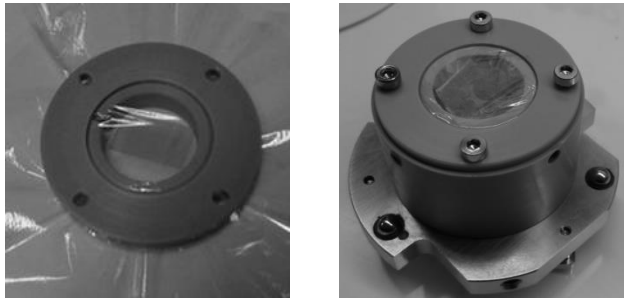

E

Introduced to the x-ray microscope and placed in high vacuum

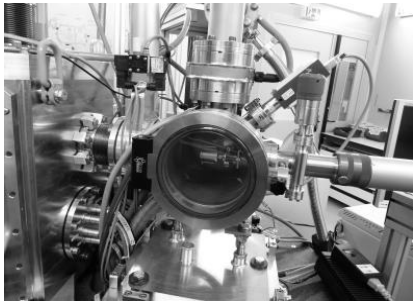

F

Thirteen randomly chosen regions across the diameter of the cornea – Acquisition of spectra

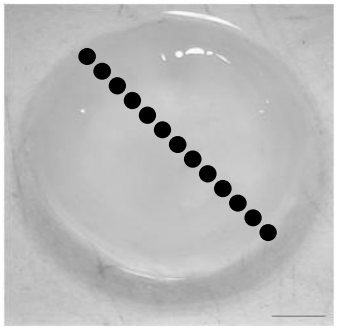

Figure 3.2: Schematic diagram illustrating the sample procedure for the XANES spectroscopy experiments at the endstation ID21 at the ESRF.

3.2.4. Computational Analysis

Experiments that use synchrotron facilities generate massive, complicated data sets, with a large number of variables. Therefore, it is crucial to use computational tools to facilitate meaningful data analysis by breaking down the data set into a number of components which show important variance within the data.

Principal component analysis (PCA) and linear discriminant analysis (LDA) are powerful computational tools that are widely used to classify enormous, complicated data sets and to reduce the dimensionality of the data (Davies and Fearn, 2005; Martin, et al., 2010). PCA and LDA are linear multivariant transformation techniques that will convert data in a new coordinate system, creating new coordinate axes, named principal components (PCs) and linear discriminant (LD) factors in the PCA and LDA approach, respectively. In the new coordinate system the new variables are linear combinations of the optimally weighted observed original variables. While PCA is an unsupervised method (i.e. select principal components on the basis of maximal variance without taking into account the classes), LDA is a supervised method, classes are taken into account and factors that have maximal variance are generated.

PCA has been frequently used for the interrogation of mid-infrared spectroscopy data (Martin et al, 2010; Taylor et al, 2011; Kelly et al, 2009; Patel et al, 2011) and more seldom in XANES spectroscopy data (Beauchemin et al, 2002; Anunziata et al, 2011).

In the current study, XRF and XANES data have been subjected to PCA followed by LDA multivariate analysis using MATLAB R2009b software with the use of an in-house graphical user toolkit for spectroscopy, provided by our collaborators at Lancaster University (Trevisan

et al, 2010). PCA is an unsupervised technique and has been applied to the data for preliminary data reduction and also to visualize similarities and differences of spectra between each cornea, in a select number of PCs. The number of PCs in MATLAB R2009b and the in-house graphical user toolkit for spectroscopy used here, is always set up to reduce the observed variables into a maximum of ten PCs. PC1 represents the majority of the variables in the data compared to PC2, PC3 and others. Unlike PCA which is an unsupervised technique, LDA is a supervised technique so the groups to be discriminated must be defined. LDA was applied to highlight the maximum variance between the corneas at different embryonic stages.

The information obtained from the multivariate analysis is represented by scores plots, loadings and cluster vectors plots. The scores plots show the relationships between the corneas, whereas the loadings plots show information about the variables and basically indicate what each component is. The cluster vectors plot compares one class with the remaining classes (Martin et al., 2007). For instance, in this study, cluster vectors plot compare the average representative spectra of embryonic chicks corneas at day 12, with the average representative spectra of chicks corneas at day 14 and day 16.

3.3. Results

3.3.1. XRF microscopy of the developing chick cornea

XRF microscopy using the scanning x-ray microscope at the ID21 beamline station of the ESRF was used to perform non-destructive elemental analysis in embryonic chick corneas at day 12, day 14 and day 16. Four corneas for each embryonic stage were analysed and for every corneal sample, five spectral acquisitions were acquired from five different randomly selected

regions. Thus, for every development stage, twenty independent spectral acquisitions were attained.

After extracting all the spectra, with the use of PyMCA software (Solé et al, 2007), the major elements present in every sample were identified and determined by looking at the emission energy values and comparing those with tabulated energy values for XRF emission lines, as shown in Figure 3.3. Table 3.1 shows the energies of K-alpha fluorescence emission lines for the major elements present in the embryonic corneas.

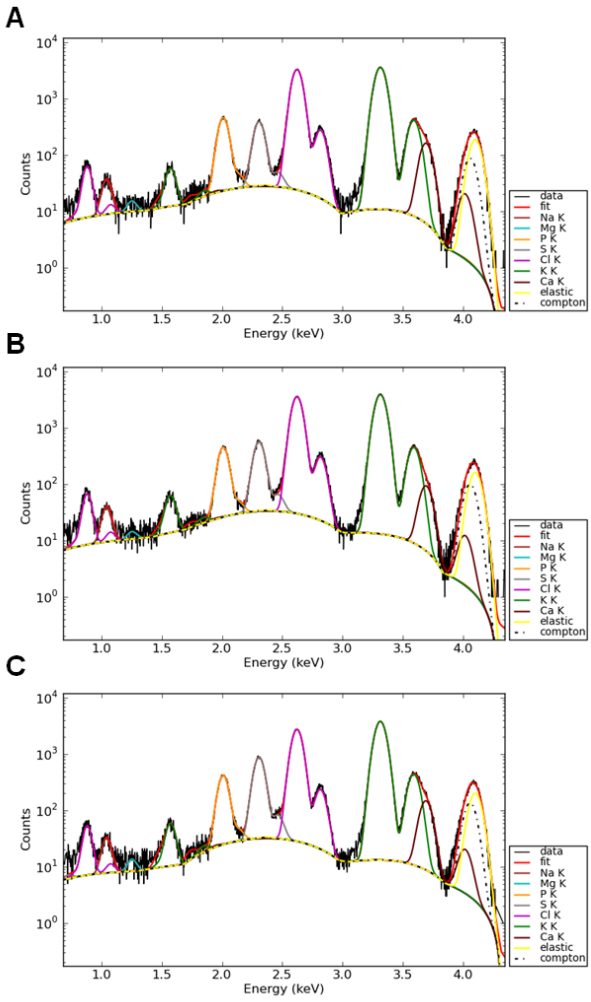

Figure 3.3: XRF spectra of the chick corneas at days 12, 14 and 16 of development fitted using PyMCA. Experimental X-Ray Fluorescence spectrum acquired on a random spot (100 µm diameter) of cornea at (A) embryonic day 12 (black), (B) embryonic day 14 (black), (C) embryonic day 16 and their best fitting curve (red) calculated with PyMCA (Solé et al, 2007). The main individual components of the fit due to the different elements, to the elastic (Rayleigh) and the inelastic (Compton) scattering are shown. The background is shown by the lower solid line.

Table 3.1: K-alpha edge x-ray fluorescence energy values for various elements.

Element	K-alpha edge energy (keV)
Phosphorus (P)	2.015
Sulphur (S)	2.308
Chlorine (Cl)	2.622
Potassium (K)	3.313
Calcium (Ca)	3.691

Comparison of the XRF microscopy average spectra of developing chick corneas at day 12 (red), day 14 (blue) and day 16 (green) (Figure 3.4) highlighted noticeable differentiation at the spectral ranges, 2000-2300 eV and 2620-3311 eV which denotes that there some changes in phosphorus (P), S, chlorine (Cl) and potassium (K) with development. These elemental differences suggest that there are changes in the elemental character and/or the concentration of the elements encountered within these spectral ranges. Looking at the XRF microscopy average spectra of the chick corneas at different developmental stages one can reach the conclusion that the concentration of Cl and K is higher at the embryonic day 14 (blue). However, it is of major importance to state that in this study we cannot conclude anything significant regarding alterations in the concentration of an element due to the fact that the thickness of the corneas per embryonic day varies.

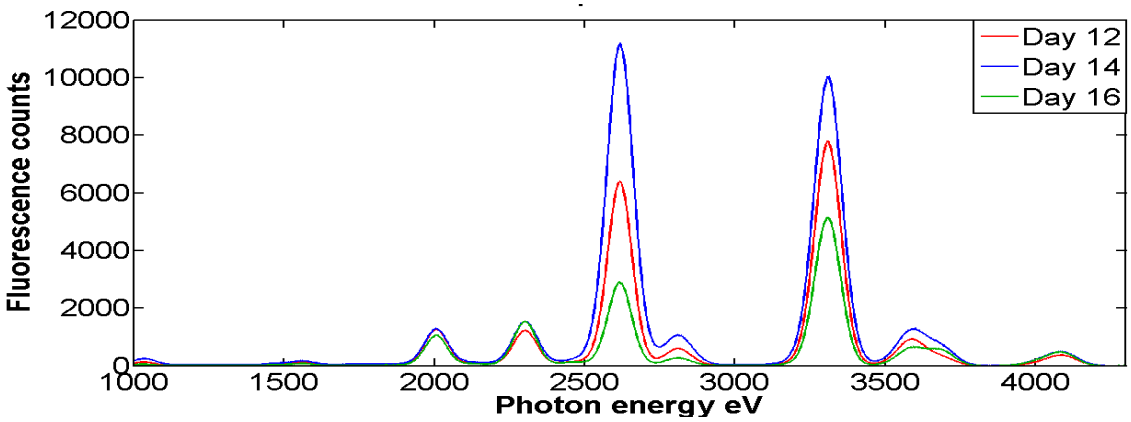

Figure 3.4: XRF microscopy average spectra of the developing chick cornea. The chemical composition of the chick corneas at embryonic day 12 (red), 14 (blue) and 16 (green) was assessed by XRF microscopy using the scanning x-ray microscope at the ID21 beamline at the ESRF. Four corneas per embryonic day were analysed and for every corneal sample, five independent spectra were obtained at five randomly selected areas.

3.3.1.1. Computational analysis with PCA

In order to uncover the most critical alterations in the elemental composition in the embryonic chick corneas, XRF spectra in the photon energy region range 1000-4300 eV were subjected to multivariate computational analysis with PCA. PCA facilitated preliminary data reduction and, as explained above in the Materials and Methods section, 3.2.4., it transformed the data to a new coordinate system in which it was possible to identify the key discriminating elemental composition which accounts for between-class variation. In this study, there are three classes/categories as the corneas from a particular day of development constituted one class.

As shown in figure 3.5, PCA analysis did not provided clear segregation between the embryonic chick corneas to allow us to reach any observable conclusions with respect to differences and similarities between the three classes.

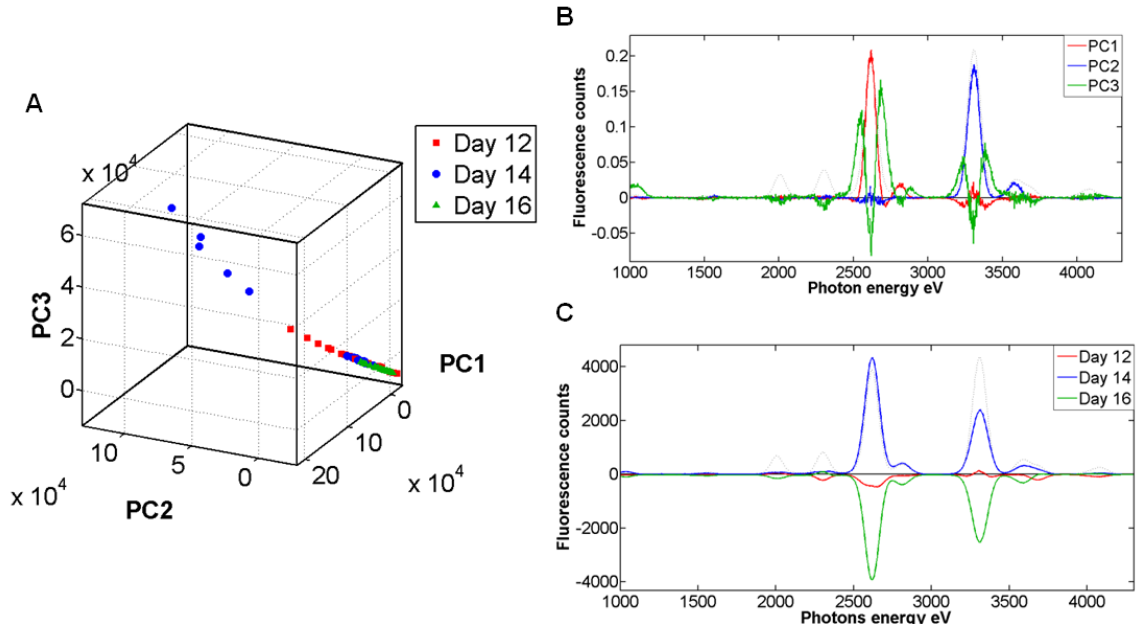

Figure 3.5: Multivariate computational analysis of the XRF microscopy spectra of the embryonic chick cornea with PCA. (A) Three-dimensional PCA scores plot performed on a dataset including embryonic chick corneas at day 12 (red squares), day 14 (blue circles) and day 16 (green triangles) with three principal components (PCs), PC1, PC2 and PC3. (B) PCA loadings plot with PC1 depicted in red, PC2 in blue and PC3 in green. (C) PCA cluster vectors plot. Classes are indicated as: chick corneas at day 12 (red), chick corneas at day 14 (blue) and chick corneas at day 16 (green). Cornea at developmental day 12 was compared against cornea at developmental day 14 and day 16.

3.3.1.2. Computational analysis with PCA-LDA

Following multivariate analysis with PCA, the data was further subjected to multivariate analysis with LDA, a supervised technique, to achieve better separation between the classes and subsequently extract the major discriminating elements that account for maximal separation of the three classes.

Indeed, PCA-LDA multivariate computational analysis provided a better degree of segregation of the embryonic chick corneas at different developmental stages clusters along the 1st linear discriminant (LD1) factor (Figure 3.6A). In particular, LD1 segregated chick corneas at day 16 versus chick corneas at day 12 and day 14 as no observable differences were found between chick corneas at day 12 and day 14 along LD1. The 2nd linear discriminant (LD2) factor appear to segregate chick corneas at day 14 versus chick corneas at day 12 and day 16 (Figure 3.6A). It is important to point out that the larger the distance between two points, the greater the biochemical difference between them. Looking at the PCA-LDA scores plot clustering it can be clearly seen that chick corneas at developmental day 12 and day 14 are more heterogeneous opposed to chick corneas at day 16 which are more homogeneous (Figure 3.6A). PCA-LDA loadings plot provide information about the elemental entities that account for the separation of the XRF microscopy average spectrum of each class, (corneas from one developmental day form one class), from the average spectra of the other classes. Examination of the PCA-LDA loadings plot (Figure 3.6B) revealed that, with respect to LD1, the major elemental groups responsible for segregation of chick corneas at day 16 against chick corneas at day 12 and day 14 in order of importance, are P (2012 eV), S (2306 eV), Cl (2620 eV) and calcium (Ca; 3688 eV). With regards to LD2, the main distinctive elements

accountable for compositional separation of chick corneas at day 14 versus chick corneas at day 12 and day 16, listed in order of importance, are Cl, P, K (3312 eV) and Ca (Figure 3.6B).

The PCA-LDA cluster vectors plot which is a linear combination of the PCA-LDA loadings plot derived from the center of the PCA-LDA scores cluster reveals the main elemental groupings responsible for class segregation from multiple loadings in a single plot. Exploiting the derived PCA-LDA cluster vectors plot (Figure 3.6C), it can be concluded that P, followed by S and Cl are the key distinctive elements responsible for the compositional diversity noticed between chick corneas at different developmental stages, whereas K and Ca seem to play less role in the separation between the classes.

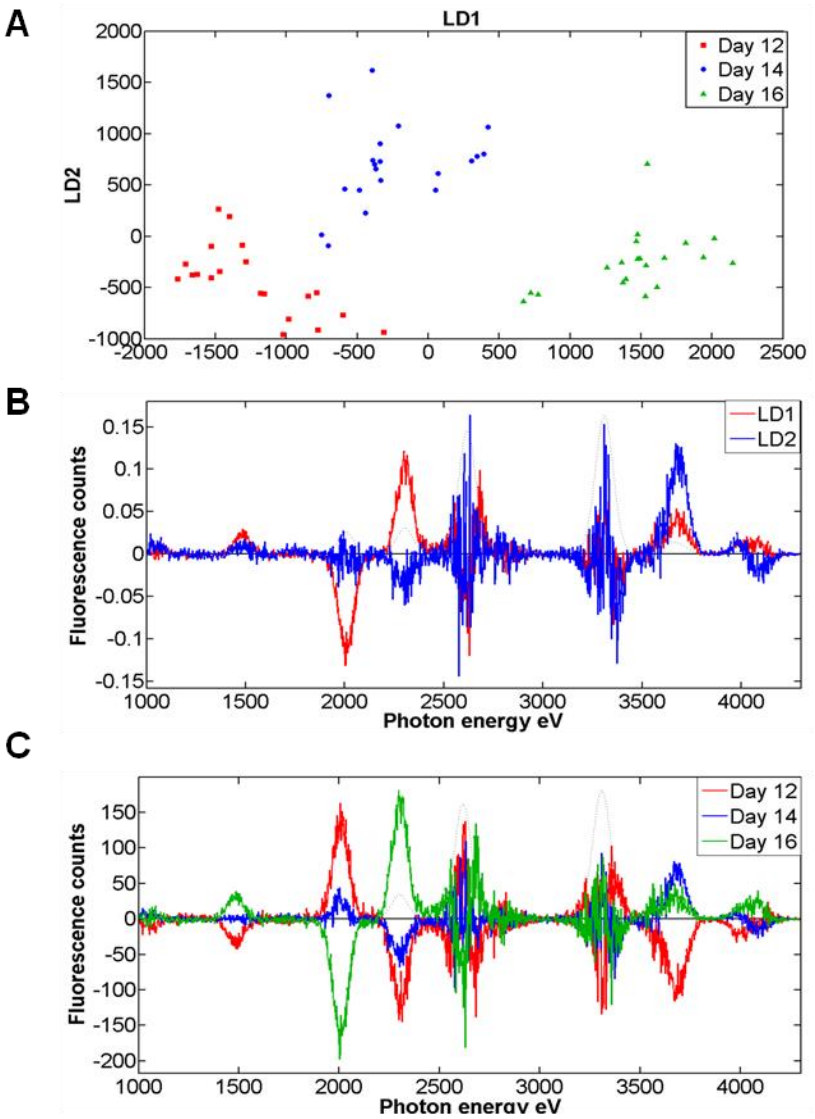

Figure 3.6: Compositional changes in the chemistry of the chick cornea with development using multivariate computational analysis with PCA-LDA, following XRF microscopy. (A) Two-dimensional PCA-LDA scores plot performed on the XRF spectra of embryonic chick corneas at day 12 (red squares), at day 14 (blue circles), at day 16 (green triangles). **(B)** PCA-LDA loadings plot with two linear discriminant components; LD1 indicated in red and LD2 indicated in blue. **(C)** Embryonic chick cornea PCA-LDA cluster vectors plot. Cornea at developmental day 12 was compared against cornea at developmental day 14 and day 16.

3.3.2. S K-edge XANES spectroscopy of the embryonic chick cornea

Taking into account the importance of the degree of sulfation of the corneal glycosaminoglycans in corneal structure and function, S is one of the most critical elements present in cornea and examination of the potential role of S-containing compounds at the embryonic chick cornea is of high importance in terms of getting a better understanding of how the immature cornea becomes transparent.

Examination of the near-edge spectrum provides valuable information about the electronic structure and subsequently the chemical form. Thus, in addition to XRF microscopy, this study applied S K-edge XANES spectroscopy as a probe of corneal S biochemistry in corneal development. S XANES experiments were conducted using the scanning electron microscope at the ID21 beamline station of the ESRF with the aim to discover the chemical identity of the S-containing compounds in the embryonic chick cornea at different developmental days, day 12, day 14 and day 16.

Three corneal samples per embryonic day 12 and day 14, as well as four corneal samples of embryonic day 16 were analysed. Thirteen selected areas along the diameter of the cornea were analysed per corneal per embryonic day and for every selected area, five XANES spectra were acquired. It is well known that alterations in the spectra range, 2469-2483 eV account for distinct S-containing species (Pickering et al., 1998; Prietzel et al. 2003). A number of studies have recorded the energies for a number of S-containing standard compounds (Morra et al., 1997; Vairavamurthy et al., 1997; Sarret et al., 1999). In this study, evaluation of the S species encountered in the corneal samples was achieved by comparing the absolute energy values obtained to the respective energy values for standard S species recorded from previous studies. Table 3.2 summarises the respective energies for standard S-containing compounds

obtained from other investigators and used as reference for the assessment of the corneal S species. As it can be clearly noted by looking at table 3.2, the peak energies of the first-order x-ray resonance lines for inorganic sulphate (SO_4^{2-}) and ester sulphate (R-O-SO_3) are very similar (2482.5 ± 0.5 eV) rendering their separation impossible.

Table 3.2: The absolute energy values of the peaks of a number of S-containing compounds recorded by other S k-edge XANES spectroscopy studies (compilation of literature data).

S chemical form		Example	Peak energy eV (Morra et al, 1997)	Peak energy eV (Vairavamurthy et al, 1997)	Peak energy eV (Sarret et al, 1999)
Elemental S	S^o		2472.5	2472.5	
Organic polysulphide	R-S-S-S-R′			2473	
Organic disulphide	R-S-S-R′	Cystine	2472.8	2473	2472
Thiols	R-SH	Cysteine		2473.5	2473.5
Organic monosulphides	R-S-R′	Methionine	2473.1	2473.5	2473.5
Sulphoxide	R-S=O	Methionine sulphoxide		2476	2476
Ester sulphate	R-O-SO_3	Chondroitin sulphate	2482.5	2483.5	2482
Inorganic sulphate	SO_4^{2-}	Sodium sulphate	2482.5	2483.5	2483

This similarity is in accordance with previous studies that investigated the S speciation using XANES spectromicroscopy in humic and fulvic acids (Morra et al., 1997), in marine sediments (Vairavamurthy et al., 1994) and in soils and soil particles (Prietzel et al., 2003). Moreover, if we also look at the XANES spectra peak energies of thiols (R-SH) and organic monosulfides (R-

S-R') the same situation appears (i.e. it is not possible to distinguish these two different S species). This agrees with previous findings of Xia et al. (1998).

Figure 3.7 shows the average S XANES spectra of the embryonic chick corneas at day 12, day 14 and day 16. Observable differences are apparent in the character of the main chemical forms of S, thiols and organic monosulfides (2.4734 keV), inorganic sulphate and ester sulphate (2.4835 keV), as the chick cornea develops and becomes transparent.

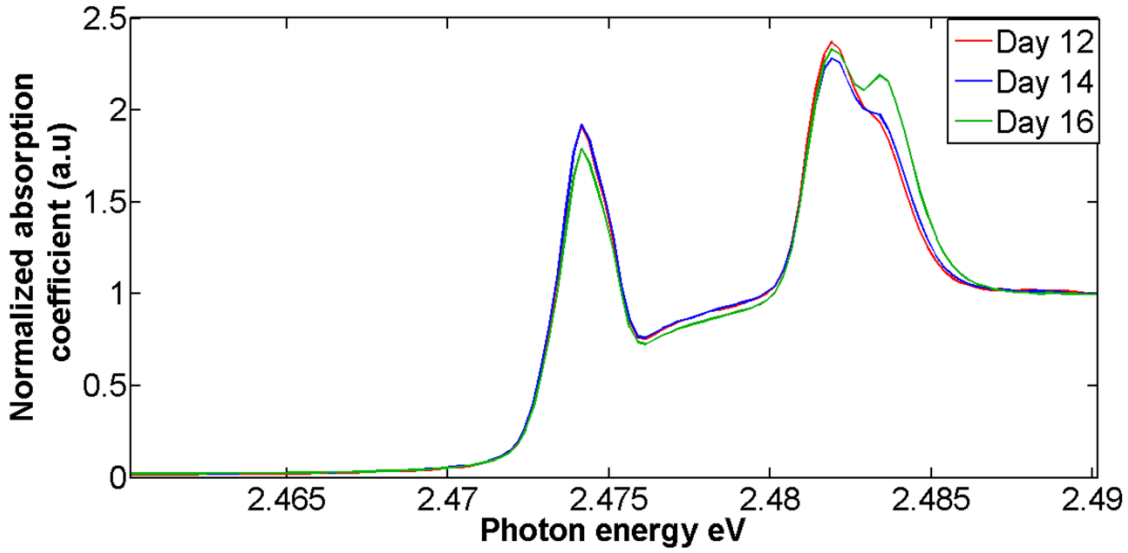

Figure 3.7: S K-edge XANES average spectra of the developing chick cornea. The S speciation of the developmental chick cornea at days 12 (red), 14 (blue) and 16 (green) was investigated by S K-edge XANES spectroscopy at the ID21 beamline at the ESRF. For every corneal sample, thirteen areas along the diameter were selected and for each area, five XANES spectra were acquired. The XANES peak energy at 2.4734 keV corresponds to thiols and organic monosulfides, whereas the peak energy at 2.4835 keV corresponds to inorganic sulphate and ester sulphate.

3.3.2.1. Computational analysis with PCA

Likewise with the XRF microscopy data, S k-edge XANES spectroscopy data was subjected in multivariate computational analysis with PCA to firstly reduce the data and also to demonstrate separation between the chick corneas at different developmental days in an unsupervised manner in the energy range 2.46-2.49 keV (Figure 3.8).

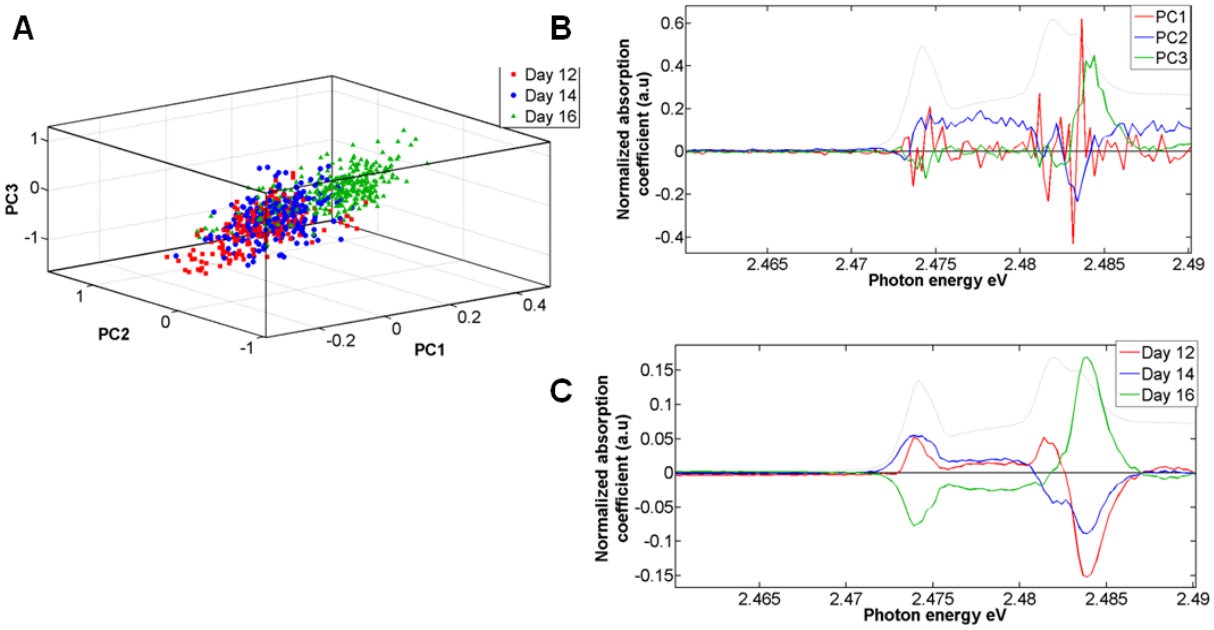

Figure 3.8: Identification of the S species associated with spectral clusters of different developmental chick corneas with the use of PCA multivariate computational analysis, following S k-edge XANES spectroscopy. **(A)**Three-dimensional PCA scores plot of S XANES spectra of embryonic chick corneas at distinct developmental days. Classes are labelled as: developmental chick corneas at day 12 (red squares), developmental chick corneas at day 14 (blue circles), developmental chick corneas at day 16 (green triangles). **(B)** PCA loadings plot of the developing chick cornea with principal components (PCs). PC1 is shown in red, PC2 is shown in blue and PC3 is indicated in green. **(C)** PCA cluster vectors plot of embryonic chick cornea at day 12 (red) against chick cornea at day 14 (blue) against chick cornea at day 16 (green). Chick cornea at day 12 was compared against cornea at developmental day 14 and day 16.

3.3.2.2. Computational analysis with PCA-LDA

PCA analysis failed to provide clear segregation between the different classes; therefore XANES spectroscopy data were further subjected in multivariate analysis with LDA to better demonstrate between-class differences and similarities.

PCA-LDA S-kedge XANES spectra analysis resulted in good segregation of the classes (Figure 3.9A). The PCA-LDA scores plot in Figure 3.9A illustrates the large degree of overlap between chick corneas at developmental day 12 and day 14 indicating that there are progressive chemical changes in the molecular character of the chick cornea with development. Unlike chick corneas at day 12 of development, chick corneas at day 14 and day 16 are more homogeneous on the subject of their content of S-containing compounds. It is obvious that LD1 segregates chick corneas at day 16 of development against developmental corneas at day 12 and day 14 and examination of the corresponding PCA-LDA loadings plots (Figure 3.9B) reveals that the main S chemical forms that contribute to this segregation are listed in order of importance, inorganic sulfate and ester sulfate (2.483 keV) and thiols and organic monosulfides (2.4736 keV). LD2 discriminated developmental corneas at day 12 versus developmental corneas at day 14 and it is noticeable that LD2 primarily contributes to intraclass distinction at day 12. The PCA-LDA loadings plot (Figure 3.9B) showed that the main S species that account for segregation along LD2 are mainly thiols and organic monosulfides followed by inorganic sulfate and ester sulfate. The derived PCA-LDA cluster vectors plot (Figure 3.9C) highlights the major S species that contribute for segregation of developmental corneas at day 12 against the other classes (developmental corneas at day 14 and day 16). The influential discriminating S species are thiols and organic monosulfides (2.4725 keV),

inorganic sulfate and ester sulfate, which all displayed noteworthy differences among the developmental corneas.

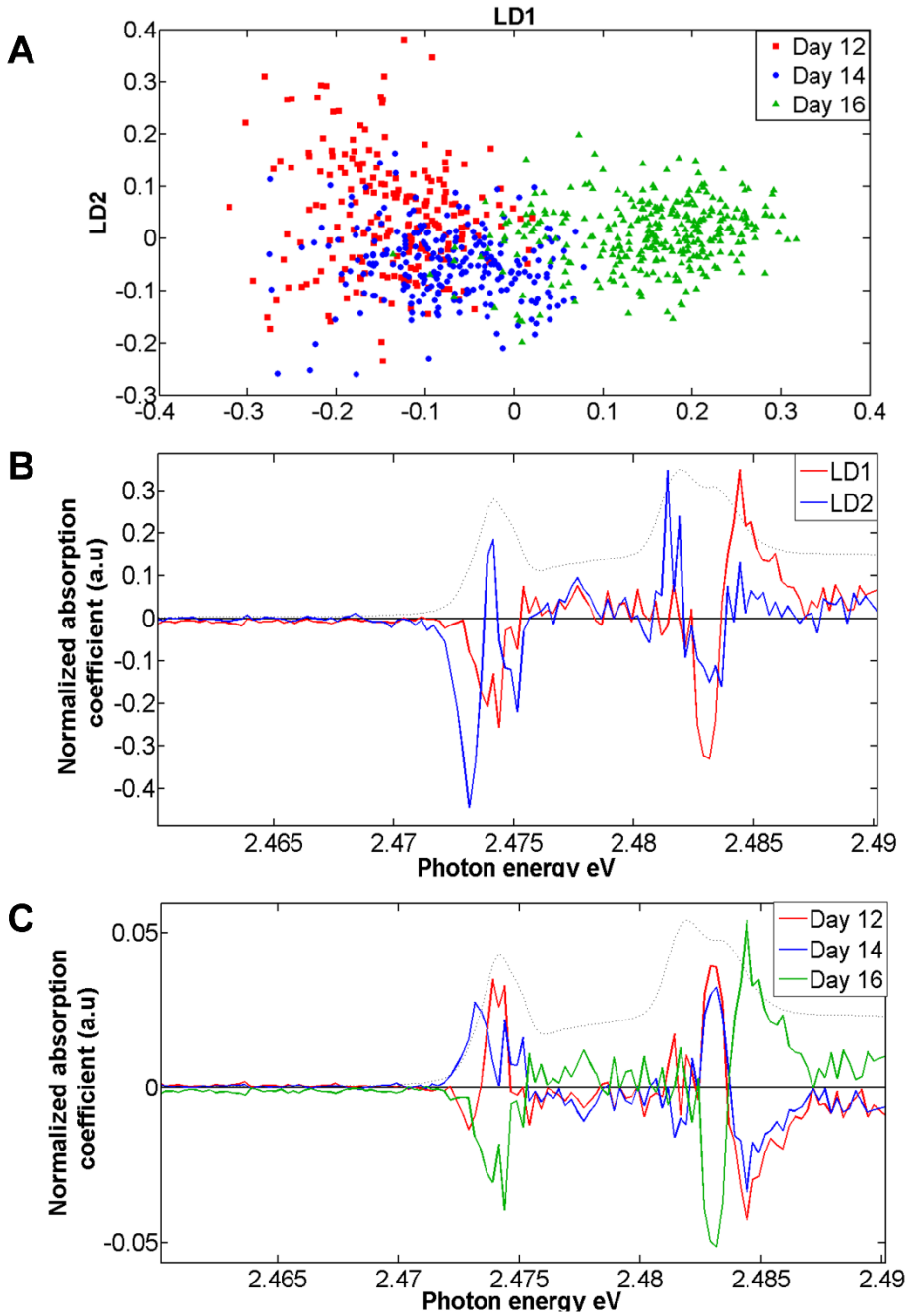

Figure 3.9: Analysis of the S K-edge XANES spectra and identification of developmental changes in the S speciation of the chick cornea. (A) Two-dimensional PCA-LDA scores plot carried out on a dataset including embryonic chick corneas at day 12 (red squares), at day 14 (blue circles) and at day 16 (green triangles). **(B)** PCA-LDA loadings plot with LD1 shown in red and LD2 shown in blue. **(C)** Embryonic chick cornea PCA-LDA cluster vectors plot with chick cornea at developmental day 12 used as the comparator.

3.3.2.3. PCA-LDA analysis of the chick cornea at developmental day 12 versus chick cornea at developmental day 14

In order to get a better understanding on the developmental alterations of S species additional analysis was carried out. The XANES spectra obtained from the chick corneas at developmental day 12 were compared and contrasted to the XANES spectra acquired from the chick corneas at developmental day 14 using multivariate computational analysis with PCA-LDA. The derived PCA-LDA scores plot (Figure 3.10A) illustrates that there is a remarkable overlap between the two classes. The most important S-containing compounds in distinguishing chick cornea at day 12 versus chick cornea at day 14 and vice versa are thiols and organic monosulfides, inorganic sulfate and ester sufate (Figure 3.10B).

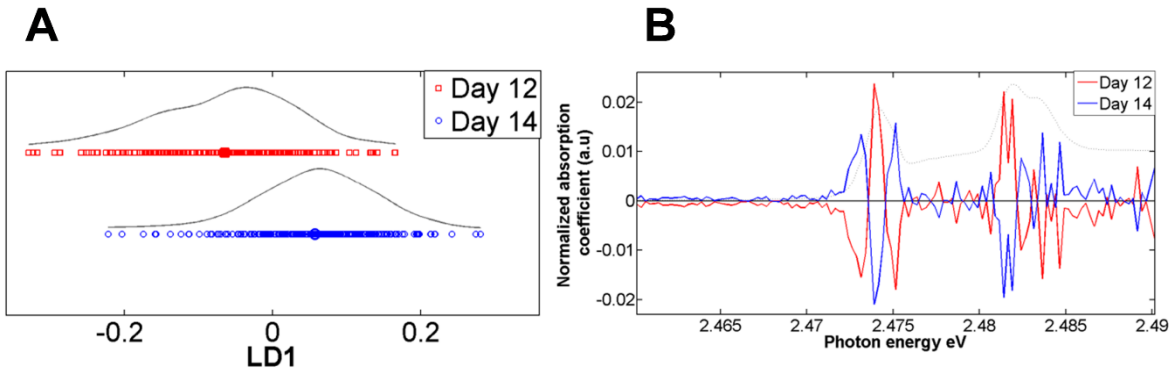

Figure 3.10: Investigation of the S species alterations in developmental chick corneas at day 12 and day 14 using PCA-LDA multivariate computational analysis. (A) One-dimensional PCA-LDA scores plot performed on a XANES spectra dataset of embryonic chick corneas at day 12 (red squares) versus embryonic chick corneas at day 14 (blue circles). **(B)** PCA-LDA cluster vectors plot of embryonic chick corneas at day 12 (red) versus embryonic chick corneas at day 14 (blue).

3.3.2.4. PCA-LDA analysis of the chick cornea at developmental day 12 versus chick cornea at developmental day 16

Multivariate computational analysis with PCA-LDA was also performed to compare and contrast the XANES spectra data acquired from chick corneas at day 12 versus the data obtained from chick corneas at day 16. In Figure 3.11A, the PCA-LDA scores plot shows a very small overlap between chick corneas at day 12 and chick corneas at day 16, in contrast to chick corneas at day 12 and chick corneas at day 14. The more overlap there is between two classes, the more similar they are with respect to their content of S species. Hence, there are critical differences in the S chemical forms between embryonic day 12 and embryonic day 16. The distinguishing S-containing compounds accountable for the segregation observed within this developmental period, are mainly inorganic sulfate and ester sulfate followed by thiols and organic monosulfides (Figure 3.11B).

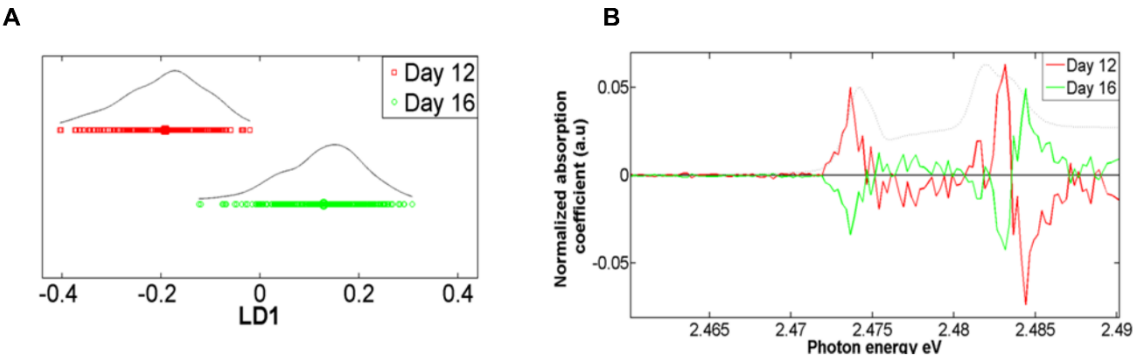

Figure 3.11: Investigation of the S species alterations in developmental chick corneas at day 12 and day 16 using PCA-LDA multivariate computational analysis. (A) One-dimensional PCA-LDA scores plot performed on a XANES spectra dataset of embryonic chick corneas at day 12 (red squares) versus embryonic chick corneas at day 16 (green circles). **(B)** PCA-LDA cluster vectors plot of embryonic chick corneas at day 12 (red) versus embryonic chick corneas at day 16 (green).

3.3.2.5. PCA-LDA analysis of the chick cornea at developmental day 14 versus chick cornea at developmental day 16

Further PCA-LDA multivariate analysis of data from chick corneas at developmental day 14 versus developmental day 16 demonstrated that there is a clear overlap between the two embryonic days (Figure 3.12A), reflecting similarities in their S speciation. Nevertheless, there are also differences in the S content of these two embryonic days and it can be clearly observed by looking at their corresponding cluster vectors plot (Figure 3.12B). The cluster vectors plot indicates S species that contribute to a not complete overlap between chick corneas at developmental day 14 versus developmental day 16 to be inorganic sulfate and ester sulfate. Thiols and organic monuslfides also play a role for separating S XANES spectra of embryonic day 14 from the data of embryonic day 16 but at a lesser extent.

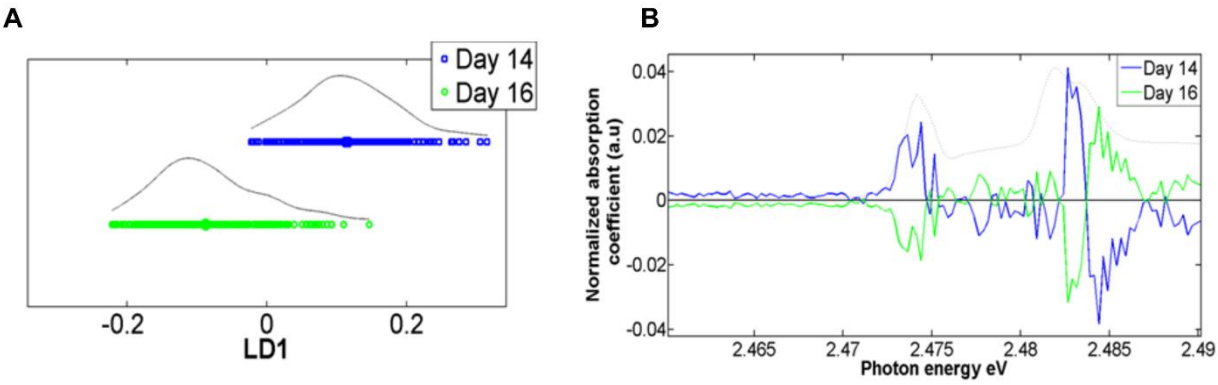

Figure 3.12: Investigation of the S species alterations in developmental chick corneas at day 14 and day 16 using PCA-LDA multivariate computational analysis. (A) One-dimensional PCA-LDA scores plot performed on a XANES spectra dataset of embryonic chick corneas at day 14 (blue squares) versus embryonic chick corneas at day 16 (green circles). **(B)** PCA-LDA cluster vectors plot of embryonic chick corneas at day 14 (blue) versus embryonic chick corneas at day 16 (green).

3.4. Discussion

In this study, synchrotron XRF microscopy and S k-edge XANES spectroscopy were used to explore similarities and differences in the chemical composition and S speciation between chick developmental corneas at day 12, day 14 and day 16, respectively. XRF microscopy and S k-edge XANES spectroscopy data sets were subjected to multivariate computational analysis by PCA-LDA and the results obtained from this study emphasised the applicability of these techniques with high specificity and sensitivity for the investigation of alterations in the molecular signature of extracellular matrix components during tissue morphogenesis as the chick cornea develops and become transparent. The information extracted by the PCA-LDA multivariate analysis was presented in scores, loadings and cluster vectors plots. Scores plots generate clusters between the data point with relative distances, based on similarities and differences amongst them and thus provide information about intra- and inter-class variations (corneas from a particular day formed one class). Loadings and cluster vectors plot provide information about the discriminating entities responsible for segregation between classes.

XRF microscopy experiments showed that the biochemical character of the embryonic chick cornea alters with development since alterations in the chemical environment of particular elements were noticeable among the developmental corneas. In particular, the elemental profiles of Cl, K and Ca were shown to undergo changes during development of the chick cornea and are responsible for separation between embryonic chick corneas at day 12, day 14 and day 16. In general, ions have a direct effect on ionic compounds as their charge and size impact their electrostatic attractions that hold these compounds together. Under physiological conditions, transient mobile ion binding phenomena establish the generation of

the corneal ECM (Elliot and Hodson, 1998) and a number of ions, including Cl, K and Ca, influence the corneal fixed negative charge density. It is therefore plausible to propose that the changes in the chemical environment of Cl, K and Ca between chick corneas at distinct developmental stages, noted in the current study, are indicative of developmental changes in the ionic compounds of the corneal ECM and subsequently changes in the corneal fixed negative charge density which occur with development and help the tissue to acquire transparency. Collagen fibrils are one of the most critical components of the ECM of the cornea. Corneal transparency lies behind the unique organisation of the collagen fibrils at a uniform diameter and spacing, an arrangement which allows light transmission in a specific pattern of interference from light scattered by individual collagen fibrils (Maurice, 1957; Benedek, 1971; Farrell and McCally, 2000). Ion binding phenomena have an impact on the net surface charge on collagen fibrils and consecutively influence the interactions between collagen fibrils, proteoglycans and mobile ions in the interfibrillar space, which in turn governs their arrangement (Elliot and Hodson, 1998). Chloride ion binding is said to play a dual role in maintaining corneal transparency in the adult cornea. During studies of corneas loaded with various concentrations of chloride it was established that there is a strong dependence of the corneal transparency, and the ratio that chloride ions are absorbed onto the matrix regulates the fixed negative charge of corneal matrix (Kostyuk et al., 2002). Along these lines, the developmental alterations in the element profile of Cl seen here, may be associated with binding of chloride atoms to the collagen matrix in the corneal stroma, influencing its fibrillar architecture and help make the tissue transparent to light. Nevertheless, it is important to take into consideration that chloride ions solely cannot greatly change the fixed charge of the corneal matrix as its charge is always balanced. Likewise, in cases where the net positive charge of the tissue is enhanced, negative charge carriers including Cl^- help the tissue to

maintain its fixed charge. In a similar manner, changes in the molecular signature of K and Ca elements may denote their action to balance an increase in the net negative charge resulted by an enhancement in the degree of sulfation of glycosaminoglycans in the corneal matrix. One can assume that the ionic differences noticed in the developing corneas may be related to the ion transport mechanisms in the corneal endothelium towards maintaining corneal stroma hydration and transparency (Potts, 1962; Bonanno, 2003), however, due to the experimental design (dried corneas were analysed) this concept cannot annotate the results obtained.

In addition to changes in the molecular signature of Cl, K and Ca elements, PCA-LDA analysis also demonstrated developmental alterations in the biochemical character of P. The DNA and RNA backbone structure consists of many phosphates and nucleotides of the DNA or RNA strand are linked together by phosphodiester bonds. The changes in the element profile of P over the developmental period between embryonic day 12 and day 16, are likely to reflect changes in the genetic material of the corneal keratocytes. During the developmental period under investigation in this study, corneal keratocytes differentiate; they become more compact and their morphology changes from a rounded shape to a more flattened one (Hay and Revel, 1969; Connon et al., 2003). Therefore, it is possible that the biochemical changes of P that segregate the developing chick corneas at days 12, 14 and 16 of embryogenesis illustrate these changes in the presumptive keratocyte population and an inhomogeneous distribution of P in the corneal stroma as a function of the density of keratocytes.

As mentioned earlier, the tissue-specific organisation of collagen fibrils in the corneal matrix is essential for light scattering properties and transparency of the cornea. Along with collagen fibrils, sulfated proteoglycans also play a fundamental role in governing tissue structure and

function and the degree of sulfation of glycosaminoglycans has been shown to be associated with progress of transparency (Anseth, 1961; Hart, 1976; Nakazawa et al., 1995; Zhang et al., 2005; Gealy et al., 2007; Young et al., 2007; Liles et al., 2010). It is well established that collagen-proteoglycans architecture and interactions determine matrix morphogenesis that ultimately fulfils the requirements for the transparency of the cornea (Anseth, 1961; Conrad, 1970; Hart, 1976; Cornuet et al., 1994; Zhang et al., 2005; Gealy et al., 2007; Young et al., 2007; Liles et al., 2010).

S k-edge XANES investigation of the developing embryonic chick cornea showed that there are remarkable changes in the S content among the developmental corneas at days 12, 14 and 16, and with the use of computational analysis with PCA-LDA identification of the S discriminating species was achieved. The S-containing compounds whose signature was found to alter between embryonic days 12, 14 and 16 are thiols, organic monosulfides, ester sulfate and inorganic sulfate. The developmental alterations in thiols observed in this study, are likely to be related to the corneal SLRPs (lumican, keratocan and mimecan) and more precisely to their negatively charged N-terminal domain which is known to contain sulphated disulfide bonds (Iozzo, 1999; Schaefer and Iozzo, 2008). Researchers explored the role of the highly conserved N-terminal cysteine containing domain of lumican proposing that it is involved in collagen fibrillogenesis and matrix organisation (Carlson et al., 2003). Variation in the organic monosulfides species over the developmental period between embryonic day 12 and day 16 probably reflects changes in protein synthesis and is linked to the S methionine amino acid.

Besides the biochemical changes in the thiols and organic monosulfides species with development of the chick cornea, changes in the ester sulphate and inorganic sulphate

biochemical peak were also observed. The changes in these S entities are believed to be associated with alterations in the profiles of KS and CS/DS glycosaminoglycans. In fact, there is experimental evidence that CS displays a peak near 2.482 keV (Dauphin et al., 2003; Dauphin et al., 2006), which is compatible with the findings of this study and, thus, it is attractive to propose that the variation in the ester sulphate are possibly related to this molecule.

Interestingly, early studies by Anseth (1961) showed that as the cornea develops, especially around developmental day 14, the chemical and physic-chemical properties of the corneal glycosaminoglycans are altered (Anseth, 1961). Since then, a number of investigators have given some ingenious insights into the expression of proteoglycans during chick corneal embryogenesis. With respect to the KS proteoglycan, keratocan, Gealy and colleagues illustrated that that the distribution of keratocan in the developing chick corneal matrix diverges, undergoing structural and distributional reorganisation, as the cornea matures and becomes transparent (Gealy et al., 2007). This concept is supported by other studies that reported variation in the concentration of sulphated dissacharides from KS and CS/DS in the developing chick cornea (Zhang et al., 2005). Notably, it was shown that the concentration of sulphated KS dissacharides was significantly increased around developmental day 14. On the other hand, the concentration of CS/DS dissacharides was found to decrease during chick corneal embryogenesis. Furthermore, it is crucial to consider the fact that the degree of sulfation of KS epitopes on glycosaminoglycan side chains varies. More importantly, Liles et al. examined the expression of glycosaminoglycan side chains that bear low- and high-sulphated KS epitopes in the developing chick corneal stroma and reported that the expression of lesser and highly sulphated KS varies over the developmental period between

embryonic day 12 and day 15 (Liles et al., 2010). The findings from all these studies, support the conclusion that the S k-edge XANES data and results obtained from this study are highly associated with the sulphated pattern of corneal glycosaminoglycans and reflect differences amongst lesser and highly sulphated glycosaminoglycan side chains. Taking into account the fact that the glycosaminoglycan side chains extend into the extrafibrillar space and serve to help define the regular spatial organisation of collagen fibrils in bundles into the ECM, the sulfation status of glycosaminoglycan side chains is highly important. More specifically, alterations in the sulphated pattern of glycosaminoglycans will have an impact on the negative charge of the chains and consequently will affect not only the corneal hydration status and its hydrophilic properties but also the interactions between glycosaminoglycans and other glycosaminoglycans, all of which play a fundamental role in the proper fibrillar architecture of the corneal stroma required for transparency.

To sum up, the results obtained by this study demonstrate that synchrotron XRF microscopy and XANES spectroscopy are alternative biomedical techniques that have the potential to explore the biomolecular character of an intact biological tissue in a noninvasive fashion. Data analysis with PCA-LDA revealed that there are critical changes in the chemical composition and S speciation of the chick cornea during embryonic development; all of them being influential in the transition of an immature opaque tissue to a mature transparent one.

Chapter 4: XANES spectroscopy for the interrogation of the S speciation of the mature corneal tissue

4.1. Introduction

As previously mentioned the unique organisation of collagen fibrils in the corneal stroma is a primary necessity for corneal transparency. Proteoglycans play a fundamental role in governing the collagen fibril arrangement in the corneal matrix since they bind to collagen fibrils at specific binding sites via their core protein and proteoglycan-collagen interactions regulate collagen fibril assembly and, in part, function (Scott and Haigh, 1985; Meek et al., 1986). A characteristic component of the proteoglycan molecule by which important proteoglycan functions are dependent from, are the sulphated glycosaminoglycan side chains which extend in the extrafibrillar space interacting with other glycosaminoglycans and other ECM molecules (Knupp et al., 2009; Lewis et al., 2010; Parfitt et al., 2010).

The sulphated character of the corneal glycosaminoglycans defines the hydrophilic corneal stroma and various studies have examined the function of KS and CS/DS glycosaminoglycans in the hydration process supporting the idea that different glycosaminoglycans maintain corneal hydration in distinct ways (Hedbys, 1961; Anseth and Fransson, 1969; Praus and Coldman, 1970; Bettelheim and Plessy, 1975; Borcherding et al., 1975; Bettelheim and Goetz; 1976, Castoro et al., 1988). Variation in the water absorption and retention properties of glycosaminoglycans, along with differences on the sulfation patterns of the corneal glycosaminoglycans, highlight their importance in defining the hydrophilic properties of the cornea. Evidence for this statement arises from studies that have investigated the distribution of the corneal glycosaminoglycans across the cornea showing that not only the sulfation

profile of glycosaminoglycans is uneven across the cornea but their distribution varies as well (Bettelheim and Plessy, 1975; Borcherding et al., 1975; Bettelheim and Goetz; 1976, Castoro et al., 1988; Scott et al., 1988; Scott and Bosworth, 1990). More specifically, it was shown that at the anterior segment of the corneal stroma (epithelium) CS/DS glycosaminoglycans are more prevalent in contrast to KS glycosaminoglycans which are more prevalent in deeper regions of the stroma towards the posterior end (endothelium) (Bettelheim and Plessy, 1975; Borcherding et al., 1975; Bettelheim and Goetz; 1976, Castoro et al., 1988; Scott et al., 1988; Scott and Bosworth, 1990). This points towards a relationship between the function of corneal glycosaminoglycans in maintaining corneal hydration and this particular trend of their distribution in the corneal stroma. Sulfated CS/DS glycosaminoglycans have great water retentive ability and low water sorptive capacity explaining the rationale behind their prevalent distribution close to the epithelium as they maintain corneal hydration by preventing water loss through dehydration (Bettelheim and Ehrlich, 1963; Borcherding et al., 1975; Bettelheim and Goetz; 1976, Castoro et al., 1988). On the other hand, proteoglycans bearing KS glycosaminoglycan side chains are more prevalent at the posterior part of the corneal stroma and affect corneal hydration based on the low retentive capacity of KS glycosaminoglycans and the fact they can absorb large amounts of water, thus, facilitating water movement into and through the corneal stroma (Plessy and Bettelheim, 1975; Borcherding et al., 1975; Bettelheim and Goetz; 1976, Castoro et al., 1988).

The findings from all these studies have provided vital information on the sulfation pattern of proteoglycans, and their distribution and function in the corneal stroma. Whilst investigating the S speciation of the embryonic chick corneas observable differences were noted on the S content among the developmental period under investigation, developmental day 12 to

developmental day 16. Despite that all these studies emphasise the importance of S element, no studies to date have investigated other S species in the mature corneal stroma.

This study aims to examine the S species content of the mature corneal stroma in a depth-profiled manner. S k-edge XANES was, therefore, applied to look at the different S-containing compounds from the anterior stroma, close to the epithelium, towards the deeper regions of the corneal stroma, close to the endothelium.

4.2. Materials and Methods

4.2.1. Sample preparation

Mature cattle eyes were used for the purpose of this investigation, obtained from the Ensors abattoir (Cinderford, Gloucestershire, UK). Cattle eyes were carefully dissected with the use of surgical tools and dissected bovine corneas were then cut in half (Figure 4.1A and Figure 4.1B). Since the aim of the current study was to look at the S speciation in a depth-profiled manner in the mature corneal stroma, it was required to obtain tissue sections. Hence, straight after dissection, tissue was prepared for cryosectioning by embedding the tissue in optimal cutting temperature (OCT) embedding medium at liquid N_2 temperature (Figure 4.1C), a well-recognised sample preparation method for tissue preservation and elemental speciation (Hackell et al., 2012). The OCT embedding medium helps with tissue freezing by taking the heat away from the sample. Also, OCT embedding medium prevents the tissue from drying whilst in storage and holds the tissue in place supporting sectioning. A cryostat (Bright OTF 5000) was then used to obtain 10-µm thick sections, cut transversely so that each section contained the epithelial layer, the stroma and the endothelial layer. The tissue sections were collected onto Ultralene® foil-covered glass microscope slides (Figure 4.1D) and

kept frozen at -20^{o}C. Ultralene® foil was used to cover the glass microscope slides so that once the tissue sections were collected onto them, it was easy to sandwich them between Ultralene® foil, a necessity prior sample introduction into the x-ray scanning electron microscope for subsequent analysis. All the experiments were adhered to the Association for Research in Vision and Ophthalmology statement for the use of animals for Ophthalmic and Vision Research and local ethical regulations.

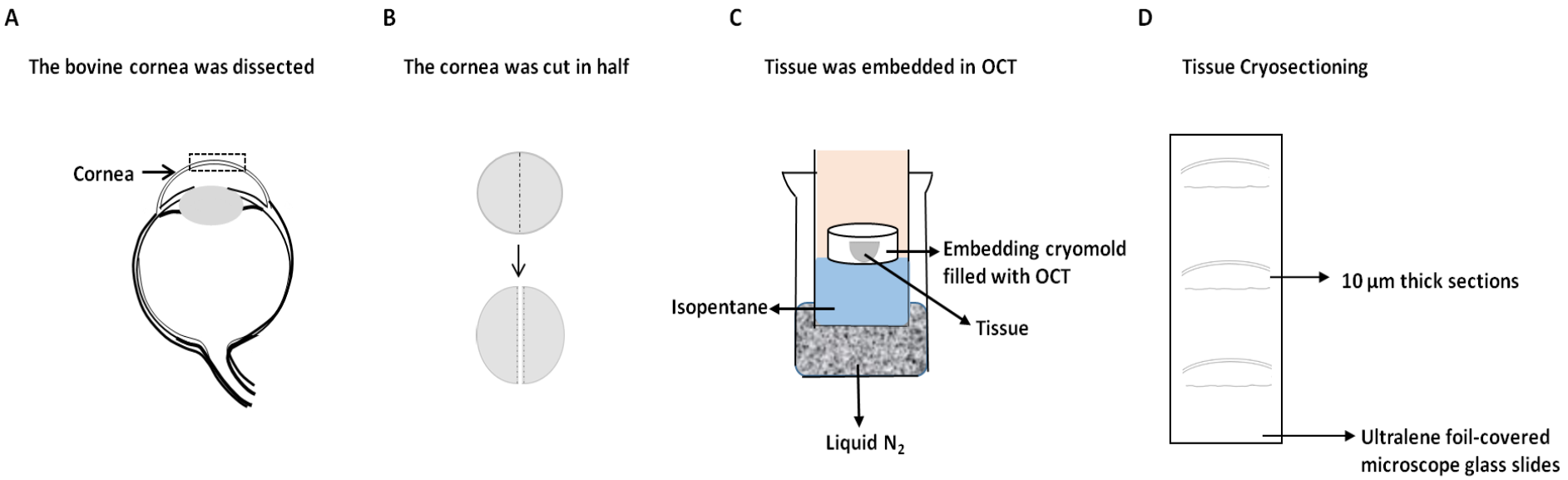

Figure 4.1: Schematic diagram illustrating the sample preparation prior investigation using the scanning electron microscope at the endstation ID21 at the ESRF. (A) Bovine corneas were dissected and then **(B)** divided in half. **(C)** Immediately after dissection, the tissue was cryofixed in liquid N_2 and embedded in specific cryomolds used for cryosectioning. **(D)** Tissue cryosectioning was then carried out and 10 µm thick sections were obtained on ultralene foil-covered microsope glass slides.

4.2.2. S k-edge XANES spectroscopy

The S k-edge XANES spectroscopy experiments were carried out using the x-ray scanning electron microscope at the beamline ID21 of the ESRF to probe the S species across the depth of the mature corneal stroma. The tissue sections were transported in dry ice at the endstation ID 21 at the ESRF and stored again at -20^{o}C until the experiments were conducted. On the day of the experiment, it was necessary to defrost the tissue sections whilst preventing any oxidation events to occur, therefore, samples were left to defrost in a chamber with slow nitrogen flow for about 1 h prior to the experiment.

A total of four distinct corneal tissue sections were analysed and XANES spectra along the depth of the corneal stroma were acquired. For every corneal tissue section, thirteen regions from the stromal region closest to the epithelium towards the deeper stromal region, adjacent to the endothelium, were examined (Figure 4.2). For every region, twenty individual XANES spectra were obtained and averaged to get a good signal-to-noise ratio. The x-ray beam size was set to 50 µm, equal to the distance between the centres of consecutive areas under investigation, resulting in a photon flux of 1.4 x 10^{9} photons/s and an integration time of 2 s per point. The x-ray incoming photon energy was tuned between 2,460 to 2,530 eV in 0.25 eV energy steps.

4.2.2.1. Data analysis

Following XANES spectra extraction with the use of PyMCA software (Solé et al, 2007), background subtraction and normalisation of XANES spectra was carried out. Quantitative data analysis was performed to establish the relative percentage of the major S species present in the corneal tissue by means of Gaussian peak fitting of the absorption edge

features. Fityk software (Wojdyr, 2010) was used to perform least-square fitting to experimental data and obtain the two best-fitting curves that mimic the jump at the S k-edge absorption edge and five Gaussian curves; four Gaussian curves for each of the chemical S form found in the cornea and a fifth one around the energy 2,497 *eV* which accounts for the cumulative multiple scattering contribution of all the species. The area under the curve for every Gaussian peak is proportional to the amount of the S species responsible for that resonance; therefore the relative concentrations of S species can be calculated by dividing the area of its peak by the sum of all peaks' areas, proportional to the total amount of S in the probed region.

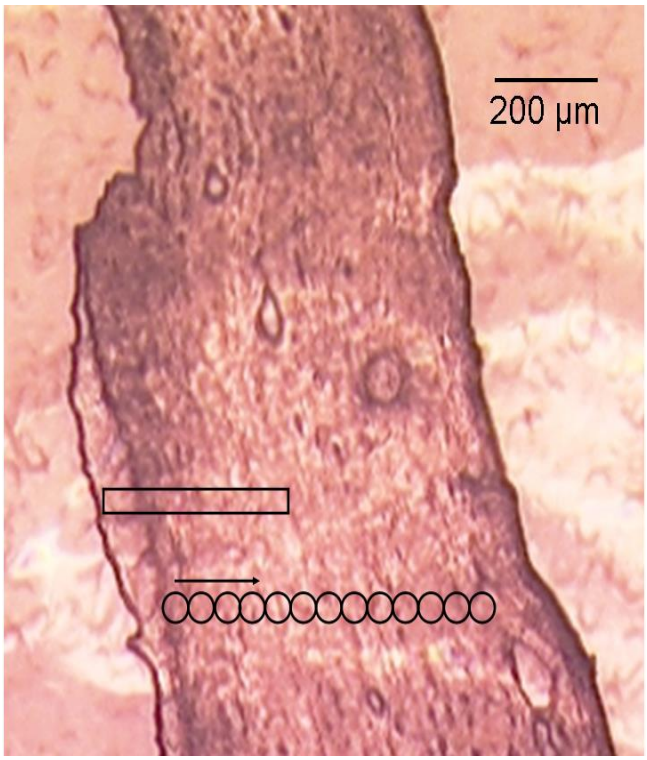

Figure 4.2: Micrograph of a mature bovine corneal section (10µm thick) taken by the visible microscope prior sample introduction into the scanning electron microscope. The circled areas indicate the areas where XANES spectra were acquired from the epithelial layer towards the endothelial layer as shown by the arrow. The rectangular area shows one of the areas subjected for µ-XRF image mapping. Scale bar equals to 200 µm. Adapted from Veronesi et al., 2013.

4.2.3. Micro x-ray fluorescence (µXRF) chemical contrast imaging

In addition to the XANES experiments, the corneal tissue sections were subjected to S k-edge micro x-ray fluorescence (µXRF) imaging. µXRF imaging technique was applied to map the distribution of the different chemical forms of S present in the corneal stroma (Thiols and organic monosulfides, inorganic sulphate and ester sulphate) at the micrometer scale. The concept of µXRF imaging technique is to irradiate a region of interest in the specimen at distinct energies which are compatible to the maximum absorption in the XANES spectra for every molecular group under investigation. As a result, the x-ray absorption for every molecular group under investigation is enhanced and the fluorescence signals along with the image maps obtained are proportional to the amount of every S species of interest (Pickering et al., 2009).

For this study, two µXRF maps were acquired, both produce comparable results. It is important to mention that the locations selected for fluorescence mapping were distant and different to the regions where XANES spectroscopy was conducted for two critical reasons. One, in order to avoid the investigation of already irradiated areas and secondly to make sure that the distribution of the S-containing compounds is the same across the diameter of the cornea. For the S k-edge *µXRF experiments the x-ray beam was focused to 0.9 x 0.2* μm^2 (horizontal x vertical). For every chosen region of interest, one of them is illustrated as the rectangular region shown in Figure 4.2, three image maps were obtained at the resonance energy of thiols and organic monosulfides (2.4735 keV), of ester sulphate and inorganic sulphate (2.47826 keV) and at the post-edge energy of 2.51 keV, with a step size of 1 x 1 μm^2 and a dwell time of 500 ms (Figure 4.3). The fluorescence maps obtained for the thiols and organic monosulfides, ester sulphate and inorganic sulphate were normalised against the

image map obtained at the energy acquired at 2.51 keV and the incoming current. µXRF maps were analysed using PyMCA software (Solé et al, 2007).

4.2.3.1 Data analysis

The µXRF maps were analysed using PyMCA software and the ROI imaging tool (Solé et al, 2007). Least-square fitting of the XRF data and normalisation by the incoming flux (iodet) were performed.

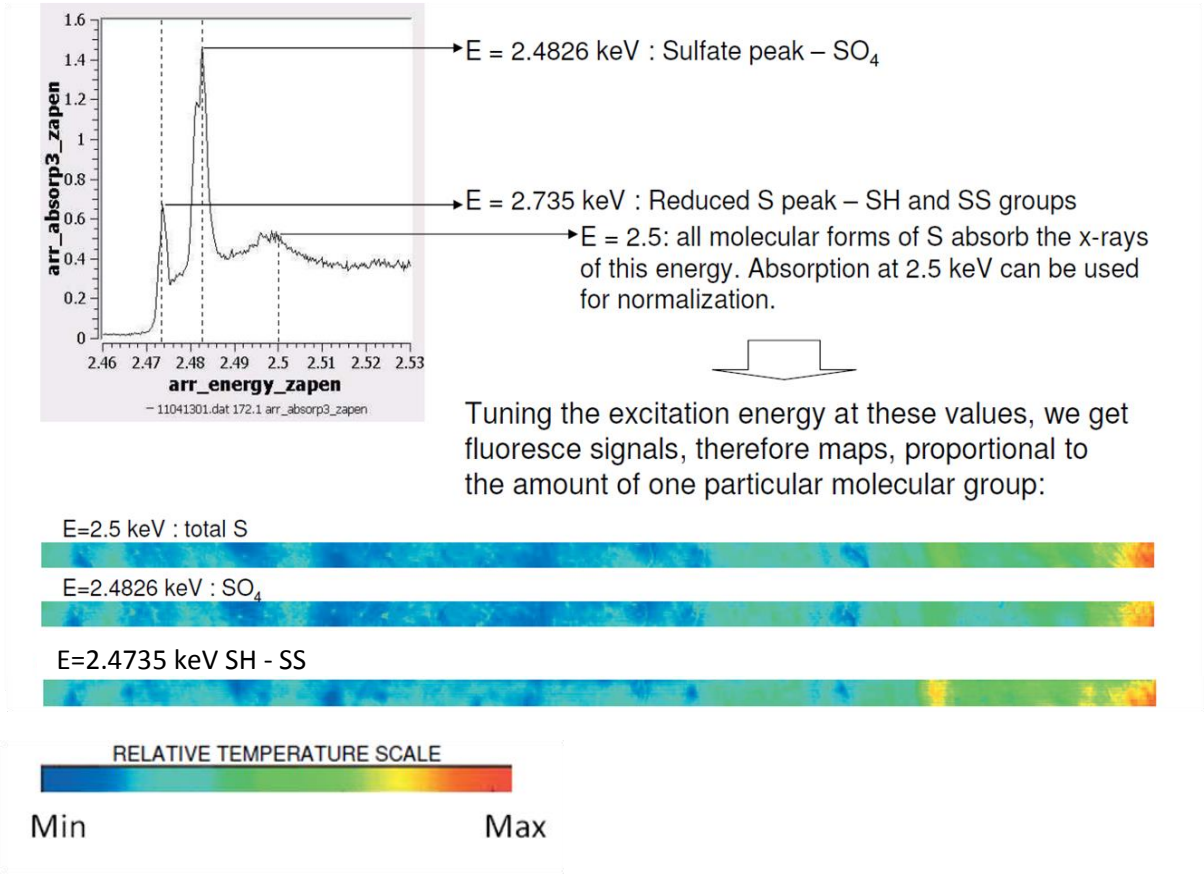

Figure 4.3: The principle of µXRF chemical contrast imaging. Three µXRF maps are acquired at three distinct energies (2.4735 keV, 2.4826 keV, 2.5 keV) to enable qualitatively analysis of the S species distribution in the mature corneal stroma. Example data from non-corneal specimens kindly provided by Dr Gulia Veronesi.

4.3. Results

The current study applied S k-edge XANES spectroscopy to probe the different chemical S forms across the depth of the corneal tissue, from the stromal region closest to the epithelial layer towards the deepest stromal regions adjacent to the endothelium. A total of four corneal tissue sections, 10 μm thick, were analysed and for each one thirteen points across the depth of the tissue an average spectrum of twenty individual scans was obtained. The distance between the different regions examined was 50 μm, measured from the center of each interrogated spot.

Figure 4.4 shows the XANES spectra obtained at distinct regions across the mature bovine corneal stroma. In particular, the first four XANES spectra from the starting point for XANES acquisition located at the stromal region closest to the epithelium (0 μm, 50 μm, 100 μm and 150 μm), as well as the last two XANES spectra obtained from the deepest stromal region closest to the endothelium (550 μm and 600 μm) are shown. The XANES spectra between 150 μm – 550 μm acquired from the central regions of the corneal stroma are not shown due to the fact they were almost identical to the XANES spectra encountered before and after.

Examination of the XANES spectra of the mature corneal stroma was characterised by the presence of four energy peaks that correspond to distinct S species, depicted by the dotted lines in Figure 4.4. Comparison of the peak energies highlighted the major S-containing compounds that attribute for the presence of these peaks and these are thiols (R-S-H) and organic monosulfides (R-S-R) at the energy peak 2,4736 eV, sulfoxides (R-(S=O)-R) at the energy peak 2,4763 eV, sulfonates (R-S$(=O)_2$O) at 2,4811 eV and inorganic sulphate (SO_4^{2-}) and ester sulphate groups (R-O-SO_3) peaked at 2,4827 eV (Prietzel et al., 2003; Bohic et al., 2008; Prietzel et al., 2011).

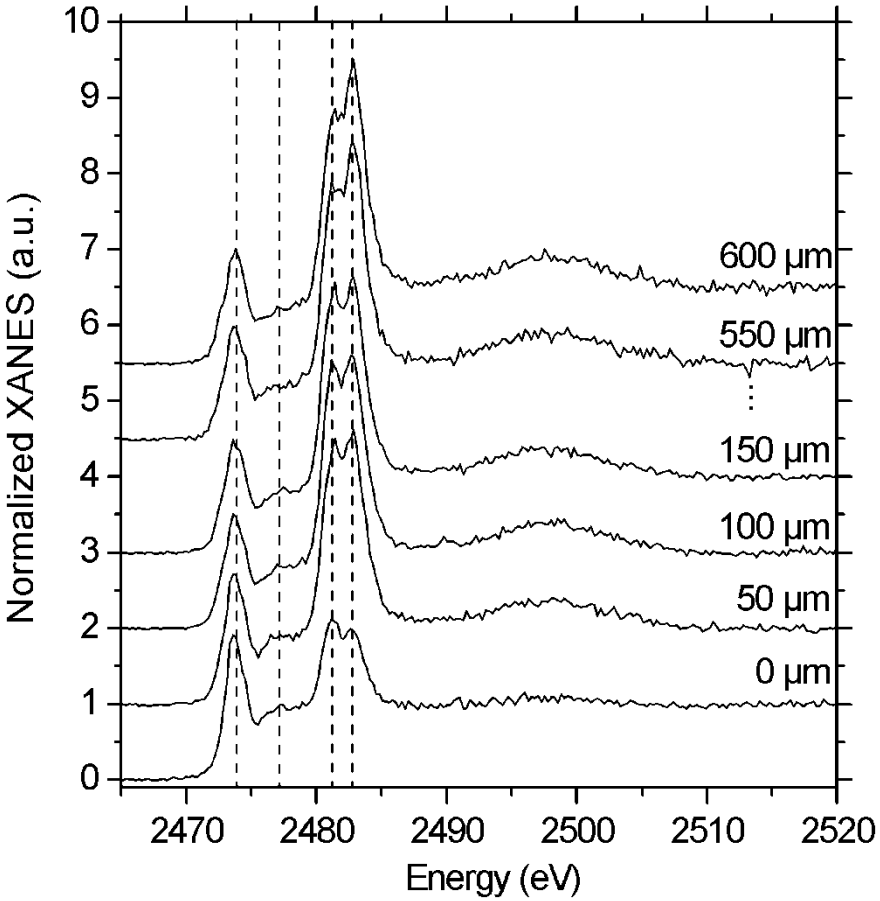

Figure 4.4: S k-edge XANES spectra acquired across the depth of the mature bovine cornea. XANES spectra were acquired at different regions throughout the depth of the tissue; from the area adjacent to the epithelium (0 µm) towards the endothelial region (600 µm). The dotted lines highly the four energy peaks within the spectra corresponding to distinct S species. The XANES spectra were normalised for the incoming current and the jump from the pre-edge region was set to 1, showing that spectra are measurements of the x-ray absorption coefficient around S absorption edge (see Section 3.2.3). Adapted from Veronesi et al., 2013.

Qualitatively looking at the averaged normalised XANES spectra obtained at different depths across the corneal stroma it is clearly notable that there is a heterogeneity in the content of S-containing compounds. Observable differences in the S speciation profile of the cornea are noted in the first 50 µm of stromal depth. More specifically, it is obvious that thiols and organic monosulfides are more predominant in the first 50 µm of stromal depth with their energy peak reaching a stable minimum that does not appear to alter as you move deeper in

the stroma. On the contrary, in the first 50 µm of stromal depth inorganic sulphate and ester sulphate groups are less predominant opposed to thiols and organic monosulfides, however,

deeper in the corneal stroma the contribution of inorganic sulphate and ester sulphate groups is markedly increased. Interestingly, the energy peaks that contribute to sulfoxides and sulfonates show minimal input across the corneal stroma compared to the other S species; thiols and organic monosulfites, inorganic sulphate and ester sulfate.

Gaussian Curve fitting approach facilitated quantitatively analysis of the XANES spectra and Figure 4.5 illustrates an example of fit applied to the experimental data. The experimental data is shown by black dots, the individual Gaussian curves composing the fitting model that correspond to various S species and the cumulative multiple scattering contribution of all the species are shown in different colours while its best fitting curve is displayed in continuous black line.

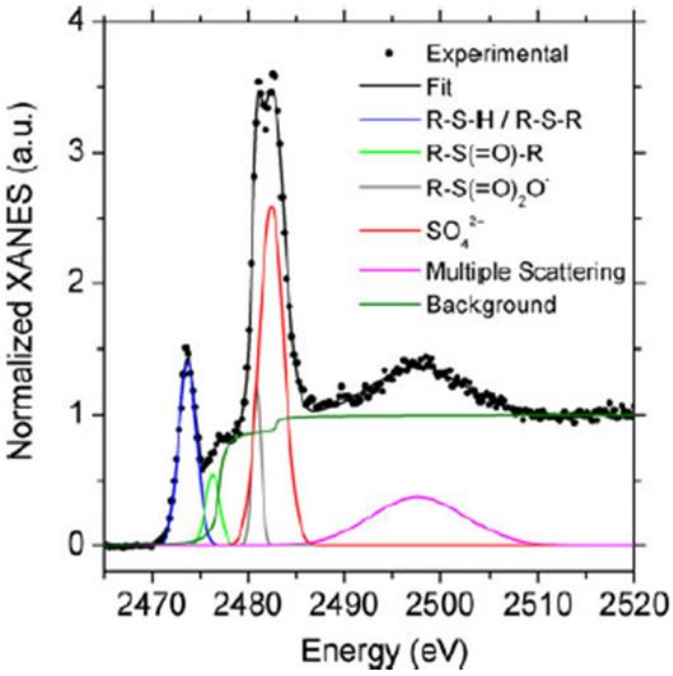

Figure 4.5: Example of the fitting model to the experimental data. Experimental data is shown in black dots while the best fit is shown as a continuous black line. The four individual curves corresponding to various S species present in our sample are shown in blue, green, grey and red colour while the curve corresponding to multiple scattering is shown in pink. Background is shown in green. Adapted from Veronesi et al., 2013.

Table 4.1 shows the best fitting energy values obtained for the various S species encountered within the mature corneal stroma along with the energy values reported by other investigators, either via Gaussian curve fitting approach or by experimentally measuring standard S-containing compounds (Prietzel et al., 2003; Bohic et al., 2008; Prietzel et al., 2011). Comparing the energy values for distinct S species reported by previous investigations with the ones obtained by this study it can be seen that our values are comparable with the ones collected by other scientists. A slight variation is probably attributed to different synchrotron endstations or due to sample discrepancies (solid versus dissolved).

Table 4.1: The energy values for distinct S-containing compounds. The energy values obtained from the current study as well as from other investigators are shown. Adapted from Veronesi et al., 2013

	This study	Bohic et al. (2008)	Prietzel et al. (2003)	Prietzel et al. (2011)
R-S-H/R-S-R	2473.7 $\pm$ 0.2	2473.6	2473.4	2473.5 $\pm$ 0.2
R-S(=O)-R	2476.5 $\pm$ 0.2	2476.3	2475.8	2476.2 $\pm$ 0.2
R-S(=O)$_2$O$^-$	2480.8 $\pm$ 0.2	2481.1	2481.3	2481.3 $\pm$ 0.1
SO_4^{2-}	2482.4 $\pm$ 0.2	2482.7	2482.5	2482.7 $\pm$ 0.1

Gaussian curve fitting approach was applied to all the S XANES data obtained and reported in Figure 4.4. The relative concentration, expressed as a percentage for each S chemical form over the total amount of S, for all the S-containing compounds encountered throughout the whole corneal stromal depth was calculated. This facilitated a more detailed evaluation of the

proportions and type of the several S species in the mature cornea in a depth-profile manner. Figure 4.6 illustrates the outcome of the quantitative analysis of the S species across the corneal depth. The results obtained by the quantitative measure of the proportion of the corneal chemical forms of S against corneal depth are in good agreement with the results acquired from the qualitative analysis which are shown in Figure 4.4. Quantitative data indicates that the stromal region adjacent to the epithelial layer to 50 μm in the depth of the corneal stroma is characterised by a distinctive S distribution trend, whereas from a depth of about 100 μm from the epithelium towards the deepest stromal regions closest to the endothelium, at about 600 μm from the epithelium, the S distribution is more consistent. More precisely, at a distance of 50 to about 100 μm from the epithelium the corneal stroma is primarily composed of a protein form of S, or in other words, of thiols and organic monosulfides (blue squares) with a relative percentage of 57.2±0.7 % followed by 16.0±0.9 % accountable for the composition of inorganic sulphate and ester sulphate (red triangles). It is interesting to note that in the deeper stromal regions, at a depth of about 100 μm down to the stromal regions adjacent to the endothelium (down to 600 μm) the level of thiols and organic monosulfides is markedly decrease to 41±1 % while the contribution from inorganic sulphate and ester sulphate is increased to 42 %, very close to the share of the protein forms of S. With respect to the content of sulfoxides (green circles) and sulfonates (black diamonds) within this range of stromal range is 8±1 % and 9±1 %, respectively.

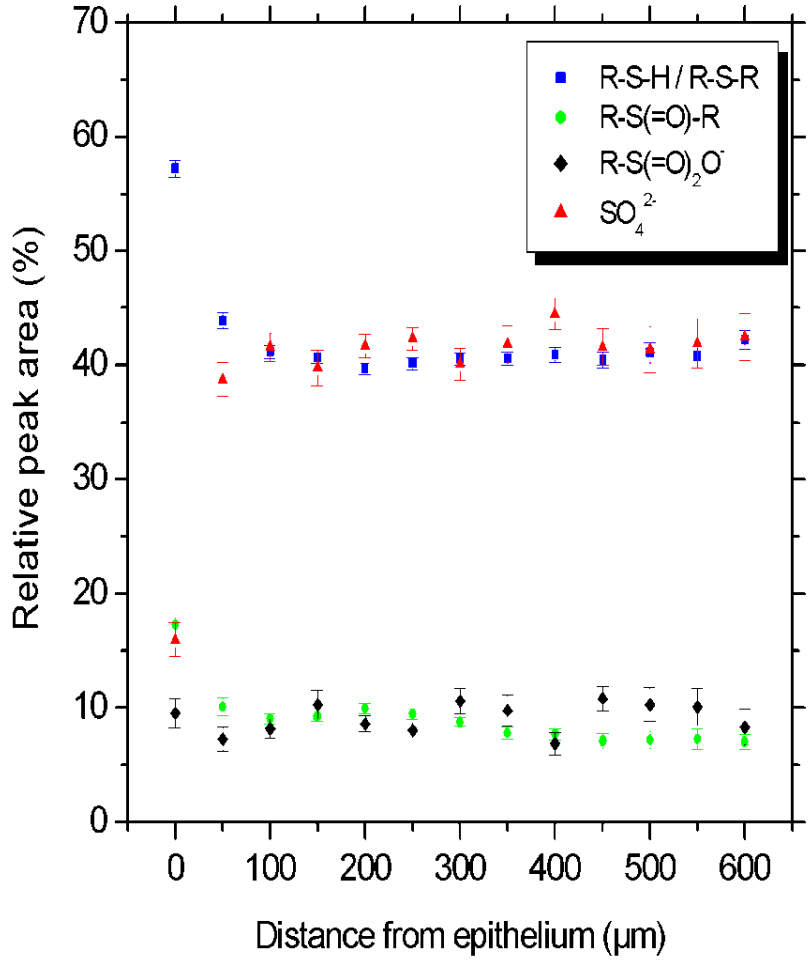

Figure 4.6: The relative percentage of the various S-containing compounds throughout the corneal depth. The relative percentage of the S species from the stromal region closest to the epithelium (0 µm) towards the endothelium (600µm) is shown. Thiols and organic monosulfides are shown in blue squares, sulfoxides in green circles, sulfonate groups in black diamonds and sulphate in red triangles. Adapted from Veronesi et al., 2013.

In addition to the S k-edge XANES experiments and the quantitative analysis, µXRF imaging mapping at the micrometer scale was carried out to probe the topographic distribution of the protein (thiols and organic monosulfides) and sulphate profiles in thin sections of the corneal stroma and enhance our understanding of S speciation across tissue depth. The sample area chosen for µXRF imaging mapping was irradiated at the resonance energy of thiols and organic monosulfides (2,4737 eV), inorganic sulphate and ester sulphate (2,4824 eV) and at

the energy of 2,510 eV (for normalisation purposes) providing a total of three image maps. It is important to mention that the image map obtained at the energy of 2,510 eV provides the distribution of several elements, including the individual distribution of S and phosphorus (P) and was used for normalisation. Moreover, the image map obtained at the energy of 2,510 eV was also used to demonstrate the relative distribution of the different S species over the sum of all S present in the sample, throughout the mapped region and hence the corneal depth. In particular, the protein peak energy (thiols and organic monosulfides) and the sulphate peak energy (inorganic sulphate and ester sulphate) were both divided by the one acquired at 2510 eV. Overlapping the maps obtained at the different energies enables one to detect co-localisation of the protein S forms, sulphates and the element of interest. This study was interested in the detection of co-localisation regions across the corneal stromal depth between protein S forms, sulphates and P.

Two sample areas were examined in this study; both returning the same S species distribution across the corneal stromal depth. The µXRF image maps (360 x 40 μm^2) acquired at the energies of thiols and organic monosulfides (R-S-R / R-S-H versus P) and inorganic sulphate and ester sulphate (SO_4^{2-} versus P) for one of the selected sample area chosen for µXRF imaging mapping are shown in Figure 4.7. The distribution of reduced S and sulphates is represented in red while the distribution of P is depicted in green, in both maps. The mapped areas in yellow colour denote co-localisation between the S species and P.

The µXRF imaging mapping analysis provides a higher spatial resolution understanding with regards to the distribution of the different S species encountered across the corneal depth. Investigation of the upper map in Figure 4.7 which is a sulphate-enhanced map reveals that in the stromal region closest to the epithelium, at a distance up to approximately 100 µm, P

distribution (green) is predominant in contrast to sulphates (red) which are absent. Furthermore, no co-localisation of sulphates and P can be observed. It is of great interest to note that the situation appears to be the opposite in the deeper regions of the corneal stroma, at the distance range 100-600 μm, where a sulphate-rich region is clearly noted and P is visualised as isolated spots. The lower map in Figure 4.7 which is now a thiols- and organic monosulfides-enhanced map highlights that the first approximately 100 μm of the anterior stroma is a protein-rich region with thiols and organic monosulfides (red) persistently present. Also, it is clearly indicated that in the anterior region of the stroma (adjacent to the epithelium) thiols/organic monosulfides are co-localised with P, depicted in yellow colour, illustrating their simultaneously presence to the same molecules. In the rest of the corneal stromal depth the distribution of thiols/organic monosulfides is shown to be quite homogeneous and as indicated by the upper map P distribution presents hot spots of a few microns size. These findings are consisted and confirm the results observed by the previous experiments conducted in the current study.

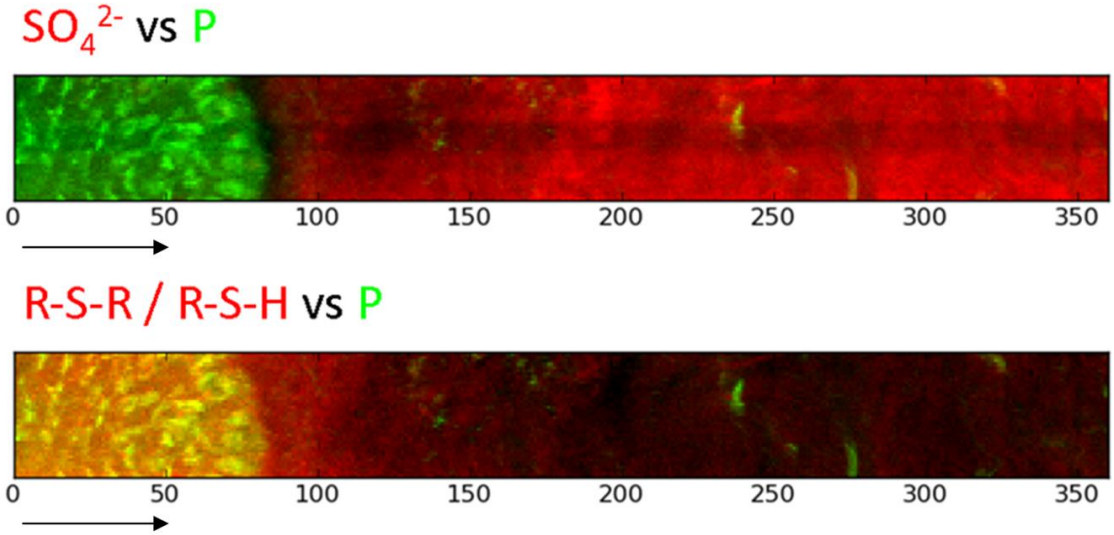

Figure 4.7: µXRF image maps of the mature bovine corneal stroma. Upper map: The spatial distribution of sulphate (red) and P (green) from the region closest to the epithelium towards the deepest regions of the stroma (350µm) is shown. **Lower map:** The spatial distribution of the thiols and organic monosulphides depicted in red and P (green) from the anterior stroma through the deeper stroma. Yellow regions indicate co-localisation of the S species and P. Image map size = 360 x 40 μm^2. Arrows show the direction from the epithelial region towards the endothelial region. Adapted and modified from Veronesi et al., 2013.

4.4. Discussion

As previously introduced at Chapter 1, the cornea is classically described as the transparent window located at the front of the eye. The cornea is composed of five distinct layers and these are the epithelium, Bowman's layer, stroma, Descemet's membrane and endothelium. There are key differences in the physicochemical architecture, elemental composition and subsequently the function between the corneal layers; all of them being highly important in health and disease.

The corneal stroma is mainly composed of collagen fibrils, proteoglycans that bear sulphated glycosaminoglycan side chains, the major of them being KS and CS/DS glycosaminoglycans, and stromal cells namely keratocytes. The unique arrangement of the collagen fibrils which to a major extent is controlled and regulated by the sulphated proteoglycans, fulfils the corneal requirements for transparency since collagen fibrils are light scatters facilitating transmission through the cornea (Maurice, 1957; Hart and Farrell, 1969; Benedek, 1971; Scott and Haigh, 1985; Meek et al., 1986; Komai and Ushiki, 1991; Knupp et al., 2009; Lewis et al., 2010; Parfitt et al., 2010). As stated above, the sulfation profile of the corneal proteoglycans/glycosaminoglycans plays a fundamental role in maintaining the hydrophilic signature and swelling properties of the cornea (Bettelheim and Plessy, 1975; Bettelheim and Goetz, 1976; Castoro et al., 1988). With this concept in mind, the current study applied S k-edge XANES spectroscopy and µXRF chemical contrast imaging techniques to probe the S speciation in the mature cornea throughout its depth, as a function of tissue location.

In this study mature bovine corneas were cut transversely in order to examine the whole corneal depth from the anterior side closest to the epithelium to the posterior side closest to the endothelium and 10 µm thick tissue sections were analysed by S k-edge XANES spectroscopy. According to the S k-edge XANES spectroscopy data, the S-containing compounds present in the mature cornea throughout its depth are thiols and organic monosulfides (2,4736 eV), sulfoxides (2,4763 eV), sulfonates (2,4811 eV), inorganic sulphate and ester sulphate (2,4827 eV). One caveat of S k-edge XANES spectroscopy, as previously discussed in Chapter 3; section 3.3.2., is that it is not possible to distinguish thiols and organic monosulfides because these chemical forms of S have almost identital peak energies. This is the case for inorganic sulphate and ester sulphate which also have very similar peak energies. Qualitative data analysis indicated that the S speciation across the mature corneal stromal

depth is not uniform. While the S speciation between about 100 μm from the epithelial side and 600 μm of the stroma, adjacent to the endothelium is uniformly consistent with thiols/organic monosulfides and inorganic sulphate/sulphate, heterogeneity in the content of S is clearly noted in the first 50 μm of tissue depth. More specifically, the first 50 μm of corneal depth was found to be a protein-rich region since the thiols and organic monosulfides energy peak was outstanding compared to the energy peak for the other S species. The thiols and organic monosulfides are vital components of the proteins found in the corneal stroma as they are linked to cysteine and methionine amino acids, respectively. This heterogeneity in the S profile within the first 50 μm of the cornea opposed to deeper regions of the stroma can be explained by the fact that the anterior corneal stroma is anatomically and hence biochemically different from the posterior part of the corneal stroma. At the most anterior part of the corneal stroma, just below the epithelial basement membrane, Bowman's layer is found. Bowman's layer is an acellular layer composed of collagen fibrils that are randomly interwoven giving the appearance of a dense felt-like sheet, unlike the collagen fibrils in the underlying stroma which are uniquely organised to form distinctive collagen lamellae (Komai and Ushiki, 1991; Wilson and Hong, 2000; Hayashi et al., 2002; Kobayashi, et al., 2006). The thickness of Bowman's layer is 5 μm thick in cattle and approximately 10-12 μm thick in human (Hayashi, et al., 2002).

Taking into account that the proteoglycans are interacting with the collagen fibrils along with the fact that proteoglycan-collagen interactions regulate collagen fibril organisation and architecture, it is ostensible to propose that the variation in the S speciation between the anterior part and the deeper parts of the corneal stroma observed here underlie differences in the biochemical signature of the proteoglycans and consequently sulphated glycosaminoglycans in Bowman's layer versus the proteoglycans and glycosaminoglycans

present in the corneal stroma. Little is known regarding the sulfation profile of the glycosaminoglycans in Bowman's layer mainly because biochemical quantification is particularly difficult due to the thickness of the layer itself. However, it has been shown by immunoelectron microscopy that less KS, CS and HS proteoglycans are present in Bowman's layer in contrast to normal organ-cultured human corneas, reported by Bairaktaris and colleagues (Bairaktaris et al., 1988). It can be therefore speculated that the heterogeneity in the composition of S at a distance of 50 μm from the anterior side of the corneal stroma, including Bowman's layer, reflects alterations in the biochemical signature of proteoglycans/glycosaminoglycans encompassed in Bowman's layer when compared to rest of the corneal stroma proposing that the transition between the two corneal layers occurs gradually. This is agreement with a recent study by Morishige and co-workers who examined the three-dimensional structure of collagen lamellae in the anterior stroma of the cornea and found that collagen lamellae at the anterior corneal stroma are interwoven and adhere tightly to Bowman's layer (Morishige et al., 2011).

In addition to XANES spectroscopy and qualitative analysis, quantitatively data analysis was carried out and provided the relative percentage of the different S chemical forms throughout the corneal stromal depth, as a function of the total S amount. The results obtained revealed once again that at a depth of about 50 μm from the anterior part of the stroma the distribution of the main S species varies whereas throughout the rest of the stromal depth a fairly consistent distribution of S-containing compounds is noted. The consistency in the S speciation throughout the deeper regions of the corneal stroma, from 100 μm to 600 μm, is very interesting and unexpected considering that previous studies have provided evidence supporting that there are differences in the sulfation pattern of the KS and CS/DS corneal glycosaminoglycans as a function of corneal depth (Scott et al., 1988; Scott et al., 1990).

Moreover, a number of previous investigators have also supported that apart from the differences in the sulfation pattern of glycosaminoglycans throughout the whole corneal depth, there are additionally observable differences in their distribution too (Bettelheim and Plessy, 1975; Borcherding et al., 1975; Bettelheim and Goetz; 1976, Castoro et al., 1988; Scott et al., 1988; Scott and Bosworth, 1990). These investigators proposed that the amount of CS/DS glycosaminoglycans is higher at the anterior corneal stroma than KS glycosaminoglycans. On the other hand, KS glycosaminoglycans are more prevalent in deeper regions of the stroma towards the posterior end, compared to CS/DS glycosaminoglycans. This finding leads to the conclusion that the differences in the sulfation status of the major corneal glycosaminoglycans do not significantly affect the overall distribution of the corneal S species. Also, this finding might be indicative of a balancing phenomenon that neutralise the differences among the distribution of the major corneal glycosaminoglycans and as a result the effect on overall S speciation across the tissue depth is negligible.

In the present study, μXRF chemical contrast imaging technique was performed to get an even more insightful understanding of the S speciation as a function of the corneal stromal depth as this technique facilitated the topographic distribution of the main S species at the micrometer scale. The results obtained by μXRF chemical contrast imaging confirm the findings from the S k-edge XANES experiment indicating the occurrence of a sulphate-depleted and thiol/organic monosulfide-rich region at the first 50 μm of the anterior most stroma and the homogenous character with respect to S speciation throughout the rest of the corneal stromal depth. The μXRF image maps highlighted the presence of P as isolated micrometric spots. This is very likely to denote the presence of keratocytes, the corneal stromal cells since the genetic material is known to contain lots of phosphate bonds.

In conclusion, taken together, these findings provide strong evidence that the S speciation throughout the whole mature corneal depth is not uniform. The most anterior part of the corneal troma, adjacent to the epithelium, is rich in thiols and organic monosulfides (57.2±0.7 %) which are associated to the corneal proteins. Despite that the sulphate groups, inorganic sulphate and ester sulphate, were also found at the most anterior part of the corneal stroma (16.0±0.9%); they were more prevalent in the deeper regions of the stroma (42±1 %). The relative concentration of thiols and organic monosulfides decreased as you move through the tissue depth, with their relative concentration being 41±1 %, almost identical to the one calculated for the sulphate groups. The heterogeneous nature of the S speciation in the most anterior part of the corneal stroma, at the interface with the Bowman's layer supports that the differentiation and the transition between these two corneal layers is not very abrupt. The rest of the corneal stromal depth does not show any differences regarding its content in the S-containing compounds indicating that the distribution and sulfation status of the corneal glycosaminoglycans have very little impact on the overall S speciation. The analytical techniques employed in this study provided new insights into the biochemical physiology of the mature corneal stroma, with a particular focus on the S element physiology, as a function of tissue location.

4.4.1 Future Directions

The findings obtained from the current study but also from the study described in Chapter 3, where the chemical composition and S speciation of the embryonic chick cornea was investigated, emphasise the fundamental role of elemental entities in establishing the proper tissue architecture and function in biological tissues such as cornea.

In regards to the findings obtained in Chapter 3, important changes in the biochemical signature of elements like P, S, Cl, K and Ca were noted during chick corneal development at

embryonic days 12, 14 and 16. Further research should be undertaken to examine more in depth these elements in the chemical composition of the embryonic chick cornea. In particular, it will be very interesting to examine how the chemical composition of the embryonic chick cornea is altering during other developmental stages, from the earlier days of embryonic development towards the later stages, just before hatching.

The results obtained by the XRF microscopy experiments revealed that there are qualitatively alterations in the biochemical signature of the embryonic chick cornea. How about the actual concentration of those elements? For instance, is S or Cl concentration increased between day 12, day 14 and day 16? This is an important question that needs to be answered as it will enhance our understanding on the controlled developmental events, with respect to the chemical composition, that take place resulting to a mature corneal tissue. μXRF chemical contrasting imaging approach has been applied to demonstrate the spatial distribution of the S species present in the mature corneal stroma. It would be exciting to apply this technique to study the spatial distribution of other elements like Cl, K, and Ca in both the embryonic corneal and the mature corneal stroma.

As previously discussed, S is one of the major elemental entities in the cornea and it has a high impact on the establishment of the transparency (sulphated glycosaminoglycans–collagen interactions). The S speciation in the embryonic chick cornea and in the mature bovine cornea as a function of tissue depth have been examined here; highlighting once again that it is a critical player in the corneal transparency and function. Further studies with more focus on S should be carried out. It would be attractive to examine the S spatial distribution in the embryonic chick corneal stroma across the depth of the tissue at several developmental stages. It will be even more appealing to compare and contrast the S speciation, concentration, as well as spatial distribution of a clear transparent cornea opposed to a

diseased cornea where the transparency it is impaired. This might help us define not only the function of S in the establishment of corneal transparency but also its association with diseased opaque corneas.

All in all, there is certainly abundant room for further progress in an attempt to understand the transparency of the cornea and the relationship between the elemental entities present within this tissue.

Chapter 5: Three-dimensional architecture of collagen type VI in the human trabecular meshwork

5.1. Introduction

Collagen type VI is an important component of the ECM of many connective tissues, notably skin and cornea (Kielty et al., 2003; Trüeb et al., 1987; Keene et al., 1988). A number of investigators have showed that collagen type VI is also one of the major structural components of the ECM of the human trabecular meshwork (Lütjen-Drecoll et al., 1989; Tripathy et al., 1994; Dietlein et al., 1998). It was originally identified in pepsin fragments of human aortic intima and designated as "intima collagen" (Chung et al., 1976). After further electron microscopy and biochemical studies, intima collagen was renamed type VI collagen, and a detailed structural model for this type of collagen was proposed (Keene et al., 1988; Furthmayr et al., 1983; Von der mark et al., 1984; Odermatt et al., 1983; Hessle and Engvall, 1984; Engel et al., 1985; Kuo et al., 1995; Knupp and Squire, 2001; Baldock et al., 2003; Knupp et al., 2006).

Type VI collagen is a heterotrimer and was long thought of as being composed of three genetically distinct alpha 1 (VI), alpha 2 (VI), and alpha 3 (VI) chains (Jander et al., 1983; Chu et al., 1988). However, recently, three novel collagen VI alpha chains have been discovered in humans, the alpha 4 (VI), alpha 5 (VI) and alpha 6 (VI) chains (Fitzgerald et al., 2008; Gara et al., 2008). After secretion into the extracellular matrix, alpha chains assemble to form type VI collagen molecules possessing a central collagenous triple-helical segment, about 105 nm long, delimited at both ends by a globular domain (Furthmayr et al., 1983, Figure 5.1a). Pairs

of collagen VI molecules coil together in an antiparallel fashion (Furthmayr et al., 1983; Knupp and Squire, 2001) with a 30 nm axial shift to form dimers (Figure 5.1b). Two dimers associate laterally with no axial shift to give rise to a tetramer (Figure 5.1c), which can be considered as the basic structural unit of collagen VI microfibrils (Furthmayr et al., 1983; Von der Mark et al., 1984; Bruns, 1984, Figure 5.1d). Cysteine residues form disulphide bridges between monomers in dimers and between dimers in tetramers, and they stabilize the main collagen VI structural unit (Ayad, 1994). Tetramers can be described as possessing an inner rod-like region and two outer rod-like regions separated by, and ending with, the collagen VI globular domains of the four molecules forming them (Figure 5.1c).

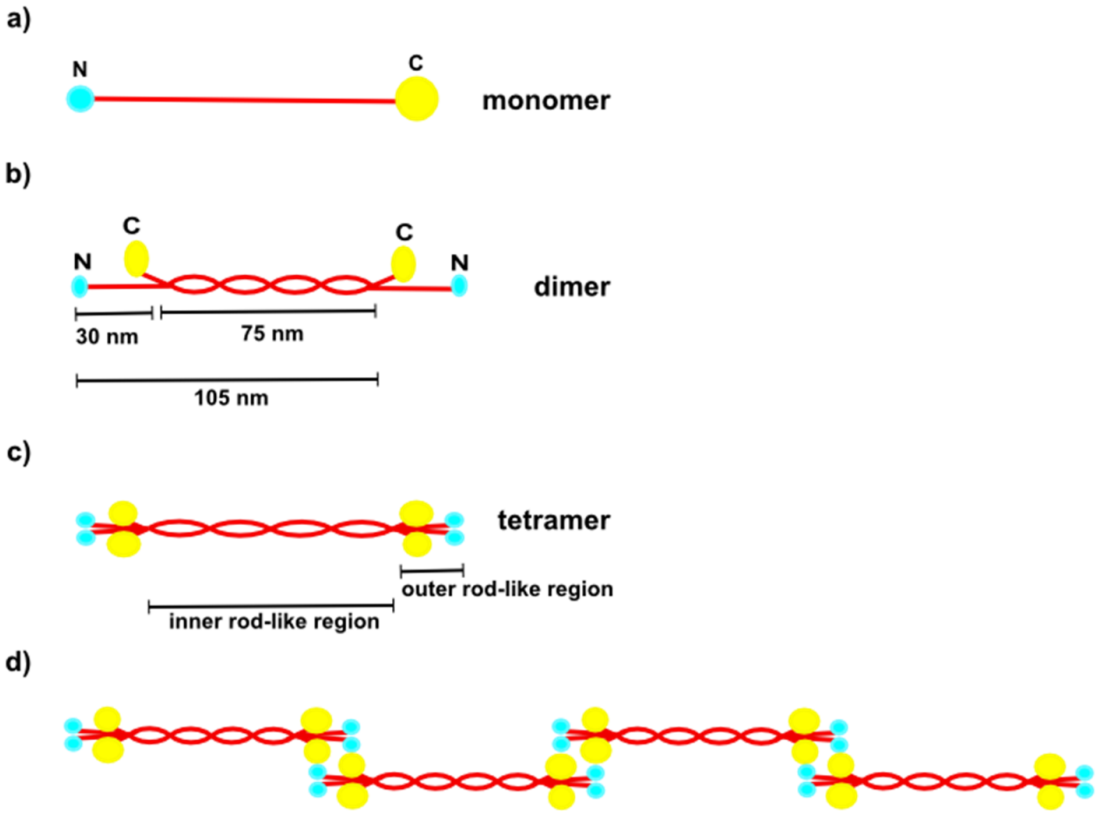

Figure 5.1: Schematic drawings of the structures of (a) monomer, (b) dimer, (c) tetramer and (d) microfibrils of type VI collagen. (a) N (NH2) and C (COOH) are the amino and carboxy – terminal domains, represented in blue and yellow respectively. The collagenous triple-helices (red in colour) associate laterally with a 30 nm axial shift in dimers **(b)**. Pairs of dimers associate laterally to form tetramers **(c)**. Tetramers can be described as possessing an inner rod-like region and two outer rod-like regions separated by and ending with the collagen VI globular domains. Limited resolution of collagen VI fibrils in micrographs causes the globular domains to appear as transverse electron-dense bands **(d)**.

Unlike the more abundant type I collagen, type VI collagen gives rise to cross-banded aggregates that are characterized by a pattern of pairs of transverse bands, approximately 30nm apart with a periodicity of about 105 nm (Keene et al., 1988; Furthmayr et al., 1983; Von der mark et al., 1984; Odermatt et al., 1983; Hessle and Engvall, 1984; Engel et al., 1985; Kuo et al., 1995; Bruns, 1984). In particular, non-covalent bonds between the C- and N-terminal globular domains at each end of the outer rod-like regions of two adjacent tetramers produce end-to-end cross-banded pseudo-fibrillar aggregates (Figure 5.1d) with a repeated ~30-75nm spacing (Furthmayr et al., 1983; Von der mark et al., 1984; Wu et al., 1987). The same interactions between globular domains of the tetramers account also for the formation of more extended collagen VI aggregates resembling open networks (Knupp and Squire, 2005). The basic way in which collagen type VI tetramers can assemble explains the organization of morphologically distinct aggregates which also depends on the structure and physiology of the tissue in which they are found (Reale et al., 2001; Linsenmayer et al., 1986; Hirano et al., 1989; Shuttleworth et al., 1992; Rittig et al., 1990; Garrone and Feeney, 1959; Leeson and Speakman, 1961).

It is widely accepted that type VI collagen interacts with ECM constituents in a number of connective tissues (Specks et al., 1992; Burg et al., 1996; Sabatelli et al., 2001; Wiberg et al., 2003; Kuo et al., 1997). Moreover, collagen type VI is associated with several human disorders. For example, individuals suffering from Bethlem myopathy exhibit mutations of the collagen type VI genes (COL6A1, COL6A2, COL6A3) that affect the N- terminal domains (Pepe et al., 1995; Lampe et al., 2005; Scacheri et al., 2002). Collagen type VI assemblies are also involved with pathogenesis of ocular disorders including Age-Related Macular Degeneration (Knupp et al., 2002a) and Sorsby's Fundus Dystrophy (Knupp et al., 2002b).

The aim of this study is to examine the three-dimensional organization of collagen type VI aggregates in the human trabecular meshwork using transmission electron tomography in an attempt to elucidate the ultrastructure, assembly and possible functional roles of collagen VI in the trabecular meshwork. As it was previously mentioned, the ECM of the human trabecular meshwork provides flow resistance to aqueous humor leaving the anterior chamber of the eye and which thus plays a role in the regulation of intraocular pressure (Bill and Maepea, 1994). This study also aims to investigate proteoglycan-collagen VI interactions within the human trabecular meshwork from a structural point of view.

5.2 Materials and Methods

5.2.1 Specimen preparation and TEM

Ocular tissues containing trabecular meshwork were dissected out from both eyes of a 69-year-old female donor. Tissue, which was obtained from the Bristol Eye Bank, UK, with full informed consent, was immediately fixed in 2.5% glutaraldehyde in 25 mM sodium acetate buffer (pH 5.7) containing 0.1 M magnesium chloride and 0.05% Cuprolinic blue dye (the dye was included to stain sulfated proteoglycans). Samples were then washed in sodium acetate buffer to remove the glutaraldehyde fixative and Cuprolinic blue dye. Immersion in 0.5% sodium tungstate was carried out to add contrast to the stained proteoglycans, and dehydration was accomplished by exposing the tissue to a graded series of ethanol (50-100%). Following conventional processing with epoxy resin embedding, ultrathin sections, approximately 90nm-thick, were cut on an Ultracut E ultramicrotome (Reichert-Jung) and contrasted for TEM by staining with saturated aqueous uranyl acetate followed by washes in filtered distilled water for 12 and 4 x 1 min, respectively. Sections obtained from three

different blocks were examined with a JEOL 1010 transmission electron microscope operating at 80 kV. Experiments were conducted in accordance with the ethical principles that have their origin in the Declaration of Helsinki, and in line with the requirements of the UK Human Tissue Act.

5.2.2 Electron tomography

For electron tomography, 120 nm-thick sections were cut and collected on naked 200 mesh copper grids. After uranyl acetate staining as indicated above, 10nm colloidal gold particles (BBI, Cardiff, UK) were deposited on both sides of the grid to serve as fiducial markers. A single-axis tilt series of electron micrographs of collagen type VI assemblies was obtained from +60^{o} to -60^{o} in both one and two degree increments. Images were acquired using a Gatan ORIUS SC1000 CCD camera at ×20k magnification. Micrographs were aligned at a pixel size of 0.4 nm based on the position of the colloidal gold particles on each image. Tomographic reconstructions of longitudinal sections of trabecular meshwork type VI collagen aggregates and stained proteoglycan filaments were generated with the IMOD software package (Kremer et al., 1996). Segmentation of the tomograms, three-dimensional analysis and visualization were accomplished via the use of EM3D software (Ress et al., 2004). Visualization of the reconstructed image stacks and the generation of animated stereo views were achieved with the 3DViewer plug-in of the imageJ software package (Schmid et al., 2010; Schneider et al., 2012).

5.3. Results

Transverse banded collagenous assemblies were found to be widespread throughout the ECM of the human trabecular meshwork beams and the juxtacanalicular region. These assemblies, displaying an axial periodicity of 109 ±13 nm (SD, n=47), form clusters of different sizes, which often line the intra-trabecular spaces and which are surrounded by interstitial collagen fibrils displaying the typical 67nm axial periodicity (Figure 5.2). These assemblies, from their general appearance and periodicity, resemble closely the assemblies of collagen VI molecules found in other tissues (Knupp and Squire, 2005). One main difference is that, in the trabecular meshwork, the transverse bands are single instead of double bands. In typical collagen VI assemblies, the transverse bands arise from the electron dense material of the globular N- and C- terminal domains of the collagen type VI molecules and are split into pairs. As introduced above, these double bands are characteristic and indicative of collagen type VI assemblies, and come about as a consequence of the axial alignment of the N- and C- globular domains of the outer rod-like regions of collagen type VI tetramers, which are about 30 nm apart axially.

In the aggregates studied here, as well as in those of collagen VI described previously in other tissues (Keene et al., 1988; Furthmayr et al., 1983; Von der mark et al., 1984; Odermatt et al., 1983; Hessle and Engvall, 1984; Engel et al., 1985; Kuo et al., 1995; Knupp and Squire, 2001; Knupp et al., 2006), electron dense filaments are seen running perpendicular, or nearly perpendicular, to the transverse bands and crossing them. In the case of the collagen VI assemblies, these filaments are interpreted as arising from the inner and outer rod-like segments of the type VI collagen tetramers which form the assemblies (Figure 5.3) (Knupp et al, 2002a,b).

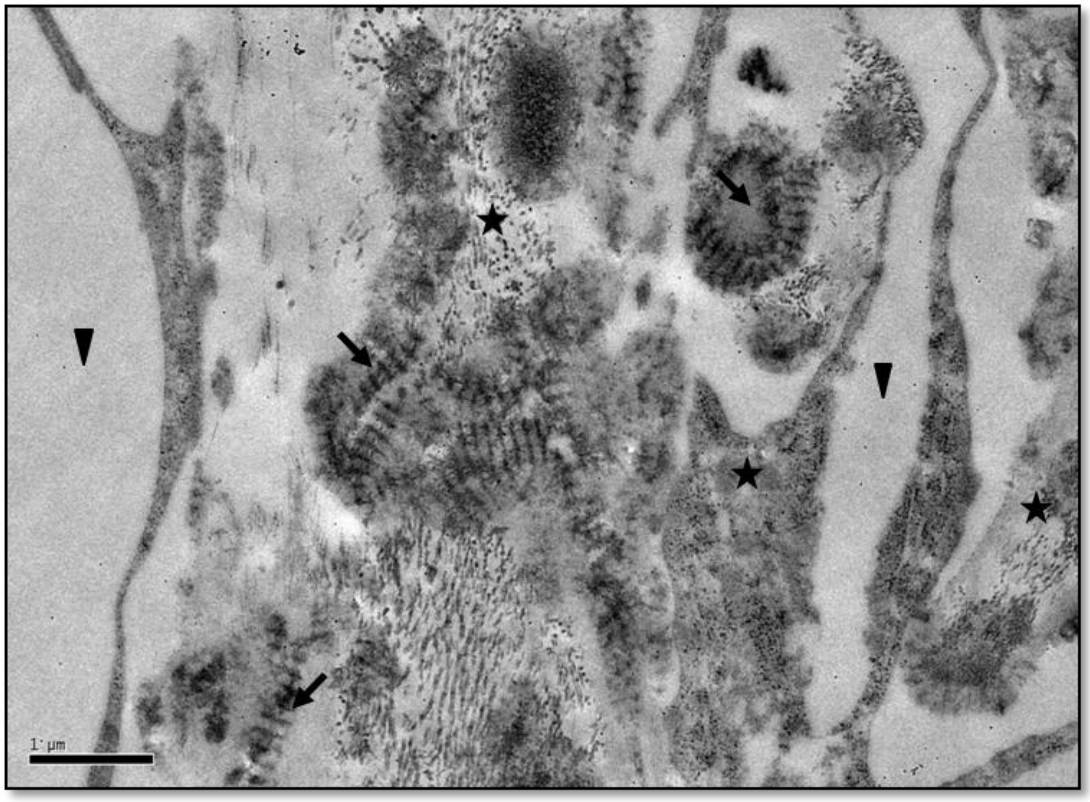

Figure 5.2: Transmission electron micrograph of the human trabecular meshwork. A series of parallel layers of connective tissue, known as the trabecular sheets (stars), and inter-trabecular spaces forming irregular channels (arrowheads) are visible. The trabecular sheets consist of collagen fibrils orientated both transversely and longitudinally and thin trabecular endothelial cells. Type VI aggregates (arrows) are distributed throughout the entire width of the sheet surrounded by collagen fibrils. The black dots dispersed throughout the trabecular meshwork represent 10 nm colloidal gold particles used for tomography. Scale bar = 1 µm

The many structural similarities between the assemblies in this study of trabecular meshwork and the collagen VI assemblies examined elsewhere (Knupp et al, 2000, 2002a,b, 2006) suggest that they are all made of collagen VI, with the tetramers arranged in essentially the same way. The fact that here they present single instead of double transverse bands may indicate that the globular domains and/or the outer rod-like segments of the tetramers interact with extracellular matrix material found in the trabecular meshwork, which fills the space between the globular domains. However, if this is the case, there is a possibility that the material occupying the spaces between the double bands does not do so uniformly, and that occasionally the double bands are still visible. This was the case for the collagen VI assemblies in Bruch's membrane of a patient suffering from Sorsby's Fundus Dystrophy (Knupp et al, 2000b), where single transverse bands, instead of double bands were prevalent. In this study, finding evidence of single bands reverting to double bands would further confirm assemblies being made of collagen.

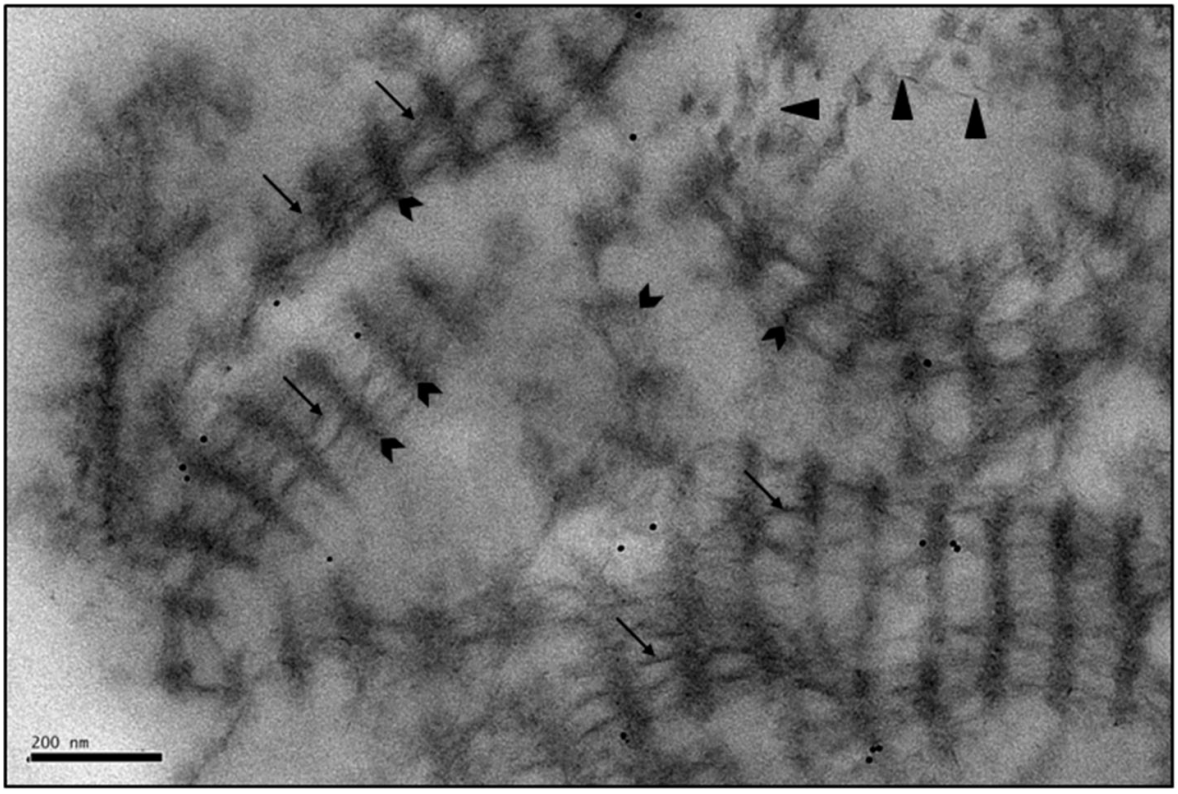

Figure 5.3: High magnification longitudinal view of the type VI collagen aggregates in the trabecular sheets. Only single transverse bands are evident (chevrons) and their axial periodicity is approximately 109 nm. The rod-like segments of the collagen VI tetramers (arrows) cross the transverse bands at different angles. Proteoglycans are also seen in the matrix (arrowheads). Several 10 nm gold particles used for tomographic reconstruction appear as black dots in the electron micrograph. Scale bar = 200 nm.

An exhaustive search at the microscope which included tilting the specimens at different angles produced clear evidence of single bands splitting into double bands in a small number of assemblies (Figure 5.4). These double bands are revealed only for a limited tilt angle range, appearing as single transverse bands at a 0^{O} tilt angle, splitting into double bands at higher angles (about 20^{O} in the cases shown in Figure 5.4) and reverting to single, but much narrower bands at higher tilt angles. The axial distance between double bands in these assemblies is not regular, ranging between 112 nm and 85 nm. This would be expected if the tetramers in the assemblies were forming transient links and had not yet settled into a stable configuration.

The ratio between the smaller and the larger gaps between the double bands in the most regular assemblies is about 0.2, which is consistent with that of other collagen VI assemblies. The existence of the double bands confirms the presence of collagen VI in the assemblies. The fact that double bands are infrequently seen is indicative that the interaction between the collagen VI tetramers and the extracellular material is extensive and uniform throughout the trabecular meshwork, with the extracellular material efficiently filling the gaps between the double bands.

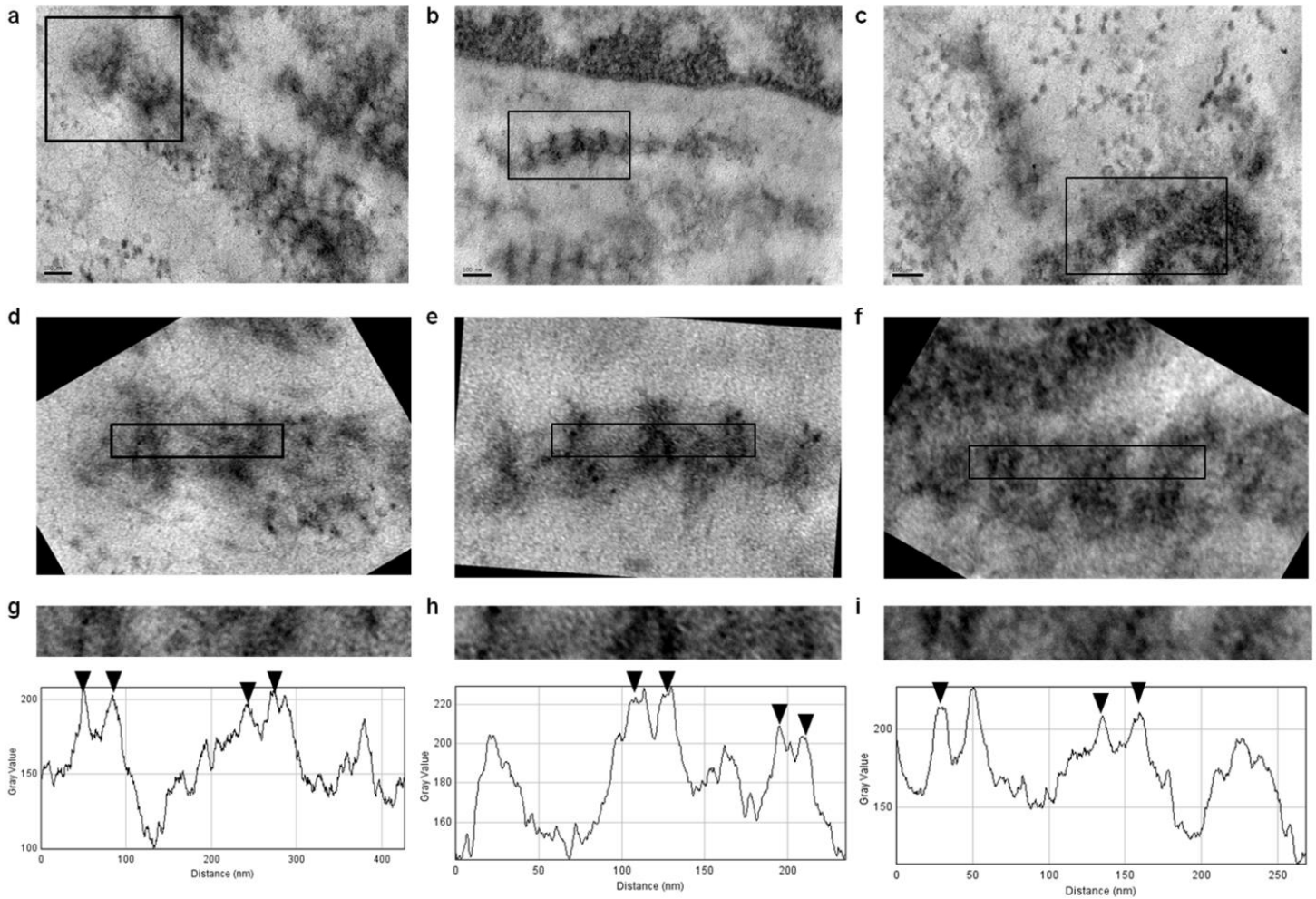

Figure 5.4: Representative collagen VI assemblies showing pairs of transverse double bands. a, b and c show some representative collagen VI assemblies found in the human trabecular meshwork during this study. The boxed regions in a, b and c are magnified in d, e and f. g, h and i show a magnified view and a profile density plot of the boxed regions in d, e and f. The horizontal-axis of the plots corresponds to distance along the long axis of the rectangular selections. The density profile was obtained by integrating the electron density in the rectangular selection along a vertical path. Arrows indicate peaks on the profile plots that correspond to the dark double transverse band of collagen VI assemblies. Scale bars = 100nm.

To achieve a better understanding of the way in which collagen type VI molecules interact with each other in the trabecular meshwork, three-dimensional tomographic reconstructions of the assemblies from single axis tilt-series of electron micrographs were generated. This type of analysis can reveal details of the molecular organization of collagen type VI aggregates that are not accessible from conventional two-dimensional transmission electron microscopy (Figure 5.3), and can offer new insights into the way collagen type VI molecules are assembled in the matrix of the human trabecular meshwork. Figure 5.5 presents one typical three-dimensional reconstruction that has been produced of a type VI collagen assembly. Figure 5.5a is a 8.57 nm thick slice through the reconstruction, while figure 5.5b is a surface rendering of the same reconstruction. Figure 5.5c represents a manual segmentation of the same view. In the surface rendering in figure 5.5b, the presence of globular domains (highlighted with red arrows; also see Supplementary video S1 and S3) can be noticed within a transverse band. Globular domains such these, when not interacting with other material of the extracellular matrix, are likely to be responsible for the double bands seen in typical collagen VI assemblies, as well as in the assemblies seen in Figure 5.4. In the trabecular meshwork, the inner rod-like segments collagen type VI tetramers assemblies present an unsystematic irregular lateral arrangement (Figure 5.5b; yellow arrowheads).

Figure 5.6 shows are additional three-dimensional reconstruction of the tilted type VI collagen aggregates (Figure 5.3) highlighting once again the presence of the double transverse bands (red arrowheads) formed by N- and C-globular domains of type VI collagen. Looking at the two-dimensional projection, Figure 5.3, this feature is not clearly seen pointing out the dynamics of electron tomography technique for ultrastructural studies. Moreover, looking at figure 5.6 it is clearly noted that the collagenous triple helices (yellow arrowheads) run almost perpendicular to the dark transverse bands.

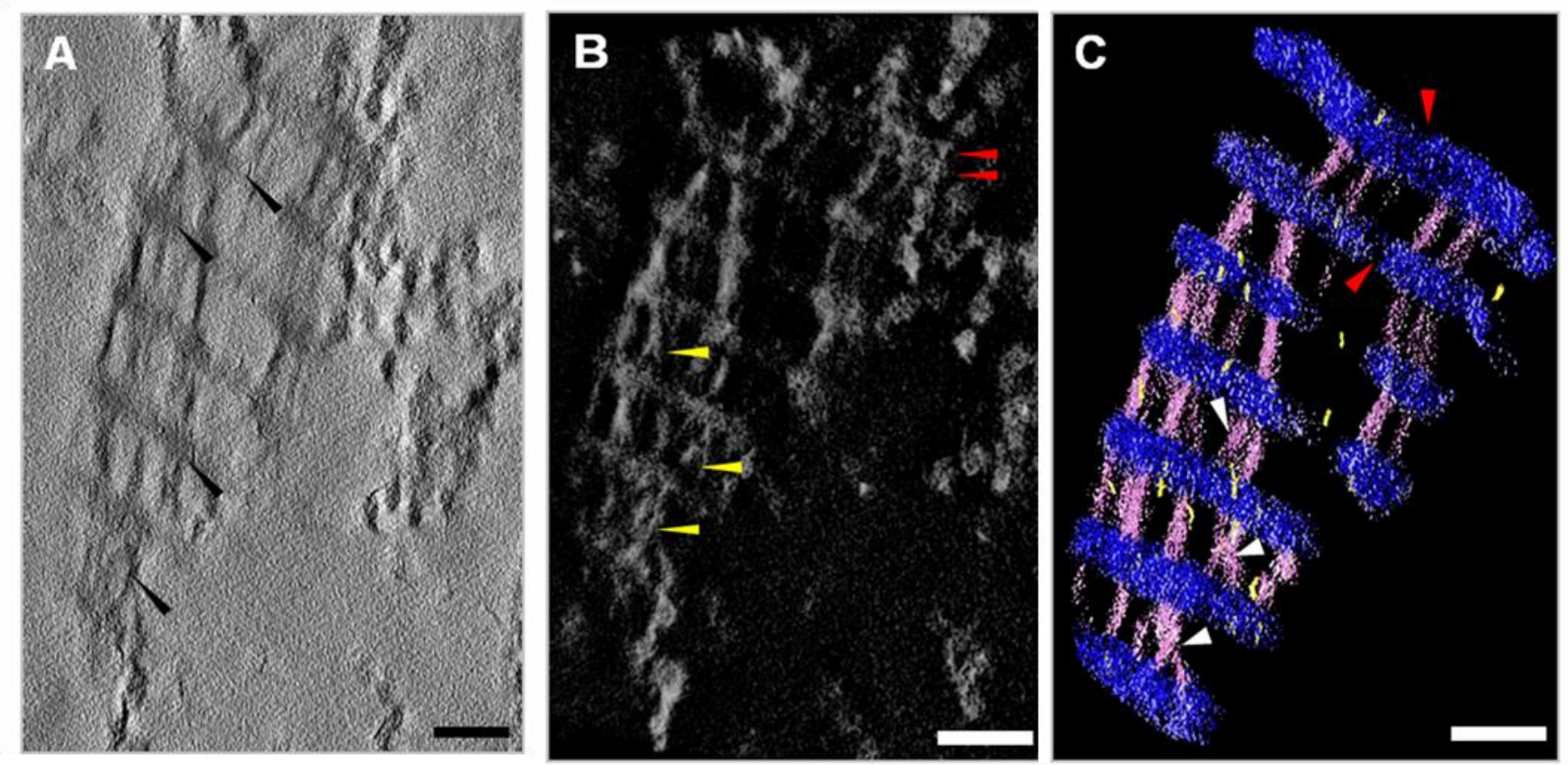

Figure 5.5: Tomographic reconstructions and segmentation of type VI collagen in the human trabecular meshwork. (A) 8.57 nm thick slice through a tomographic reconstruction of a collagen VI assembly. Arrowheads indicate proteoglycans interacting with collagen VI. **(B)** Two-dimensional surface representation of a 3D reconstruction. The 3D reconstruction has been contrast inverted and therefore the proteins are shown in white whereas the background is shown in black. The red arrowheads highlight two globular domains. The tetramer's rod-like segments (yellow arrowheads) run across the transverse bands and adopt an irregular organization (also see Supplementary video S1) **(C)** Manually segmented volume of the collagen VI assembly. The transverse bands are shown in blue, the rod-like segments of the collagen VI tetramers in pink, and proteoglycans in yellow. Proteoglycans vary in size and interact with the collagen Vl globular domains and/or the tetramer's rod-like segments (also see Supplementary video S3) Scale bar = 100 nm.

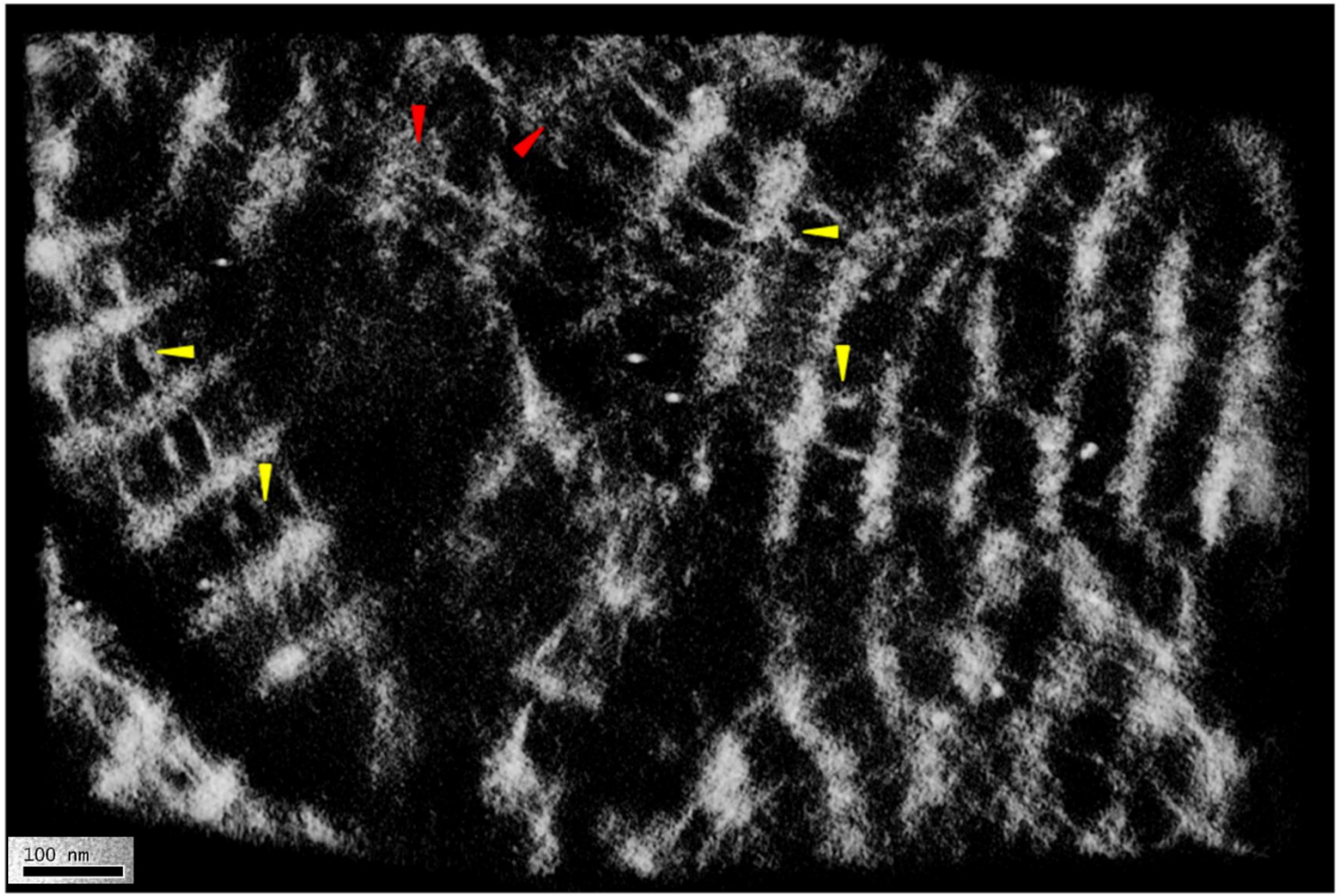

Figure 5.6: A surface representation of a 3D reconstruction of the tilted type VI collagen aggregates. A tilt series was acquired by tilting the specimen around a single tilt axis, in two degree increments over a limited tilt range (+60°,- 60°). The image stack has been contrast-inverted and therefore the proteins are shown in white whereas the background is shown in black. The red arrowheads highlight the double dark transverse bands, formed by N- and C- globular domains of type VI collagen. The collagenous triple-helices (yellow arrowheads) run nearly perpendicular to the dark bands (also see Supplementary video S2).

The tilted image sequence of type VI collagen aggregates shown in figure 5.3 and figure 5.6 (also see Supplementary video S2) was further subjected to segmentation and rendering analytical approaches using EM3D software. The final aligned three-dimensional reconstruction obtained from this data set is shown in figure 5.7. A still image captured from a single slice through a tomographic reconstruction of this data set is indicated in figure 5.7A while the reconstructed volume of the collagen VI molecules along with proteoglycans is presented in figure 5.7B also (see Supplementary video S4).

The three-dimensional reconstructions of the trabecular meshwork shown in the current study demonstrate the presence of sulfated proteoglycans filaments, which as well as populating the fibrillar matrix, also are seen to co-associate with collagen type VI assemblies (Figure 5.3, Figure 5.5, Figure 5.6 and Figure 5.7). Proteoglycans were found to associate close to the N- and C- globular domains of type VI collagen, as well as to the rod-like segments (Figure 5.5 and Figure 5.7). In addition to this, proteoglycans seemed to vary in morphology and size which is consistent with the fact that different types of proteoglycans can interact with collagen type VI aggregates, as indicated by other investigators (Sallcup et al., 1990; Bidanset et al., 1992; Acott and Kelley, 2008).

There is also some evidence of interaction between separate assemblies leading to the formation of larger collagen VI complexes, as indicated for example in figure 5.3. In general, it can be seen that the alignment between distinct assemblies within a larger complex occurs by keeping the transverse bands in axial register (Figure 5.3, Figure 5.5 and Figure 5.7).

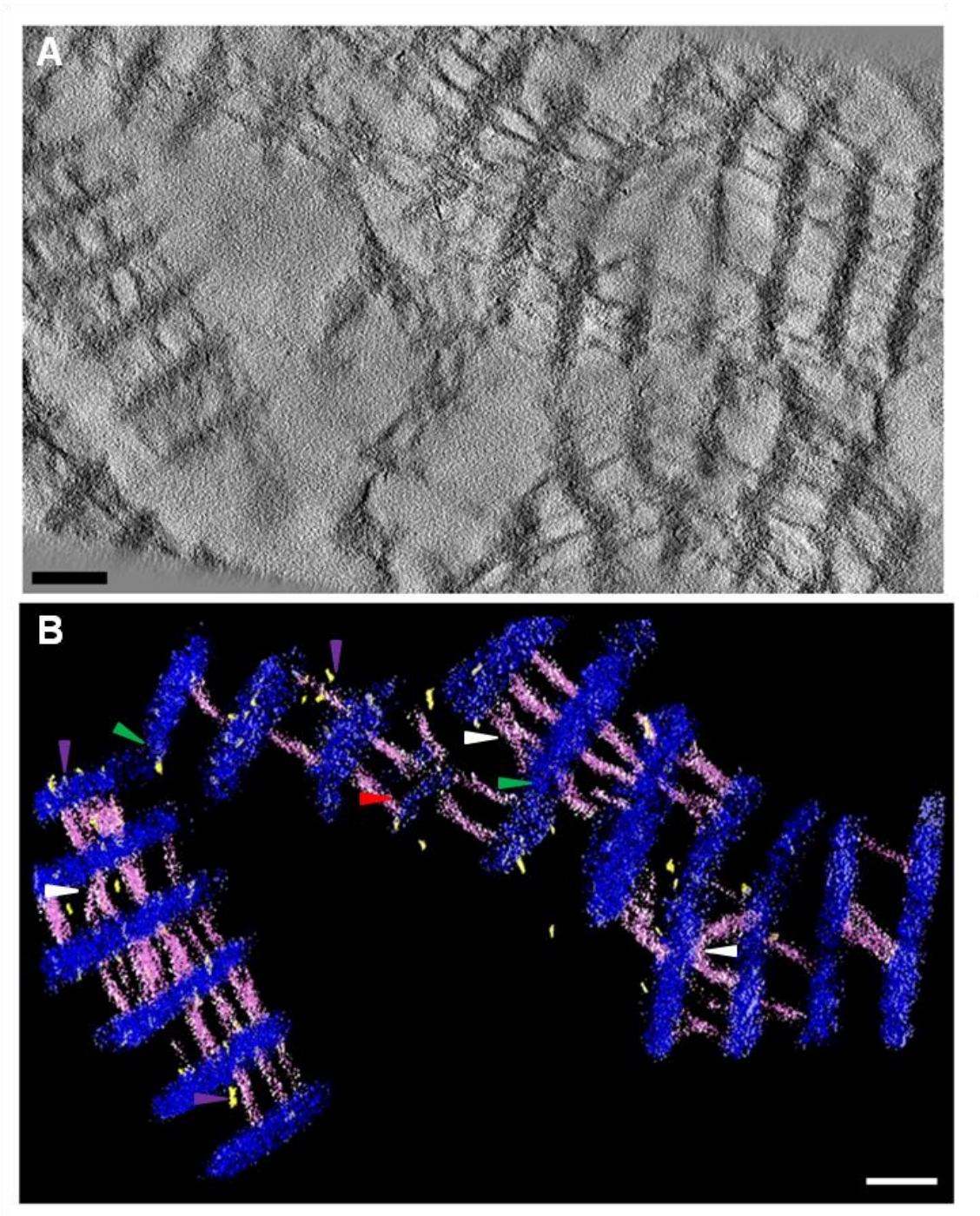

Figure 5.7: Tomographic reconstruction and segmentation of type VI collagen molecules in the human trabecular meshwork. (A) Still image from a single slice through a tomographic reconstruction. **(B)** Manually-segmented reconstructed volume of the collagen VI molecules and proteoglycans, depicted in (A). The dark transverse bands (N- and C- globular domains) are shown in blue, the collagenous triple-helices in pink, and proteoglycans in yellow. Proteoglycans vary in size and interact with the terminal globular domains and/or the triple-helices (purple arrowheads). White arrowheads point to interacting collagenous domains. Lateral associations of adjacent aggregates are indicated by the green arrowheads. A red arrowhead indicates a double band, characteristic of collagen VI (also see Supplementary video S4) Scale bar = 100 nm

5.4 Discussion

Type VI collagen can form morphologically distinct aggregates whose molecular organization appears to be related to tissue morphology and physiology (Reale et al., 2001; Linsenmayer et al., 1986; Hirano et al., 1989; Shuttleworth et al., 1992; Rittig et al., 1990; Garrone and Feeney, 1959; Leeson and Speakman, 1961). Previous workers have demonstrated that collagen type VI is a key extracellular matrix component of the trabecular meshwork (Lütjen-Drecoll et al., 1989; Marshall et al., 1991; Ueda et al., 2002). The current investigation is the first to study the architecture and association with proteoglycans of collagen type VI assemblies in the human trabecular meshwork by three-dimensional electron tomography.

The three-dimensional reconstructions obtained from this study show that collagen type VI tetramers -- identified as such from their morphology, periodicity, and the characteristic double banded structure arising from the arrangement of the globular domains -- were aggregated in a more disordered way in the trabecular meshwork, as compared to other collagen type VI-rich tissues, in which the collagen VI assemblies show an extended structural regularity (see for example Knupp et al 2000, 2002a,b, 2006). This suggests that the molecular and/or physiological environment of the trabecular meshwork matrix could interfere with the typical organization of collagen VI assemblies.

In figure 5.8a a schematic model of the collagen VI assemblies presenting two double-banded aggregates which arise from the alignment of the N- and C- globular domains of the collagen VI tetramers is shown. However, the findings from this study also revealed the presence of collagen VI assemblies presenting a single transverse band. A proposed structural model for the collagen VI assemblies presenting a single transverse band as observed in the trabecular meshwork matrix is illustrated in figure 5.8b. This particular structural model for the collagen

VI assemblies in the human trabecular meshwork is based on the interaction of collagen type VI tetramers through their globular domains. These interactions provide stability to the network of type VI collagen. Collagen VI tetramers are the building blocks in this model and they assemble together via non- covalent bonds between the N-terminal globular domains of one tetramer and the C-terminal globular domains of an adjacent tetramer. The electron dense mass of the globular domains would produce, in a different environment, two transverse bands at the position of the C- and N- terminal domains. The fact that single-banded assemblies are largely prevalent, suggests that extra material accumulates in the space between the globular domains. It is possible that one or more of the proteins present in the trabecular meshwork interact with the N- and C-terminal globular domains, or with the outer rod-like segments of the tetramers, explaining why double-banded aggregates are not always visible in the human trabecular meshwork.

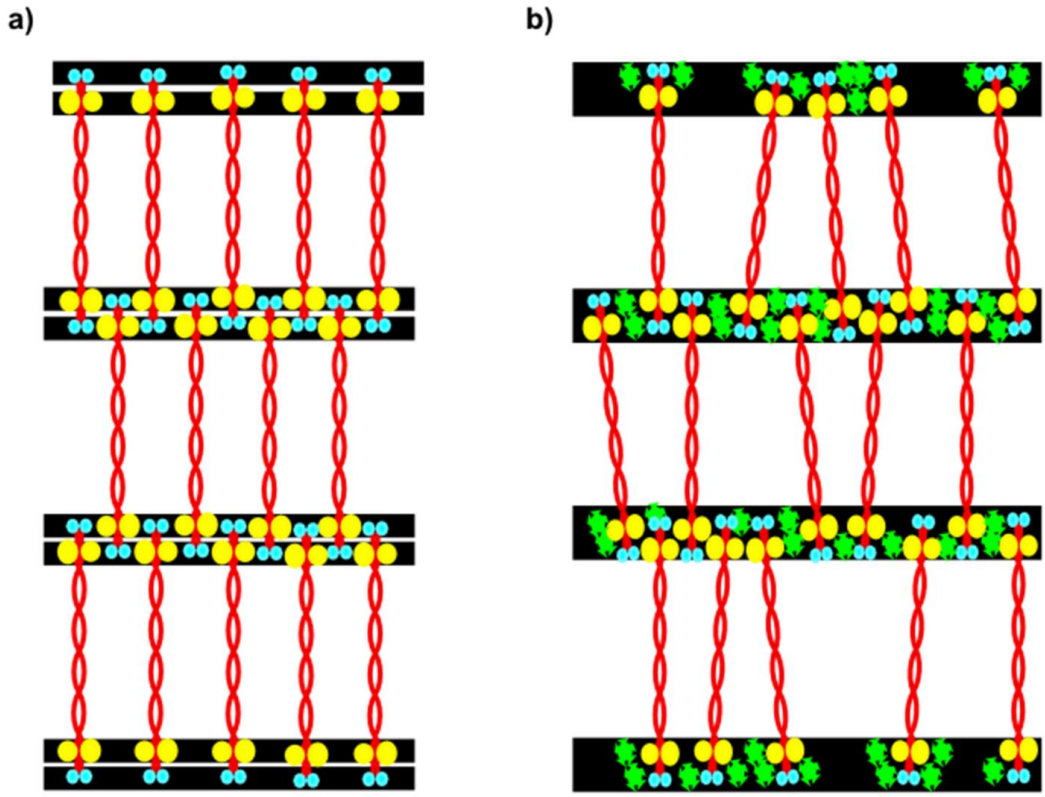

Figure 5.8: Schematic model of the collagen VI assembly found in the human trabecular sheets. N- and C- termini are depicted in blue and yellow, and the collagenous triple- helices in red. (a) Model for the double-banded aggregates arising from the alignment of the N- and C- globular domains of the collagen VI tetramers. The black rectangles highlight the position of the transverse bands as seen in the electron micrographs. (b) Model for the assemblies presenting a single transverse band. The single band arises from a double band with extra material (in green) filling the spaces between globular domains.

It is apparent from the data presented here that there is no extended lateral regularity in the arrangement of the collagen type VI tetramers, since not only is their separation variable, but so are the relative angles that the inner and outer rod-like segments of the tetramers make with the transverse bands of the assemblies. This might be an effect of the ionic microenvironment of the trabecular matrix itself. In fact, trabecular meshwork cells have the potential to manipulate the aqueous humor outflow by altering the extracellular ionic microenvironment of their matrix, modulating ECM composition, including, for example, the

size and degree of extension of meshwork proteoglycans (Gard et al., 1993). Following the principle of ionic modulation of flow resistance by the trabecular meshwork cells, a simple supposition would be that changes in the physico-chemical properties of the trabecular meshwork would also affect the interactions between the globular domains of the type VI collagen molecules. On this basis, interactions between the globular domains that hold together adjacent tetramers would be disturbed, and this would have an effect on the structural stability of collagen type VI aggregates.

A second possibility is that the structural irregularity of the collagen type VI assemblies in the human trabecular meshwork is the consequence of interactions between the N- and C-terminal domains which is somehow modulated by other factors or molecules. It should also taken into consideration that trabecular meshwork cells sense changes in mechanical stress or intraocular pressure which might trigger remodeling of the matrix in order to adjust the outflow resistance and maintain intraocular pressure homeostasis. A number of matrix proteins are often involved in reorganization of the ECM and changes in cell-matrix interactions and some of these proteins may interact with the collagen VI assemblies.

Sulfated proteoglycans have been documented previously in the human trabecular meshwork, where they interact with fibrillar collagen and are likely to contribute to aqueous outflow resistance (Tawara et al., 1989). In this study, it was noted that these negatively charged macromolecules co-associate with collagen type VI assemblies. In three-dimensions, it is clear that while the binding site for a proportion of proteoglycans is located on rod-like segments of the collagen VI tetramers, there are also some proteoglycans associated with the transverse bands where the globular domains of collagen type VI are found. The results obtained by the current study align with other studies which have shown that collagen type

VI interacts with the neuron-glial antigen 2 (NG2) chondroitin sulfate proteoglycan, a cell-surface molecule, and also with biglycan and decorin, members of the small leucine-rich repeat proteoglycan family (Sallcup et al., 1990; Bidanset et al., 1992; Acott and Kelley, 2008). The interaction of NG2 and collagen type VI is thought to be important in ECM organization, as well as in cell-matrix interactions which determine cell morphology with respect to the matrix. The possibility of multiple proteoglycan binding sites is also in line with previous investigations indicating that biglycan and decorin are localized near the N-terminal region of the triple helical domain and the following globular domain of type VI collagen tetramers (Wiberg et al., 2001).

In conclusion, the current study describes the assembly of collagen type VI in the human trabecular meshwork in three-dimensions, and its co-association with sulfated proteoglycans. No specific, regular organization of the tetramers was found and it is proposed that this is due to the tissue environment and physiology. Major ECM components, in particular, ions, electrolytes and proteins that are abundant in the trabecular meshwork are likely to be influential in modulating the assembly of collagen type VI tetramers into the aggregates found in this tissue. Furthermore, it is ostensible to propose that the new insights regarding the assembly of collagen type VI in the human trabecular meshwork might be related to a specific functional role of this molecule in the aqueous humor outflow pathway. It is likely that collagen type VI interacts with the proteoglycans in the ECM of the trabecular meshwork and stabilizes the tissue architecture.

5.4.1 Future Directions

Key areas of future investigations comprise a better characterization of the assembly of the collagen type VI in the trabecular meshwork matrix and examination of any structural

alterations in the collagen assembly in glaucomatous tissues in order to reveal the function of this molecule in the trabecular meshwork. If collagen type VI plays a role in the maintenance of the aqueous humor outflow pathway one would suspect that the collagen type VI ultrastructure and also its interaction with proteoglycans in the trabecular meshwork would be altered or even disrupted in diseased tissues.

Chapter 6: Three-dimensional aspects of the ultrastructure and outflow resistance in the human juxtacanalicular tissue

6.1. Introduction

As previously introduced in Chapter 1 there are two outflow pathways; the uveoscleral (unconventional) and the trabecular (conventional) outflow pathway. It is well known that the trabecular outflow pathway is the primary drainage outflow pathway accounting for the majority of the aqueous humor outflow. In regards to the trabecular outflow pathway, the aqueous humor passes through the trabecular meshwork, drains into Schlemm's canal and subsequently flows through the collector channels and exits the anterior chamber via the scleral veins (Goldmann, 1950; Ascher, 1954). It is well accepted that obstruction of the aqueous humor outflow pathway can be deleterious to the eye since it is very likely to cause increased IOP, which is a well-known risk factor for the development of glaucoma.

Numerous studies have investigated the trabecular outflow pathway and particular attention has been given to the study of the endothelial lining of the inner wall of Schlemm's canal and especially to the analysis of intracellular outpouchings, known as giant vacuoles (Hogan et al., 1971; Tripathi, 1972; Gong et al., 1996). It is believed that the pressure gradient associated with aqueous humor outflow, as for instance, when the aqueous humor exerts force on the endothelial lining of Schlemm's canal results to the formation of the giant vacuoles (Johnstone and Grant, 1973). Several studies have shown that a high population of these vacuoles possess openings or pores and these can be categorised as basal or apical, depending on the site of the opening (Holmberg, 1959; Speakman, 1960; Rohen, 1961; Hogan et al., 1971; Tripathi, 1972; Gong et al., 1996). More specifically, basal pores have openings into the connective

tissue of JCT whereas apical pores have openings towards the lumen of Schlemm's canal. Interestingly it has been also shown that some vacuoles have both basal and apical pores. As such, the giant vacuoles are thought to offer some kind of intracellular pathway for the drainage of aqueous humor into Schlemm's canal.

The ECM components of the trabecular meshwork also play a role in the aqueous humor outflow pathway. Collagen type VI maybe in association with proteoglycans might play a role too, as discussed in the previous chapter.

It is very important to identify the major locus within the trabecular outflow pathway that is accountable for the generation of aqueous outflow resistance both in terms of revealing the mechanism of aqueous humor outflow and for possible novel future therapeutic approaches to glaucoma. Several studies suggest that the JCT, which lies adjacent to the inner wall of Schlemm's canal and mainly consists of optically empty spaces, and connective tissue matrix on microscopical inspection, is a strong candidate for being the principal site of aqueous outflow resistance (Maepea and Bill, 1989; Maepea and Bill, 1972; Gong et al., 2002). Nevertheless, despite all of the existing knowledge on the structural aspects of the trabecular outflow pathway and the generation of outflow resistance, the definite mechanism that regulates aqueous humor outflow and thus resistance still remains to be elucidated.

To address this issue, the current study applies serial block face scanning electron microscopy, a recently advanced technique capable of generating large volume, three-dimensional reconstruction of tissue nanostructure, for the investigation of the human trabecular meshwork with a particular interest in the endothelial lining of Schlemm's canal and giant vacuoles. Additionally, this study aims to study the ultrastructure of the JCT and the

distribution of the optically empty spaces versus distance from the inner wall of Schlemm's canal, towards the trabecular meshwork.

6.2. Materials and Methods

6.2.1. Tissue Processing

Biopsies of the human trabecular meshwork were carefully dissected from an ostensibly normal eye of a 76 years old female donor, obtained from the Bristol Eye Bank. To obtain the correct region of the trabecular meshwork, the dissection was performed by our colleague from Kyoto Prefectural University of Medicine, Dr Morio Ueno, a glaucoma surgeon. There was no report of previous ocular disease. Time of death-to enucleation was 18hrs, after which the eye was held overnight and placed into 4% paraformaldehyde fixative the next morning. After dissection the tissue was fixed in 2.5% glutaraldehyde in 0.1M sodium cacodylate buffer pH 7.2-7.4 for 3h at room temperature. In order to increase the backscatter electron signal for serial block face scanning electron microscopy, tissue was infiltrated with 1% osmium tetroxide containing 1.5% potassium ferricyanide in 0.1M sodium cacodylate for 1h and 1% tannic acid for an additional hour. Specimens were then dehydrated in a graded series of ethanol (50%, 70%, 90% and twice in 100%) and afterwards embedded in Araldite CY212 resin. Experiments were conducted in accordance with the ethical principles that have their origin in the Declaration of Helsinki, and in line with the requirements of the UK Human Tissue Act.

6.2.2. Transmission electron microscopy

Following tissue embedding, tissue resin blocks were investigated by transmission electron microscopy. Initially a preliminary histological analysis was carried out by obtaining 3 µm thick

sections using an Ultracut E ultramicrotome (Reichert-Jung). Semi-thin sections were stained with 1% toluidine blue and visualised under a Leica DMRA2 light microscope (Figure 6.1). Once optimizing the plane of section and identifying a suitable area of interest, 100 nm thick sections were also cut and investigated using a transmission electron microscope (JEM 1010, JEOL, Japan) operating at 80kv. An 11-megapixel CCD camera (Orius SC1000, Gatan, Pleasanton,CA) was used to acquire the transmission electron micrographs.

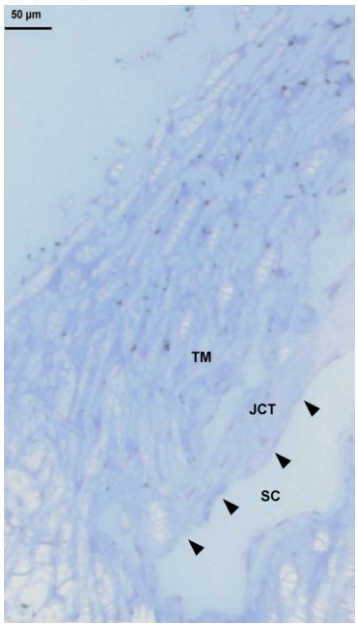

Figure 6.1: Light micrograph of the human trabecular meshwork stained with toluidine blue dye. The inner wall of Schlemm's canal (SC) is indicated by the arrowheads. The juxtacanalicular tissue (JCT) lies adjacent to the inner wall of SC and next to it the trabecular meshwork beams are found (TM). Scale bar = 50 µm.

6.2.3. Serial block face scanning electron microscopy

Serial block face scanning electron microscopy was then carried out using a FEI Quanta FEG 250 scanning electron microscope fitted with a Gatan 3View® system at the Wellcome Centre for Cell Matrix Research, Faculty of Life Science, University of Manchester, UK. These

experiments facilitated volume three-dimensional reconstruction of the human trabecular meshwork nanostructure. The principle behind serial block face scanning electron microscopy is to repeatedly image the tissue block surface after renewal of the block face by sectioning using a microtome, located inside the microscope. A scan resolution of 4,096 x 4,096 pixels^2 (Figure 6.2A) with a magnification of 27 nm/pixel was investigated in this study, entailing 500 serial backscatter electron images, 125 nm thick, that were collected at 3.8 kv, with a dwell time of 10 µsec. The total area of the inner wall of Schlemm's canal analysed in the current study was 3,170 µm^2.

6.2.4. Quantitative ultrastructural analysis

An area of 1,588 x 1,844 pixels^2 was selected (Figure 6.2B; also see Supplementary video S5) for investigation in the current study. The relationships between giant vacuoles in terms of the distribution of the vacuoles, as well as the type of pore present within a vacuole were characterised. In addition to this, the relationship between the optically empty spaces of the JCT, the volume occupied by these empty spaces against cells and extracellular matrix material versus distance from the borders of the inner wall of Schlemm's canal were also examined.

6.2.4.1 Giant vacuoles

A total of thirty-seven vacuoles were analysed in the selected area of the trabecular meshwork through the whole stack of 500 serial micrographs (62. 5 µm long). The vacuoles were counted and categorized into four distinct stages based on whether the vacuoles presented no openings, whether the vacuoles had openings towards either the JCT region or the lumen of Schlemm's canal or openings towards both JCT and Schlemm's canal. The incidence of vacuoles across the tissue from the initial point of sectioning was recorded. The

vacuoles were traced by hand in every section in which the vacuole was visible. Once manually segmented, Image J was used via the region-of-interest (ROI) manager to measure the perimeter and the area of each vacuole for every section. The maximum diameter of the pores within giant vacuoles through the sections was also calculated. When necessary, data was combined to determine the average values, SD and SE. Plots were created using Microsoft Office Excel (Microsoft Office).

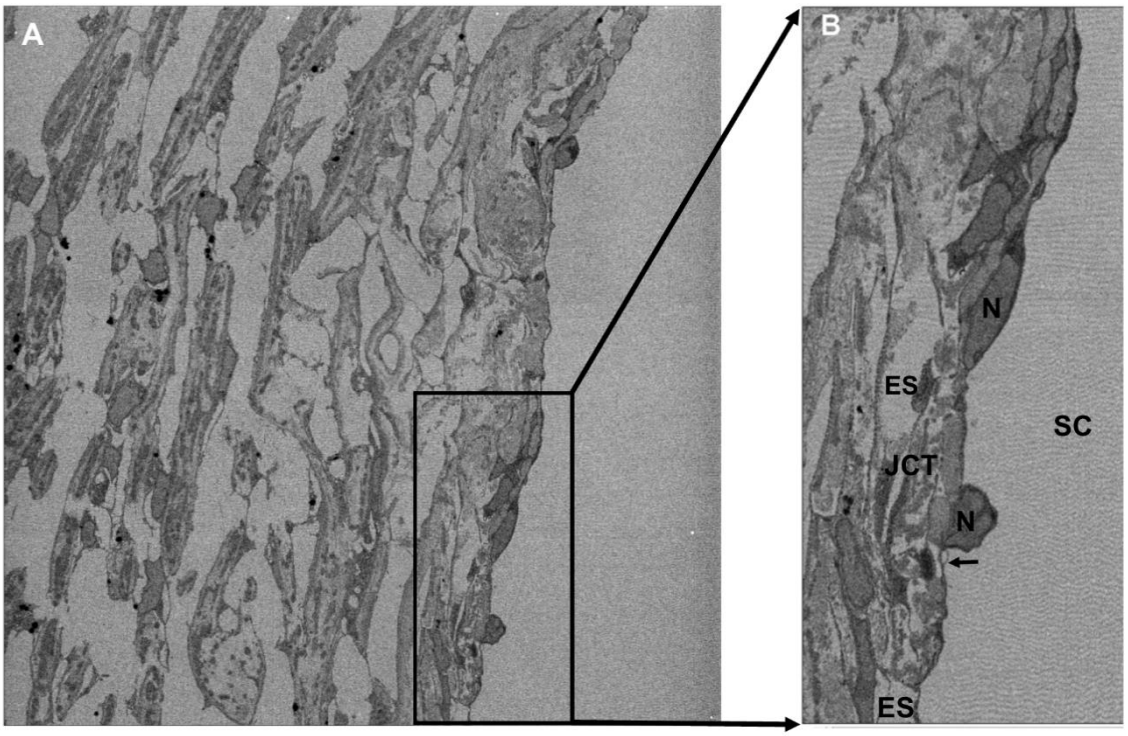

Figure 6.2: Serial block face scanning electron microscopy of the human trabecular meshwork. (A) Serial sectioning SEM was conducted in an area of 4,096 x 4,096 with a magnification equating to 27 nm/pixel and data sets of up to 500 images were acquired of the block face, renewed by substitute slicing at 125 nm. An area of 1,588 x 1,844 was selected for this study, showing in the boxed region. **(B)** An isolated view of the boxed region shown in A. Also see Supplementary video S5.

6.2.4.2 Intertrabecular spaces of JCT versus distance from the borders of Schlemm's canal

In order to aid our ultrastructure analysis with respect to the volume occupied by the optically empty spaces of the JCT against the distance from the borders of the Schlemm's canal, data was subdivided into four distinct regions as shown in Figure 6.3A. This was done to examine spatial variation along the inner wall of Schlemm's canal. For this part of this study the first 100 micrographs were excluded to benefit consistency of the quantitative analysis as the JCT region of interest was not fully visible in the first sections. It is important to note the extent of each region is actually the length along the circumferential direction of Schlemm's canal. Each region consisted of 100 micrographs, with the first region starting at a position 12.5 µm from the arbitary starting point of tissue block surface sectioning, the second one starting at 25 µm, the third one starting at 37.5 µm and the forth region starting at 50 µm. Within each of the four regions, four slices were analysed.

The borders of the inner wall of Schlemm's canal varied between the four regions and also within the four slices of each region. Therefore, the borders of Schlemm's canal were traced and adjusted by hand for every region. A macro was utilized to create six segments that had a distance of 2.7 µm, 5.4 µm, 8.1 µm, 10.8 µm, 13.5 µm and 16.2 µm from the borders of the inner wall of Schlemm's canal (Figure 6.3B). For every segment the total volume of all the electron lucent spaces was determined by manually tracing around the perimeter of each space, calculating its area and then summing the areas. This data was normalised against the area of the box in the occasional cases where the box partially exceeded the edge of the micrograph. Area measurements were converted to volumes by multiplying by the thickness of the cut section (125 nm). The volume of electron lucent space in the JCT, averaged across

all four regions examined, was then plotted as a function of distance from the inner wall of Schlemm's canal. The SD and SE were calculated and plots were created using Microsoft Office Excel (Microsoft Office).

6.2.5. Three-dimensional reconstruction

Image processing, quantitative analysis and three-dimensional reconstructions were conducted with the use of Image J software package (Schmid et al., 2010; Schneider et al., 2012). Selected sequences were presented in three dimensions using 3D Viewer plugin of Image J.

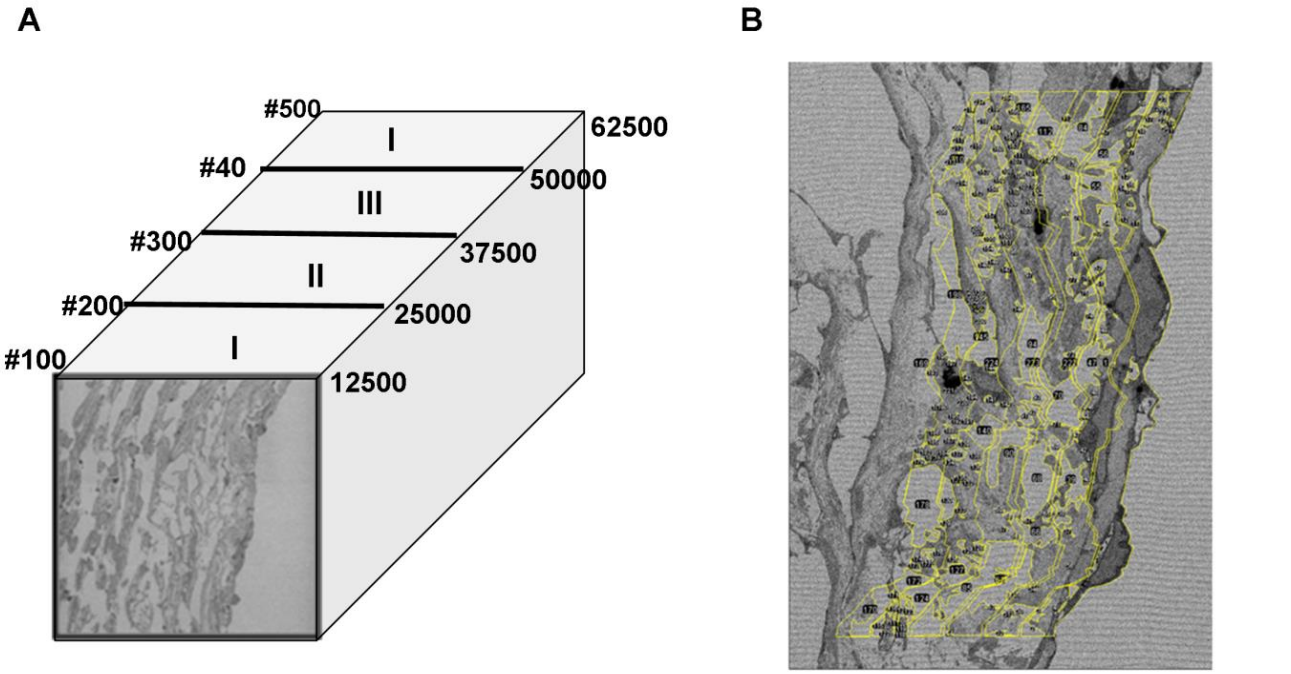

Figure 6.3: Quantitative data analysis of the optically empty spaces of the juxtacanalicular tissue (JCT). (A) For purposes of this study, data set was subdivided into four distinct regions (I, II, III, IV) starting from #100 which corresponds to a distance of 12500 nm from the block face. Each region is consisted of a 100 micrographs. **(B)** As you move through the slices of the image stack the borders of Schlemm's canal (SC) vary and therefore the borders of SC were always manually traced and adjusted within each slice within every of the four regions. A macro was then utilized to create six segments at a distance of 2700 nm, 5400 nm, 8100 nm, 10800, 13500 nm and 16200 nm from the borders of SC, respectively. The optically empty spaces within every of the six segments were manually traced, the perimeter was calculated and the percentage of the volume occupied within each segment was determined.

6.3. Results

6.3.1. Giant vacuoles

Thirty-seven vacuoles were counted and manually segmented, using Image J, on the inner wall of Schlemm's canal within an area of 1,588 x 1,844 pixels^2. The vacuoles were categorised into four distinct stages based on pore detection, as well as pore type within the vacuoles. This categorisation approach is based on the endothelial vacuolation cycle proposed by Tripathi (1972). Vacuoles were categorised into four different stages based on whether they possessed no pores (Figure 6.4A) or, in cases where they had pores, based on whether the pores were opening towards the JCT (Figure 6.4B) towards the lumen of Schlemm's canal (Figure 6.4C) or both (Figure 6.4D).

The majority of the vacuoles had no pores, followed by vacuoles which had pores opening towards both the JCT and the lumen of Schlemm's canal, followed by vacuoles with pores openings towards the JCT only, and finally by vacuoles with openings towards the lumen of the canal only (Figure 6.5).

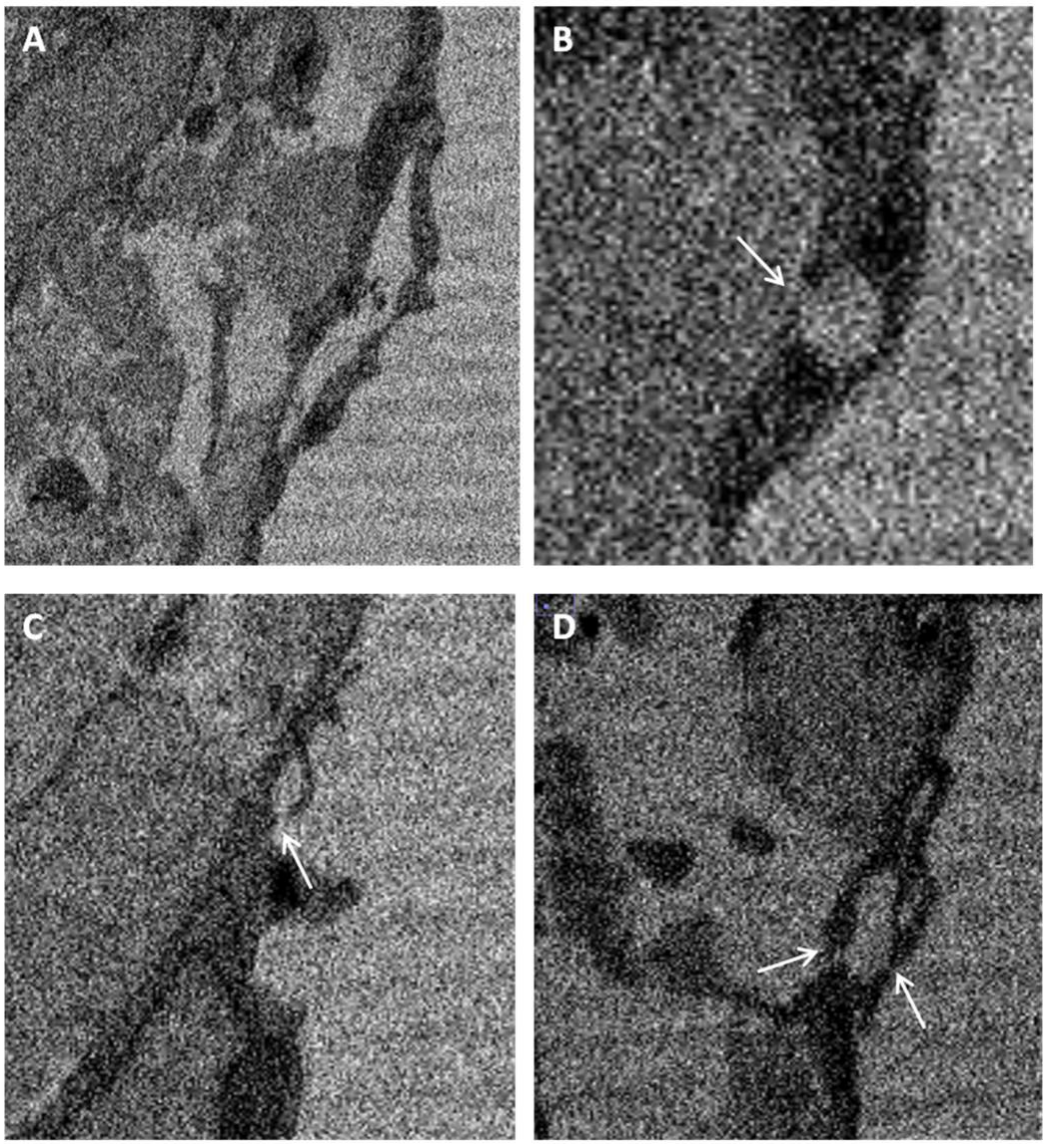

Figure 6.4: Giant vacuoles present at the endothelial cell lining of the inner wall of Schlemm's canal. (A) A portion of the vacuoles did not possess any intracellular pores. **(B)** On the other hand, some of the vacuoles had pores openings either towards the JCT aspect, **(C)** or towards the lumen of the canal **(D)** or even towards both the JCT and Schlemm's canal. White arrows indicate the apical and basal pores.

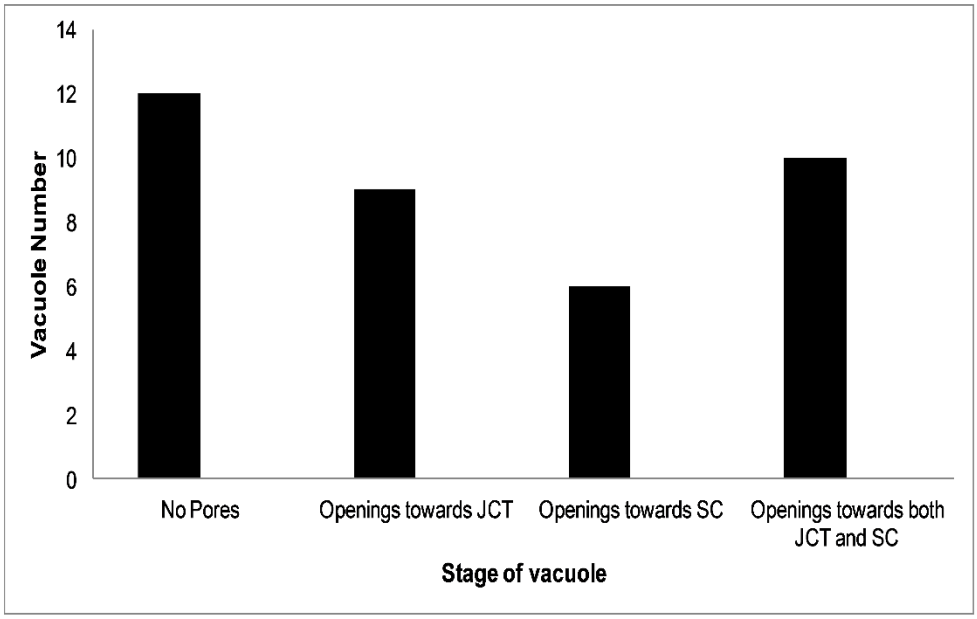

Figure 6.5: Proportion of distinct vacuole types. The number of vacuoles that possess intracellular pores either towards the JCT and/or towards the lumen of Schlemm's canal.

It is important to note that tissues studied further away from the block face represent a distance moving circumferentially around the anterior chamber of the eye. Observable differences in terms of the prevalence, as well as the quantity of the vacuoles related to each stage of the endothelial vacuolation cycle were observed through the stack. Figure 6.6 shows the spatial distribution of vacuole type (i.e with pore(s) versus without pores) at regular distances from the block face. It is clear that not only the incidence of vacuoles, in general, varies but also the number of vacuole at each stage differs. At a distance of 12.5 µm from the face block surface, we perceive the highest percentage of vacuoles with pores (83%) whereas at a distance of 25 µm and 37.5 µm we notice a percentage of 75% and 62%, respectively. Interestingly, at a distance of either 50 or 62.5 µm we observe the same percentage of vacuoles with and without any pores. The data point to a significant variation of type of

vacuole with distance around small volumes of the inner wall of Schlemm's canal following circumference of the anterior chamber.

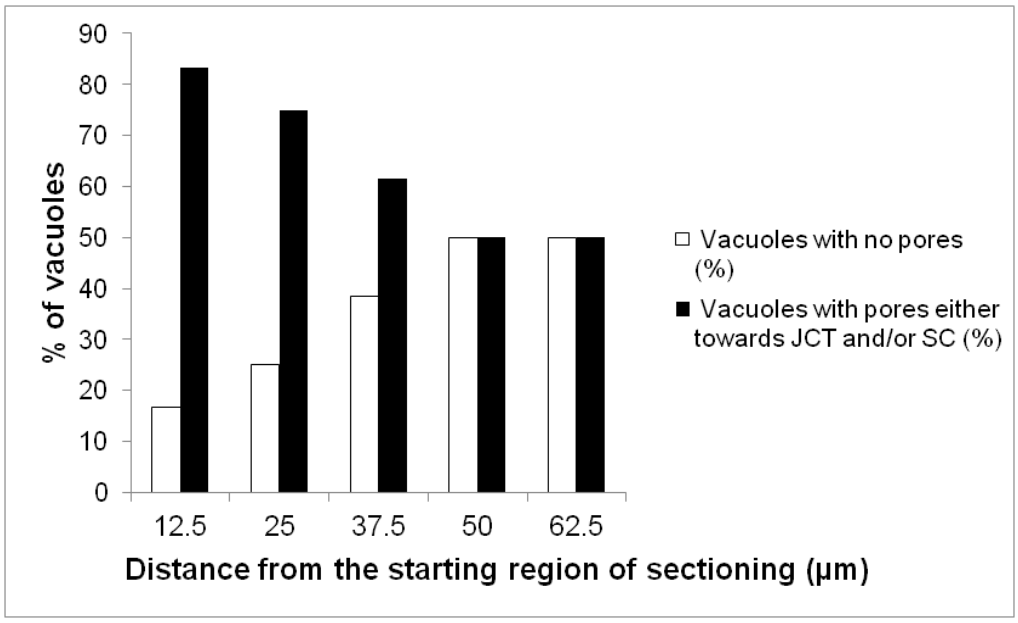

Figure 6.6: Frequency of vacuoles with apical or basal pores. The incidence of vacuoles with either no pores (white bars) or with pores opening towards the JCT and/or the lumen of Schlemm's canal (black bars), expressed as a percentage, at distinct regions of the human trabecular meshwork from the starting point of tissue sectioning and analysis.

The pore diameters of the vacuoles with apical pores opening to Schlemm's canal and basal pores opening to the JCT was also measured and the results are presented in figure 6.7. The vacuoles with pores opening towards the lumen of Schlemm's canal presented the smallest pores with an average pore diameter of 236 ± 67 nm (n=6), compared to the size of the pores of the other vacuoles at different stages. The average pore diameter of the vacuoles which opened towards the JCT was 485 ± 75 nm (n=9). The average pore diameter of the vacuoles with pores opening towards both JCT and Schlemm's canal was noted to be the biggest than the average pore diameter of the vacuoles existing at a different stage, with an average pore diameter of 554 ± 94 and 533 ± 109 (n=10), respectively. Intriguingly, the pore size at this

stage of the vacuolation cycle is very similar, no matter the region in which the pore is opening.

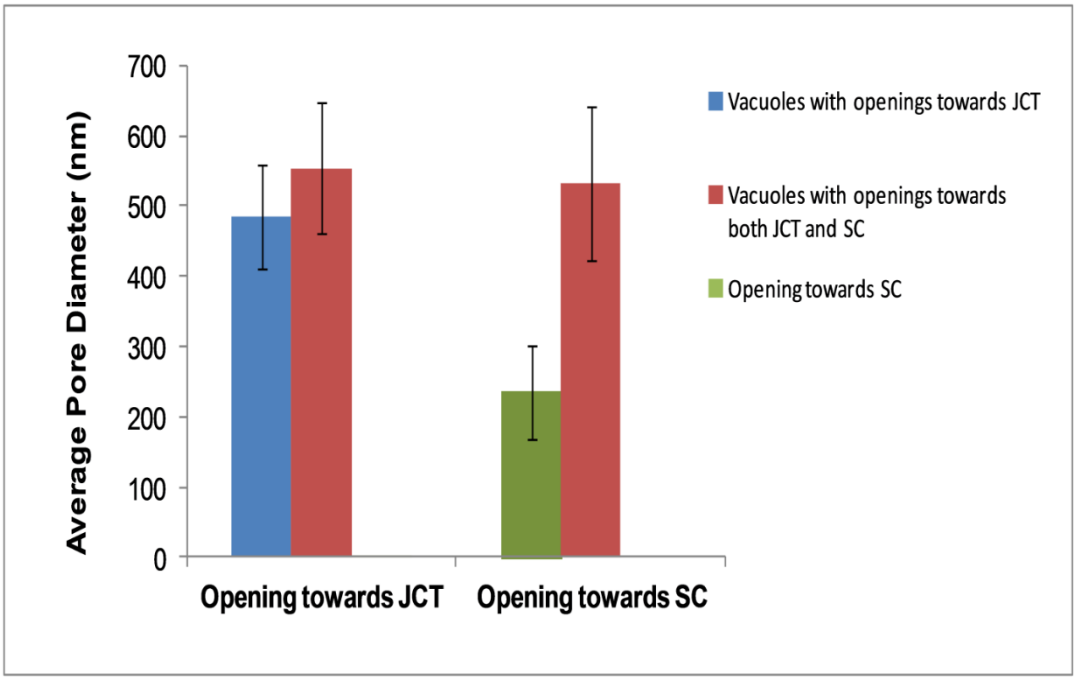

Figure 6.7: Pore diameter of the vacuoles with basal and/or apical pores. The average pore diameter of giant vacuoles possessing pores that either open towards the JCT (blue) or towards the lumen of Schlemm's canal (SC, green) or that possess pores openings to both JCT and Schlemm's canal (red). Error bars represent the standard deviation.

6.3.2. Ultrastructural analysis of the JCT

High resolution analysis of the ultrastructure of the JCT, located adjacent to the inner wall of Schlemm's canal was achieved by serial block face scanning electron microscopy. This allowed us to conclude that there is no homogeneity in the structure of the JCT. Notable, qualitative structural differences could be observed between the thickness of the JCT and the distance from the inner wall of Schlemm's canal towards the trabecular meshwork beams. These structural differences include differences in the proportion of the electron lucent spaces

versus the combined proportion of the trabecular cells and extracellular matrix components, such as for example, collagen and elastic fibres.

Subsequently, quantitative analysis was performed to investigate the relationship between the volume occupied by the electron lucent spaces and the distance from the inner wall of Schlemm's canal. The image stack was subdivided into four distinct regions (I, II, III, IV) corresponding to different regions of tissue from the inner wall of Schlemm's canal outwardly into the JCT. These distances were chosen as 12.5 µm, 25 µm, 37.5 µm and 50 µm, respectively. Each region constitutes of 100 serial slices, 125 nm thick. We assessed the volume occupied by the electron lucent spaces of the JCT by exploring four slices within each of the four regions. This slice analysis approach involves the subdivision of each slice within six segments in order to address the volume of the electron lucent spaces opposed to various distances extending from the inner wall of Schlemm's canal and across the JCT thickness. In this manner, we achieved a standard range of distances across JCT thickness, starting from 2.7 µm to 16.2 µm. Figure 6.8 represents example of the data obtained from one slice from each of the four regions, depicting the six segments used to measure the volume occupied by the electron lucent spaces as a function of tissue depth (i.e. distance from the inner wall of Schlemm's canal).

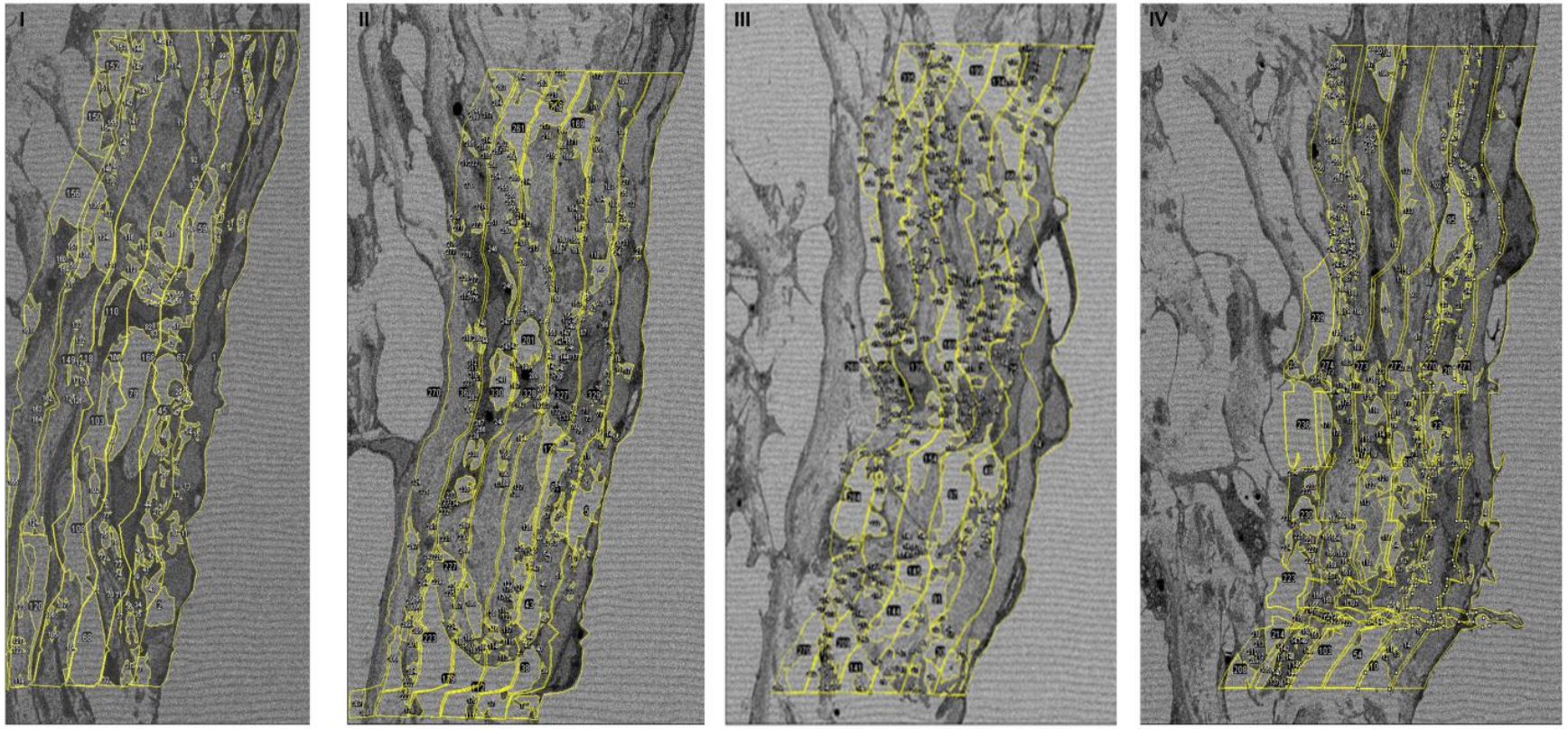

Figure 6.8: Screenshots of each of the four distinct data set regions I, II, III, and IV. Quantitative image analysis of the optically empty spaces of the human JCT was performed for four images per data set region. The inner wall of SC for each image analysed within each data set region was manually segmented and with the use of a macro six identical segments were created at a distance of 2.7 µm, 5.4 µm, 8.1 µm, 10.8 µm, 13.5 µm and 16.2 µm from the borders of SC, respectively. The optically empty spaces were also manually traced and designated as distinct regions-of-interest. Image J provided all the necessary measurements needed for our quantitative analysis.

Measurements of the proportional volume of electron lucent space in the JCT as a function of distance from the inner wall of Schlemm's canal revealed that there is a common pattern of the volume occupied by the empty spaces against matrix material as a function of the distance from the borders of Schlemm's canal. Thus, measurements from each of the six segments per slice per stack region (see Appendix 1) were combined to determine the average values and standard error. Analysis of the average measurements obtained by the four stack regions of the JCT that were derived at either 2.7 µm, 5.4 µm, 8.1 µm, 10.8 µm, 13.5 µm, or 16.2 µm from the block face (Figure 6.9) revealed that the volume occupied by the electron lucent spaces as opposed to matrix material resembles within the first 2.7 µm from the inner wall of Schlemm's canal was less than in the regions farther away from the canal. Moving further away from the border of Schlemm's canal- i.e. at a distance of 5.4 µm, there is a clear increase in the quantity and thus the volume occupied by the empty spaces (26 ± 2%) compared to 7 ± 1% closer to Schlemm's canal. Thereafter the electron lucent volume fluctuates between approximately 25% and 35% of whole tissue volume up to a distance of over 16 µm from the inner wall of Schlemm's canal. Given that the JCT is estimated to be between 2 µm and 20 µm thick in humans, data are representative of the majority of the JCT's thickness.

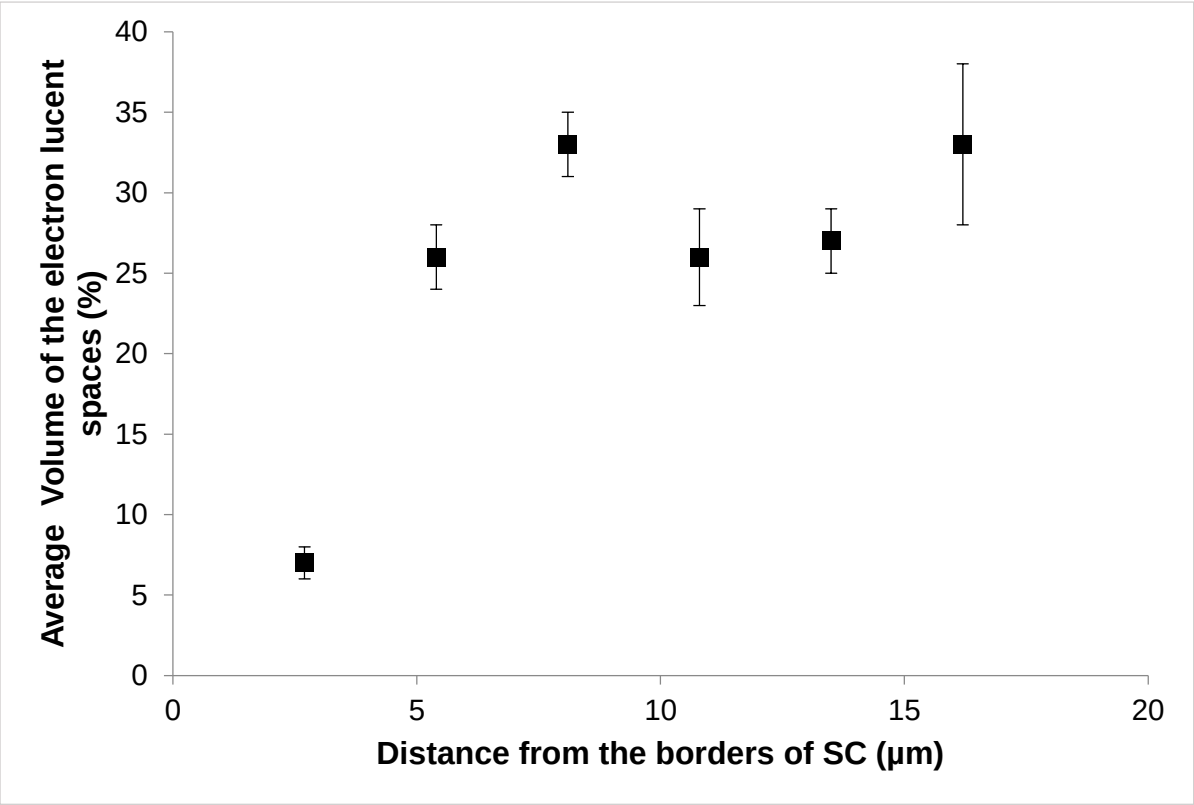

Figure 6.9: Volume contained by the electron lucent spaces of the JCT. The average volume, expressed as a percentage, occupied by the optically empty spaces of the JCT against various distances from the borders of the inner wall of Schlemm's canal (SC). Values obtained for every data set region for every segment of were averaged. Error bars represent the standard error of the average values.

6.4 Discussion

Serial block face scanning electron microscopy allows the study of three-dimensional ultrastructure of large volumes at high resolution. This study has employed this approach for the visualisation and investigation of the human trabecular meshwork, a sponge-like tissue that plays a fundamental role in the trabecular, also known as conventional, aqueous humor outflow pathway, in order to get a better understanding of the ultrastructure of this highly important tissue, as well as to shed light on possible hydrodynamic mechanisms accountable for the generation and regulation of the aqueous humor outflow resistance. The first part of

this study investigated the ultrastructure of the giant vacuoles which are cellular outpouchings, formed by the endothelial cell lining of the inner wall of Schlemm's canal. The second part of this study focused on the JCT, the tissue located between the trabecular meshwork and the inner wall of Schlemm's canal.

6.4.1 Giant vacuoles

The large volume three-dimensional reconstructions, at high resolution, of the human trabecular meshwork obtained from the present study clearly revealed the presence of the giant vacuoles along the inner wall of Schlemm's canal. Thirty-seven giant vacuoles were identified in the area under investigation through the whole stack of 500 serial micrographs, each 125 nm thick and 62.5 µm long. Some vacuoles had openings or pores towards either the connective tissue matrix of the JCT (basal pores) or towards the lumen of Schlemm's canal (apical pores) (Figure 6.4). More interestingly, some vacuoles appeared to possess both basal and apical pores. Some had none.

These findings accord with previous research into the study of the inner wall of Schlemm's canal and the endothelial cell layer that lines the border of the wall. Early studies showed that the endothelial cells of the inner wall of Schlemm's canal in response to the pressure gradient associated with aqueous humor outflow form intracellular outpouchings, called giant vacuoles (Hogan et al., 1971; Johnstone and Grant, 1973; Tripathi, 1972; Gong et al., 1996). It has been shown that the shape and size of the giant vacuoles varies (Tripathi, 1972) and this was also observed in the current study. Moreover, it was previously noted that the majority of the giant vacuoles form intracellular pores that have openings into the JCT and that a small population of giant vacuoles possess pores with openings on the Schlemm's canal luminal aspect as well (Holmberg, 1959; Speakman, 1960; Rohen, 1961; Hogan et al., 1971; Tripathi,

1972; Gong et al., 1996). It has additionally reported that some of these vacuoles possess both basal and apical pores. The findings from these studies led to the hypothesis that these vacuoles serve as intracellular channels that aid the drainage of the aqueous humor from the JCT towards the lumen of Schlemm's canal.

Whilst, previous investigators have reported that the majority of the vacuoles have basal openings, followed by less numerous vacuoles with apical openings, and a small number of vacuoles have both basal and apical pores, this study was unable to demonstrate this. In particular, amongst the vacuoles examined here, the majority had no pores followed by those that had both basal and apical pores (Figure 6.5). Subsequently, the vacuoles were categorised into four distinct classes based on pore detection, as well as pore type within the vacuoles. The vacuole volume was estimated and compared between the different vacuole categories.

Investigation of the prevalence, as well as the quantity of the different types of vacuoles at distinct regions of the inner wall of Schlemm's canal highlighted heterogeneity in the distribution of the different types of vacuoles along different areas of Schlemm's canal (Figure 6.6). Some regions of the inner wall of Schlemm's canal were found to be highly populated in vacuoles that had pores either opening towards the JCT and/or the lumen of the canal. On the other hand, it was found that there are also some areas of Schlemm's canal that seemed to be equally populated with the various vacuole types, with or without pores. The variation in the vacuole type distribution between different regions of the inner wall of Schlemm's canal may be explained by recent findings that support the fact that there are preferential aqueous humor drainage outflow routes (Hann and Fautsch, 2009). Thus, it is ostensible to propose that the areas that were shown to be highly populated in vacuoles that possess basal

and/or apical pores, opposed to the ones with no pores represent preferential aqueous humor outflow pathways.

This study also carried out a further investigation into the pores formed by the giant vacuoles of the endothelial cell layer of the inner wall of Schlemm's canal. To be more precise, the average pore diameter of the vacuoles with basal and/or apical pores was determined (Figure 6.7). It is interesting to note that the average pore diameter for the different types of vacuoles estimated here is smaller from previous investigations that reported that the pores have dimensions which range between 0.3 to 2 μm in diameter (Hogan et al., 1971; Tripathi, 1972; Gong et al., 1996).

Probably the most interesting finding from this specific part of the current investigation was the actual occurrence of the giant vacuoles in a non-perfused human donor eye. As discussed avove, it is widely accepted that the vacuoles are formed as a result of the pressure gradient generated with aqueous humor outflow and one would not expect to see their formation in a non-perfused human donor eye. However, taking into consideration that the moment the donor eye was dissected it automatically caused some stress and pressure might explain these findings, and thus the presence of the vacuoles along the inner wall of Schlemm's canal. Alternatively, it is possible that vacuoles remain at ambient pressures for many hours post-mortem.

6.4.2 Ultrastructural analysis of the JCT

This study also examined the ultrastructure of the JCT, with a particular interest on investigating the distribution of the electron lucent spaces versus distance from the inner wall

of Schlemm's canal, towards the trabecular meshwork. This was done in an attempt to better understand the aqueous humor outflow mechanism.

As discussed above, a number of studies support the conclusion that the principal site of normal outflow resistance and increased outflow resistance, in glaucoma cases, resides in the JCT and the inner wall endothelium along with its basement membrane. As such, it is strongly believed amongst the scientific community that the mechanism of outflow resistance underlines a coupled action of the JCT, the inner wall endothelium of Schlemm's canal and its basement membrane.

Johnson and co-workers, 1992 first proposed the so-called "funneling model" of outflow resistance (Johnson et al., 1992). Taking into consideration the formation of transecullar pores by the giant vacuoles of the inner wall endothelium of Schlemm's canal aligned to the appearance of paracellular pores along the wall of the canal, as well as the work by Hamanaka and Bill (1987, 1988) who showed ruptures of the inner wall endothelium upon perfusion with a chelating agent or a proteolytic enzyme, they calculated the outflow resistance generated by the JCT examining the potential of a synergistic action between the JCT and the inner wall of Schlemm's canal (Johnson et al., 1992; Hamanaka and Bill, 1987; Hamanaka and Bill, 1988). Unlike any previous theoretical studies, their work was conducted under the assumption that the JCT is a homogeneously distributed porous material upstream of a low porosity filter (i.e. the inner wall of Schlemm's canal). Their results showed that the pores of the inner wall force a funneling mechanism by directing fluid flow through those regions of the JCT that are located nearest to the inner wall pores (Figure 6.10). As a result, the available area for fluid drainage is reduced leading to an increased effective outflow resistance. The fundamental feature of the funneling model is that the resistance of the JCT and the inner wall when

coupled together is greater than the sum of the resistance of these tissues when estimated separately. It is important to mention that the funneling model proposed by Johnston et al., 1992 takes place under certain circumstances. These circumstances enclose that the pores of the inner wall endothelium are static open structures, that the permeability of JCT is homogeneous and at last that the size and distribution of the pores is uniform along the inner wall of Schlemm's canal.

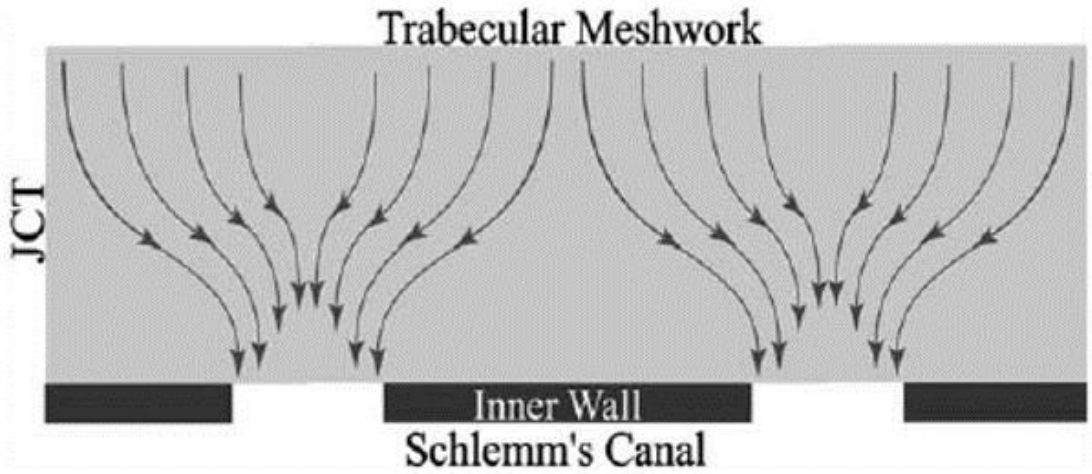

Figure 6.10: The "funnelling model". Schematic diagram of the funnelling aqueous humor outflow through the pores and vacuoles of the inner wall endothelium of SC. Adapted from Johnson, 2006.

Even though some studies are in disagreement with the funneling model as they did not find any correlation between outflow facility and pore density (Sit et al., 1997; Ethier and Coloma, 1999), other studies support the funneling hypothesis as they have showed a decrease in the number of pores in glaucomatous eyes as opposed to normal eyes (Allingham, 1992; Johnson et al., 2002). This suggests that the increased outflow resistance observed in glaucomatous eyes might be caused by pore funneling. Supplementary support for the funneling model comes from two studies investigating the washout effect -- the gradual decrease in flow resistance that follows prolonged perfusion (Bárány, 1953; Yan et al., 1991; Van Buskirk and Brett, 1978) -- and showed that washout is the result of separation of the JCT from the inner wall of Schlemm's canal (Overby et al., 2002; Scot et al., 2007).

The funneling hypothesis emphasises the importance of the connectivity between the JCT and the inner wall of Schlemm's canal in the regulation of outflow resistance. Moreover, the importance of cell-matrix and matrix-matrix interactions and adhesions are also highlighted and their role in the maintenance of outflow resistance. Elimination of the funneling model through a loss of the connectivity between the two structures would result to a uniform aqueous humor drainage, an increase in outflow facility and subsequently a decrease in the outflow resistance.

The outcome of the research presented here is appealing since it was notable that there is variation in the average volume occupied by the electron lucent spaces in regions at distinct distances from the inner wall of Schlemm's canal (Figure 6.9). More specifically, it was found that at a distance of 2.7 μm from the inner wall of Schlemm's canal less electron lucent spaces are present compared to other regions that are further away from the canal. In 2000, Parc and colleagues investigated whether there are any differences in the proportion of optically

empty spaces in areas with and without vacuoles and what they found was that there was no difference between areas with vacuoles and areas without vacuoles (Parc et al., 2000).

Taking into account these findings, a proposed model of the aqueous humor outflow through the JCT towards the lumen of Schlemm's canal has been developed (Figure 6.11). The proposed model illustrates that the variation in the volume of the electron lucent spaces within the JCT aids the establishment of a funnelled aqueous humor flow. The fact that the JCT region closest to the inner wall of Schlemm's canal (at a distance of 2.7 μm) is almost depleted by optically empty spaces in contrast to cellular and ECM components further away from the wall of Schlemm's canal suggests this particular ultrastructure may provide a supportive barrier preventing collapse of Schlemm's canal by uncontrolled aqueous humor flow. Additionally, the proposed aqueous humor outflow model corroborates the findings of a great deal of the previous work in this field investigating the mechanism of aqueous humor outflow and the funnelling model of outflow resistance, first proposed by Johnson and co-workers in 1992 (Johnson et al., 1992). However, as mentioned above, the funneling model proposed by Johnson and colleagues was proposed under the assumption that the permeability of JCT is homogeneous and that the size and distribution of the pores is uniform along the inner wall of Schlemm's canal. On the contrary, despite the fact that in this study it is proposed that the aqueous humor flow is funneled through the JCT into Schlemm's canal, it does not support that the permeability of JCT is homogeneous neither that the size and distribution of the pores is uniform along the inner wall of Schlemm's canal.

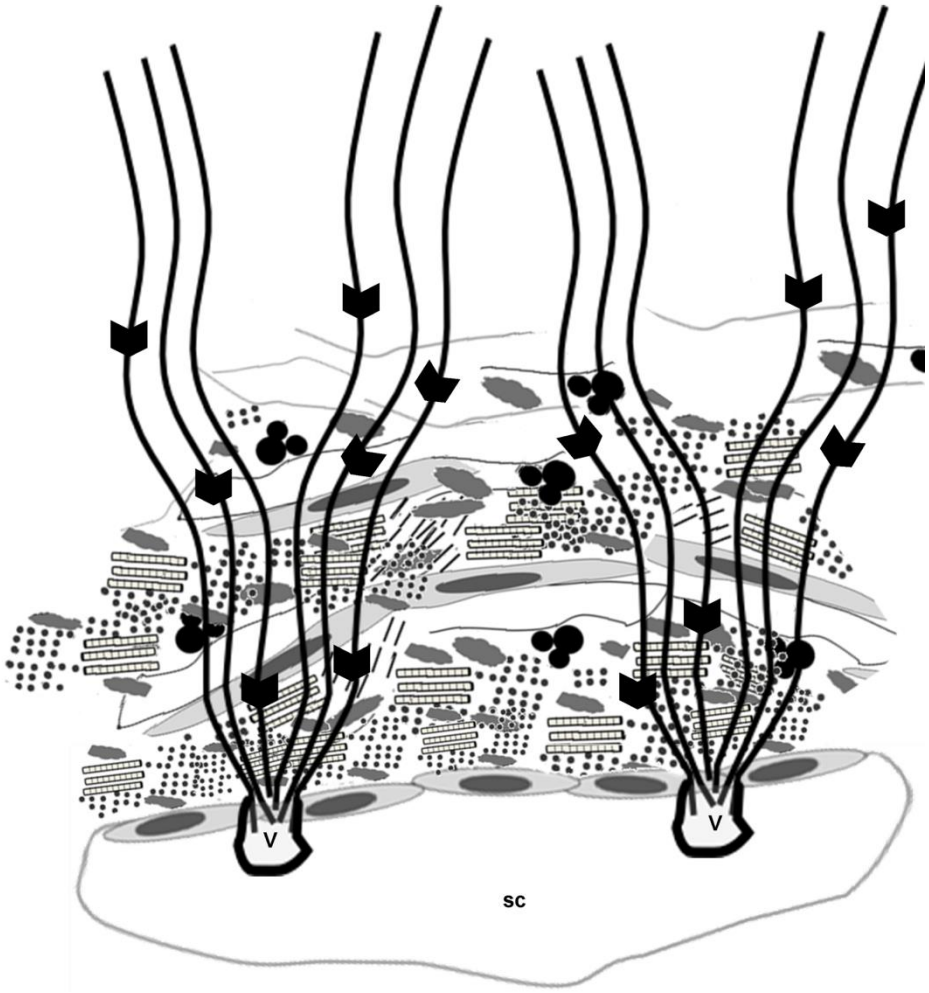

Figure 6.11: Proposed model of the aqueous humor outflow via the JCT into Schlemm's canal. Aqueous humor is funneled through the JCT based on the distinct distribution of optically empty spaces and the cellular and ECM components across the depth of the tissue.

6.4.3 Future Directions

Further research should be carried out to enhance our understanding of segmental aqueous humor outflow towards the lumen of Schlemm's canal through the JCT and assess how it is associated with outflow resistance generation. Serial block face scanning electron microscopy is a powerful technique and should be used for the investigation of additional areas of the JCT

and the inner wall, despite that data analysis requires a lot amount of time the results will be very rewarding.

In future investigations it might be possible to perfuse the donor eyes at a constant pressure prior examination of the aqueous humor outflow and visualisation under serial block face scanning electron microscopy. Eyes perfusion will definitely be advantageous for a better assessment of the vacuole structure and function.

It will also be highly also beneficial to investigate whether there is any relation in the amount of the electron lucent spaces in the JCT between preferential aqueous humor outflow routes and non-preferential regions. Are there are any variations in the ultrastructure of the JCT? In addition to this, glaucomatous eyes should be studied as well and explore any differences in the ultrastructure of the JCT and the inner wall of Schlemm's canal.

As previously mentioned in Chapter 5, collagen type VI is one of the major components of the ECM of the trabecular meshwork (Lütjen-Drecoll et al., 1989; Tripathy et al., 1994; Dietlein et al., 1998). It is plausible to suggest that the distribution of collagen type VI within the trabecular meshwork in association with sulphated proteoglycans might also influence the aqueous humor outflow pathway. Recalling that the distribution of the sulphated glycosaminoglycans across the cornea is not homogeneous in order to aid the hydrophilic corneal stroma, it will be very interesting for future studies to examine the distribution of collagen VI-proteoglycans in the human trabecular meshwork and elucidate whether collagen VI-proteoglycans exhibit a uniform distribution across tissue's depth or not.

There are definitely numerous research questions that are needed to be answered before we truly establish the aqueous humor outflow pathway and subsequently identify what is the main factor that leads to glaucomatous eye damage.

References

Acott, T.S., Kelley, M.J. 2008. Extracellular matrix in the trabecular meshwork. *Exp Eye Res.* 86, 543-561

Allingham, R.R.,et al., 1992. The relationship between pore density and outflow facility in human eyes. *Invest Ophthalmol Vis Sci.* 33, 1661-1669

Anseth, A., 1961. Glycosaminoglycans in the developing corneal stroma. *Exp Eye Res.* 1, 116-121

Anseth, A., Fransson, L., 1969. Studies on corneal polysaccharides. VI. Isolation of dermatan sulfate from corneal scar tissue. Exp Eye Res. 8, 302- 309

Anunziata, O.A., et al., 2011. XANES-PCA analysis of Ti- species in MCM-41 mesoporous silica synthesized by different method. *Appl Catal A,* 397, 22-26

Ascher, K.W., 1954. Veins of the aqueous humor in glaucoma. *Boll Ocul*. 33, 129-144

Ayad, S., 1994. The extracellular matrix facts book. *Academic Press*, London, UK

Bairaktaris, G., et al., 1998. An ultrastructural investigation into proteoglycan distribution in human corneas. *Cornea*. 17,396–402

Baldock, A., et al. 2003. The supramolecular organization of collagen VI microfibrils. *Journal of Mol Biol.* 330, 297-307

Bárány, E.H., 1953. In vitro studies of the resistance to flow through the angle of the anterior chamber. *Acta Soc Med Ups.* 59, 260-276

Bárány, E.H., Scotchbrook, S., 1954. Influence of testicular hyaluronidase on the resistance to flow through the angle of the anterior chamber. *Acta Physiol Scand.* 30, 240-248

Barrett, R., et al. 2000. Current status of the scanning X-ray microscope at the ESRF. *AIP conference proceedings.* 507**,** 458-463

Baud, C.A., Balvoine, C., 1953. The intimate structure of Descement's membrane and its pathological derivatives. *Br J Ophthalmol.* 126, 290-294

Baumeister, W., 2002. Electron tomography: towards visualizing the molecular organization of the cytoplasm. *Curr Opin Struct Biol.* 12, 679–684

Beales, M.P., et al., 1999. Proteoglycan synthesis by bovine keratocytes and corneal fibroblasts: maintenance of the keratocyte phenotype in culture. *Invest Ophthalmol Vis Sci.* **40,** 1658–1663

Beauchemin, S., et al., 2002. Principal component analysis approach for modeling sulfur K-XANES spectra of humic acids. *Soil Sci Soc Am J.* 66, 83-91

Benedek, G.B., 1971. Theory and transparency of the eye. *Appl Opt.* 10, 459-473

Bethlem, J., Wijngaarden, G.K., 1976. Benign myopathy, with autosomal dominant inheritance. A report on three pedigrees. *Brain.* 99, 91-100

Bettelheim, F. A., Ehrlich, S. H., 1963. Water vapor sorption of mucopolysaccharides. *J Phys Chem*. 67, 1948-1953

Bettelheim, F.A., Goetz, D., 1976. Distribution of hexosamines in bovine cornea. *Invest Ophthalmol Vis Sci.* 15, 301-304

Bettelheim, F.A., Plessy, B., 1975. The hydration of proteoglycans of bovine cornea. *Biochim Biophys Acta.* 381, 203-214

Bidanset, D.J., et al., 1992. Binding of the proteoglycan decorin to collagen type VI. *J Biol Chem.* 267, 5250-5256

Bill A., Phillips CI., 1971. Uveoscleral drainage of aqueous humour in human eyes. *Exp Eye Res*. 12, 275-281

Bill, A., 1965. The aqueous humor drainage mechanism in the cynomolgus monkey (Macaca irus) with evidence for unconventional routes. *Invest Ophthalmol.* 4, 911-919

Bill, A., 1966a. Conventional and uveo-scleral drainage of aqueous humour in the cynomolgus monkey (Macaca irus) at normal and high intraocular pressures. *Exp Eye Res.* 5, 45-54

Bill, A., 1966b. The routes for bulk drainage of aqueous humour in the vervet monkey (Cercopithecus ethiops). *Exp Eye Res.* 5, 55-57

Bill, A., 1975. Blood circulation and fluid dynamics in the eye. *Physiol Rev.* 55, 383-417

Bill, A., et al., 1980. Effects of intracameral NA_2EDTA and EGTA on aqueous outflow routes in the monkey eye. *Invest Ophthalmol Vis Sci*. 19, 492-504

Bill, A., Hellsing, K., 1965. Production and drainage of aqueous humor in the cynomolgus monkey (Macaca irus). *Invest Ophthalmol.* 4, 920-926

Bill, A., Maepea, O., 1994. Mechanisms and routes of aqueous humor drainage. In *Principles and Practices of Ophthalmology* Philadelphia. W B Saunders, DM Albert, FA Jakotiec, pp. 206-226

Bill, A., Svedbergh, B., 1972. Scanning electron microscopic studies of the trabecular meshwork and the canal of Schlemm – an attempt to localize the main resistance to outflow of aqueous humour in man. *Acta Ophthalmol.* 50, 295-320

Birk, D.E., et al., 1986. Organization of collagen Types I and V in the embryonic chicken cornea. *Invest Ophthalmol Vis Sci.* 27, 1470–1477

Birk, D.E., et al., 1988. Collagen type I and type V are present in the same fibril in the avian corneal stroma. *J Cell Biol.* 106, 999-1008

Birk, D.E., et al., 1990. Collagen fibrillogenesis in vitro: Interaction of types I and V collagen regulates fibril diameter. *J Cell Sci.* 95, 649-657

Blochberger, T.C., et al., 1992a. cDNA to chick lumican (corneal keratan sulfate proteoglycan) reveals homology to the small interstitial proteoglycan gene family and expression in muscle and intestine. *J Biol Chem.* 267, 347-352

Blochberger, T.C., et al., 1992b. Isolation and partial organization of lumican and decorin from adult chicken corneas. A keratan sulfate- containing isoform of decorin is developmentally regulated. *J Biol Chem.* 267, 20613-20619

Bohic, S., et al., 2008. Intracellular chemical imaging of the developmental phases of human neuromelanin using synchrotron x-ray microspectroscopy. *Anal Chem.* 80, 9557-9566

Bonanno, J.A., 2003. Identity and regulation of ion transport mechanisms in the corneal endothelium. *Prog Retin Eye Res.* 22, 69-94

Borcherding, M.S., et al., 1975. Proteoglycans and collagen fibre organization in human corneoscleral tissue. *Exp Eye Res.* 21, 59-70

Bron, A.J., et al., 2001. Wolff's anatomy of the eye and orbital. 8th ed. *Oxford University Press*.

Brouwer, P., 2010. Theory of XRF. Getting acquainted with the principles. 3rd Ed, *PANanalytical B.V.,* Almelo, The Netherlands

Brubaker, R.F., 1975. The effect of intraocular pressure on conventional outflow resistance in the enucleated human eye. *Invest Ophthalmol Vis Sci.* 14, 286-292

Bruns, R.R., 1984. Beaded filaments and long-spacing fibrils: relation to type VI collagen. *J Ultrastruct Res.* 89, 136-145

Burg, M.A., et al., 1996. Binding of the NG2 proteoglycan to type VI collagen and other extracellular matrix molecules. *J Biol Chem*. 271, 26110-26116

Carlson, E.C., et al., 2003. Role of Cys41 in the N-terminal domain of lumican in ex vivo collagen fibrillogenesis by cultured corneal stromal cells. *Biochem J.* 369, 461-468

Castoro, J.A., et al., 1988. Water grasients across bovine cornea. *Invest Ophthalmol Vis Sci.* 29, 963-968

Chakravarti, S., et al., 1998. Lumican regulates collagen fibril assembly: Skin fragility and corneal opacity in the absence of lumican. *J Cell Biol.* 141, 1277-1286

Chakravarti, S., et al., 2000. Corneal opacity in lumican-null mice: defects in collagen fibril structure and packing in the posterior stroma. *Invest Ophthalmol Vis Sci.* 41, 3365–3373

Chapman, J.A., et al., 1990. The collagen fibril--a model system for studying the staining and fixation of a protein. *Electron Microsc Rev.* 3, 143-182

Chu, M.L., et al., 1988. Amino acid sequence of the triple-helical domain of human collagen type VI. *J Biol Chem*. 263, 18601–18606

Chung, E., et al., 1976. Isolation of three collagenous components of probable basement membrane origin from several tissues. *Biochem Biophys Res Commun*. 71, 1167-1174

Cintron, C., et al., 1988. Heterogeneity of collagens in rabbit corneas: type III collagen. *Invest Ophthalmol Vis Sci.* 29**,** 767–775

Connon, C.J., et al., 2003. Proteoglycan alterations and collagen reorganisation in the secondary avian cornea during development. *Ophthalmic Res.* 35, 177-184

Conrad, G.W., 1970. Collagen and mucopolysaccharide biosynthesis in the developing chick cornea. *Dev Biol.* 21, 292-317

Cornuet, P.K., et al., 1994. Molecular polymorphism of lumican during development. *Invest Ophthalmol Vis Sci.* 5, 870-877

Corpuz, L.M., et al., 1996. Molecular cloning and tissue distribution of keratocan: bovine corneal keratan sulfate proteoglycan 37A. *J Biol Chem.* 271, 9759-9763

Coulombre, A., Coulombre, J., 1961. The development of the structural and optical properties of the cornea. New York, Academic press.

Cox, J., et al., 1970. The transparency of the mammalian cornea. *J Physiol.* 210, 601-616

Dauphin, Y., et al., 2003. In situ mapping of growth lines in the calcitic prismatic layers of mollusc shells using X-ray absorption near-edge structure (XANES) spectroscopy at the sulphur K-edge. *Mar Biol.* 142, 299-304

Dauphin, Y., et al., 2006. Microstructure and chemical composition of giant avian eegshells. *Anal Bioanal Chem.* 386, 1761-1771

Davies, A.M.C., Fearn, T., 2005. Back to basics: the principles of principal component analyisis. *Spectrosc Eur.* Tony Davies Column April/May

Davies, Y., et al., 1999. Proteoglycans on normal and migrating human corneal endothelium. *Exp Eye Res.* 68, 303-311

Davison, F., et al., 1979. Quantitative analysis of the collagens in the bovine cornea. *Exp Eye Res.* 29, 97–107

Dietlein, T.S., et al., 1998. Immunohistochemical distribution of type VI collagen in normal and glaucomatous human trabecular meshwork. *Graefes Arch Clin Exp Ophthalmol.* 236, 597-601

Dua, H.S., et al., 2013. Human corneal anatomy redefined: a novel pre-Descemet's layer (Dua's layer). *Ophthalmol.* 120, 1778-1785

Dunlevy, J.R., et al., 1998. Identification of the N-linked oligosaccharides in chick corneal lumican and keratocan that receive keratan sulfate. *J Biol Chem.* 273, 9615-9621

Dunlevy, J.R., et al., 2000. Expression of keratan sulfate proteoglycans lumican, keratocan and osteoglycin/mimecan during chick corneal development. *Exp Eye Res.* 70, 349-362

Dvorak-Theobald, G., 1934. Schlemm's canal: its anastomoses and anatomic relations. *Trans Am Ophthalmol Soc.* 32, 574-595

Ellingsen, B.A., Grant, W.M., 1972. Trabeculotomy and sinosotomy in enucleated human eyes. *Invest Ophthalmol.* 11, 21–28

Elliott, G.F., Hodson, S.A., 1998. Cornea, and the swelling of polyelectrolyte gels of biological interest. *Rep Prog Phys.* 61**,** 1325-1365

Engel, J., et al., 1985. Structure and macromolecular organization of type VI collagen. *Ann N Y Acad Sci.* 460, 25–37

Erikson, A., Svedbergh, B., 1980. Transcellular aqueous humor outflow: A theortical and experimental study. *Albrecht Von Graefes Arch Klin Exp Ophthalmol.* 212, 187-197

Ethier, C.R., Coloma, F.M., 1999. Effects of ethacrynic acid on Schlemm's canal inner wall and outflow facility in human eyes. *Invest Ophthalmol Vis Sci.* 40, 1599-15607

Ethier, C.R., et al. 2006. Effects of Latrunculin-B on Outflow Facility and Trabecular Meshwork Structure in Human Eyes. *Invest Ophthalmol Vis Sci.* 47, 1991-1998

Ethier, C.R., et al., 1986. Calculations of flow resistance in the juxtacanalicular meshwork. *Invest Ophthalmol Vis Sci.* 27, 1741-1750

Ethier, C.R., et al., 1998. Two pore types in the inner wall endothelium of Schlemm's canal. *Invest Ophthalmol Vis Sci.* 39, 2041-2048

Fahrni, C.J., 2007. Biological applications of x-ray fluorescence microscopy: exploring the subcellular topography and speciation of transition metals. *Curr Opin Chem Biol*. 11, 121-127

Farrell, R.A., McCally, R.L., 2000. Corneal transparency. In Principles and Practice of Ophthalmology. D.M. Albert, and F.A. Jakobiec,editors. PA:WB Saunders/Philadelphia. 629-643

Feeney, M.L., Wissig, S., 1966. Outflow studies using an electron dense tracer. *Trans Amer Acad Opthal Otolaryng.* 70, 791- 798

Fitzgerald, J., et al., 2008. Three novel collagen VI chains, alpha4(VI), alpha5(VI), and alpha6(VI). *J Biol Chem.* 283, 20170–20180

Flocks, M., 1956. The anatomy of the trabecular meshwork as seen in tangential section. *AMA Arch Ophthalmol.*40: 257-282

Font, B., et al., 1993. Binding of collagen XIV with the dermatan sulfate side chain of decorin. *J Biol Chem.* 268, 25015-25018

Freund, D.E., et al., 1995. Ultrastructure in anterior and posterior stroma of perfused human and rabbit corneas. Relation to transparency. *Invest Ophthalmol Vis Sci.* 36, 1508-1523

Funderburgh, J.L., 1997. Mimecan, the 25-kDa corneal keratan sulfate proteoglycan, is a product of the gene producing osteoglycin. *J Biol Chem.* 272, 28089-28095

Funderburgh, J.L., 2000. Keratan sulfate, biosynthesis, and function. *Glycobiology* 10, 951-958

Funderburgh, J.L., et al., 1988. Immunoanalysis of keratan sulphate proteoglycan from corneal scars. *Invest Ophthalmol Vis Sci.* 29, 1116-1124

Funderburgh, J.L., et al., 1989. Altered keratan sulphate epitopes in keratoconus. *Invest Ophthalmol Vis Sci.* 30, 2278-2281

Funderburgh, J.L., et al., 1995. Sequence, molecular properties and chromosomal mapping of mouse lumican. *Invest Ophthalmol Vis Sci.* 36, 2296-22303

Furthmayr, H., et al., 1983. Electron- microscopical approach to a structural model of intima collagen. *Biochem J.* 211, 303-311

Gandhi, N,S., Mancera, R.L., 2008. The structure of glycosaminoglycans and their interactions with proteins. *Chem Biol Drug Des.* 72, 455-482

Gara, S.K., et al., 2008. Three novel collagen VI chains with high homology to the alpha3 chain. *J Biol Chem.* 283, 10658–10670

Gard, T.L., et al., 1993. Ionic modulation of flow resistance in an immobilized proteoglycan model of the trabecular meshwork. *J Glaucoma*. 2, 183-192

Garrone, L.K., Feeney, M.L., 1959. Electron microscopic studies of the human eye. II. Study of the trabeculae by light and electron microscopy. *Arch Ophthalmol*. 62, 966-973

Gealy, E.C., et al., 2007. Differential expression of the keratan sulphate proteoglycan, keratocan, during chick corneal embryogenesis. *Histochem Cell Biol*. 128, 551-555

Gelse, K., et al., 2003. Collagens-structure, function and biosynthesis. *Adv Drug Deliv Rev.* 55, 1531-1546

Goldman, I.N., et al., 1968. Structural alterations affecting transparency in swollen human corneas. *Invest Ophthalmol Vis Sci.* 7, 501-519

Goldman, J.N., Benedek, G.B., 1967. The relationship between morphology and transparency in the

Goldmann, H., 1950. Minute volume of the aqueous in the anterior chamber of the human eye in normal state and in primary glaucomaA. *Ophthalmologica.* 120, 19-21

Gong, H., et al., 1992. Age-related changes of sulfated proteoglycans in the normal human trabecular meshwork. *Exp Eye Res.* 55, 691-709

Gong, H., et al., 1996. Morphology of the aqueous outflow pathway. *Microsc Res Tech*. 33, 336-367

Gong, H., et al., 2002. A new view of the human trabecular meshwork using quick-freeze, deep-etch electron microscopy. *Exp Eye Res.* 75, 347-358

Gordon, M.K., et al., 1989. Type XII collagen. A larger multidomain molecule with partial homology to type IX collagen. *J Biol Chem*. 264, 19772-19778

Gordon, M.K., et al., 1994. Type V collagen and Bowman's membrane. *J Biol Chem.* 269, 2459-2466

Grant, W.M., 1958. Further studies on facility of flow through the trabecular meshwork. *Arch Ophthalmol.* 60, 523-533

Grant, W.M., 1963. Experimental aqueous perfusion in enucleated human eyes. *Arch Ophthalmol.* 69, 783-801

Greiling, H., Scott, J.E., 1989. Keratan sulphate proteoglycans: Chemistry and biosynthesis of the linkage regions. In: Keratan sulphate. Chemistry, biology, chemical pathology. *TransMedica Europe Ltd Conference Unit,* chapter 7.

Grierson, I., et al., 1978. Associations between the cells of the walls of Schlemm's canal. *Albrecht Von Graefes Arch Klin Exp Ophthalmol.* 208, 33-47

Grover, J., et al., 1995. The human lumican gene. Organization, chromosomal location and expression in articular cartilage. *J Biol Chem.* 270, 21942-21949

Hackell, M.J., et al., 2012. X-ray absorption spectroscopy at the sulphur k-edge: a new tool to investigate the biochemical mechanism of neurodegeneration. *ACS Chem Neurosci.* 3, 178-185

Haefliger, I.O., 1997. Risk factors associated with glaucoma [in French]. *Klin Monbl Augenheilkd.* 210, 265– 268

Hamanaka, T., Bill, A., 1987. Morphological and functional effects of NA_2EDTA on the outflow routes for aqueous humor in monkeys. *Exp Eye Res.* 44, 171-190

Hamanaka, T., Bill, A., 1988. Effects of alpha-chymotrypsin on the outflow routes for aqueous humor. *Exp Eye Res.* 46, 323-341

Hamburger, V., 1992. The stage series of the chick embryo. *Dev Dyn.* 195, 273-275

Hamburger, V., Hamilton, H., 1951. A series of normal stages in development of the chick embryo. *J Morphol* 88: 49-92

Hann, C.R., et al., 2001. Ultrastructural localization of collagen IV, fibronectin and laminin in the trabecular meshwork of normal and glaucomatous eyes. *Ophthalmic Res.* 33, 314-324

Hann, C.R., Fautsch, M.P., 2009. Preferential fluid flow in the human trabecular meshwork near collector channels. *Invest Ophthalmol Vis Sci.* 50, 1692-1697

Hanna, C., et al., 1961. Cell turnover in the adult human eye. *Arch Ophthal.* 65, 695-698

Hart, G., 1976. Biosynthesis of glycosaminoglycans during corneal development. *J Biol Chem.* 251, 6573-6521

Hart, R., Farrell, R., 1969. Light Scattering in the Cornea. *J Opt Soc Am.* 59, 776-773

Hassell, J.R., Birk, D.E., 2010. The molecular basis of corneal transparency. *Exp Eye Res.* 91, 326-335

Hassell, J.R., et al., 1980. Macular corneal dystrophy: failure to synthesize a mature keratan sulfate proteoglycan. *Proc Natl Acad Sci USA.* 77, 3705-3709

Hassell, J.R., et al., 1983. Proteoglycan changes during restoration of transparency in corneal scars. *Arch Biochem Biophys.* 222, 362-369

Hassell, J.R., et al., 1986. Proteoglycan core protein families. *Ann Rev Biochem.* 55, 539-567

Hay, E.D., Revel, J-P., 1969. Fine structure of the developing avian cornea. In: Monographs in developmental biology. A. Wolsky, Tarrytown, N.Y P.S. Chen, Zürich (eds) *Basel S. Karger New York*

Hayashaki, S., et al., 2002. Comparative observations on corneas, with special reference to Bowman's layer and Descemet's membrane in mammals and amphibians. *J Morphol.* 254, 247-258

Hedbys, B.O., 1961. The role of polysaccharides in corneal swelling. *Exp Eye Res.* 1, 81- 91

Hessle, H., Engvall, E., 1984. Type Collagen. Studies on its localization, structure, and biosynthetic form with monoclonal antibodies. *J Biol Chem*. 259, 3955–3961

Hirano, K., et al., 1989. Experimental formation of 100 nm periodic fibrils in the mouse corneal stroma and trabecular meshwork. *Invest Ophthalmol Vis Sci.* 30, 869-874

Hocking, A.M., et al., 1998. Leucine-rich repeat glycoproteins of the extracellular matrix. *Matrix Biol.* 17, 1-19

Hodson, S., Miller, F., 1976. The bicarbonate ion pump in the endothelium which regulates the hydration of rabbit cornea. *J Physiol.* 263, 563-577

Hogan, M.J, Alvarado, J.A., Weddell, J.E. 1971. Histology of the human eye. An atlas and textbook. Saunders, Philadelphia.

Holmberg, A., 1959. The fine structure of the inner wall of Schlemm's canal. *Arch Ophthalmol.* 62, 956-958

Inomata, H., Bill, A., 1977. Exit sites of uveoscleral flow of aqueous humor in cynomolgus monkey eyes. *Exp Eye Res.* 25, 113–118

Inomata, H., et al., 1972. Aqueous humor outflow pathways through the trabecular meshwork and into Schlemm's canal in the cynomolgus monkey (Macaca irus). An electron microscopic study. *Am J Ophthalmol.* 73, 760-789

Iozzo, R.V., 1999. The biology of the small leucine-rich proteoglycans. *J Biol Chem.* 2, 18843-18846

Itano, N., 2008. Simple primary structure, complex turnover regulation and multiple roles of hayluronan. *J Biochem.* 144, 131-137

Jackson, R.L., et al., 1991. Glycosaminoglycans: molecular properties, protein interactions, and role in physiological processes. *Physiol Rev.* 71, 481-539

Jacobsen, I.E., et al., 1984. Structure and composition of Bowman's membrane. Study by frozen resin cracking. *Acta Ophthalmol.* 62, 39-53

Jakus, M.A., 1956. Studies on the cornea. II. The fine structure of Descemet's membrane. *J Biophysic and Biochem Cytol*. 2, 243-255

Jander, R., et al., 1983. Further characterization of the three polypeptide chains of bovine and human short-chain collagen (intima collagen). *Eur J Biochem*. 133, 39–46

Jester, J.V., Chang, J.H., 2003. Modulation of cultured corneal keratocyte phenotype by growth factors/cytokines control in vitro contractility and extracellular matrix contraction. *Exp Eye Res.* 77, 581-592

Jester, J.V., et al., 1994. Corneal keratocytes: in situ and in vitro organization of cytoskeletal contractile proteins. *Invest Ophthalmol Vis Sci.* 35, 730-743

Johnson, D.H., et al., 1982. The ultrastructure of Descemet's membrane. I Changes with age in normal corneas. *Arch Ophthalmol.* 100, 1942-1947

Johnson, M, Erickson, K., 2000. Mechanisms and routes of aqueous humor drainage. In: Albert DM, Jakobiec FA, editors. Principles and practice of ophthalmology. Philadelphia: WB Saunders

Johnson, M., 2006. What controls aqueous humour outflow resistance? *Exp Eye Res.* 82, 545-557

Johnson, M., et al., 1992. Modulation of outflow resistance by the pores of the inner wall endothelium. *Invest Ophthalmol Vis Sci.* 33, 1670-1675

Johnson, M., et al., 2002. The pore density in the inner wall endothelium of schlemm's canal of glaucomatous eyes. *Invest Ophthalmol Vis Sci*. 43, 2950-2955

Johnson, M., Kamm, R.D., 1983. The role of Schlemm's canal in aqueous outflow from the human eye. *Invest Ophthalmol Vis Sci.* 24, 320-325

Johnson, M., Tamm, E.R., 2010. Biomechanics of aqueous humor outflow resistance. Encyclopedia of the Eye. Chapter 93. Academic Press

Johnstone, M.A., Grant, W.G., 1973. Pressure-dependent changes in structures of the aqueous outflow system of human and monkey eyes. *Am J Ophthalmol.* 75, 365-383

Jun, A.S., et al., 2006. Aging changes of mouse corneal endothelium and descemet's membrane. *Exp Eye Res.* 83, 890-896

Kadler, K.E., et al., 1996. Collagen Fibril Formation *Biochem J.* 316, 1-11

Kayes, J., 1967. Pore structure of the inner wall of Schlemm's canal. *Invest Ophthalmol Vis Sci.* 6, 381-394

Keene, D.R., et al., 1987. Type III collagen can be present on banded collagen fibrils regardless of fibril diameter. *J Cell Biol.* 105, 2393-2402

Keene, D.R., et al., 1988. Ultrastructure of type VI collagen in human skin and cartilage suggest an anchoring function for this filamentous network. *J Cell Biol*. 107, 1995-2006

Kefalides, N., et al., 1976. Biosynthesis of basement membrane collagen by rabbit corneal endothelium in vitro. *J Biol Chem*. 251, 730-733

Keller, K.E., Acott, T.S., 2013. The juxtacanalicular region of ocular trabecular meshwork: a tissue with a unique extracellular matrix and specialized function. *J Ocular Biol.* 1, 10-17

Keller, K.E., et al., 2008. Effects of modifiers of glycosaminoglycan biosynthesis on outflow facility in perfusion culture. *Invest Ophthalmol Vis Sci.* 49, 2495-2505

Kelly, J.G., et al., 2009 Discrimination of Base Differences in Oligonucleotides Using Mid-Infrared Spectroscopy and Multivariate Analysis. *Anal Chem.* 51, 5314-5319

Kielty, C.M., et al., 2002. Elastic fibers. *J Cell Sci*. 115, 2817-2828

Kielty, C.M., Grant, M.E., 2003. The Collagen Family: Structure, Assembly, and Organization in the Extracellular Matrix, in Connective Tissue and Its Heritable Disorders: Molecular, Genetic, and Medical Aspects, 2nd ed (eds P. M. Royce and B. Steinmann), *John Wiley & Sons, Inc., Hoboken, NJ, USA.* doi: 10.1002/0471221929.ch2

Kjellén, L., Lindahl, U., 1991. Proteoglycans: Structures and interactions. *Ann Rev Biochem.* 60, 443-475

Klintworth, G.K., 2008. Genetic disorders of the cornea. In: Klintworth GK, Garner A (eds) Pathobiology of ocular disease, erd edn. *Informa Healthcare, New York,* 615-713

Klintworth, G.K., et al., 1997. Macular corneal dystrophy in Saudi Arabia: a study of 56 cases and recognition of a new immunophenotype. *Am J Ophthalmol.* 124, 9-18

Knepper, P.A. et al., 1984. Exogenous hyaluronidases and degradation of hyaluronic acid in the rabbit eye. *Invest Ophthalmol Vis Sci.* 25, 286-293

Knies, M., 1875. Die resorption von blut in der vorderen augenkammer. *Arch Pathol Anat Physiol Klin Med*. 62, 537-553

Knupp, C., et al., 2000. Structure of abnormal molecular assemblies (collagen VI) associated with human full thickness macular holes. *J Struct Biol.* 129, 38-47

Knupp, C., et al., 2002a. Collagen VI assemblies in age-related macular degeneration. *J Struct Biol.* 139, 181-189

Knupp, C., et al., 2002b. Analysis of the collagen VI assemblies associated with Sorby's Fundus Dystrophy. *J Struct Biol.* 137, 31-40

Knupp, C., et al., 2006. Structural correlation between collagen VI microfibrils and collagen VI banded aggregates. *J Struct Biol*. 154, 312-326

Knupp, C., et al., 2009. The architecture of the cornea and structural basis of its transparency. *Adv Prot Chem Struct Biol.* 78, 25-49

Knupp, C., Squire, J.M., 2001. A new twist in the collagen story- the type VI segmented supercoil. *EMBO J.* 20, 372-376

Knupp, C., Squire, J.M., 2005. Molecular packing in network-forming collagens. *Adv Protein Chem.* 70, 375-403

Kobayashi, A., et al., 2006. In vivo laser confocal microscopy of Bowman's layer of the cornea. *Ophthalmol.* 113, 2203-2208

Komai, Y., Ushiki, T., 1991. The three-dimensional organisation of collagen fibrils in the human cornea and sclera. *Invest Ophthalmol Vis Sci.* 32, 2244-2258

Kostyuk, O., et al., 2002. Transparency of the bovine corneal stroma at physiological hydration and its dependence on concentration of the ambient anion. *J Physiol.* 543, 633-642

Kremer, J.R., et al., 1996. Computer visualization of three-dimensional image data using IMOD. *J Struct Biol.* 116, 71–76

Kuo, H.J., et al., 1995. The macromolecular structure of type-VI collagen. Formation and stability of filaments. *Eur J Biochem.* 232, 364–372

Kuo, H.J., et al., 1997. Type VI collagen anchors endothelial basement membranes by interacting with type IV collagen. *J Biol Chem.* 272, 26522-26529

Lampe, A., et al., 2005. Automated genomic sequence analysis of the three collagen VI genes: applications to Ullrich congenital muscular dystrophy and Bethlem myopathy. *J Med Genet.* 42, 108-120

Leber, T., 1873. *Studien über den Flüssigkeitswechsel im Auge. Graefes Arch Clin Exp Ophthalmol*. 19, 87- 185

Lee, W.R., Grierson, I., 1975. Pressure effects on the endothelium of the trabecular wall of Schlemm's canal: a study by scanning electron microscopy. *Albrecht Von Graefes Arch Klin Exp Ophthalmol.* 196, 255-265

Leeson, T.S., Speakman, J.S., 1961. The fine extracellular material in the pectinate ligament (trabecular meshwork) of the human iris. *Acta Anat. (Basel).* 46, 363-379

Leonard, D., Meek, K., 1997. Refractive indices of the collagen fibrils and extrafibrillar material in the corneal stroma. *Biophys J.* 72, 1382-1387

Lewis, et al., 2010. Structural interactions between collagens and proteoglycans are elucidated by three-dimensional electron tomography of bovine cornea. *Structure.* 18, 239-245

Li, W., et al., 1992. cDNA clone to chick corneal chondroitin dermatan sulfate proteoglycan reveals identity to decorin. *Arch Biochem Biophys.* 296, 190-197

Liles, M., et al., 2010. Differential relative sulphation of keratan sulfate glycosaminoglycan in the chick cornea during embryonic development. *Invest Ophthalmol Vis Sci.* 51, 1365-1372

Linsenmayer, T.F., et al., 1986a. Avian type VI collagen. Monoclonal antibody production and immunohistochemical identification as a major connective tissue component of cornea and skeletal muscle. *Exp Cell Res*. 165, 518-529

Linsenmayer, T.F., et al., 1986b. Type VI collagen: immunohistochemical identification as a filamentous component of the extracellular matrix of the developing avian corneal stroma. *Dev Biol.* 118, 425-431

Lisenmayer, T.F., 1991. Collagens. In: Cell biology of extracellular matrix. E.D. Hay (ed) 2nd ed. *Plenum Press, New York* , 6-44

Llobet, A., et al., 2003. Understanding trabecular meshwork physiology: A key to the control of intraocular pressure? *News Physiol Sci.* 18, 205-209

Lütjen-Drecoll, E., et al., (1981) Ultrahistochemical studies on tangential sections of the trabecular meshwork in normal and glaucomatous eyes. *Invest Ophthalmol Vis Sci.* 21, 563-573

Lütjen-Drecoll, E., et al., 1989. Immunomicroscopical study of type VI Collagen in the trabecular meshwork of normal and glaucomatous eyes. *Exp Eye Res*. 48, 139–147

Maepea, O., Bill, A., 1989. The pressures in the episcleral veins, Schlemm's canal and the trabecular meshwork in monkeys: effects of changes in intraocular pressure. *Exp Eye Res*. 49, 645–663

Maepea, O., Bill, A., 1992. Pressures in the juxtacanalicular tissue and Schlemm's canal in monkeys. *Exp Eye Res.* 54, 879–883

Marshall, G.E., et al., 1991. Immunogold ultrastructural localization of collagens in the aged human outflow system. *Opthalmology.* 98, 692-700

Marshall, G.E., et al., 1991a. Immunogold fine structural localization of extracellular matrix components in aged human cornea. I. Collagen types I–IV and laminin. *Graefes Arch Clin Exp Ophthalmol.* 229, 157–63

Marshall, G.E., et al., 1991b. Immunogold fine structural localization of extracellular matrix components in aged human cornea. II. Collagen types V and VI. *Graefes Arch Clin Exp Ophthalmol.* 229, 164-171

Martin, F.L., 2007. Identifying variables responsible for clustering in discriminant analysis of data from infrared microscpectroscopy of a biological sample. *J Comput Biol.* 14, 1176-1184

Martin, F.L., et al. 2010. Distinguishing cell types or populations based on the computational analysis of their infrared spectra. *Nature Protocol.* 5, 1748- 1760

Maurice, D.M., 1957. The structure and transparency of the corneal stroma. *J Physiol.* 136, 263-286

Maurice, D.M., 1972. The location of the fluid pump in the cornea. *J Physiol.* 221, 43-54

McEwen, B. F., Marko., M., 2001. The emergence of electron tomography as an important tool for investigating cellular ultrastructure. *J Histochem Cytochem*. 49,553–564

McEwen, W.K., 1958. Application of Poisseuille's law to aqueous outflow. *Arch Ophthalmol.* 60, 290-294

Meek, K.M., et al., 1981. Interpretation of the meridional x-ray diffraction pattern from collagen fibrils in corneal stroma. *J Mol Biol.* 149, 477-488

Meek, K.M., et al., 1986. A synchrotron x-ray diffraction study of bovine cornea stained with cupromeronic blue. *Coll Relat Res.* 6, 203-218

Meek, K.M., Holmes, D.F., 1983. Interpretation of the electron microscopical appearance of collagen fibrils from corneal stroma. *Int J Biol Macromol.* 5, 17–25

Meek, K.M., Quantock, A.J., 2001. The use of x-ray scattering techniques to determine corneal ultrastructure. *Prog Retin Eye Res.* 20, 95-137

Michelacci, Y.M., 2003. Collagens and proteoglycans of the corneal extracellular matrix. *Braz J Med Biol Res.* 36, 1037-1046

Morishige, N., et al., 2011. Three-dimensional analysis of collagen lamellae in the anterior stroma of the human cornea visualized by second harmonic generation imaging microscopy. *Invest Ophthalmol Vis Sci.* 52, 911-915

Morra, M.J., et al., 1997. Speciation of sulfur in humic and fulvic acids using X-ray absorption near-edge structure (XANES) spectroscopy. *Geochim Cosmochim Ac.* 61, 683-688

Moseley, H., et al., 1983. Mathematical modelling of aqueous humor outflow from the eye through the pores in the lining of Schlemm's canal. *Clin Phys Physiol Meas. 4, 47-63*

Moses, R.A., 1977. The effect of intraocular pressure on resistance to outflow. *Surv Ophthalmol.* 22, 88-100

Moses, R.A., 1979. Circumferential flow in Schlemm's canal. *Am J Ophthalmol.* 88, 585–591

Müller, L.J., et al., 1995. Novel aspects of the ultrastructural organization of human corneal keratocytes. *Invest Ophthalmol Vis Sci.* 36, 2557-2567

Müller, L.J., et al., 2004. A new three-dimensional model of the organization of proteoglycans and collagen fibrils in the human corneal stroma. *Exp Eye Res.* 78, 493-501

Nakamura, K., 2003. Interaction between injured corneal epithelial cells and stromal cells. *Cornea.* 22, S35-S47

Nakamura, M., et al., 1993. Observation of 100 nm periodic fibrils in mouse corneal stroma by cryoultramicrotomy. *J Electron Microsc.* 42, 185-188

Nakamura, M., et al., 1997. Type VI collagen bound to collagen fibrils by chondroitin/dermatan sulphate glycosaminoglycan in mouse corneal stroma. *Jpn J Ophthalmol.* 41, 71-76

Nakazawa, K., et al., 1995. Proteoglycan synthesis by corneal explants from developing embryonic chicken. *J Biochem.* 117, 707-718

Newville, M., 2004. Fundamentals of XAFS. Consortium for Advanced Radiation Sources, University of Chicago, Chicago, IL.

Nilsson, S.F., 1997. The uveoscleral outflow routes. *Eye*. 11, 149-154

nonswelling corneal stroma of the shark. *Invest Ophthalmol*. 6, 574–600

Odermatt, E., et al., 1983. Structural diversity and domain composition of a unique collagenous fragment (intima collagen) obtained from human placenta. *Biochem J.* 211, 295–302

Oeben ,M., et al., 1987. Constant and variable domains if different disaccharide structure in corneal keratan sulfate chains. *Biochem J.* 248, 85-93

Overby, D.R. et al., 2009. The changing paradigm of outflow resistance generation: Towards synergistic models of the JCT and inner wall endothelium. *Exp Eye Res.* 88, 656-670

Parc, C.E., et al., 2000. Giant vacuoles are found preferentially near collector channels. *Invest Ophthalmol Vis Sci.* 41, 2984-2990

Parfitt, et al., 2010. Three-dimensional reconstruction of collagen-proteoglycan interactions in the mouse corneal stroma by electron tomography. *J Struct Biol.* 170, 392-397

Patel, I.I.,et al., 2011. Segregation of human prostate tissues classified high-risk (UK) versus low-risk (India) for adenocarcinoma using Fourier-transform infrared or Raman microspectroscopy coupled with discriminant analysis. *Anal Bioanal Chem.* 401**,** 969-982

Patel, S., et al., 1995. Refractive index of the human corneal epithelium and stroma. *J Refract Surg.* 11, 100-105

Pederson, J.E., Gaasterland, D.E., MacLellan, H.M., 1977. Uveoscleral aqueous outflow in the rhesus monkey: Importance of uveal reabsorption. *Invest Ophthalmol Vis Sci*. 16, 1008-1017

Pepe, G., et al., 1995. A novel de novo mutation in the triple helix of the COL6A3 gene in a two-generation Italian family affected by Bethlem myopathy. A diagnostic approach in the mutations' screening of type VI collagen. *Neuromuscul Disord.* 9, 264-271

Peterson, W.S., Jocson, V.L., 1974. Hyaluronidase effects on aqueous outflow resistance. *Am J Ophthalmol.* 77, 573–577

Pickering, I.J., et al., 1998. Sulfur K-edge X-ray absorption spectroscopy for determining the chemical speciation of sulfur in biological systems. *FEBS letters.* 441, 11-14

Pickering, I.J., et al., 2009. Localizing the chemical forms of sulfur in vivo using x-ray fluorescence spectroscopic imaging: Application to onion (allium cepa) tissues. *Biochemistry.* 48, 6846-6853

Plessy, B., Bettelheim, F. A., 1975. Water vapor sorption of keratan sulphate. *Mol Cell Biochem.* 6, 85-91

Potts, A.M., 1962. Some aspects of the interrelation between corneal hydration and corneal transparency. *Invest Ophthalmol Vis Sci.* 1, 163-169

Praus, R., Goldman, J. N., 1970. Glycosaminoglycans in the nonswelling corneal stroma of dogfish shark. *Invest Ophthalmol Vis Sci.* 9, 131- 136

Prietzel, J., et al., 2003. Speciation of sulphur in soils and soil particles by X-ray spectromicroscopy. *Eur J Soil Sci.* 54, 423-433

Prietzel, J., et al., 2011. Sulfur speciation in soil by s k-edge xanes spectroscopy: Comparison of spectral deconvolution and linear combination fitting. *Environ Sci Technol.* 45, 2878-2886

Prockop, D.J., Kivirikko, K.I, 1995. Collagens: Molecular biology, diseases and potentials for therapy. *Ann Rev Biochem.* 64, 403-434

Quantock, A.J, 1994. An erroneous glycosaminoglycan metabolism leads to corneal opacification in macular corneal dystrophy. *Glycosylation Dis.* 1, 143-151

Quantock, A.J., et al., 1998. A Synchotron X-ray diffraction study of developing chick corneas. *Biophys J.* 74, 995-998

Quantock, A.J., et al., 2001. An x-ray diffraction investigation of corneal structure in lumican-deficient mice. *Invest Ophthalmol Vis Sci.* 42, 1750-1756

Quigley, H.A., Broman, A.T., 2006. The number of people with glaucoma worldwide in 2010 and 2020. *Br J Ophthalmol*. 90, 262-267

Rada, J.A., et al., 1993. Regulation of corneal collagen fibrillogenesis in vitro by corneal proteoglycan (lumican and decorin) core proteins. *Exp Eye Res.* 56, 635-648

Radner, W., et al., 1998. Interlacing and cross-angle distribution of collagen lamellae in the human cornea. *Cornea.* 17, 537-543

Raouf, A., et al., 2002. Lumican is a major proteoglycan component of the bone matrix. *Matrix Biol.* 4, 361-367

Raviola, G., Raviola, E., 1981. Paracellular route of aqueous outflow in the trabecular meshwork and canal of Schlemm. *Invest Ophthalmol Vis Sci.* 21, 52-72

Reale, E., et al., 2001. In the mammalian eye type VI collagen tetramers form three morphologically different aggregates. *Matrix Biol*. 20, 37–51

Ress, D.B., et al., 2004. Methods for generating high-resolution structural models from electron microscope tomography data. *Structure*. 12, 1763–1774

Rittig, M., et al., 1990. Type-VI collagen in the human iris and ciliary body. *Cell Tissue Res.* 259, 305-312

Robert, L., et al., 2001. Corneal collagens. *Pathol Biol.* 49, 353-363

Rohen, J.W., et al., 1981. The fine structure of the cribriform meshwork in normal and glaucomatous eyes as seen in tangential sections. *Invest Ophthalmol Vis Sci.* 21, 574–585

Rohen, J.W., Lütjen-Drecoll, E., 1989. Morphology of aqueous outflow pathways in normal and glaucomatous eyes. In: The Glaucomas. R. Ritch, M.B. Shields, T. Krupin, eds. C.V. Mosby Co. St Luis. MO, pp. 41-74

Rohen, J.W., Rentsch, F.J., 1968. Morphology of Schlemm's canal and related vessels in the human eye. *Albrecht Von Graefes Arch Klin Exp Ophthalmol.* 176, 309-329

Rosenquist, J.W., et al., 1989. Outflow resistance of enucleated human eyes at two different perfusion pressures and different extents of trabeculotomy. *Curr Eye Res.* 8, 1233-1240

Sabatelli, P., et al., 2001. Collagen VI deficiency affects the organization of fibronectin in the extracellular matrix of cultured fibroblasts. *Matrix Biol.* 20, 475-486

Sallcup, W.B., et al., 1990. Interaction of the NG2 chondroiting sulfate proteoglycan with type VI collagen. *J Cell Biol.* 11, 3177-3188

Sarret, G., et al., 1999. Chemical forms of sulfur in geological and archaeological asphaltenes from Middle East, France, and Spain determined by sulfur K- and L-edge X-ray absorption near-edge spectroscopy. *Geochimi Cosmochim Ac.* 63, 3767-3779

Scacheri, P.C., et al., 2002. Novel mutations in collagen VI genes: expansion of the Bethlem myopathy phenotype. *Neurology.* 58, 593-602

Schaefer, L., Iozzo, R.V., 2008. Biological functions of the small leucine-rich proteoglycans: From genetics to signal transduction. *J Biol Chem.*283, 21305-21309

Schmid, B., et al., 2010. A high-level 3D visualization API for Java and ImageJ. *BMC Bioinformatics* 11, 1471-2105

Schneider, C.A., et al., 2012. NIH Image to ImageJ: 25 years of image analysis. *Nat Methods*. 9, 671-675

Schwarz, W.H. 2013. 100th Anniversary of Bohr's model of the atom. *Angew Chem Int Ed Engl.* [Epub ahead of print]

Scott, J.E., 1985. 'Small-proteoglycan:collagen interactions: keratan sulphate proteoglycan associated with rabbit corneal collagen fibrils at the 'a' and 'c' bands. *Biosci Rep*. 5, 765-774

Scott, J.E., Bosworth, T.R., 1990. A comparative biochemical and ultrastructural study of proteoglyca-collagen interactions in corneal stroma. *Biochem J.* 270, 491-497

Scott, J.E., et al., 1988. Keratan sulphate is unevenly distributed from back to front of bovine cornea. *Biochem Soc Trans*. 16, 333-334

Scott, J.E., Haigh, M., 1988. Identification of specific binding sites for keratan sulphate proteoglycans and chondroitin-dermatan sulphate proteoglycans on collagen fibrils in cornea by the use of Cupromeronic Blue in 'critical-electrolyte-concentration' techniques. *Biochem J.* 253, 607-610

Segawa, K., 1973. Pore structures of the endothelial cells of the aqueous humor outflow. *Jpn J Ophthalmol.* 17, 133-139

Seiler, T., Wollensak, J., 1985. The resistance of the trabecular meshwork to aqueous humor outflow. *Albrecht Von Graefes Arch Klin Exp Ophthalmol.* 223, 88-91

Sherman, S.H., Green, K., Laties, A.M., 1978. The fate of anterior chamber fluorescein in the monkey eye. I: The anterior chamber outflow pathways. *Exp Eye Res*. 27, 159-173

Sherrard, E.S., et al., 1987. Age-related changes in the corneal endothelium and stroma as seen in vivo by specular microscopy. *Eye.* 1, 197-203

Shuttleworth, C.A., et al., 1992. Microfibrillar components in dental pulp: presence of both type VI collagen and fibrillin-containing microfibrils. *Arch Oral Biol*. 37, 1079–1084

Siegler, V., Quantock, A., 2002. Two-stage compaction of the secondary avian cornea during development. *Exp Eye Res.* 74, 427–431

Sit, A.J., et al., 1997. Factors affecting the pores of the inner wall endothelium of Schlemm's canal. *Invest Ophthalmol Vis Sci.* 38, 1517-1525

Smith, J.W., 1969. The transparency of the corneal stroma. Vision Res. **9**, 393–396

Smith, P., 1888. On the escape of fluid from the aqueous and vitreous chambers under different pressure. *Opthalmol Rev.*7, 193-208

Solé, A.V., et al., 2007. A multiplatform code for the analysis of energy- dispersive X-ray fluorescence spectra. *Spectrochim Acta Part B.* 62, 63-68

Sommer, A., et al., 1991. Baltimore Eye Survey Research Group. Relationship between intraocular pressure and primary open angle glaucoma among white and black Americans: the Baltimore Eye Survey. *Arch Ophthalmol*. 109, 1090 –1095

Specks, U., et al., 1992. Structure of recombinant N-terminal globule of type VI collagen alpha 3 chain and its binding to heparin and hyaluronan. *EMBO J.* 11, 4281-4290

Subramaniam, S., et al., 2003. Electron Tomography: a Powerful Tool for 3D Cellular Microscopy. Technical refinements enable investigators to locate proteins inside cells and to anticipate tomographic reconstructions of bacteria. *ASM News Y.* 69, 240-245

Suzuki, M., 1939. Prosthetic group of corneamucoid. *J Biochem.* 30, 185-191

Svedbergh, B., 1976. Effects of intraocular pressure on the pores of the inner wall of Schlemm's canal: A scanning electron microscopic study. *Jpn J Ophthalmol.* 20, 127

Tamm, E.R., 2009. The trabecular meshwork outflow pathways: Structural and functional aspects. *Exp Eye Res.* 88, 648-655

Tamura, Y., et al., 1991. Tissue Distribution of Type VIII Collagen in Human Adult and Fetal Eyes. *Invest Ophthalmol Vis Sci.* 32, 2636-2644

Tawara, A., et al., 1989. Distribution and characterization of sulfated proteoglycans in the human trabecular meshwork. *Invest Ophthalmol Vis Sci.* 30, 2215-2231

Taylor, S.E., et al., 2011. Infrared spectroscopy with multivariate analysis to interrogate endometrial tissue: a novel and objective diagnostic approach. *Br J Cancer.* 104, 790-797

Ten Hulzen, R.D., Johnson, D.H., 1996. Effect of fixation pressure on juxtacanalicular tissue and Schlemm's canal. *Invest Ophthalmol Vis Sci*. 37; 114-124

Tisdale, A.S., et al., 1988. Development of anchoring structures of the epithelium in rabbit and human fetal corneas. *Invest Ophthalmol Vis Sci.* 29, 727–36

Toole, B.P., 1997. Hyaluronan in morphogenesis. *J Intern Med.* 242: 35-40

Toole, B.P., Trelstad, R.L., 1971. Hayluronate production and removal during corneal development in the chick. *Dev Biol.* 26, 28-35

Trevisan, J., et al., 2010. Syrian hamster embryo (SHE) assay (pH 6.7) coupled with infrared spectroscopy and chemometrics towards toxicological assessment. *Analyst***.** 135, 3266-3272

Tripathi, B.J., et al., 1994. Identification of type VI collagen in the trabecular meshwork and expression of its mRNA by trabecular cells. *Exp Eye Res.* 58, 181-187

Tripathi, R.C., 1971. Mechanism of the aqueous outflow across the trabecular wall of Schlemm's canal. *Exp Eye Res.* 11, 116-121

Tripathi, R.C., 1972. Aqueous outflow pathway in normal and glaucomatous eyes. *Brit J Ophthalmol*. 56, 157-174

Tripathi, R.C., Tripathi, B.J., 1972. The mechanism of aqueous outflow in lower mammals. *Exp Eye Res.* 14, 73-79

Trüeb, B., et al., 1987. Type VI collagen represents a major fraction of connective tissue collagens*. Eur J Biochem.*166, 699–703

Tseng, S.C., 1989. Concept and application of limbal stem cells. *Eye.* 3, 141-157

Turss, R., et al., 1971. Glucose concentration and hydration of the corneal stroma. *Ophthal Res.* 2, 253-260

Ueda, J., et al., 2002. Distribution of myocilin and extracellular matrix components in the juxtacanalicular tissue of human eyes. *Invest Ophthalmol Vis Sci*. 43, 1068-1076

Vairavamurthy, A., et al., 1997. Characterization of sulfur-containing functional groups in sedimentary humic substances by X-ray absorption near-edge spectroscopy. *Energ Fuel.* 11, 546-553

Van Burskirk, E.M., 1976. Changes in the facility of aqueous outflow induced by lens depression and intraocular pressure in excised human eyes. *Am J Ophthalmol.* 82, 736-740

Van Buskirk, E.M., 1977. Trabeculotomy in the immature, enucleated human eye. *Invest Ophthalmol Vis Sci*. 16, 63–66

Van Buskirk, E.M., Grant, W.M., 1973. Lens depression and aqueous outflow in enucleated primate eyes. *Am J Ophthalmol*. 72, 632–640

Van Buskirk, M.S., Brett, J., 1978. The canine eye: in vitro dissolution of the barriers to aqueous outflow. *Invest Ophthalmol Vis Sci.* 17, 258-263

Van der Rest, M., Garrone, R., 1991. Collagen family of proteins. *FASEB J.* 5, 2814

Veronesi, G., et al. 2013. X-ray Absorption Near-Edge Structure (XANES) Spectroscopy Identifies Differential Sulfur Speciation in Corneal Tissue. *Anal Bioanal Chem*. 405: 6613-6620

Virchow, H., 1910. Graefe-Saemisch Handbuch der gesammten Augenheilkunde. 2nd Edition. Leipzig, Engelmann

Von der Mark, H., et al., 1984. Immunohistochemistry, genuine size and tissue localization of collagen VI. *Eur J Biochem*. 142, 493-502

Weber, I., et al., 1996. Model structure of decorin and implications for collagen fibrillogenesis. *J Biol Chem.* 271, 31767-31770

Wessel, H., et al., 1997. Type XII collagen contributes to diversities in human corneal and limbal extracellular matrices. *Invest Ophthalmol Vis Sci.* 38, 2408–2422

Wiberg, C., et al., 2001. Biglycan and Decorin bind close to the N-terminal region of the collagen VI triple helix. *J Biol Chem.* 276, 18947-18952

Wiberg, C., et al., 2003. Complexes of matrilin-1 and biglycan or decorin connect collagen VI microfibrils to both collagen II and aggrecan. *J Biol Chem*. 278, 37698-37704

Wilson, S.E., Hong, J.W. 2000. Bowman's layer structure and function. Critical or dispensable to corneal function? A hypothesis. *Cornea.* 19, 417-420

Wise, J.B., Witter, S.L., 1979. Argon laser therapy for open-engle glaucoma. A pilot study. *Arch Ophthalmol.* 97, 319–322

Wojdyr, M., 2010. Fityk: a general-purpose peak fitting programm. *Appl Cryst.* 43, 1126-1128

Wolosin, J.M., et al., 2000. Stem cells and differentiation stages in the limbo-corneal epithelium. *Prog Retin Eye Res.* 19, 223-255

Wu, J.J., et al., 1987. Type VI collagen of the intervertebral disc. Biochemical and electron-microscopic characterization of the native protein. *Biochem. J*. 248, 373–381

Wulle, K.G., 1992. Electron microscopy of the fetal development of the corneal endothelium and Descemet's membrane of the human eye. *Invest Ophthalmol Vis Sci.* 11, 897-904

Xia, K., et al., 1998. XANES studies of oxidation states of sulfur in aquatic and soil humic substances. *Soil Sci Soc Am J.* 62, 1240-1246

Yan, D.B. et al., 1991. Effects of hydrogen peroxide-induced oxidative damage on outflow facility and washout in pig eyes. *Invest Ophthalmol Vis Sci.* 32, 2515-2520

Yang, C.J., et al., 1988. Immunohistochemical evidence of heterogeneity in macular corneal dystrophy. *Am J Ophthalmol.* 106, 65-71

Young, B.B., et al., 2002. The roles of types XII and XIV collagen in fibrillogenesis and matrix assembly in the developing cornea. *J Cell Biochem.* 87, 208-220

Young, R.D., et al., 2007. Keratan sulfate glycosaminoglycan and the association with collagen fibrils in rudimentary lamellae in the developing avian cornea. *Invest Ophthalmol Vis Sci.* 48, 3083-3088

Zhang, G., et al., 2009. Genetic evidence for the coordinated regulation of collagen fibrillogenesis in the cornea by decorin and biglycan. *J Biol Chem.* 284, 8888-8897

Zhang, Y., et al., 2005. Detection and quantification of sulfated disaccharides from keratan sulfate and chondroitin/dermatan sulfate during chick corneal development by ESI-MS/MS. *Invest Ophthalmol Vis Sci.*46, 1604-1614

Zimmerman, D.R., et al., 1986**.** Type VI collagen is a major component of the human cornea. *FEBS Lett.* 197, 55–58

Figures

Figure 1.1 adapted from:

http://bio3400.nicerweb.com/bio1151/Locked/media/ch05/collagen.html

Figure 1.5 adapted from:

http://www.studyblue.com/notes/note/n/lecture-6-intro-to-carbs/deck/6708629

Figure 2.3 adapted from:

http://www.niton.com/sf-images/general-images/xrf-excitation-diagram.jpg?sfvrsn=2.

Figure 2.5 adapted from:
http://leung.uwaterloo.ca/MNS/102/Lectures%202007/SSNT4Surface%20Structure%20Determination%20Techniques%20I_files/image027.gif

Appendix I

Chapter 6: Three-dimensional aspects of the ultrastructure and outflow resistance in the human juxtacanalicular tissue

1st Region- #100 - #200

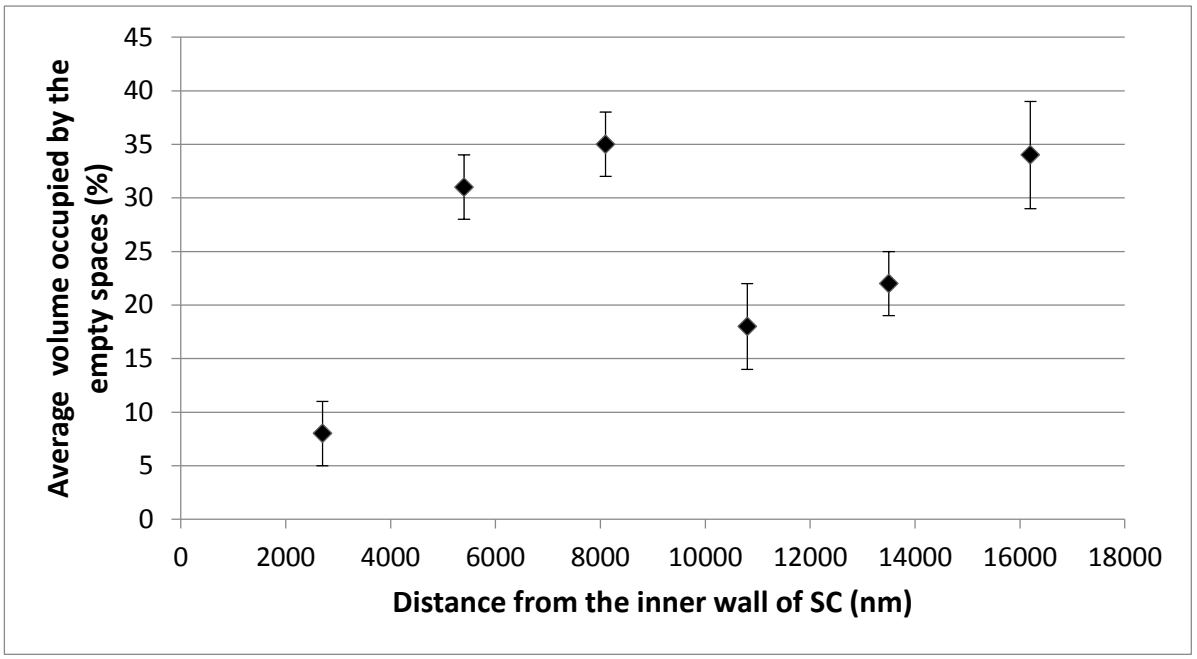

Figure 1: Volume contained by the optically empty spaces of the JCT within the 1st region of the dataset. The average volume, expressed as a percentage, occupied by the optically empty spaces of the JCT against various distances from the borders of the inner wall of SC. Error bars show the standard deviation.

2nd Region- #200 - #300

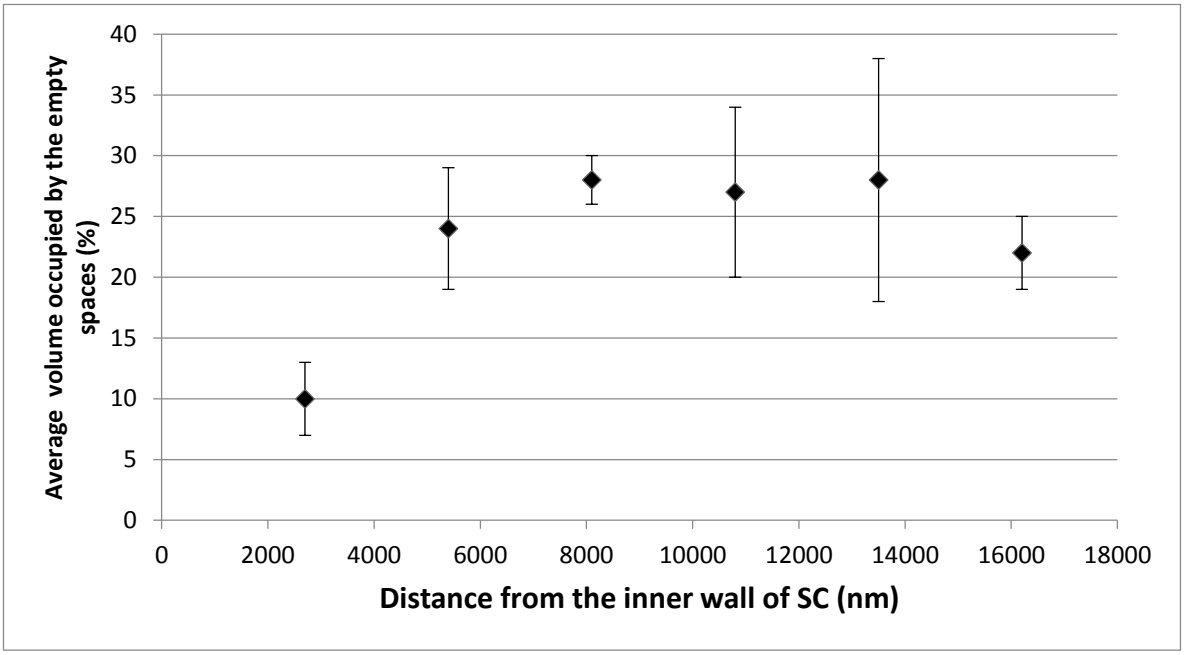

Figure2: Volume contained by the optically empty spaces of the JCT within the 2nd region of the dataset. The average volume, expressed as a percentage, occupied by the optically empty spaces of the JCT against various distances from the borders of the inner wall of SC. Error bars show the standard deviation.

3rd Region- #300 - #400

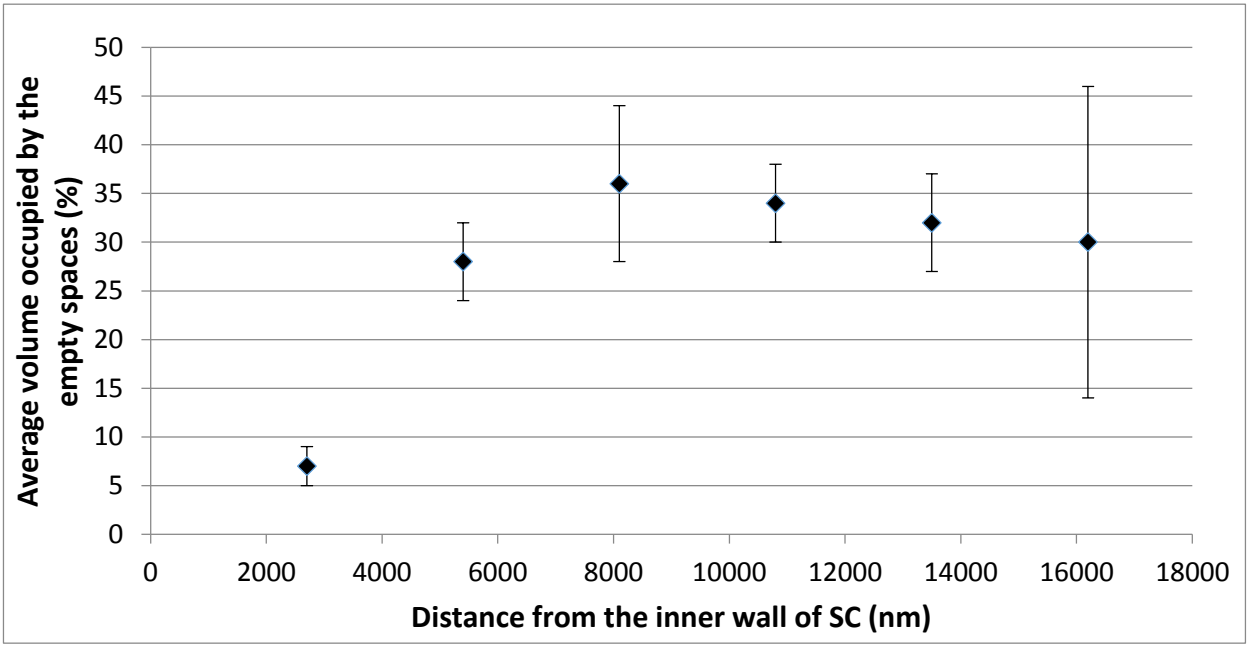

Figure 3: Volume contained by the optically empty spaces of the JCT within the 3rd region of the dataset. The average volume, expressed as a percentage, occupied by the optically empty spaces of the JCT against various distances from the borders of the inner wall of SC. Error bars show the standard deviation.

4th Region- #400 - #500

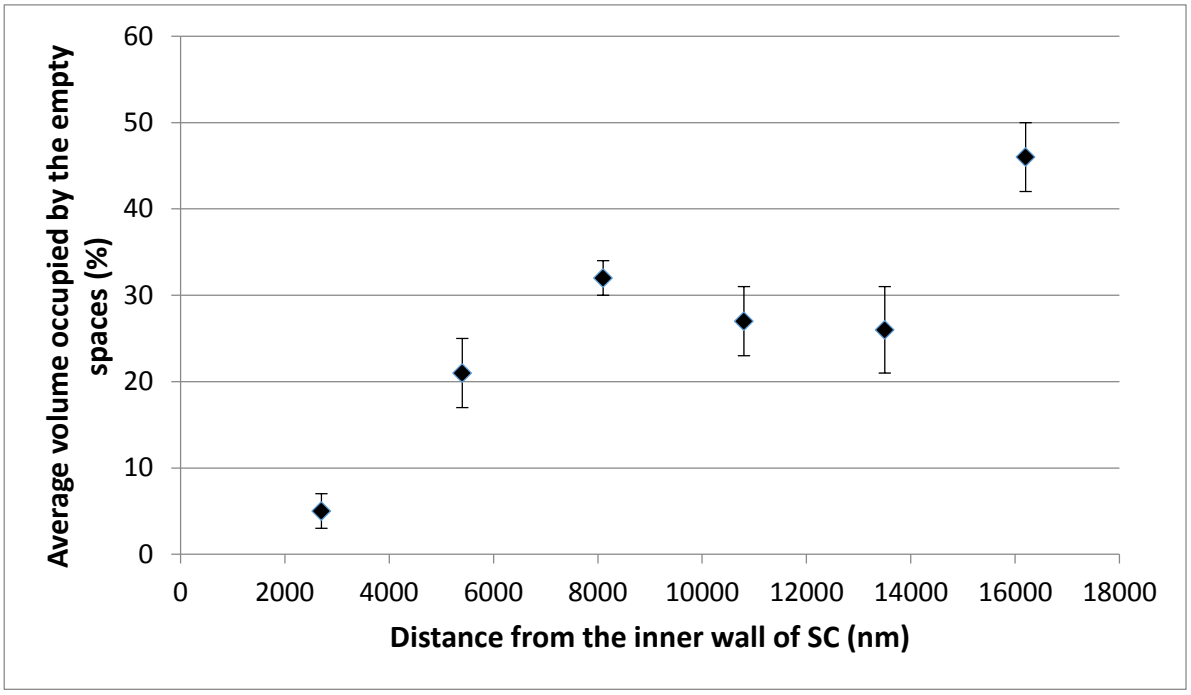

Figure 4: Volume contained by the optically empty spaces of the JCT within the 4th region of the dataset. The average volume, expressed as a percentage, occupied by the optically empty spaces of the JCT against various distances from the borders of the inner wall of SC. Error bars show the standard deviation.

Please cite this article in press as: Koudouna et al., Chemical Composition and Sulfur Speciation in Bulk Tissue by X-Ray Spectroscopy and X-Ray Microscopy: Corneal Development during Embryogenesis, Biophysical Journal (2012), doi:10.1016/j.bpj.2012.05.036

Chemical Composition and Sulfur Speciation in Bulk Tissue by X-Ray Spectroscopy and X-Ray Microscopy: Corneal Development during Embryogenesis

Elena Koudouna,[†] Giulia Veronesi,[‡] Imran I. Patel,[§] Marine Cotte,[‡] Carlo Knupp,[†] Francis L. Martin,[§] and Andrew J. Quantock[†]*

[†]Structural Biophysics Group, School of Optometry and Vision Sciences, Cardiff University, Wales, United Kingdom; [‡]X-ray Microscopy Beamline ID21, European Synchrotron Radiation Facility, Grenoble cedex, France; and [§]Centre for Biophotonics, Lancaster Environment Centre, Lancaster University, Bailrigg, Lancaster, United Kingdom

ABSTRACT The chemical composition and sulfur (S) speciation of developing chick corneas at embryonic days 12, 14, and 16 were investigated using synchrotron scanning x-ray fluorescence microscopy and x-ray absorption near-edge structure spectroscopy. The aim was to develop techniques for the analysis of bulk tissue and identify critical physicochemical variations that correlate with changes in corneal structure-function relationships. Derived data were subjected to principal component analysis and linear discriminant analysis, which highlighted differences in the elemental and S species composition at different stages of embryonic growth. Notably, distinct elemental compositions of chlorine, potassium, calcium, phosphorus, and S altered with development during the transition of the immature opaque cornea to a mature transparent tissue. S x-ray absorption near-edge structure spectroscopy discovered developmentally regulated alterations in thiols, organic monosulfides, ester sulfate, and inorganic sulfate species. The transient molecular structures and compositional changes reported here provide a deeper understanding of the underlying basis of corneal development during the acquisition of transparency. The experimental and analytical approach is new, to our knowledge, and has wide potential applicability in the life sciences.

INTRODUCTION

Developmentally regulated changes in the biochemical composition of the cornea are believed to underlie the acquisition of transparency (1,2). Pioneering early studies characterized tissue morphogenesis and microanatomical restructuring (3,4), whereas others suggested that pivotal changes in the chemical and physicochemical signatures, particularly of sulfated glycosaminoglycans (GAGs), might underlie the maturation of the corneal extracellular matrix, the establishment of its architecture, and the onset of transparency (5–7). More contemporary studies have sought to characterize the transition of the embryonic cornea from an opaque structure to an optically transparent one using a variety of biochemical, immunochemical, or spectroscopic approaches (8–12). In the main, these have been directed at the sulfation patterns of GAGs in the corneal stroma. Investigators have long used synchrotron radiation to probe the ultrastructure of collagen-rich tissues such as cornea, including that of the developing chick (13,14). Now, advances in x-ray absorption spectroscopy and fluorescence microscopy at synchrotron sources provide noninvasive alternatives to traditional biochemical characterizations of biological tissues. This offers scope to enhance our understanding of molecular changes in intact tissues, and allows for study of altered physiology or pathology, wound healing events or age-related changes. Here, we apply these techniques to the study of the chick cornea during embryonic development at day 12 (Fig. 1 *A*), day 14 (Fig.1 *B*), and day 16 (Fig. 1 *C*).

Synchrotron x-ray microscopy and spectroscopy generate large, complex data sets containing a high number of variables; these require powerful computational data reduction and visualization algorithms to facilitate exploratory analysis. Principal component analysis (PCA) followed by linear discriminant analysis (LDA) is a valuable approach for the interrogation of such complex data (15). PCA and LDA techniques are linear transformations, which transform data to a new coordinate system such that the new set of variables are linear combinations of the original variables. For preliminary data reduction and to further visualize variances of spectra in a select number of principal components, PCA has had widespread usage in the exploration of derived data sets following midinfrared spectroscopy (15–18) and, less commonly, x-ray absorption near-edge structure (XANES) spectroscopy (19,20). The PCA-LDA approach for XANES data analysis is an alternative to standard curve fitting methods, because it allows one to readily handle a much larger data set and, therefore, to increase the statistical significance of the results; moreover, when applied to x-ray fluorescence (XRF) data, it allows revealing of differential ionic contents, providing therefore a valuable semiquantitative standard-free alternative to the more commonly employed standard-based fully quantitative methods, when relative changes in concentrations are sought. In this study,

Submitted January 17, 2012, and accepted for publication May 2, 2012.

*Correspondence: quantockaj@cardiff.ac.uk

Editor: James Grotberg.

0006-3495/12/07/0001/8 $2.00

doi: 10.1016/j.bpj.2012.05.036

Please cite this article in press as: Koudouna et al., Chemical Composition and Sulfur Speciation in Bulk Tissue by X-Ray Spectroscopy and X-Ray Microscopy: Corneal Development during Embryogenesis, Biophysical Journal (2012), doi:10.1016/j.bpj.2012.05.036

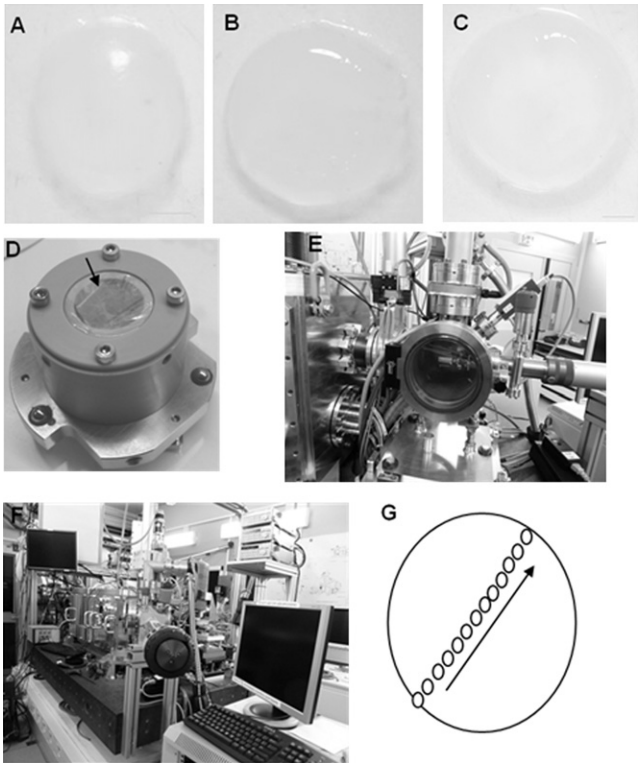

FIGURE 1 Sample preparation for acquisition of XRF and XANES spectra. (*A*) Dissected chick cornea at embryonic day 12, (*B*) day 14, and (*C*) day 16. (*D*) The sample is sandwiched between two sheets of ultralene foil and mounted on the sample holder. The arrow indicates the surface that will be exposed to the x-ray beam. (*E*) The Simulatore di Ambiente Spaziale (SAS) vacuum chamber for sample mounting. Once the sample is placed inside the SAS is pumped. When high vacuum is reached the sample can be introduced into the scanning x-ray microscope by means of a transfer cane. (*F*) Photograph of the scanning x-ray microscope at the end station ID 21, ESRF. Scale bar equals to 1 mm. (*G*) Diagram indicating from where the S speciation XANES point spectra for every developing chick cornea were obtained. For each sample spot, five XANES spectra were acquired. Black arrow shows the direction at which ~13 points were selected to be analyzed.

we set out to establish XRF and XANES spectroscopy as technologies to interrogate intact biological tissue, with subsequent application of PCA-LDA to investigate the changing chemical environment in corneal development during embryogenesis.

MATERIALS AND METHODS

Sample preparation

Fertilized chicken eggs were obtained from a commercial hatchery (Henry Stewart & Co., Louth, Lincolnshire, UK) and incubated at 37.5°C in a humidified chamber (Brinsea Products, Sandford, UK). At embryonic days 12, 14, and 16 of incubation, as validated by Hamilton-Hamburger staging (21,22), corneas were carefully dissected at their edge using surgical tools. All animal work was carried out in accordance with the Association for Research in Vision and Ophthalmology statement for the use of animals for ophthalmic and vision research and in agreement with local ethical rules.

Synchrotron XRF microscopy

For XRF microscopy studies, four corneas per embryonic day were sandwiched between parafilm-covered glass slides and allowed to dry overnight at room temperature. Data were collected at the endstation ID 21 of the European Synchrotron Radiation Facility (ESRF, Grenoble, France) using a scanning x-ray microscope working in the energy range 2–9.2 keV and optimized for x-ray microfluorescence and microspectroscopy imaging of elemental distributions (23). The samples were held between Ultralene foil (SPEX-CERTIPREP), mounted in air at room temperature on the sample holder (Fig.1 *D*, Fig. 1 *E*), and then introduced to the x-ray microscope and measured at high vacuum. Five regions per cornea per embryonic day were selected from the central region of the cornea and an XRF spectrum with an integration time of 60 s was acquired at each location. The incoming photon energy was tuned at 4.1 keV to excite the core electrons of elements up to Ca, with a flux of 3.6×10^9 photons/s. A beam size of 100 μm was obtained using a pinhole. The emitted fluorescence signals were measured with an energy dispersive silicon drift diode detector (XFlash 5100 from Bruker, Germany). The elemental composition of the developing corneas was obtained by extracting the XRF spectra using PyMCA software (24). Thanks to the detecting geometry and operation under vacuum, the background contribution to the XRF spectra was very low, thus background subtraction was not necessary before PCA analysis (see Supporting Material Fig. S1). The distance between the silicon drift diode detector and the sample, and the size of the beam (and therefore the photon flux at sample) were kept constant throughout the experiments to assure the comparability of spectra. Data analyzes were restricted to the range 1.0–4.3 keV and were performed using OPUS 5.5 software (Bruker Optics).

Synchrotron x-ray microspectroscopy

S XANES spectroscopy experiments were performed with the scanning x-ray microscope (Fig.1 *F*) at beamline ID 21 at the ESRF to interrogate developmental changes in sulfur speciation. The instrumentation used was the same as described for XRF. Three corneas at embryonic days 12 and 14, and four at embryonic day 16 were flattened and sandwiched between ultralene foil-covered glass slides. To minimize degradation, the corneas were placed onto dry ice and transferred to −80°C storage until the synchrotron x-ray microspectroscopy experiments could be conducted. Approximately 1 h prior the experiment, slow nitrogen flow was used to defrost the corneas and avoid oxidation events. The samples were then mounted in air at room temperature on the sample holder before being measured at high vacuum. Thirteen locations were interrogated across the diameter of the cornea (Fig.1 *G*). The S speciation of the selected areas was assessed by acquiring five spectra per spot. The x-ray energy was tuned from 2.46 to 2.53 keV with a flux of 5.4×10^9 photons/s, a step size of 0.25eV, and an integration time per energy point of 0.1 s. This resulted in a total integration time of 0.5 s per point over the five spectra. The XANES spectrum was extracted using PyMCA, and a linear background extrapolated from a linear fit of the preedge region was subtracted using OPUS (Bruker Optics). XANES spectra were normalized by setting the edge jump to 1 in MATLAB (The MathWorks, Natick, MA).

Computational analysis

Multivariate analysis was performed on the XRF and XANES spectra using MATLAB R2009b software with an in-house graphical user toolkit for spectroscopy (25). PCA and LDA were applied to the data. PCA was used for preliminary data reduction and visualization of variance between each cornea in an unsupervised manner. LDA, a supervised method, was then applied to allow visualization of the maximum variance between the different developmental corneas. Scores plots, loadings, and cluster vector plots were derived to interpret the results of multivariate analysis.

Please cite this article in press as: Koudouna et al., Chemical Composition and Sulfur Speciation in Bulk Tissue by X-Ray Spectroscopy and X-Ray Microscopy: Corneal Development during Embryogenesis, Biophysical Journal (2012), doi:10.1016/j.bpj.2012.05.036

RESULTS

XRF spectra of the developing chick cornea

Four isolated chick corneas at days 12, 14, and 16 of development were analyzed using the scanning x-ray microscope at the ID 21 beamline of the ESRF. For every corneal sample, 20 independent spectral acquisitions were obtained, derived from five randomly selected areas. PyMCA software (24) was used to extract all the spectra, and identification of the different elements present in the corneal sample was assessed by comparison with tabulated energy values for XRF emission lines (Fig. 2 and Table S1).

Observable differences were apparent in the average spectral ranges, 2000–2300 eV and 2620–3311 eV (Fig. S1). To further extract the major discriminating elemental composition responsible for between-category variation (corneas from a particular day formed one category), multivariate computational analysis with PCA (Fig. S2) followed by LDA (Fig. 3 *A*) was employed in the photon energy region range 1000–4300 eV. In this analysis, chick corneas at days 12, 14, and 16 were discovered to be segregated along the 1st linear discriminant (LD1) factor. Corneas at developmental day 16 vs. days 12 and 14 were shown to be distinct, whereas no clear difference in LD1 was seen between day 12 and day 14. The 2nd linear discriminant (LD2) factor discriminated day 14 from days 12 and 16. No distinction in LD2 was found between day 12 and day 16. PCA-LDA clustering indicated a degree of within-category heterogeneity in the corneas at developmental days 12 and 14, whereas data for the day 16 corneas was more homogeneous. Exploiting the derived loadings plot (Fig. 3 *B*), it is possible to identify the major elemental groupings responsible for distinguishing the average spectrum of each category (i.e., each developmental day) from the average spectra of the other categories. Along LD1, the main distinctive elements responsible for the compositional segregation of chick corneas at day 16 compared to earlier developmental days, listed in order of importance, are phosphorus (P; 2012 eV), sulfur (S; 2306 eV), chlorine (Cl; 2620 eV), and calcium (Ca; 3688 eV). Along LD2, the major elements responsible for discrimination of corneas at day 14 compared to days 12 and 16 are Cl, P, potassium (K; 3312 eV), and Ca. The generation of a cluster vectors plot of the data, which is a linear combination of the PCA-LDA loadings, was obtained from the center of the PCA-LDA scores cluster (Fig. 3 *C*). This allows us to obtain differences from multiple loadings in a single plot, rather than along a single axis (e.g., LD1 or LD2) (15). This analysis indicates that P followed by S and Cl are the main elements that contribute to the

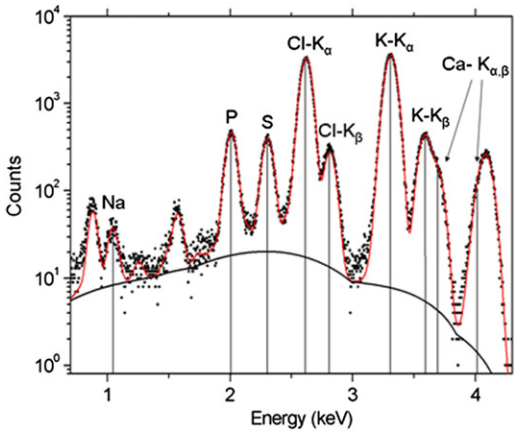

FIGURE 2 XRF spectrum fitted with PyMCA. Experimental XRF spectrum (*dots*) acquired on a 100 μm- diameter region of cornea at embryonic day 14, and its best fitting curve (*upper solid line*) calculated with PyMCA; the background is indicated by the lower solid line. The emission energies relative to the main elemental species encountered in the specimen are reported on the graph, labeled with the corresponding elemental symbol.

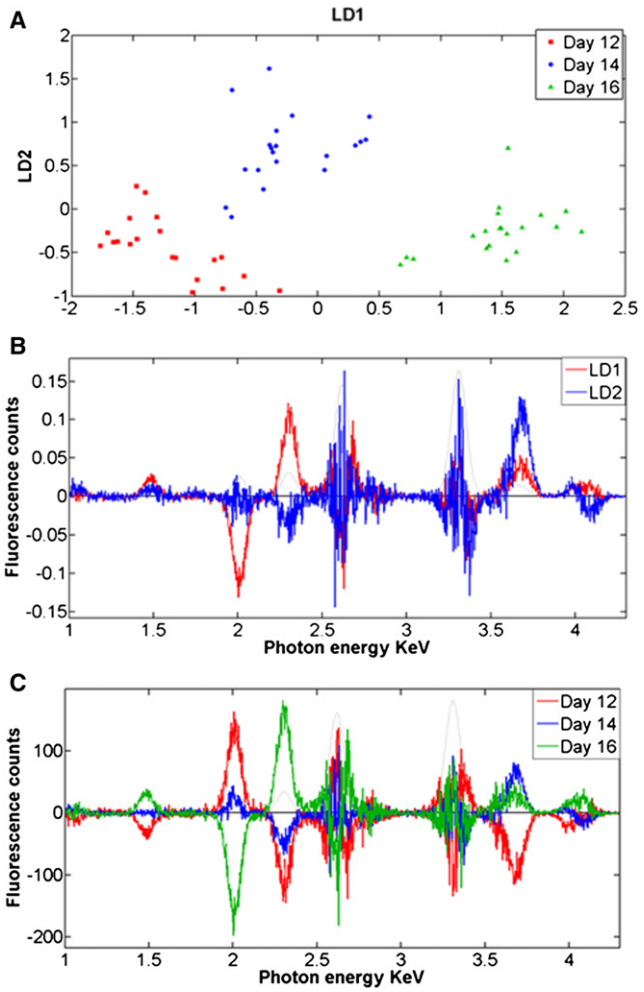

FIGURE 3 Identification of chemical composition alterations of developing chick corneas using PCA-LDA computation of XRF spectra. (*A*) 2D PCA-LDA scores plot of chick corneas at different developmental days: day 12 (*red squares*) vs. day 14 (*blue circles*) vs. day 16 (*green triangles*). (*B*) PCA-LDA loadings plot of developmental chick corneas at day 12, day 14, and day 16 with linear discriminant components (LDs) as follows: LD1 (*red*) and LD2 (*blue*). (*C*) Corresponding PCA-LDA cluster vectors plot of developmental chick corneas at day 12 vs. day 14 vs. day 16.

Please cite this article in press as: Koudouna et al., Chemical Composition and Sulfur Speciation in Bulk Tissue by X-Ray Spectroscopy and X-Ray Microscopy: Corneal Development during Embryogenesis, Biophysical Journal (2012), doi:10.1016/j.bpj.2012.05.036

biochemical diversity between categories as the chick cornea develops and becomes transparent. K and Ca have little impact on the XRF microscopy differences between corneas at distinct developmental stages.

X-ray absorption near-edge structure spectroscopy of the developing chick cornea

Given the presumed importance of the sulfonation status of corneal GAGs in corneal structural modulation, S K-edge XANES spectroscopy was performed to assess the role of this element's speciation in corneal development. Three corneal samples per embryonic day 12 and 14 along with four corneal samples of embryonic day 16 were interrogated and S XANES point spectra were acquired. The energy position of the peaks in the near-edge region of the absorption coefficient of S alters in the range 2469–2483 eV (26). The assorted S-containing compounds in the corneal samples were evaluated by comparing the absolute energy values to the respective energies for standard sulfur compounds obtained from previous studies as summarized in Table 1. It should be noted that it is not possible to distinguish between inorganic sulfate (SO_4^{2-}) and ester sulfate (R-O-SO_3) because their XANES spectra peak energies are identical (2482.5 ± 0.5 eV), as has been reported in previous studies that investigated the S speciation by XANES microspectroscopy in humic and fulvic acids (27), in marine sediments (28), and in soils and soil particles (26). This is also the case for the differentiation between thiols (R-SH) and organic monosulfides (R-S-R′) because the peak energies of these S-containing compounds are also similar (Table 1) (29). These caveats aside, XANES data can provide important information about the biomolecular status of S in tissues. Our data clearly disclose changes in the character of S during corneal morphogenesis with corresponding average S XANES spectra (Fig. 4) providing information on the major S species, thiols, and organic monosulfides (2.4734 keV), inorganic sulfate, and ester sulfate (2.4835 keV).

A large number of XANES point spectra were acquired to achieve study robustness. Otherwise, it is difficult to distinguish whether similarities or differences in the S species are within-category or between-category. Thus, multivariate analysis was applied to the 2.46–2.49 keV spectral region. PCA was performed to reduce the data and visualize segregation in an unsupervised fashion (Fig. S3), whereas PCA-LDA was applied to extract variance in a supervised manner and highlight between-category differences (Fig. 5 *A*). The analysis reveals distinct clustering and between-category segregation. Specifically, PCA-LDA showed that corneas at days 14 and 16 of development are more homogeneous with respect to their content of S species. In contrast, day 12 corneas exhibited more heterogeneity. Noticeably, some overlap is seen between corneas of developmental days 12 and 14 suggestive of progressive chemical alterations. PCA-LDA loadings plots (Fig. 5 *B*) highlighted the S forms that are responsible for spectral variance and intercategory discrimination. Certainly, LD1 contributes toward segregation of developmental corneas at day 16 vs. days 12 and 14 with contributions mainly associated with inorganic sulfate and ester sulfate (2.483 keV), but also with thiols and organic monosulfides (2.4736 keV). LD2 contributes to day 12 and day 14 segregation, but its spread mainly reflects an intracategory variation at day 12. The data indicate that thiols and organic monosulfides are primary contributors

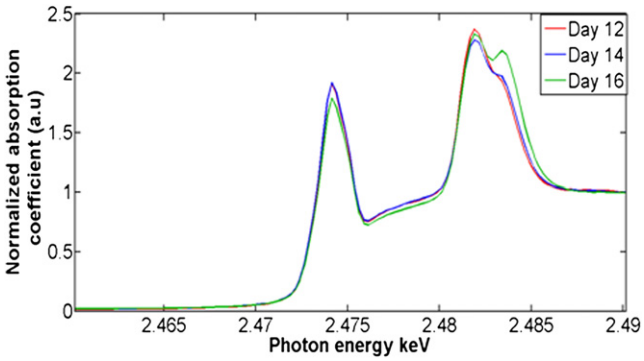

FIGURE 4 S speciation alterations in the developing chick cornea. S K-edge x-ray absorption near-edge spectroscopy means spectra for the embryonic chick corneas at days 12 (*red*), 14 (*blue*), and 16 (*green*) of development.

TABLE 1 Peak energies of the first-order X-ray resonance lines for S species (compilation of literature data)

			Peak energies eV (Reference number)		
S form		Example	(27)	(37)	(38)
Elemental S	S^o		2472.5	2472.5	
Organic polysulfide	R-S-S-S-R′			2473	
Organic disulfide	R-S-S-R′	Cystine	2472.8	2473	2472
Thiols	R-SH	Cysteine		2473.5	2473.5
Organic monosulfides	R-S-R′	Methionine	2473.1	2473.5	2473.5
Sulfoxide	R-S=O	Methionine sulfoxide		2476	2476
Ester sulfate	R-O-SO_3	Chondroitin sulfate	2482.5	2483.5	2482
Inorganic sulfate	SO_4^{2-}	Sodium sulfate	2482.5	2483.5	2483

Peak energies of the first-order x-ray resonance lines for S-containing compounds vary in the range between 2469 and 2483 eV. The absolute peak energy values for distinct sulfur species obtained by other researchers differ slightly from one another.

Please cite this article in press as: Koudouna et al., Chemical Composition and Sulfur Speciation in Bulk Tissue by X-Ray Spectroscopy and X-Ray Microscopy: Corneal Development during Embryogenesis, Biophysical Journal (2012), doi:10.1016/j.bpj.2012.05.036

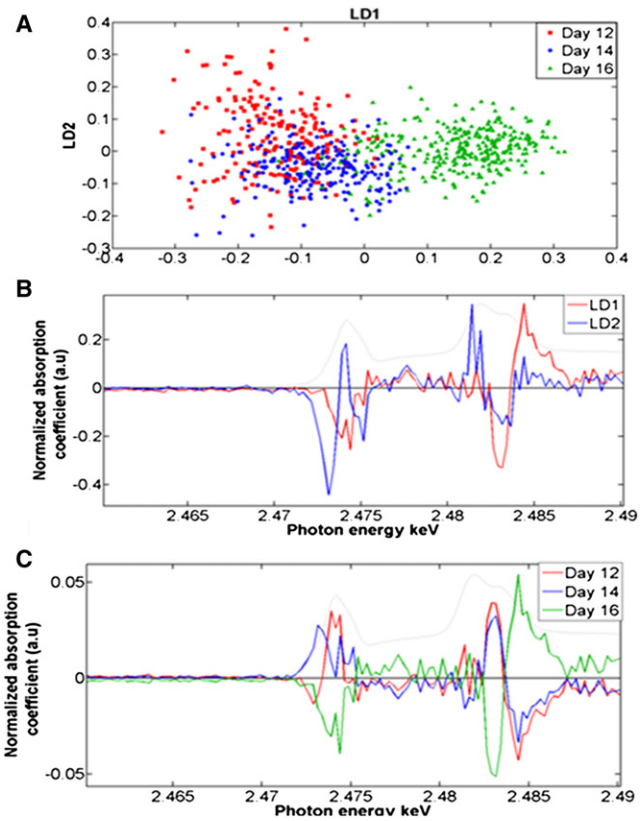

FIGURE 5 Identification of distinct S species alterations in developmental chick corneas using PCA-LDA computation following XANES spectroscopy. (*A*) 2D PCA-LDA scores plot of chick corneas at different developmental days: day 12 (*red squares*) vs. day 14 (*blue circles*) vs. day 16 (*green triangles*). (*B*) PCA-LDA loadings plot of developing corneas at day 12 vs. day 14 vs. day 16 with LD components as follows: LD1 (*red*) and LD2 (*blue*). (*C*) Corresponding PCA-LDA cluster vectors plot of developmental chick cornea at day 12 vs. day 14 vs. day 16.

for separation followed by inorganic sulfate and ester sulfate. A cluster vectors plot indicated that the influential discriminating sulfur species are thiols and organic monosulfides, organic disulfides (2.4725 keV), inorganic sulfate, and ester sulfate, which all showed remarkable differences among the developmental corneas (Fig. 5 *C*) at days 12, 14, and 16.

Embryonic day 12 vs. embryonic day 14

Further analysis was carried out on chick corneas at embryonic day 12 vs. embryonic day 14 to elucidate the differences and similarities at this developmental period just before the cornea starts to become transparent. PCA-LDA scores plots disclosed a marked overlap in the data sets from day 12 and day 14 corneas (Fig. 6 *A*). The corresponding cluster vectors plot (Fig. 6 *B*) compares day 12 vs. day 14 spectra on the vector plot and vice versa, indicating that the distinguishing species are thiols and organic monosulfides, inorganic sulfate, and ester sulfate.

Embryonic day 12 vs. embryonic day 16

Unlike the day 12 vs. day 14 comparison, further multivariate analysis of data from chick corneas at embryonic day 12 vs. embryonic day 16 showed clear segregation of the two categories. The 1-D PCA-LDA scores plot revealed a relatively small overlap between the two categories (Fig. 6 *C*) reflecting the variance in the S speciation between the two embryonic days. The corresponding cluster vectors plot showed the key distinguishing S species associated with the segregation of the two categories (Fig. 6 *D*), and these, in order of importance are inorganic sulfate and ester sulfate, thiols, and organic monosulfides.

Embryonic day 14 vs. embryonic day 16

Chick corneas at day 14 of development were compared and contrasted to embryonic day 16 corneas and the corresponding PCA-LDA scores plot indicated a clear overlap between the two categories (Fig. 6 *E*). In regard to the cluster vectors plot (Fig. 6 *F*), however, there are major differences in the S speciation between the two developmental time points. The S species that are responsible for the segregation between the two categories are primarily inorganic sulfate and ester sulfate. Minor variance is also observed in the thiols and organic monosulfides species between the two developmental stages.

DISCUSSION

XRF microscopy and XANES spectroscopy with subsequent multivariate analysis (PCA-LDA) were used to provide new, to our knowledge, insights into the biochemical changes of extracellular matrix molecules during tissue morphogenesis in the chick cornea. PCA-LDA scores plots indicated differences between embryonic corneas at days 12, 14, and 16 of development on the basis of the distances between clusters. Loadings plots and cluster vectors plots further identified the chemical entities responsible for segregation of the tissue samples.

Importantly, our results revealed changes in the chemical environment of Cl, K, and Ca elements that contribute to the segregation of data sets at days 12, 14, and 16 of development. These are potentially important ions that will impact on the fixed negative charge density in the corneal extracellular matrix, which itself, is predominantly generated by transient mobile ion binding (30). Developmental alterations in the ionic environment of Cl^{-}, K^{+}, and Ca^{2+} may underlie changes in the physicochemical corneal architecture that help make the tissue transparent to light. The corneal stroma is predominantly composed of collagen fibrils that are uniform in diameter and regularly spaced. This tissue-specific arrangement allows light transmission through the cornea and is based on the interference of light scattered by individual collagen fibrils (31–33). Ion binding

Please cite this article in press as: Koudouna et al., Chemical Composition and Sulfur Speciation in Bulk Tissue by X-Ray Spectroscopy and X-Ray Microscopy: Corneal Development during Embryogenesis, Biophysical Journal (2012), doi:10.1016/j.bpj.2012.05.036

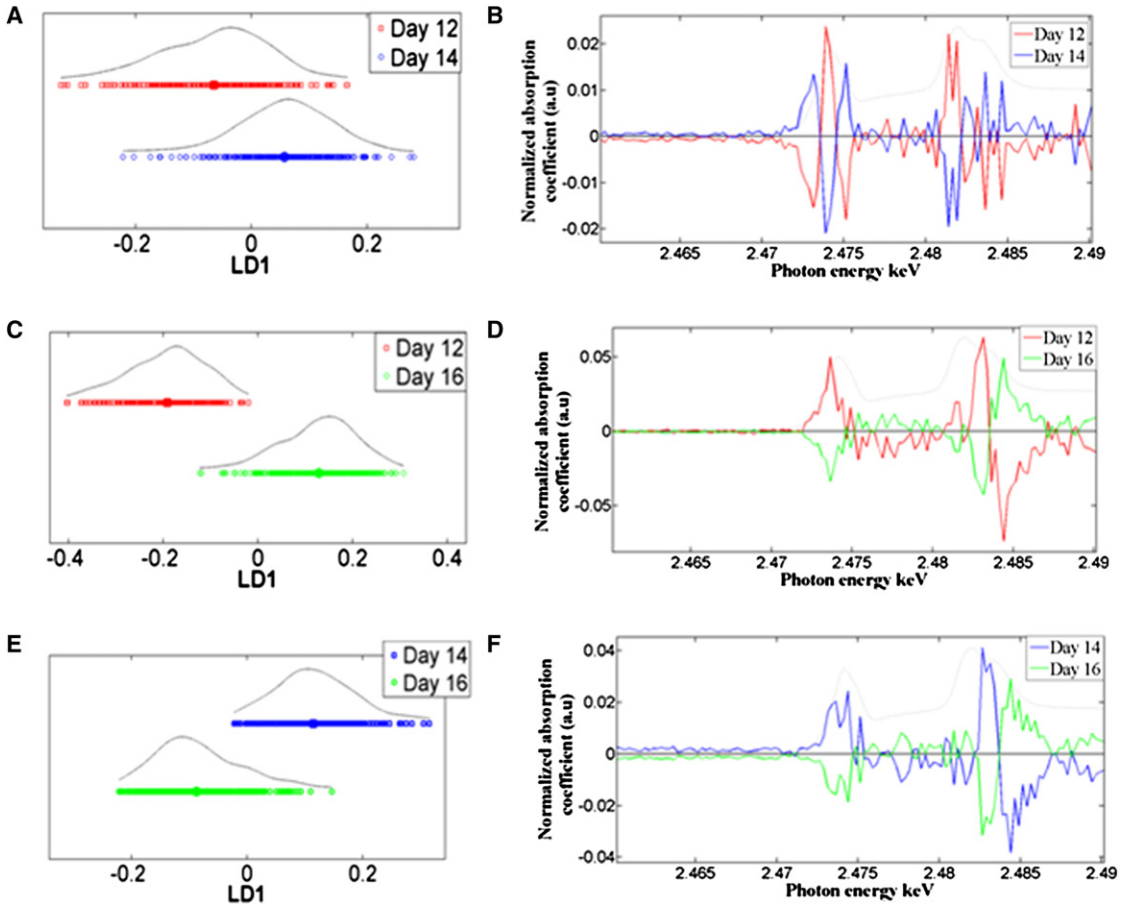

FIGURE 6 PCA-LDA scores and cluster vectors plots of embryonic corneas at days 12, 14, and 16 of development following XANES spectroscopy analysis. (*A*) 1D PCA-LDA scores plot of embryonic day 12 vs. embryonic day 14 and (*B*) the corresponding cluster vectors plot. (*C*) 1D PCA-LDA scores plot of embryonic day 12 vs. embryonic day 16, and (*D*) the corresponding cluster vectors plot. (*E*) 1D PCA-LDA scores plot of embryonic day 14 vs. embryonic day 16, and (*F*) the corresponding cluster vectors plot.

within the cornea is believed to be crucial in determining the net surface charge on collagen fibrils, which in turn helps govern the surface-to surface interactions between fibrils, and hence their arrangement (30). This concept is supported by studies of corneas loaded with various concentrations of chloride in which it was shown that chloride ions regulated the fixed negative charge of the corneal matrix and led to a strong dependence on tissue transparency (34). Thus, changes of the chemical environment of Cl may involve binding of chloride ions to collagen fibrils in the corneal stroma, reflecting the changes of the corneal molecular environment and fibrillar architecture. This may well be manifest in the transition of the developing chick corneas from an opaque tissue at days 12 and 14 to a more transparent one at day 16. We also point out that as the charge must be balanced regardless of the involved charge carriers, chloride ions alone are unlikely to be able to influence the tissue charge. There might be an increase in basic residues (amino acids) that lead to an increase in the net positive charge, which in turn must be balanced by chloride ions as negative charge carriers. Similarly, the degree of sulfonation of GAG might affect the concentration of cations such as K+ or Ca^{2+} to balance the negative charge. In this sense, chloride or potassium only reflect the changes in the molecular environment (proteins and glycans) and cannot affect the net charge independently. Correlating the results of the scores, loadings and cluster vector plots it was further discovered that the molecular environment of P changed markedly over the developmental period between embryonic day 12 and day 16. DNA and RNA exhibit numerous phosphate groups, thus, changes in the biochemical character of P are likely related to changes in the presumptive keratocyte population over time and an altered genetic component within these cells.

Sulfated proteoglycans are believed to be key drivers of matrix morphogenesis in developing chick corneas during the acquisition of transparency (5–12). The current study reports clear changes in the molecular signature of S that occurred between embryonic days 12–16. Subsequent XANES spectroscopy investigation of alterations in the S species present in the developing cornea, followed by PCA-LDA multivariate analysis, highlighted the biochemical

Please cite this article in press as: Koudouna et al., Chemical Composition and Sulfur Speciation in Bulk Tissue by X-Ray Spectroscopy and X-Ray Microscopy: Corneal Development during Embryogenesis, Biophysical Journal (2012), doi:10.1016/j.bpj.2012.05.036

molecules that discriminate embryonic corneas at day 12 vs. day 14 vs. day 16. Thiols, organic monosulfides, ester sulfate, and inorganic sulfate were the discriminating variables that underwent a compositional transition during the development of the chick cornea. Variation in the thiol species during embryonic development is likely linked to the N-terminal cysteine consensus sequence region of the small leucine-rich corneal proteoglycans. Developmental differences in the organic monosulfide biochemical peak between days 12–16 are predicted to be associated with protein synthesis and the S methionine amino acid.

Analysis of the XANES spectra suggest that changes in the ester sulfate and inorganic sulfate species that arise during development might be measures of alterations in the keratan sulfate (KS) and chondroitin sulfate/dermatan sulfate (CS/DS) molecular populations. This contention is consistent with studies that report a peak near 2.482 keV, which is attributed to CS (35,36) and document progressive changes in the profiles of KS and CS/DS disaccharides during chick corneal development (9). More specifically, Zhang et al. reported a significant increase in the concentration of sulfated KS around embryonic day 14, in contrast to the concentration of CS/DS disaccharides, which was found to decrease during embryonic development. Mention should also be made of the phenomenon of both low- and high-sulfated KS epitopes existing within individual GAG side chains, and the fact that a differential expression of lesser and highly sulfated KS was evident at developmental days 12 and 15 in experiments conducted using sulfation-specific monoclonal antibodies (12). It is therefore plausible to propose that the changes in the S speciation observed in this study may reflect changes in the degree of sulfonation of low- and high-sulfated GAG side chains. It is instructive to consider the importance of the sulfation pattern of KS for corneal hydration and transparency. In the cornea, the core protein region of a proteoglycan associates with the collagen fibril, whereas the GAG chain extends into the extrafibrillar space. The sulfation status of GAGs is important because it will affect the negative charge of the chains. This, in turn, determines the interactions with other GAGs, the hydrophilic character of the stroma, tissue hydration, and the characteristic fibrillar architecture of the cornea that is necessary for corneal transparency. The current data provide noninvasive evidence, which describe specific changes in the elemental composition of the connective tissue matrix of the embryonic cornea as it develops and becomes transparent, and report how XRF microscopy and XANES spectroscopy can be applied to gain biomolecular information of bulk biological tissue.

SUPPORTING MATERIAL

Supplementary information, three figures, and one table are available at http://www.biophysj.org/biophysj/supplemental/S0006-3495(12)00616-9.

The authors thank Dr. Rob Young and Ms. Frances Jones for help with specimen preparation.

This work was supported by a project grant from the UK Engineering and Physical Sciences Research Council (grant EP/F034970 to AJQ). E.K. is the recipient of a Cardiff University President's Studentship. We thank the European Synchrotron Radiation Facility (ESRF) (http://www.esrf.eu) for providing access to beamtime.

REFERENCES

1. Linsenmayer, T. F., J. M. Fitch, …, D. E. Birk. 1998. Development and roles of collagenous matrices in the embryonic avian cornea. *Prog. Retin. Eye Res.* 17:231–265.
2. Quantock, A. J., and R. D. Young. 2008. Development of the corneal stroma, and the collage-proteoglycan associations that help define its structure and function. *Dev. Dyn.* 237:2607–2621.
3. Coulombre, A. J., and J. L. Coulombre. 1958. Corneal development. I. Corneal transparency. *J. Cell. Physiol.* 51:1–11.
4. Hay, E. D., and J.-P. Revel. 1969. Fine structure of the developing avian cornea. *In* Monographs in Developmental Biology. I. A. Wolsky, N. Y. Tarrytown, and P. S. Chen, editors. S. Karger, Basel, Switzerland, New York. 1–44.
5. Anseth, A. 1961. Glycosaminoglycans in the developing corneal stroma. *Exp. Eye Res.* 1:116–121.
6. Conrad, G. W. 1970. Collagen and mucopolysaccharide biosynthesis in the developing chick cornea. *Dev. Biol.* 21:292–317.
7. Hart, G. W. 1976. Biosynthesis of glycosaminolgycans during corneal development. *J. Biol. Chem.* 251:6513–6521.
8. Cornuet, P. K., T. C. Blochberger, and J. R. Hassell. 1994. Molecular polymorphism of lumican during corneal development. *Invest. Ophthalmol. Vis. Sci.* 35:870–877.
9. Zhang, Y., A. H. Conrad, …, G. W. Conrad. 2005. Detection and quantification of sulfated disaccharides from keratan sulfate and chondroitin/dermatan sulfate during chick corneal development by ESI-MS/MS. *Invest. Ophthalmol. Vis. Sci.* 46:1604–1614.
10. Gealy, E. C., B. C. Kerr, …, J. R. Ralphs. 2007. Differential expression of the keratan sulphate proteoglycan, keratocan, during chick corneal embryogenesis. *Histochem. Cell Biol.* 128:551–555.
11. Young, R. D., E. C. Gealy, …, A. J. Quantock. 2007. Keratan sulfate glycosaminoglycan and the association with collagen fibrils in rudimentary lamellae in the developing avian cornea. *Invest. Ophthalmol. Vis. Sci.* 48:3083–3088.
12. Liles, M., B. P. Palka, …, A. J. Quantock. 2010. Differential relative sulfation of Keratan sulfate glycosaminoglycan in the chick cornea during embryonic development. *Invest. Ophthalmol. Vis. Sci.* 51:1365–1372.
13. Quantock, A. J., S. Kinoshita, …, D. J. Schanzlin. 1998. A synchrotron x-ray diffraction study of developing chick corneas. *Biophys. J.* 74:995–998.
14. Meek, K. M., and A. J. Quantock. 2001. The use of x-ray scattering techniques to determine corneal ultrastructure. *Prog. Retin. Eye Res.* 20:95–137.
15. Martin, F. L., J. G. Kelly, …, M. J. Walsh. 2010. Distinguishing cell types or populations based on the computational analysis of their infrared spectra. *Nat. Protoc.* 5:1748–1760.
16. Kelly, J. G., P. L. Martin-Hirsch, and F. L. Martin. 2009. Discrimination of base differences in oligonucleotides using mid-infrared spectroscopy and multivariate analysis. *Anal. Chem.* 81:5314–5319.
17. Patel, I. I., J. Trevisan, …, F. L. Martin. 2011. Segregation of human prostate tissues classified high-risk (UK) versus low-risk (India) for adenocarcinoma using Fourier-transform infrared or Raman microspectroscopy coupled with discriminant analysis. *Anal. Bioanal. Chem.* 401:969–982.

Please cite this article in press as: Koudouna et al., Chemical Composition and Sulfur Speciation in Bulk Tissue by X-Ray Spectroscopy and X-Ray Microscopy: Corneal Development during Embryogenesis, Biophysical Journal (2012), doi:10.1016/j.bpj.2012.05.036

18. Taylor, S. E., K. T. Cheung, …, F. L. Martin. 2011. Infrared spectroscopy with multivariate analysis to interrogate endometrial tissue: a novel and objective diagnostic approach. *Br. J. Cancer.* 104:790–797.

19. Beauchemin, S., D. Hesterberg, and M. Beauchemin. 2002. Principal component analysis approach for modeling sulfur K-XANES spectra of humic acids. *Soil. Sci. Soc. Am. J.* 66:83–91.

20. Anunziata, O. A., A. R. Beltramone, …, E. Lede. 2011. XANES-PCA analysis of Ti- species in MCM-41 mesoporous silica synthesized by different method. *Appl. Catal. A Gen.* 397:22–26.

21. Hamburger, V., and H. Hamilton. 1951. A series of normal stages in development of the chick embryo. *J. Morphol.* 88:49–92.

22. Hamburger, V. 1992. The stage series of the chick embryo. *Dev. Dyn.* 195:273–275.

23. Barrett, R., B. Kaulich, …, J. Susini. 2000. Current status of the scanning x-ray microscope at the ESRF. *AIP Conf. Proc.* 507:458–463.

24. Solé, A. V., E. Papillon, …, J. Susini. 2007. A multiplatform code for the analysis of energy- dispersive x-ray fluorescence spectra. *Spectrochim. Acta. B.* 62:63–68.

25. Trevisan, J., P. P. Angelov, …, F. L. Martin. 2010. Syrian hamster embryo (SHE) assay (pH 6.7) coupled with infrared spectroscopy and chemometrics towards toxicological assessment. *Analyst (Lond.).* 135:3266–3272.

26. Prietzel, J., J. Thieme, …, I. Kögel-Knabner. 2003. Speciation of sulphur in soils and soil particles by x-ray spectromicroscopy. *Eur. J. Soil Sci.* 54:423–433.

27. Morra, M. J., S. E. Fendorf, and P. D. Brown. 1997. Speciation of sulfur in humic and fulvic acids using x-ray absorption near-edge structure (XANES) spectroscopy. *Geochim. Cosmochim. Acta.* 61:683–688.

28. Vairavamurthy, A., W. Zhou, …, B. Manowitz. 1994. Sulfonates: a novel class of organic sulfur compounds in marine sediments. *Geochim. Cosmochim. Acta.* 58:4681–4687.

29. Xia, K., F. Weesner, …, P. A. Helmke. 1998. XANES studies of oxidation states of sulfur in aquatic and soil humic substances. *Soil. Sci. Soc. Am. J.* 62:1240–1246.

30. Elliott, G. F., and S. A. Hodson. 1998. Cornea, and the swelling of polyelectrolyte gels of biological interest. *Rep. Prog. Phys.* 61:1325–1365.

31. Maurice, D. M. 1957. The structure and transparency of the cornea. *J. Physiol.* 136:263–286.

32. Benedek, G. B. 1971. Theory of transparency of the eye. *Appl. Opt.* 10:459–473.

33. Farrell, R. A., and R. L. McCally. 2000. Corneal transparency. *In* Principles and Practice of Ophthalmology. D. M. Albert and F. A. Jakobiec, editors. WB Saunders, Philadelphia, PA. 629–643.

34. Kostyuk, O., O. Nalovina, …, S. A. Hodson. 2002. Transparency of the bovine corneal stroma at physiological hydration and its dependence on concentration of the ambient anion. *J. Physiol.* 543:633–642.

35. Dauphin, Y., E. J. P. Cuif, …, E. C. T. Williams. 2003. In situ mapping of growth lines in the calcitic prismatic layers of mollusc shells using x-ray absorption near-edge structure (XANES) spectroscopy at the sulphur K-edge. *Mar. Biol.* 142:299–304.

36. Dauphin, Y., J. P. Cuif, …, C. T. Williams. 2006. Microstructure and chemical composition of giant avian eggshells. *Anal. Bioanal. Chem.* 386:1761–1771.

37. Sarret, G., J. Connan, …, L. Eybert-Bèrard. 1999. Chemical forms of sulfur in geological and archaeological asphaltenes from Middle East, France, and Spain determined by sulfur K- and L-edge x-ray absorption near-edge spectroscopy. *Geochim. Cosmochim. Acta.* 63:3767–3779.

38. Vairavamurthy, A., D. Maletic, …, T. Lyons. 1997. Characterization of sulfur-containing functional groups in sedimentary humic substances by x-ray absorption near-edge spectroscopy. *Energy Fuels.* 11:546–553.

Anal Bioanal Chem
DOI 10.1007/s00216-013-7120-x

RESEARCH PAPER

X-ray absorption near-edge structure (XANES) spectroscopy identifies differential sulfur speciation in corneal tissue

Giulia Veronesi · Elena Koudouna · Marine Cotte · Francis L. Martin · Andrew J. Quantock

Received: 21 February 2013 / Revised: 27 May 2013 / Accepted: 5 June 2013

Abstract The chemical composition of tissues can influence their form and function. As a prime example, the lattice-like arrangement of collagen fibrils required for corneal transparency is controlled, in part, by sulfated proteoglycans, which, via core proteins, bind to the collagen at specific locations along the fibril axis. However, to date, no studies have been able to directly identify and characterize sulfur (S) in the cornea as a function of tissue location. In this study, X-ray absorption near-edge structure spectroscopy and micro-beam X-ray fluorescence (μ-XRF) chemical contrast imaging were employed to probe the nature of the mature (bovine) cornea as a function of position from the anterior sub-epithelial region into the deep stroma. Data indicate an inhomogeneity in the composition of S species in the first ≈50 μm of stromal depth. In μ-XRF chemical contrast imaging, S did not co-localize with phosphorous (P) in the deep stroma where sulfates are prominent. Rather, P is present only as isolated micrometric spots, presumably identifiable as keratocytes. This study lends novel insights into the elemental physiology of mature cornea, especially in relation to its S distribution; future studies could be applied to human tissues. Moreover, it defines an analytical protocol for the interrogation of S species in biological tissues with micrometric resolution.

Keywords XANES spectroscopy · μ-XRF Imaging · Sulfur speciation · Cornea

G. Veronesi (✉) · M. Cotte
X-Ray Microscopy Beamline ID21, European Synchrotron Radiation Facility, POB 220, Grenoble Cedex 9, France
e-mail: giulia.veronesi@esrf.fr

E. Koudouna · A. J. Quantock
Structural Biophysics Group, School of Optometry and Vision Sciences, Cardiff University, Maindy Road, Cardiff CF24 4LU, Wales, UK

F. L. Martin
Centre for Biophotonics, Lancaster Environment Centre, Lancaster University, Bailrigg, Lancaster LA1 4YQ, UK

Published online: 19 June 2013

Abbreviations

GCF	Gaussian curve fitting
LCF	Linear combination fitting
μ-XRF	Micro-beam X-ray fluorescence
XANES	X-Ray absorption near-edge structure
ESI-MS/MS	Electrospray ionization tandem mass spectrometry

Introduction

The cornea is the optically clear, collagen-rich tissue at the front of the eye. Unlike other connective tissues with no dissimilar biological compositions such as tendon, sclera, cartilage, and intervertebral disc, the cornea is transparent to light in the visible range. This crucial property is a consequence not of the corneal tissue possessing a uniform refractive index as is the case in homogeneous and amorphous materials but because of a remarkably well-ordered internal fine structure. Collagen fibrils are uniformly 25 nm in diameter and are arranged in flat belts, or lamellae, which undulate and interweave, but generally run parallel to the corneal surface [1]. Approximately 250 lamellae comprise the full corneal thickness, which is about 0.5 mm in adult humans [2]. Individual collagen fibrils scatter light, and a disordered or poorly ordered arrangement of collagen fibrils would lead to an opaque tissue; however, high levels of light transmission occur. The cornea acts somewhat like a three-dimensional diffraction grating, with light scattered by individual collagen fibrils interfering in such a way as to allow transmission through the tissue [3–9].

The arrangement of collagen fibrils required for corneal transparency is controlled, in part, by proteoglycans, which, via their core proteins, bind to collagen fibrils at specific locations along the fibril length [10, 11]. The glycosaminoglycan motifs of the proteoglycans extend into the extrafibrillar space, where they interact with each other and

with other matrix components to govern the collagen fibrillar architecture [12–14]. Importantly, the repeating disaccharides of the glycosaminoglycan chains in cornea are fairly heavily sulfated, a property which is key in defining the hydrophilic nature of the tissue. The swelling properties of the cornea and the spatial organization of the collagen fibrils are therefore reliant on the sulfation patterns of the corneal glycosaminoglycans [15–18]. The cornea, throughout its depth, however, exhibits a differential pattern of proteoglycan sulfation, particularly in the thicker corneas of larger animals (humans included) in which keratan sulfate is more prevalent in deeper regions of the stroma, away from the corneal surface [19, 20]. Most current knowledge about the sulfation status of corneal proteoglycans is derived from histochemical, immunochemical, or immunohistochemical investigations [19–23]. Keratan sulfate disaccharide sulfation has also been measured in scarred and developing cornea by electrospray ionization tandem mass spectrometry (ESI–MS/MS) [24, 25]. Recently, we applied spectroscopic approaches to study the biomolecular characteristics of embryonic avian cornea, S included, as an average throughout its entire thickness [26, 27]. However, no studies to date have been able to directly study the sulfation status of the mature cornea in a depth-profiled manner. Here, we use X-ray absorption near-edge structure (XANES) spectroscopy to examine the chemical composition of the corneal stroma as a function of tissue depth.

XANES is a core-level spectroscopy technique that provides insights about the coordination chemistry and oxidation state of a selected element in a material. The K-edge XANES spectra of S compounds are known to be rich in chemical information thanks to the presence of distinct resonance peaks whose energy position is in linear correlation with the oxidation state of the S species responsible for them [28]. These peaks are over 14 eV, which makes it possible to decompose them by means of computational methods like Gaussian curve fitting (GCF) or by comparison with standard compounds followed by linear combination fitting (LCF). The analysis of S K-edge XANES spectra has been at first adopted in a range of geochemical studies because it has proven to be an informative method for the assessment of the S fractions in coal [29], humic substances [28], and soil particles [30]; these studies, and other geochemical investigations performed over the last two decades, made use of the GCF method, which has been therefore strongly validated and continuously improved; it is currently able to provide the relative concentrations of S species with an accuracy in the range 5–10 %, much higher than that achievable with traditional chemical methods [30]. Several diverse biochemical investigations have benefited from the information derived from S XANES experiments, including shedding novel insights into the storage of sulfur globules in photosynthetic sulfur bacteria [31], the developmental pathways of neuromelanin in human brain [32], and the structural characterization of Ure2p protein fibrillar assemblies [33]; the analysis strategy chosen for these investigations was LCF.

Moreover, the peculiar sharp features of S K-edge absorption spectra can be exploited to enhance the contrast between chemical species in micro-beam X-ray fluorescence (μ-XRF) imaging [34], by tuning the excitation energy of the X-ray beam in order to maximize the absorption from the desired species. Here, we use XANES spectroscopy to probe the nature of S in the mature (bovine) cornea as a function of position within the tissue from the anterior sub-epithelial region into the deep stroma.

Materials and methods

Sample preparation

Eyes from mature cattle were obtained from the Ensors abattoir (Cinderford, Gloucestershire, UK). Corneas were carefully dissected out and embedded in OCT at liquid N_2 temperature since cryofixation is recognized as the sample preparation protocol that best preserves the tissue structures and elemental speciation [35]. Thin (10-μm-thick) sections were cut using a cryostat, placed onto glass microscope slides, and immediately covered with 4-μm-thick Ultralene® foil. The tissue sections were transported in dry ice to the European Synchrotron Radiation Facility (ESRF; www.esrf.com), where they were stored until the scheduled experiments at −20 °C. Prior to data collection, samples were allowed to reach room temperature and were dried for 30 min under a gentle N_2 flow in order to prevent oxidation events, then transferred in N_2 atmosphere to the X-ray microscope where they were measured in high vacuum. This method was preferred to freeze drying since the samples could constantly be kept in inert atmosphere; on the contrary, when transferred from the cryostat to the freeze dryer, the samples are exposed to air at room temperature, which may be responsible for artifacts detected in S speciation [35].

X-ray spectro-microscopy measurements

Measurements were performed at beamline ID21 of the ESRF, at room temperature and under high vacuum ($\approx 10^{-5}$ mbar). In order to acquire S K-edge XANES spectra, the beam size was set to 50 μm with a pinhole providing a flux of 1.4×10^9 photons/s. The energy range 2,460–2,530 eV was scanned at 0.25-eV steps with a fixed-exit double crystal Si(111) monochromator ($\Delta E/E \sim 10^{-4}$). The energy scale was calibrated with a $CaSO_4 \cdot 2H_2O$ standard (main peak at 2,482.7 eV). Each spectrum was acquired as the sum of 20 subsequent scans, at 0.1 s/energy point resulting in a total integration time of 2 s/energy. The exposure time was therefore 28 s per scan and 10 min per spectrum. Comparisons of subsequent scans

confirmed that no radiation damage occurred, and averaging of 20 individual scans was carried out to improve the signal-to-noise ratio. For the acquisition of μ-XRF maps, the X-ray beam was focused to 0.9×0.2 μm^2 (H×V) by means of a Tungsten Fresnel Zone Plate lens, giving a flux at sample of 3.0×10^9 photons/s. Different maps were collected at the fixed energies of 2,473.6 eV (thiols and monosulfides), 2,482.7 eV (sulfates), and 2,510.0 eV (post-edge for normalization), with a step size of 1×1 μm^2. The dwell time per pixel was chosen after measuring the kinetics of radiation damage in our conditions of flux and beam size: two spots were irradiated at 2,482.7 eV (sulfates) and at 2,473.6 eV (thiols and monosulfides), respectively, and their fluorescence signals collected at constant time intervals; after 500 ms, the signals due to sulfates and thiols were comparable to the ones acquired in unfocused mode, while after longer integration times the signal from sulfates rapidly drops and the one from thiols and monosulfides increases, suggesting that photoreduction occurs; the dwell time for μ-XRF maps was therefore set to 500 ms. The XRF signal from the sample, for both XANES and μ-XRF measurements, was collected with a large active area (80 mm^2) energy dispersive SDD detector [XFlash 5100 from Bruker (Germany)].

Data analysis

XANES spectra were background-subtracted and normalized by their post-edge linear trend. Least-square fits were performed with Fityk [36], defining a fitting model composed of two arctangent curves to mimic the jump at the absorption edge and five Gaussian curves: one for each significant species of S and one for the multiple scattering cumulative contribution at ~2,497.0 eV. The areas of the best-fitting peaks were calculated and multiplied by a weighting factor provided by Prietzel et al. [37], which accounts for the variation in the absorption cross section per unit mass with the S oxidation state: the white line areas, indeed, do not only depend on the amount of the corresponding species in the sample but also increase linearly with the electronic oxidation state; this linear relationship has been extracted from the measurements of a set of standard compounds representing all the existing oxidation states of S by, among others, Prietzel et al. [37]. The weighted areas of the Gaussian peaks are therefore only proportional to the amount of the corresponding S species: the relative amount of each S species was calculated as the ratio between the weighted area of its resonance peak and the sum of the weighted areas of the four single scattering peaks. μ-XRF maps were analyzed with PyMca software [38]. Individual atomic distributions were retrieved through a least-square fit of the XRF spectra of each pixel, and then normalized by the measured incoming current to correct for beam decay during map acquisition.

Results and discussion

Corneal tissue is composed of five different layers, differing in their biochemical composition and physico-chemical properties, namely epithelium, Bowman's layer, stroma, Descemet's membrane, and endothelium; Fig. 1 illustrates the localization of the cornea in the eye, as well as the distinction of the five layers along the depth. In order to investigate the depth-profiled chemical speciation of S in cornea, S K-edge XANES spectra were acquired across sections of mature bovine corneas, cut transversely, so that information could be obtained throughout the full stromal depth, from the anterior epithelial side (Fig. 2, left-hand side) to the deep stroma adjacent to the endothelium (Fig. 2, right-hand side). The distance between the centers of each successive X-ray spot was 50 μm, equal to the diameter of the spot size itself (Fig. 2). Figure 3 shows the first four and the last two XANES spectra from Fig. 2, normalized by their respective edge jumps. The origin of the distances is set to the interface between the epithelium and stroma. The spectrum labeled *n* μm refers to a probed circular region whose diameter extends from *n* to *n*+50 μm from the epithelium. The relative intensity of the different spectral features varies significantly in the first 50 μm of the stroma, after which it shows an almost constant configuration down to the deep stroma on the endothelial side of the cornea. The spectra relative to the positions between 150 μm and 550 μm from the epithelium are not reported for simplicity because their spectral features are virtually identical to the ones encountered before and after. Four main peaks are distinguishable in the spectra, and their energy positions indicate the chemical forms of S responsible for them [30, 32, 37]. The first resonance, peaked at ≈2,473.6 eV, is due to organic monosulfides (R-S-R) and thiols (R-S-H). These are essential components of corneal proteins. The second, peaked at ≈2,476.3 eV, is due to sulfoxide groups R-S(=O)-R. The third, at ≈2,481.1 eV, is attributed to sulfonate $R\text{-}S(=O)_2O^-$, and the fourth, at ≈2,482.7 eV, to sulfates SO_4^{2-}. The feature at ≈2,497.0 eV arises from cumulative multiple scattering contributions of all S species. A qualitative observation of the trend of resonance peaks in Fig. 3 suggests an heterogeneity in the composition of S species in the first ≈50 μm of stromal depth. The protein peak is prominent in the region adjacent to the epithelium and reaches a stable minimum around 50 μm, while the SO_4^{2-} peak shows the opposite trend. Part of the compositional change in the most anterior part of the corneal stroma can possibly be attributed to the fact that the stroma is anatomically different at its anterior-most aspect as compared to the rest of the cornea. In bovine cornea, as in the corneas of other animals (particularly large creatures, including humans) the anterior-most stroma on which the corneal epithelial sits is known as Bowman's layer, an acellular condensation of the stromal matrix. The collagen fibrils in this part of the stroma do not assume the characteristic corneal organization, but are

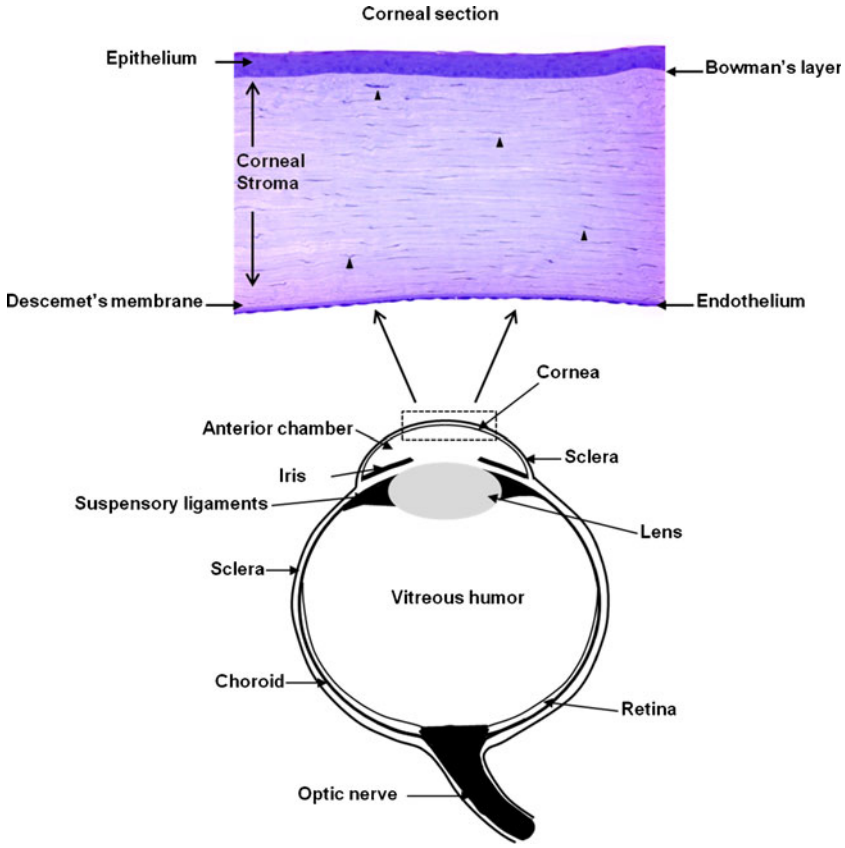

Fig. 1 Structure of the cornea. A schematic diagram of the eye and the major structures is shown at the bottom. The cornea is the transparent tissue that covers the front of the eye and is composed of five layers. The tough white layer of the eye is the sclera and along with the cornea this forms the outer tunic of the eye. Toluidine blue-stained section of a corneal section is shown at the *top*; this image was kindly provided by Dr. R. Young, Cardiff University. The layers from outer to inner are the epithelium, Bowman's layer, stroma, Descemet's membrane, and endothelium layer. *Arrowheads* indicate stromal keratocytes

disorganized and form a fairly dense network of fibrils devoid of keratocytes, the stromal cells. As stated, sulfated glycosaminoglycans influence corneal fibril organization so it would not be unexpected if the molecular character of proteoglycans and glycosaminoglycans were to be altered in Bowman's layer as suggested by the present results. Details of glycosaminoglycan sulfation patterns in Bowman's layer are sparse

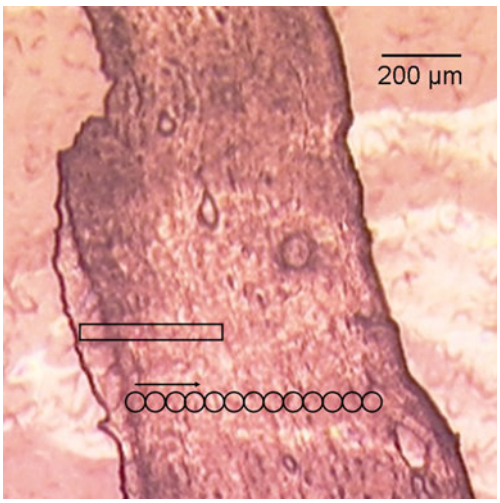

Fig. 2 Optical micrograph of a 10-µm-thick bovine cornea transversal cut; the epithelium is visible on the left-hand side. The circular regions represent the 50×50 µm^2 spots interrogated with XANES spectroscopy; the order of acquisition from the epithelium to the endothelium is indicated by the *arrow*. The rectangular region highlights one of the chosen areas for µ-XRF mapping

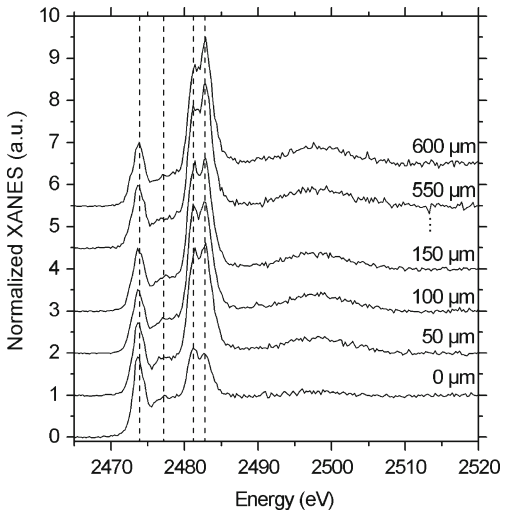

Fig. 3 Sulfur K-edge XANES spectra acquired with a 50-µm-diameter X-ray beam at different positions throughout the bovine corneal stroma depth; starting from the position adjacent to the epithelium, taken as the origin of the distances, the centers of the interrogated regions are placed at 50-µm distance from each other (labeled as 50 µm, 100 µm, 150 µm…). *Dotted straight lines* identify the four resonance peaks due to the main S chemical species common to all spectra

because biochemical quantification is difficult owing to the thickness of Bowman's layer, which in humans is 10–12 μm thick and 5 μm thick in cows. Some studies using immuno-electron microscopy, however, have shown lower numbers of nanogold particles in Bowman's layer as compared to the stroma of the human cornea when the nanogold is tagged to antibodies which recognize hepta- or larger oligosaccharides of the 6-*O*-sulfated-poly-*N*-acetylglucosamine chain of keratan sulfate or an epitope in native chondroitin 4- and 6-sulfate chains [39]. This might be indicative of an altered sulfation status of the major glycosaminoglycan subtypes in Bowman's layer, which in turn might be related to the heterogeneity in S reported here. Differential proteoglycan characteristics in Bowman's layer are possibly a result of embryonic development because immunohistochemistry of the chick cornea just before hatch reveals a clear non-labeled region of the anterior, sub-epithelial cornea extending 20 μm or more when the tissue is stained for keratocan, a keratan sulfate proteoglycan [40]. The current data indicate altered sulfation patterns in the anterior 50 μm of the stroma, a tissue region which encompasses Bowman's layer, extending posteriorly into the corneal stroma itself. This is indicative of a transition zone in terms of S status, which shows that the demarcation between Bowman's layer and the stroma is not very abrupt.

In order to turn this information into quantitative results, a GCF approach was undertaken [28–30, 37]. An example of fit to the experimental data is presented in Fig. 4 where the individual curves composing the fitting models are shown as colored lines and the curve arising from their sum is shown as a black line. The model exhibits an excellent agreement with the experimental data (dots). Two arctangent functions were chosen to reproduce the cumulative jump at the absorption edge (dark-green line in Fig. 4), according to the protocol validated by Huffman et al. [29] for the deconvolution of multi-component S K-edge XANES spectra in coal samples. The centers of the two arctangents were set to 2,477.0 and 2,483.0 eV to mimic the jump due to reduced (R-S-H/R-S-R and R-S(=O)-R) and oxidized (R-S(=O)$_2$O$^-$ and SO_4^{2-}) species, respectively, while the height and width of their steps were allowed to vary during the fit. The centers of the Gaussian curves were initially set to the energy values determined by Bohic et al. [32] in neuromelanin, where the main encountered S species are the same as in the present study. For each Gaussian curve, the width, height, and central value were allowed to vary during the fit. The convergence of the central values to energy values within ±1.0 eV with respect to the initial guesses was checked, and the fit was rejected in case of higher divergence. The best-fitting values for the white line resonance peaks of the different S species are reported in Table 1, together with a collection of values from previous studies, retrieved both computationally through GCF [30, 37] and by experimental measurements of standard compounds [32]. Considering that an energy shift of the order of 0.5 eV can occur in the white-line energy of a S species when it experiences different molecular environments, our values are in very good agreement with others reported in literature. The errors on these values, calculated by the fitting program as the mean square distance between the best-fitting curve and the experimental data, are of the order of 0.05 eV. Such a low value is due to the high signal-to-noise ratio experimental data and to the robustness of the fitting model. However, this value is negligible with respect to the intrinsic resolution of the monochromator at the S K-edge energy, which is ≈0.24 eV. The final error associated to our results stems, therefore, from the intrinsic instrumental error.

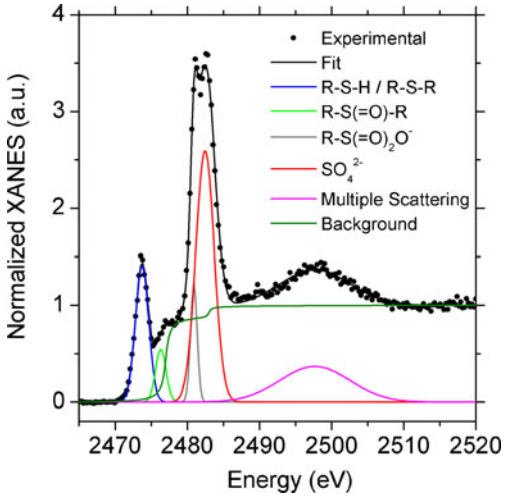

Fig. 4 Example of fit (*continuous black line*) to the experimental data (*black dots*); the experimental spectrum was collected in the stroma, 100 μm away from the epithelium. The individual curves composing the fitting model are reported as *colored lines*

Once the different Gaussian components of the XANES spectra had been decomposed through least-square fitting, their areas were calculated and weighted to quantify the relative amount of each species. This operation was carried

Table 1 Energy values (eV) of the resonance peaks due to different sulfur species in S K-edge XANES spectra

	This study	Bohic et al. (2008) [32]	Prietzel et al. (2003) [30]	Prietzel et al. (2011) [37]
R-S-H/R-S-R	2,473.7 ± 0.2	2,473.6	2,473.4	2,473.5 ± 0.2
R-S(=O)-R	2,476.5 ± 0.2	2,476.3	2,475.8	2,476.2 ± 0.2
R-S(=O)$_2$O$^-$	2,480.8 ± 0.2	2,481.1	2,481.3	2,481.3 ± 0.1
SO_4^{2-}	2,482.4 ± 0.2	2,482.7	2,482.5	2,482.7 ± 0.1

Values collected from the literature are associated to an error when this was reported in the original study

out for the XANES spectra reported in Fig. 3, and a graphical representation of the results is shown in Fig. 5. The outcome is a series of profiles throughout the whole stromal depth, which represents the percentage of each S species over the total amount of S, as a function of the position in the stroma. The profiles confirm and quantify the qualitative arguments derived from the observation of normalized spectra, which are shown in Fig. 3. The first 50 μm of the anterior-most stroma displays a peculiar distribution of S species, as discussed earlier, while from a depth of about ≈100 μm from the epithelium down to endothelium an almost constant composition (within experimental error) is encountered, consisting of a 41±1 % contribution from thiols and organic monosulfides (i.e., S from proteins), 8±1 % from sulfoxides, 9±1 % from sulfonates, and 42±1 % from sulfates; the small variations in the relative peak highs of these spectra, visible in Fig. 3, do not translate into a significant variation of the peak areas. The analysis of the XANES spectra acquired on a separate corneal section using the same experimental and analytical protocols, not reported to avoid redundancy, returns the same percentages within the error. The profiles shown in Fig. 5 also reveal the existence of a protein-rich and sulfate-depleted region in the first 50–100 μm of the stroma, where the S contribution is 57.2±0.7 % due to thiols and monosulfides, and 16.0±0.9 % due to sulfates. The fairly consistent distribution of S species below about 100 μm of the corneal stroma through to the posterior-most stromal layers is interesting and suggests that the different sulfation status of the major glycosaminoglycans in the cornea (keratan sulfate and chondroitin sulfate/dermatan sulfate) with corneal depth [19, 20] either has (1) little impact on overall S species distribution or (2) the glycosaminoglycan changes with increasing stromal depth (i.e., an increased sulfation of keratan sulfate and a decreased sulfation of chondroitin sulfate/dermatan sulfate) combine so as to negate any overall effect on overall S speciation.

The distribution of S species in thin sections of the corneal stroma was further investigated at the micrometer scale by means of μ-XRF chemical contrast imaging. The principle of this technique is based on the acquisition of μ-XRF maps of the same sample area at different energies that correspond to the maxima of absorption in the XANES spectra due to the S species of interest. The aim is to enhance the X-ray absorption of one species at a time, and to do this we focused on the protein and sulfate contributions, acquiring maps at 2,473.7 eV and 2,482.4 eV, respectively. These maps, when divided pixel by pixel for a map acquired at a post-edge energy (2,510.0 eV), represent the spatial distribution of the edge-jump due to the species of interest, i.e., they represent a quantity proportional to the amount the species itself [34]. The chosen map areas were located away from the sample regions interrogated with XANES spectroscopy which was done to avoid previously irradiated regions and to check if the S species distribution trends are constant depending on the location along the corneal diameter. The XRF contributions of the different elements were decomposed, providing individual distributions for S and phosphorous (P) in both the protein-enhanced and sulfate-enhanced maps. The co-localization of the two elements in one of the chosen regions is shown in Fig. 6, where the map area is 360×40 μm^2 and its position in the sample is visualized by a rectangle in Fig. 2. Both maps reported in Fig. 6 were normalized by the one acquired at 2,510.0 eV and by the incoming current.

The upper map in Fig. 6, which was acquired at 2,482.4 eV with the aim of enhancing the sulfate distribution (red), reveals a sulfate-depleted and thiol-rich region adjacent to the epithelium. When sulfates are represented simultaneously with P

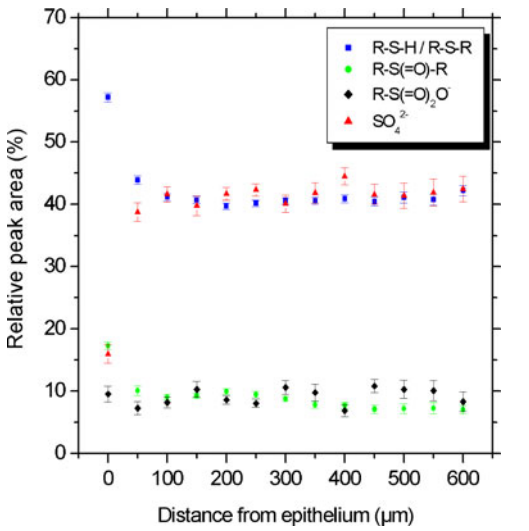

Fig. 5 Relative percentage of the different sulfur chemical species in stroma with respect to the total S amount, as a function of the distance from the epithelium. The four main species identified are thiol and organic monosulfide (R-S-H and R-S-R, *blue squares*), sulfoxide (R-S(=O)-R, *green circles*), sulfonate (R-S(=O)$_2$O$^-$, *black diamonds*), and sulfate (SO_4^{2-}, *red triangles*)

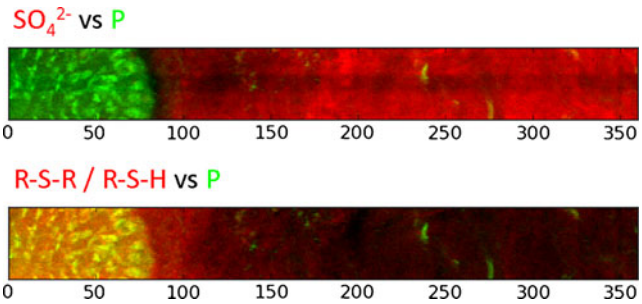

Fig. 6 Spatial distribution of S (*red*) and P (*green*) extracted from μ-XRF maps in a 360×40 μm^2 region of a bovine cornea cut scanned with 1×1 μm^2 steps. The incoming X-ray beam energy was initially set to 2,482.4 eV (*upper map*) and then to 2,473.7 eV (*lower map*) to enhance the absorption from the sulfate and thiol/monosulfide groups, respectively. The scale reported on the horizontal axis is in micrometers

(green), no co-localization is found. We also discovered that in the deep stroma sulfates are prominent, while P is present only as isolated micrometric spots, presumably identifiable as keratocytes, the corneal fibroblast cells. In the epithelium (left-hand side), P is constantly present, while sulfates are absent. The lower map in Fig. 6, acquired at 2,473.7 eV to enhance thiols and monosulfides (red), shows again a uniform distribution in the deep stroma, but the region adjacent to the epithelium is now rich in the exalted species. The yellow color in the epithelium indicates a clear co-localization between thiols/monosulfides (red) and P (green), which belong, therefore, to the same molecules. The results of the μ-XRF chemical contrast imaging confirm and complement the XANES spectroscopy results. Merging the results from the two techniques allows us to conclude that S groups from proteins and sulfates exhibit a constant concentration in the deep stroma of the mature cornea, corresponding to 41±1 % and 42±1 % of total S, respectively. Moreover, an abrupt variation in the relative concentration of S groups from proteins and sulfates is encountered in a tissue region, a few tens of micrometers deep adjacent to the corneal epithelium, where values vary up to 57.2±0.7 % and 16.0±0.9 %, respectively.

Concluding remarks

This study applied a combination of X-ray absorption near edge structure and micro-beam X-ray fluorescence chemical contrast imaging to the investigation of sulfur chemical speciation and elemental distribution in mature bovine cornea. The employed analytical methods yielded the relative percentage of each sulfur species in the tissue, and allowed disclosing their spatial distribution and co-localization with phosphorus at the micrometric scale, from the anterior subepithelial region into the deep stroma. The clear advantage of this approach with respect to histochemical and immunochemical techniques is that it does not require staining or labeling, leaving therefore the biochemical signature of the tissue unaltered.

This study lends novel insights into the elemental physiology of the cornea, especially that of sulfur, and, more in general, highlights experimental and analytical approaches for the study of biological tissues. The conceivable developments are multifold: from the extension to other mammalians, including humans, to the comparative investigation of healthy and diseased tissue.

Acknowledgments The authors would like to express their gratitude to Dr. Rob Young and Ms. Frances Jones for help with specimen preparation, and also acknowledge the ESRF (http://www.esrf.eu) for providing access to synchrotron radiation facilities. This work is supported by a project grant from the UK Engineering and Physical Sciences Research Council (grant number EP/F034970 to AJQ). EK is the recipient of a Cardiff University President's Studentship.

References

1. Komai Y, Ushiki T (1991) The three-dimensional organization of collagen fibrils in the human cornea and sclera. Investig Ophthalmol Vis Sci 32:2244–2258
2. Hogan MJ, Alvarado JA, Weddell JE (eds) (1971) The cornea. In: Histology of the human eye. An atlas and textbook. Saunders, Philadelphia
3. Maurice DM (1957) The structure and transparency of the corneal stroma. J Physiol 136:263–286
4. Hart RW, Farrell RA (1969) Light scattering in the cornea. J Opt Soc Am 59:766–774
5. Benedek GB (1971) Theory and transparency of the eye. Appl Optics 10:459–473
6. Sayers Z, Whitburn SB, Koch MHJ, Meek KM, Elliott GF (1982) Synchrotron X-ray diffraction study of corneal stroma. J Mol Biol 160:593–607
7. Worthington CR (1984) The structure of the cornea. Q Rev Biophys 17:423–451
8. Worthington CR, Inouye H (1985) X-ray diffraction study of the cornea. Int J Biol Macromol 7:2–8
9. Freund DE, McCally RL, Farrell RA (1986) Direct summation of fields for light scattering by fibrils with applications to normal corneas. Appl Optics 25:2739–2746
10. Scott JE, Haigh M (1985) 'Small'-proteoglycan:collagen interactions: keratan sulphate proteoglycan associates with rabbit corneal collagen fibrils at the 'a' and 'c' bands. Biosci Rep 5:765–774
11. Meek KM, Elliott GF, Nave C (1986) A synchrotron X-ray diffraction study of bovine cornea stained with cupromeronic blue. Coll Relat Res 6:203–218
12. Knupp C, Pinali C, Lewis PN, Parfitt GJ, Young RD, Meek KM, Quantock AJ (2009) The architecture of the cornea and structural basis of its transparency. Adv Prot Chem Struct Biol 78:25–49
13. Lewis PN, Pinali C, Young RD, Meek KM, Quantock AJ, Knupp C (2010) Structural interactions between collagen and proteoglycans are elucidated by three-dimensional electron tomography of bovine cornea. Structure 18:239–245
14. Parfitt GJ, Pinali C, Young RD, Quantock AJ, Knupp C (2010) Three-dimensional reconstruction of collagen–proteoglycan interactions in the mouse corneal stroma by electron tomography. J Struct Biol 170:392–397
15. Bettelheim FA, Plessy B (1975) The hydration of proteoglycans of bovine cornea. Biochim Biophys Acta 381:203–214
16. Bettelheim FA, Goetz D (1976) Distribution of hexosamines in bovine cornea. Investig Ophthalmol 15:301–304
17. Castoro JA, Bettelheim AA, Bettelheim FA (1988) Water gradients across bovine cornea. Investig Ophthalmol Vis Sci 29:963–968
18. Borcherding MS, Blacik LJ, Sittig RA, Bizzell JW, Breen M, Weinstein HG (1975) Proteoglycans and collagen fibre organization in human corneoscleral tissue. Exp Eye Res 21:59–70
19. Scott JE, Haigh M, Ali P (1988) Keratan sulphate is unevenly distributed from back to front of bovine cornea. Biochem Soc Trans 16:333–334
20. Scott JE, Bosworth TR (1990) A comparative biochemical and ultrastructural study of proteoglycan–collagen interactions in corneal stroma. Biochem J 270:491–497
21. Hayashida Y, Akama TO, Beecher N, Lewis P, Young RD, Meek KM, Kerr B, Hughes CE, Caterson B, Tanigami A, Nakayama J, Fukada MN, Tano Y, Nishida K, Quantock AJ (2006) Matrix morphogenesis in cornea is mediated by the modification of keratan sulfate by GlcNAc 6-O sulfotransferase. Proc Natl Acad Sci USA 103:13333–13338
22. Young RD, Gealy EC, Liles M, Caterson B, Ralphs JR, Quantock AJ (2007) Keratan sulfate glycosaminoglycan and the association with collagen fibrils in rudimentary lamellae in the developing avian cornea. Investig Ophthalmol Vis Sci 48:3083–3088

23. Liles M, Palka BP, Harris A, Kerr B, Hughes CE, Young RD, Meek KM, Caterson B, Quantock AJ (2010) Differential relative sulfation of keratan sulfate glycosaminoglycan in the chick cornea during embryonic development. Investig Ophthalmol Vis Sci 51:1365–1372
24. Zhang Y, Schmack I, Dawson DG, Grossniklaus HE, Conrad AH, Kariya Y, Suzuki K, Edelhauser HF, Conrad GW (2006) Keratan sulfate and chondroitin/dermatan sulfate in maximally recovered hypocellular stromal interface scars of postmortem human LASIK corneas. Investig Ophthalmol Vis Sci 47:2390–2396
25. Conrad AH, Zhang Y, Walker AR, Olberding LA, Hanzlick A, Zimmer AJ, Morffi R, Conrad GW (2006) Thyroxine affects expression of KSPG-related genes, the carbonic anhydrase II gene, and KS sulfation in the embryonic chicken cornea. Investig Ophthalmol Vis Sci 47:120–132
26. Pang W, Ahmadzai AA, Patel II, Qiu X, Liles M, Quantock AJ, Martin FL (2012) Alterations in the biomolecular signatures of developing chick corneas as determined by biospectroscopy and multivariate analysis. Invest Ophthalmol Vis Sci 53:1162–1168
27. Koudouna E, Veronesi G, Patel II, Cotte M, Knupp C, Martin FL, Quantock AJ (2012) Chemical composition and sulfur speciation in bulk tissue by X-ray spectroscopy and X-ray microscopy: corneal development during embryogenesis. Biophys J 103:357–364
28. Xia K, Weesner F, Bleam WF, Bloom PR, Skyllberg UL, Helmke PA (1998) XANES studies of oxidation states of sulfur in aquatic and soil humic substances. Soil Sci Soc Am J 62:1240–1246
29. Huffman GP, Mitra S, Huggins FE, Shah N, Vaidya S, Lu F (1991) Quantitative analysis of all major forms of sulfur in coal by X-ray absorption fine structure spectroscopy. Energy Fuel 5:574–581
30. Prietzel J, Thieme J, Neuhäusler U, Susini J, Kögel-Knabner I (2003) Speciation of sulphur in soils and soil particles by X-ray spectromicroscopy. Eur J Soil Sci 54:423–433
31. Pickering IJ, George GN, Yu EY, Brune DC, Tuschak C, Overmann J, Beatty JT, Prince RC (2001) Analysis of sulfur biochemistry of sulfur bacteria using X-ray absorption spectroscopy. Biochemistry 40:8138–8145
32. Bohic S, Murphy K, Paulus W, Cloetens P, Salomé M, Susini J, Double K (2008) Intracellular chemical imaging of the developmental phases of human neuromelanin using synchrotron X-ray microspectroscopy. Anal Chem 80:9557–9566
33. Fayard B, Fay N, David G, Doucet J, Melki R (2006) Packing of the prion Ure2p in protein fibrils probed by fluorescence X-ray near-edge structure spectroscopy at sulfur K-edge. J Mol Biol 356:843–849
34. Pickering IJ, Sneeden EY, Prince RC, Block E, Harris HH, Hirsch G, George GN (2009) Localizing the chemical forms of sulfur in vivo using x-ray fluorescence spectroscopic imaging: Application to onion (*Allium cepa*) tissues. Biochemistry 48:6846–6853
35. Hackett MJ, Smith ES, Paterson PG, Nichol H, Pickering IJ, George GN (2012) X-Ray absorption spectroscopy at the sulfur K-edge: a new tool to investigate the biochemical mechanism of neurodegeneration. ACS Chem Neurosci 3:178–185
36. Wojdyr M (2010) Fityk: a general-purpose peak fitting program. J Appl Crystallogr 43:1126–1128
37. Prietzel J, Botzaki A, Tyufekchieva N, Brettholle M, Thieme J, Klysubun W (2011) Sulfur speciation in soil by S K-edge XANES spectroscopy: comparison of spectral deconvolution and linear combination fitting. Environ Sci Technol 45:2878–2886
38. Solé VA, Papillon E, Cotte M, Walter P, Susini J (2007) A multiplatform code for the analysis of energy-dispersive X-ray fluorescence spectra. Spectrochim Acta B 62:63–68
39. Bairaktaris G, Lewis D, Fullwood NJ, Nieduszynski IA, Marcyniuk B, Quantock AJ, Ridgway AEA (1998) An ultrastructural investigation into proteoglycan distribution in human corneas. Cornea 17:396–402
40. Gealy CE, Kerr BC, Young RD, Tudor D, Hayes AJ, Hughes CE, Caterson B, Quantock AJ, Ralphs JR (2007) Differential expression of the keratan sulfate proteoglycan, keratocan, during chick corneal embryogenesis. Histochem Cell Biol 128:551–555